Università degli Studi di Ferrara

Doctoral course in Engineering science

Computational Modelling of the Mechanobiology of Cell Migration: from Durotaxis to Cell Invasion

Author
Gino Antonio Reho

Advisor
Prof. Elena Benvenuti

Co-Advisor
Prof. Marino Arroyo Balaguer

Year 2022/2025

38° Cycle

Università degli Studi di Ferrara

DOCTORAL COURSE IN ENGINEERING SCIENCE

CYCLE XXXVIII

COORDINATOR Prof. Pier Ruggero Spina

COMPUTATIONAL MODELLING OF THE MECHANOBIOLOGY OF CELL MIGRATION: FROM DUROTAXIS TO CELL INVASION

Scientific/Disciplinary Sector (SDS): CEAR-06/A

Candidate
Gino Antonio Reho

Supervisor
Prof. Elena Benvenuti

Co-Supervisor
Prof. Marino Arroyo Balaguer

Year 2022/2025

This thesis is dedicated to my grandmother.
I miss you.

"I would rather have questions that can't be answered
than answers that can't be questioned."
- Richard Feynman

Acknowledgements

MANY are the people to whom I wish to express my deepest gratitude, both formally and personally, for having contributed in diverse and significant ways to the realization of this PhD thesis.

First and foremost, I wish to express my deepest and most heartfelt gratitude to Professor Elena Benvenuti. Her constant and tireless guidance, combined with her inexhaustible passion for research, has accompanied me throughout my entire doctoral journey. She taught me, through her example, what it truly means to be a scientist and a researcher. I will be forever grateful for the trust she placed in me, for the time she dedicated, and for the invaluable opportunities she offered, beginning with the chance to pursue this Ph.D. in such an interesting field. My second thanks go to Professor Massimiliano Fraldi and Stefania Palumbo. Collaborating with them, particularly during the initial phase of my journey, was exceedingly instructive and, at the same time, extremely pleasant. I sincerely hope that new and fruitful opportunities for scientific collaboration will arise in the future. During my PhD, I had the invaluable opportunity to undertake a visiting period at the Universitat Politècnica de Catalunya in Barcelona. Here, I had the pleasure and honor of working with Professor Marino Arroyo Balaguer. I sincerely thank him for welcoming me into his research group and for the time he dedicated to me, both during my stay in Spain and through subsequent and productive remote meetings. I hope to be able to continue my career with the same passion he has demonstrated for his work. I thank my colleague Pau Blanco, PhD student in Professor Arroyo's group. Pau is one of the most talented researchers I have met during my journey. I thank him for the time he dedicated to me at the beginning of my visit, for solving my problems with the Hiperlife software, and for the continuous and stimulating exchange of ideas that has occurred ever since. I wish him the best for the conclusion of his doctorate and for his future career. A special thanks goes to my PhD colleagues and friends: Agnese, Franziska, Stefanos, Arash, Eduard, Kimia, Shardool, and Luan. I was happy to be their colleague, and I thank them for the time spent together and for the countless coffees we consumed.

Beyond the acknowledgments concerning the academic environment, there are other equally important debts of gratitude that I wish to settle here. I deeply thank my parents, who, even from a distance, have always supported me with their unconditional love throughout these years. Thank you, Mom, for always pushing me towards maximum independence, especially with your famous "vai a cercare sul dizionario!" Thank you, Dad, for teaching me that anything is possible "con l'arte, la scienza e un po' di pazienza." These two phrases of yours have constantly accompanied me throughout my years of study and will continue to guide me in my life. Finally, I want to thank Alice, my girlfriend. Her unconditional support and love have been the common denominator of these years, and especially during the last (and most demanding) period of thesis writing. Your words, "Tu dai il massimo e vedrai che andrà tutto bene," were particularly appreciated (even if not effective). I hope to share with you the same joy and the same love we have shared during this period, throughout all the years ahead.

Ringraziamenti

Molte sono le persone verso cui desidero esprimere la mia profonda gratitudine, sia in ambito formale che personale, per aver contribuito in modi diversie significativi alla realizzazione di questa tesi di dottorato.

Prima di tutto desidero esprimere la mia più profonda e sentita gratitudine, alla Professoressa Elena Benvenuti. La sua costante e instancabile guida, unita alla sua inesauribile passione per la ricerca, mi ha accompagnato lungo tutto il percorso di dottorato. Mi ha insegnato, con l'esempio, cosa significa realmente essere uno scienziato e un ricercatore. Le sarò per sempre riconoscente per la fiducia che ha riposto in me, per il tempo che mi ha dedicato e per le preziose opportunità che mi ha offerto, a partire dall'opportunità di perseguire questo Ph.D. in un campo così interessante. Un secondo ringraziamento va al Professore Massimiliano Fraldi e a Stefania Palumbo. Collaborare con loro, in particolare nella fase iniziale del mio percorso, è stato oltremodo istruttivo e allo stesso tempo estremamente piacevole. Auguro che si presentino in futuro nuove e fruttuose occasioni di collaborazione scientifica. Durante il dottorato ho avuto l'opportunità di svolgere un periodo di visiting presso l'Universitat Politècnica de Catalunya a Barcellona. Qui ho avuto il piacere e l'onore di lavorare con il Professor Marino Arroyo Balaguer. Lo ringrazio di cuore per avermi accolto nel suo gruppo di ricerca e per il tempo che mi ha dedicato, sia durante il mio soggiorno in Spagna sia attraverso i successivi e proficui meeting da remoto. Spero di poter continuare la mia carriera con la medesima passione che mi ha dimostrato per il suo lavoro. Ringrazio il collega Pau Blanco, PhD student del gruppo del Professor Arroyo. Pau è uno dei ricercatori più talentuosi che abbia incontrato nel mio percorso. Lo ringrazio per il tempo dedicatomi all'inizio del mio visiting, per aver risolto i miei problemi con il software Hiperlife e per il continuo e stimolante scambio di idee intercorso da allora. Gli auguro il meglio per la conclusione del suo dottorato e per il suo futuro professionale. Un ringraziamento speciale va ai miei colleghi e amici di dottorato: Agnese, Franziska, Stefanos, Arash, Eduard, Kimia, Shardool e Luan. Sono contento di essere stato loro collega, li ringrazio per il tempo passato insieme e per gli innumerevoli caffè consumati.

Oltre ai ringraziamenti che riguardano l'ambiente accademico, ci sono altri debiti di gratitudine, altrettanto importanti, che desidero quì saldare. Ringrazio profondamente i miei genitori che, anche se a distanza, mi hanno sempre sostenuto con il loro amore incondizionato in questi anni. Grazie Mamma, per avermi sempre spinto verso la massima indipendenza, specialmente con i tuoi celebri "vai a cercare sul dizionario!" Grazie Papà, per avermi insegnato che tutto è possibile "con l'arte, la scienza e un po' di pazienza." Queste vostre due frasi mi hanno costantemente accompagnato durante gli anni di studio e continueranno a guidarmi nella mia vita. Infine, voglio ringraziare Alice, la mia ragazza. Il suo incondizionato supporto e il suo amore sono stati il denominatore comune di questi anni, e soprattutto dell'ultimo (e più faticoso) periodo di stesura della tesi. Particolarmente apprezzati (anche se non efficaci) sono stati i tuoi "Tu dai il massimo e vedrai che andrà tutto bene." Spero di poter condividere con te la stessa gioia e lo stesso amore che hanno caratterizzato questo periodo, in tutti quelli a venire.

Abstract

Cell migration has a pivotal role in physiological processes, such as embryonic development and wound healing, as well as in pathological processes, including angiogenesis and cancer invasion. The mechanism governing this process relies on an internal force-generating machinery driven by actin-mediated protrusion, substrate adhesion, and cellular contraction. Particularly, the interaction between the focal adhesion complexes and the extracellular matrix allows the cell to sense and respond to chemical and physical stimuli from its surroundings, such as gradients in matrix stiffness. In pathological contexts, this migration can also become invasive, a process characterized by chemical- and force-induced remodeling of the matrix.

This thesis computationally investigates two fundamental aspects of this process. First, it will analyze the mechanical response of single cells to stiffness gradients of the extracellular environment, focusing on the recently observed and less understood phenomenon of negative durotaxis [Isomursu et al., 2022]. Second, it develops and validates a computational model that successfully reproduces cellular engulfment onto an extracellular matrix. This framework captures the dynamics of this process in both noninvasive physiological settings and during pathological invasion [Friedl and Alexander, 2011], which requires solving a complex two-moving-interface problem.

Our investigation of durotaxis employed a nonlinear tensegrity model of a contractile cell anchored by focal adhesion complexes. The system, composed of a tensile element in parallel with a buckling-prone component, is able to exchange forces with the surroundings through extracellular matrix-focal adhesion complexes, and the contractile kinematics is triggered by an inelastic contraction of the tensile component [Benvenuti et al., 2023]. This mechanical device was further enhanced to include the chemo-physical degradation process of the focal adhesion by employing an elastic-damaging cohesive law derived from a convex-concave pseudo-elastic potential. This improvement enables the investigation of both durotaxis (migration towards stiffer regions) and its opposite, negative durotaxis, or *mollitaxis*. Moreover, the derived traction-separation cohesive law enabled its use in finite element simulations, which showed the existence of an optimal stiffness

range where the contractile cells exert their maximum traction forces [Benvenuti and Reho, 2024].

To model tissue invasion, we formulate a continuum model of an active fluid (the tissue) surrounded by an external environment, interacting with a hyperelastic solid (the matrix) [Cicconofri et al., 2024]. This continuum model, framed within a Nitsche-Onsager variational formulation [Arroyo et al., 2018], accounts for the two primary engulfment mechanisms: mechanical indentation of the matrix due to active tissue tensionsa process akin to elastocapillarityand the chemical degradation of the matrix fibers, enabling the numerical investigation of the interplay between these phenomena and the resulting two-moving-interface problem. To model the complex fluid-solid system, our approach resorts to a hybrid fitted-CutFEM technique. This framework is built around the non-material moving interface between the fluid and the solid, which separates the computational domain into two subdomains. The subdomain corresponding to the solid is discretized using the Cut Finite Element Method (CutFEM) [Burman et al., 2015], with the cell aggregate finite element method (agFEM) [Badia et al., 2018b, 2021] for the stabilization of the small cut elements. The surrounding fluid subdomain is meshed with a body-fitted unstructured mesh, a choice dictated by the need for a mesh that allows for accurate local refinement at the two-phase fluid interface, whose evolution is governed by a phase-field model.

Together, these studies illustrate the critical importance of mechanical feedback in regulating cellular processes, from focal adhesion function in durotaxis to the interplay of forces and degradation during tissue invasion. The developed computational models provide excellent tools to investigate how cells mechanically sense, respond to, and remodel their surrounding environment in both physiological and pathological contexts. Moreover, the model's capacity to effectively manage complex two-interface problems allows its direct application to a wide range of problems in soft matter physics.

Contents

1 General introduction

1.1 Cell migration

Cell migration is a fundamental multistep process regulated by mechanical and chemical signals, crucial for the directed movement of a single cell or a group of cells. It supports a variety of phenomena that occur across all stages of the life cycle, including developmental, physiological, and pathological processes. From the initial phases of embryonic development, it assumes a pivotal role in tissue morphogenesis. Specifically, in the development of the nervous system, in the migration of muscle precursor cells, and notably during mammalian gastrulation, large groups of cells within the blastocyst migrate collectively as sheets to establish the three germ layers that constitute the embryo. Subsequently, these cells travel to various target regions, where they differentiate into specific cell populations, thus forming tissues and organs. [Lauffenburger and Horwitz, 1996, Horwitz and Webb, 2003, Scarpa and Mayor, 2016].

Although it is very prominent in the first stages of life, the ability of cells to migrate also persists throughout the life cycle of an individual. Indeed, an essential feature in cellular processes is the ability of some tissues to renew and repair themselves, whereby old or damaged cells are substituted through the migration of newly generated cells from underlying tissue layers, for instance, in the renewal process of skin and intestine or in the process of wound healing. Cell migration plays an analogous key role in the immune surveillance and response during infections, in which phagocytic cells migrate to the infected tissues and destroy the invading pathogens. Despite its essential role in the preservation of tissue health and homeostasis, cell migration also drives a variety of pathological conditions, including malignancies and inflammatory diseases, which are caused by undesirable migratory events. Typical examples include angiogenesis, osteoporosis, rheumatoid arthritis, mental retardation, tumor cell dissemination, and metastasis [Hall, 2009, Hideki et al., 2005, Lamalice et al., 2007, Peihong et al., 2018].

While the biological and chemical triggers are well-studied, cell migration is, at its core, a fundamental problem of physics and mechanics. A cell must generate internal forces via its cytoskeleton and actomyosin motors, transmit those forces through adhesive links to its surroundings, and sense the mechanical feed-

back from its complex environment in order to move. These convoluted processes cannot be fully understood by experimental observation alone; they require the development of analytical and computational models to decouple the contributing factors. However, the formulation of such predictive frameworks first requires a rigorous deconstruction of the physical engine driving motility. Whether traversing a two-dimensional surface or navigating a three-dimensional matrix, the cell relies on a recurring sequence of mechanical eventsprotrusion, adhesion, traction, and retraction. Defining these distinct biomechanical phases is the necessary prerequisite to understanding how cells adapt their locomotive strategies, from the adhesion-dependent crawling of mesenchymal cells to the pressure-driven squeezing of amoeboid invasion.

1.2 The mechanical basis of cell migration

The dynamic scaffold of a cell, known as the cytoskeleton, is composed of an active network of filaments (intermediate filaments, actin filaments, and microtubules) and motor proteins (like myosin). This network undergoes continuous remodeling through a stochastic addition or removal of monomers (polymerization/depolymerization) and the active ATP-dependent contraction of actomyosin motors. This coordinated remodeling, accompanied by numerous signaling pathways, allows the cell to change shape, exert forces, and ultimately move.

1.2.1 Mesenchymal cell migration: the 2D motility cycle

Mesenchymal migration is the paradigmatic mode of cellular motility, characteristically observed in fibroblasts, smooth muscle cells, and sarcoma cells. Phenotypically, it is defined by an elongated, spindle-shaped morphology, high cytoskeletal polarity, and strong adhesive coupling to the substrate [Friedl and Wolf, 2009] Unlike the rapid, gliding motion of amoeboid cells, mesenchymal migration is a relatively slow process driven by a specific architectural reorganization of the actin cytoskeleton.

On 2D surfaces, the migration mechanism typically follows the classical cyclic steps defined by Abercrombie et al. [1970] and Lauffenburger and Horwitz [1996], characterized by the following phases [Ridley et al., 2003]: The first step is characterized by the breaking of cellular symmetry, which leads to the polarization of the cytoskeleton, driven by internal signaling gradients (such as Rho GTPases, Cdc42, and Rac1). The establishment of polarity defines the leading edge (front) and trailing edge (rear) of the cell body. In the second step, the polymerization of actin filaments in the leading edge generates a protrusive force that pushes the cell membrane forward. The extension of the membrane is manifested through two distinct morphologies: lamellipodia, characterized by a dendritic-like branched network, and filopodia, consisting of long, finger-like, parallel bundles. In these structures, monomeric G-actin is assembled to form F-actin filaments. Specific regulatory components, Arp2/3 for branched networks and formins for linear bundles, coordinate this nucleation and polymerization to maintain the required architectural geometry [Pollard et al., 2000, Welch and Mullins, 2002]. The third

step is the engagement of the protrusion with the substrate, which is fundamental for stabilization. This interaction is mediated by integrins, a family of transmembrane heterodimeric receptors composed of α and β subunits, that bind to specific ligands in the extracellular matrix [Kolasangiani et al., 2022]. Initially, these interactions form nascent adhesions, small unstable clusters that form independently from the contraction Choi et al. [2008]. These nascent complexes, to effectively participate in the migration process, must mature into stable Focal Adhesions (FAs). This maturation is a force-dependent, mechanosensitive process involving the unfolding of proteins like talin, which reveals binding sites for reinforcing proteins like vinculin [Geiger et al., 2009]. The fourth step is characterized by the balance of intracellular forces and their transmission to the extracellular environment. The force balance of the migrating cell is governed by two opposing actin-driven processes. First, actin polymerization at the front generates a protruding force that pushes the actin against the membrane. Simultaneously, myosin II motors pull these filaments toward the cell center. The combination of this polymerization-dependent treadmilling and active myosin pulling creates a continuous rearward movement of the cytoskeleton known as retrograde flow [Lin et al., 1996, Gardel et al., 2008]. The mechanical coupling of this flow to the substrate is described by the molecular clutch model, originally hypothesized by Mitchison and Kirschner [1988], and subsequently formalized by Chan and Odde [2008]. When the focal adhesions, which are regarded as clutches, engage with the actomyosin complexes, they resist the retrograde flow. This resistance transforms the internal actomyosin energy into traction forces exerted on the substrate, which effectively pull the cell body forward. Finally, in the fifth step, for the cell to achieve net translocation, the adhesions at the trailing edge must be released. This step is regulated by RhoA-mediated contractility, which increases tension at the rear to promote the disassembly of old focal adhesions [Ridley et al., 2003]. Upon the removal of the rear adhesions, the trailing edge of the cell experiences elastic recoil, snapping forward toward the cell body.

This complex cycle highlights the critical interplay between internal tension and external stiffness, serving as the baseline for the mechanical models discussed in Part I.

1.2.2 3D invasive strategies

While the 2D cycle described above explains motility on flat surfaces, migration within a three-dimensional tissue imposes a fundamental physical constraint absent in 2D. Indeed, in a physiological environment, the Extracellular Matrix (ECM) acts as a physical barrier with specific pore sizes and stiffness. To navigate this dense network, cells must employ invasive strategies to overcome the confinement. These strategies are generally classified into two distinct physical modes based on how they handle the ECM barrier: the proteolytic (mesenchymal) mode and the non-proteolytic (amoeboid) mode [Wolf et al., 2003, Yamada and Sixt, 2019].

Proteolytic mesenchymal invasion

The 3D mesenchymal strategy is the direct extension of the 2D cycle into a volumetric environment, but with a critical addition: matrix remodeling. Since the pore size of the ECM is often smaller than the nuclear diameter, the generation of traction forces alone is insufficient for translocation. To overcome steric confinement, mesenchymal cells secrete Matrix Metalloproteinases (MMPs), enzymes that chemically degrade the surrounding collagen network [Friedl, 2004, Friedl and Wolf, 2009]. This proteolytic activity creates a tunnel or microtrack through the tissue, effectively widening the pores to accommodate the cell body. Mechanically, this mode is characterized by strong adhesion, governed by the binding between the integrins and the fibers, and active degradation, which, through enzymatic proteolysis, allows the matrix to degrade.

Amoeboid invasion

In contrast, amoeboid migration represents a low-adhesion, high-velocity strategy. While the amoeboid phenotype is heterogeneous, ranging from polymerization-driven gliding to pressure-driven blebbing [Lämmermann and Sixt, 2009], in the context of tissue invasion, it is best defined as a path-finding behavior that bypasses the need for proteolysis.

Mechanically, this mode often relies on propulsion via hydrostatic pressure. Driven by cortical contractility, the intracellular pressure increases, causing the membrane to bleb and flow forward [Paluch and Raz, 2013]. Crucially, this strategy relies on the cell's ability to mechanically push and deform the surrounding environment (indentation) rather than dissolving it (degradation).

From a physical standpoint, these two biological strategies represent a competition between distinct thermodynamic costs: the chemical cost of degrading the substrate (mesenchymal) and the elastic energy expenditure of substrate indentation (amoeboid). The concurrence of these two different mechanisms forms the basis of the continuum framework presented in Part II of this thesis. In that Part, we do not model the discrete pore-squeezing dynamics; instead, we treat tissue invasion as a macroscopic wetting phenomenon. We investigate how the active degradation of the matrix competes with the mechanical indentation driven by elastocapillary forces, determining whether the tissue invades by chemically consuming the substrate or by mechanically deforming it.

1.3 Thesis objectives and overview

In the broad scenario delineated by the complex multi-scale problem of cell migration, the primary objective of this thesis is to develop and apply a comprehensive suite of computational models to investigate the mechanical origins of motility. The research follows a logical progression of increasing complexity: scaling from the discrete internal mechanics of a single cell to the collective, continuum invasion of a tissue.

This thesis is structured into two distinct but complementary Parts, moving from discrete structural stability to continuum modelling, as schematically illustrated in Fig. 1.1.

Part I: mechanosensing and mechanotransduction in cells

Part I investigates the fundamental mechanisms of single-cell mechanotransduction. Based on the author's published works [Benvenuti et al., 2022, 2023, Benvenuti and Reho, 2024], this part establishes a unified mechanical framework to answer three specific questions:

1. **How does the cytoskeleton self-stabilize?** By developing a generalized nonlinear tensegrity framework, we aim to derive the stability conditions governing the antagonistic competition between actomyosin contractility and microtubule polymerization.
2. **How does asymmetry drive decision-making?** We seek to quantify how structural asymmetry and environmental external stiffness gradients drive the preferential migration and influence the adhesion dynamics.
3. **What drives the reversal of durotaxis?** By implementing elasto-damaging cohesive laws, we aim to elucidate the mechanism behind the transition from positive to negative durotaxis. The objective is to demonstrate that this reversal is not merely a biological choice but a deterministic consequence of adhesion failure on stiff substrates.

Part II: a mechanical model of tissue engulfment

While Part I resolves the static equilibrium of the single cell, it does not account for the dynamic, irreversible degradation of the matrix seen in pathological invasion. Part II addresses this limitation by upscaling the problem to the tissue level. Here, we present a novel, unpublished continuum framework based on Nitsche-Onsager variational principles. This Part aims to:

- Develop a thermodynamically consistent model for active tissue invasion that couples elastocapillarity (fluid-structure interaction) with matrix degradation.
- Investigate the competition between mechanical indentation (pushing) and degradation (dissolving), revealing how substrate stress states regulate the rate of tissue engulfment.
- Validate these numerical predictions against benchmarks, demonstrating the model's capacity to replicate complex multi-phase fluid flows on soft substrates.

Finally, Chapter 7 synthesizes the findings from both scales, discussing the limitations of the current approaches and outlining a roadmap for future research.

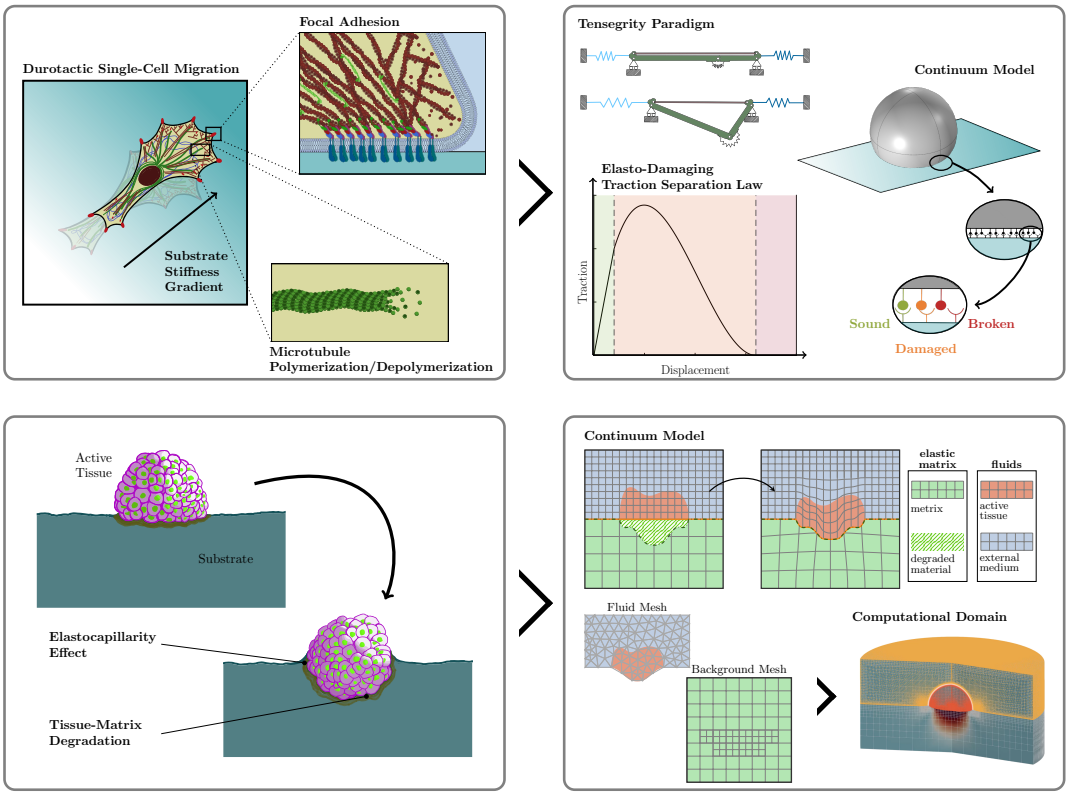

Figure 1.1: *Schematic overview of the thesis structure. The* ***top row****, corresponding to Part I of the thesis, illustrates the translation of biological cellular and subcellular mechanisms, such as cytoskeletal buckling, focal adhesion dynamics, and responses to stiffness gradients (left block), into engineering models, specifically discrete tensegrity paradigms, continuum models, and the elasto-damaging traction separation law (right block). The* ***bottom row****, corresponding to Part II of the thesis, depicts the study of collective tissue engulfment due to the mechanical indentation driven by the competition between elastocapillarity and active degradation (left block), modeled through a continuum and novel computational framework (right block).*

Part I

Mechanosensing and Mechanotransduction in Cells

This Part of this thesis synthesizes results of the following three published peer-reviewed articles:

- Benvenuti E., Reho G.A., Palumbo S. and Fraldi M., Pre-strains and buckling in mechanosensitivity of contractile cells and focal adhesions: A tensegrity device, *Journal of the Mechanical Behavior of Biomedical Materials*, 135:105413, 2022.
  doi: https://doi.org/10.1016/j.jmbbm.2022.105413

- Benvenuti E., Reho G.A., Palumbo S. and Fraldi M., Mechanics of tensegrity cell units incorporating asymmetry and insights into mollitaxis, *Journal of the Royal Society Interface*, 20:20230082, 2023.
  doi: https://doi.org/10.1098/rsif.2023.0082

- Benvenuti E. and Reho G.A., An elastic-damaging cohesive law for cell-substrate adhesion with positive and negative durotaxis. *Journal of the Mechanics and Physics of Solids*, 185:105569, 2024.
  doi: https://doi.org/10.1016/j.jmps.2024.105569

While these articles are the result of collaborative research, it is necessary to explicitly define the specific contributions of the candidate to distinguish them from the work of co-authors. The fundamental mechanical paradigm adopted in this work builds upon the methodology originally proposed by the co-authors in Palumbo et al. [2018, 2022]. However, starting from this conceptual baseline, the work presented in this thesis represents a substantial generalization and technical expansion of that framework. Although the candidate appears as the second author in these publications, the candidates contribution was central to the development of the mathematical models and the generation of results. Specifically, the candidates role is defined as follows:

- **Formal Analysis and Mathematical Derivation:** The candidate was responsible for the analytical derivation of the tensegrity equilibrium equations and the formulation of the asymmetric and elasto-damaging constitutive laws presented in Chapter 3.

- **Implementation:** The candidate solely developed and implemented the computational scripts required to solve the non-linear tensegrity systems.

- **Investigation and Validation:** All numerical simulations and data generation presented in this Part were performed by the candidate. The candidate was also responsible for the post-processing and physical interpretation of these numerical results.

- **Writing and Visualization:** The candidate produced all the figures and diagrams included in the manuscripts and played a primary role in writing the original drafts.

In summary, while the conceptualization was a joint effort with the co-authors, the operational execution, from mathematical derivation to numerical solution, is the original work of the candidate.

2

Introduction to Part I: modeling cell mechanics and mechanosensing

Part I of this thesis is dedicated to unraveling the fundamental mechanisms of cellular mechanosensing and mechanotransduction. In this introductory chapter, we establish the biological foundations of these processes, starting with the cytoskeletal architecture and the critical role of focal adhesion complexes. We then examine the various modes of directed cell migration, collectively known as taxis, with a specific focus on durotaxis, the directional movement guided by stiffness gradients. Subsequently, we review the state of the art in cell mechanics modeling, leading to the theoretical basis of the tensegrity model adopted in this work. Finally, we present the developed computational framework and outline the structure of the chapters that follow.

2.1 Cytoskeletal architecture: tension and compression

The cell migration cycle described in the General Introduction is not merely a kinematic process but a manifestation of complex internal mechanics. As defined by Fletcher and Mullins [2010], the cytoskeleton carries out three broad functions: it spatially organizes the cellular contents, it physically and biochemically connects the cell to the external environment, and it generates the coordinated forces required for shape change and motility. Despite the static connotations of the word “skeleton," this structure is not a fixed scaffold but a dynamic, adaptive composite whose polymers are in constant flux [Fletcher and Mullins, 2010, Gong et al., 2019]. This architectural complexity is built upon three distinct biopolymer families: actin filaments, microtubules, and intermediate filaments. While intermediate filaments provide essential structural continuity and resistance to large deformations [Herrmann et al., 2007], the cell's active mechanical state is primarily governed by the interplay between the first two: the contractile actin network and the resisting microtubules.

This load-bearing duality, where continuous tension is balanced by discontinuous compression, forms the physical basis of the Tensegrity (Tensional Integrity) model adopted in this work [Ingber, 1993, Sun et al., 2023].

2.1.1 Actomyosin contractility: the source of pre-stress

The actin cytoskeleton serves as the tensile element of the cellular structure. F-actin filaments, characterized by a persistence length of $\sim 17\mu$m, organize into distinct architectures depending on the presence of crosslinkers [Fletcher and Mullins, 2010]. While they form isotropic, branched meshes at the cell cortex to support the membrane, mechanical signaling is largely mediated by anisotropic bundles known as stress fibers [Pellegrin and Mellor, 2007]. Crucially, the assembly of these stress fibers is often triggered locally when cell-surface receptors (integrins) engage with the extracellular matrix [Fletcher and Mullins, 2010]. Unlike passive cables, these bundles are intrinsically active: molecular motors (Myosin II) slide filaments past one another, generating a macroscopic internal tension known as cellular pre-stress [Wang et al., 2001, Murrell et al., 2015]. From a mechanical standpoint, this pre-stress is the critical thermodynamic variable that stabilizes the cell shape. As demonstrated by Stamenović and Ingber [2002], the stiffness of the cell is linearly proportional to this pre-stress, a behavior characteristic of cable-net structures.

2.1.2 Microtubules: the active compressive struts

Balancing this tension are the microtubules (MTs), hollow cylindrical polymers composed of α- and β-tubulin. With a persistence length spanning millimeters [Gittes et al., 1993, Pampaloni et al., 2006], MTs are the stiffest filaments in the cell. They typically radiate from the centrosome, acting as compressive struts that resist the inward pull of the actin network. Biologically, MTs are highly dynamic. They exhibit dynamic instability, switching rapidly between phases of growth and catastrophic shrinkage to probe the cellular space [Mitchison and Kirschner, 1984, Bouchet et al., 2017]. However, within the context of the mechanical tensegrity models presented in this thesis, we focus on their structural role. We assume a separation of timescales where, during the maintenance of cell shape and steady migration, MTs act as persistent structural elements subject to mechanical loading rather than rapid disassembly. Given their high aspect ratio, MTs are prone to Euler buckling when this compressive load exceeds a critical threshold. In vivo observations confirm that MTs are frequently buckled, exhibiting short wavelength curvatures that defy thermal fluctuation theory [Soheilypour et al., 2015, Brangwynne et al., 2006, Robison et al., 2016]. A central hypothesis of this thesis is that this buckling is not a failure mode, but a homeostatic mechanism. As theoretically proposed by Stamenović and Ingber [2002] and formally integrated into the models in this Part, the transition to a post-buckled state allows the cytoskeleton to buffer large fluctuations in external stress, maintaining the structural integrity of the cell during migration.

2.2 The cell-substrate interface: focal adhesions

The forces generated by the internal pre-stress and by the cytoskeleton to drive migration must be transmitted to the extracellular matrix (ECM). This transmission occurs at focal adhesions (FAs) [Yamada and Geiger, 1997, Schoenwaelder

and Burridge, 1999, Geiger and Bershadsky, 2002], dynamic transmembrane junctions that act as the mechanical clutch of the cell [Kanchanawong et al., 2010, De Pascalis and Etienne-Manneville, 2017]. They operate as dynamic anchors that facilitate cytoskeletal rearrangements: at the leading edge, they stabilize actin polymerization to drive protrusion, while at the trailing edge, they transmit the actomyosin contractility required for cell body retraction.

2.2.1 Integrin activation and nascent adhesions

The molecular architecture of FAs is built upon integrins, transmembrane heterodimers composed of non-covalently associated α and β subunits. Their ectodomain binds extracellularly to ligands (e.g., fibronectin, collagen), while the cytoplasmic tail binds intracellularly to the actin cytoskeleton via adaptor proteins such as talin and vinculin [Geiger et al., 2009]. Integrins exist in conformational states ranging from 'bent-closed' (inactive) to 'extended-open' (active) [Kechagia et al., 2019]. This activation is regulated by bidirectional signaling [Li et al., 2016]:

- **Inside-out signaling.** Intracellular binding of talin to the β-integrin tail disrupts the inter-subunit interaction between the α and β tails, priming the integrin for ligand binding. This leads to lateral clustering (avidity modulation) and the formation of nascent adhesions at the cell periphery [Riveline et al., 2001, Changede and Sheetz, 2017].
- **Outside-in signaling.** Mechanical force stabilizes the extended-open conformation. This force-induced stabilization is a classic *catch-bond* behavior [Kong et al., 2009], where the bond lifetime increases with applied load up to a critical threshold, effectively locking the clutch.

2.2.2 The molecular clutch and mechanosensing

The transmission of force and the transition from nascent to mature adhesion is best described by the molecular clutch model [Mitchison and Kirschner, 1988, Elosegui-Artola et al., 2016, Sáez and Venturini, 2023]. Mechanistically, adhesion stability is determined by the competition between the rate of force buildup (loading) and the rate of bond rupture (disengagement):

- On **soft substrates**, the compliant environment dissipates energy. Force builds slowly, and the integrin-ligand bond typically fails before the force is sufficient to unfold talin. The adhesion remains nascent and unstable.
- On **stiff substrates**, the resistance to contraction generates a rapid increase in tension. The force quickly exceeds the threshold required to unfold talin, exposing cryptic vinculin binding sites (VBS) [del Rio et al., 2009, Yao et al., 2014]. This reinforces the linkage ("locking" the clutch), allowing for high traction generation.

Crucially, the threshold for this transition is not fixed but is modulated by the properties of the clutch itself. As demonstrated by Elosegui-Artola et al. [2016],

decreasing ligand density distributes the cytoskeletal load across fewer bonds, thereby increasing the force per clutch and shifting the reinforcement threshold to lower stiffnesses.

2.2.3 Biochemical regulation and turnover

While mechanical load drives reinforcement, the lifecycle of the focal adhesion is tightly regulated by upstream biochemical signaling pathways, particularly those involving the Rho-family GTPases. RhoA and its downstream effector ROCK (Rho-associated protein kinase) are the primary governors of actomyosin contractility [Ridley et al., 2003], generating the intracellular forces required to unfold talin. Simultaneously, focal adhesion kinase (FAK) regulates the dynamic turnover of these structures, orchestrating the cycle of assembly and disassembly required for migration [Webb et al., 2002, Parsons, 2003]. Therefore, the mechanical response of the FA is non-monotonic: it exhibits an initial stiffening (reinforcement) followed by softening and eventual failure (turnover) as displacement increases.

2.2.4 A phenomenological perspective: the cohesive law

From a continuum mechanics perspective, this complex molecular behavior, spanning reinforcement, peak traction, and eventual detachment, can be phenomenologically captured by a cohesive traction-separation law [Deshpande et al., 2008, Cóndor and García-Aznar, 2017, Yang et al., 2023, Benvenuti et al., 2023]. Instead of modeling individual protein kinetics, we can describe the interface thermodynamically:

1. **Elastic regime.** Represents the linear engagement of the molecular clutch.
2. **Damaging regime.** Represents the disassembly and rupture of bonds, where a scalar damage variable evolves to reduce the interface stiffness to zero.

This macroscopic approach, which we will mathematically formalize in Chapter 3, provides a rigorous method to predict the limits of cell traction and the onset of adhesion failure.

2.2.5 Implications for directed migration

Consequently, the maturation of focal adhesions acts as a local integrator that filters complex environmental cues. While mechanical loading is the primary driver of reinforcement, the stability and turnover of these anchors are also modulated by chemical signaling, ligand availability, and substrate geometry. Therefore, the focal adhesion does not merely anchor the cell; it translates diverse external gradients, whether mechanical, chemical, or geometrical, into intracellular traction asymmetries. This capability to bias motion in response to environmental heterogeneity is the fundamental physical driver behind *taxis*. In the following section, we will classify the specific forms of directed migration (e.g., durotaxis, haptotaxis, chemotaxis) that emerge from this common mechanotransduction machinery.

2.3 Different types of environmentally driven taxis

While Chapter 1 introduced cell migration as a general phenomenon, the specific trajectory of a migrating cell is rarely purely random; rather, it is biased by the extracellular environment. In physiological settings, cells leverage the focal adhesion machinery described in Section 2.2 to actively sense external gradients. These environmental signals, which can be chemical, adhesive, or mechanical, impart a specific directionality to the cellular motion. This directed migration, collectively termed *taxis*, arises because the cell perceives spatial variations in extracellular cues, which impose asymmetric boundary conditions on the cytoskeletal force balance. Common forms of directed migration include:

- *Chemotaxis*: migration guided by gradients of soluble chemical factors.
- *Haptotaxis*: migration driven by gradients in surface-bound ligand density.
- *Durotaxis*: migration driven by gradients in substrate stiffness.
- *Topotaxis*: migration guided by topographic features.
- *Galvanotaxis (or electrotaxis)*: migration induced by electric fields.

2.3.1 Durotaxis and mollitaxis

Among these various forms of directed migration, the tensegrity model derived in Part Part I of this thesis investigates the cell's mechanical response to substrate stiffness, representing a mode of guidance independent of soluble factors. We distinguish two regimes:

- **Durotaxis:** the migration up stiffness gradients, from compliant to rigid substrates [Lo et al., 2000, Isenberg et al., 2009, Sunyer and Trepat, 2020, Shellard and Mayor, 2021]. This is the dominant mode observed in mesenchymal migration, fibrosis, and wound healing. Experimentally, this is often attributed to the reinforcement of focal adhesions on stiffer substrates, which allows the cell to exert higher traction forces that pull the cell body toward the rigid region.
- **Negative durotaxis (or mollitaxis):** the migration toward softer environments [Koser et al., 2016, Isomursu et al., 2022]. Originally thought to be rare, it has recently been characterized in neurons and specific invasive cancer lines. Mechanistically, this behavior is less understood but is increasingly linked to adhesion instability or a lack of cytoskeletal reinforcement on very stiff substrates, which prevents effective traction generation [Isomursu et al., 2022, Sáez and Venturini, 2023].

Crucially, recent experimental evidence and motor-clutch model simulations suggest that these are not fixed cellular traits; rather, the same cell type can switch between these modes [Isomursu et al., 2022, Sáez and Venturini, 2023]. Understanding the mechanical origin of these opposing behaviors is a primary objective of this work. As we will demonstrate in Chapter 3, the switch between these

two modes can be mechanically explained by the interplay between cytoskeletal buckling instability and adhesion failure dynamics.

2.4 State of the art in modeling cell mechanics

The complexity of cell mechanobiology has necessitated the development of a diverse array of mathematical models, spanning from continuum multiphysics approaches to discrete structural representations. For a comprehensive review, the reader is referred to Alert and Trepat [2020] and Xu et al. [2024]. To frame the present work, we classify existing mathematical approaches based on their fundamental mechanical philosophy: continuum approximations, kinetic formulations, and discrete structural theories.

2.4.1 Continuum and bio-chemo-mechanical models

The continuum modeling of cell motility has evolved from describing isolated physical mechanisms to developing comprehensive whole-cell simulations. Early frameworks focused on the mathematical foundations of actin treadmilling and membrane protrusion. Seminal work by Mogilner and Oster [1996] established the continuum kinetics of actin polymerization, deriving how thermodynamic fluctuations generate the macroscopic protrusive force required to push the cell membrane forward. Subsequently, attention shifted to the cell rear and the retrograde flow of the cytoskeleton. Rubinstein et al. [2009] treated the actomyosin network using multiphase fluid theory, solving continuum transport equations to describe the global drift of the viscous actin gel relative to the substrate. More rigorously, the cytoskeleton has been described using Active Gel Theory, which extends liquid crystal hydrodynamics to include the non-equilibrium consumption of adenosine triphosphate (ATP), treating the cell as a complex active fluid [Kruse et al., 2005, Marchetti et al., 2013]. To bridge these transport dynamics with the structural evolution of the cytoskeleton, bio-chemo-mechanical models were developed. Distinct from purely hydrodynamic approaches, these models emphasize solid-mechanics constitutive laws. Deshpande et al. [2006] introduced a framework coupling the biochemistry of actin polymerization with the mechanics of tension generation (Hill-type contractility). Ronan et al. [2014] later utilized this approach to investigate how substrate elasticity regulates contractility, successfully predicting stress fiber alignment in 2D and 3D environments.

Most recently, research has moved towards unifying these distinct phases, protrusion, retrograde flow, and adhesion, into monolithic computational frameworks. Betorz et al. [2023] developed a comprehensive finite element model that couples advection-diffusion equations for actin and myosin densities with adhesion mechanics. Unlike earlier isolated models, this framework simulates the entire motility timeline, from symmetric spreading to polarization. Crucially, it allows for the investigation of competing forms of taxis, revealing the interaction between mechanical cues (durotaxis) and chemical signals (chemotaxis). However, while these modern frameworks provide rigorous descriptions of continuum flow and global transport, their macroscopic nature inherently homogenizes local structural

instabilities, such as the buckling of individual microtubules.

2.4.2 Kinetic approaches: the molecular clutch

While continuum models describe global cell flow, they often rely on phenomenological friction coefficients to represent adhesion. To capture the microscopic origins of this friction, the field turned to kinetic models, beginning with the molecular clutch hypothesis originally proposed by Mitchison and Kirschner [1988]. This framework posited that the retrograde flux of actin operates against a variable resistance provided by integrins, which intermittently engage the substrate. Jay [2000] subsequently revisited this hypothesis to define its molecular basis in nerve growth cones, establishing that the clutch is a functional module of interacting proteins rather than a single bond. This insight laid the groundwork for Chan and Odde [2008] to formulate the canonical mathematical model. By tracking the binding kinetics of these modules, Chan and Odde successfully predicted the biphasic relationship between traction force and substrate stiffness. Gao et al. [2011] refined this description by introducing coupled stochastic-elastic frameworks, enabling the rigorous probing of focal contact mechanics under dynamic loads.

Subsequent research expanded the model to account for the complex dynamics of clutch components. Bangasser et al. [2017] demonstrated that the density of available clutches governs the mechanosensitive range of the cell; by increasing the number of engaged molecular bonds, the cell shifts its maximal traction force to stiffer substrates. Furthermore, del Rio et al. [2009] and Yao et al. [2014] mathematically characterized the mechanical unfolding of talin, identifying it as a key mechanosensor. This allowed Elosegui-Artola et al. [2016] to demonstrate how integrin clustering reinforces adhesion under load, proving the existence of an optimal stiffness for maximal traction. Crucially, the molecular clutch framework has been expanded to verify not just stiffness sensing, but also viscotaxis. Bennett et al. [2018] demonstrated that the clutch loading rate is sensitive to substrate energy dissipation (viscosity), allowing the model to predict cell response to fluid-like matrices, a behavior that purely elastic clutch models could not capture. Recent studies have integrated these mechanisms to explain complex navigational choices. Venturini and Sáez [2023] developed a multi-scale clutch model combining actin flow, clutch engagement, and talin unfolding to calculate total traction. Isomursu et al. [2022], Beedle and Roca-Cusachs [2022] showed that variations in adhesion kinetics can induce directional reversal of migration, from positive to negative durotaxis. This behavior is not only tunable [Sáez and Venturini, 2023], but explicitly governed by the competition between elastic and viscous gradients, as demonstrated by Saez et al. [2025].

While these kinetic models effectively link migration to molecular friction, they typically simplify the bulk cytoskeleton into a linear spring, thereby neglecting the complex structural instabilities of the network.

2.4.3 Discrete structural models: networks and tensegrity

To capture the complex architectural response of the cell, where stiffness is stress-dependent and heterogeneous, discrete models are necessary [Fraldi et al., 2019]. The most prominent class of these frameworks relies on tensegrity (tensional integrity). Originally conceptualized by the architect R. Buckminster Fuller, tensegrity describes a structural system composed of discontinuous compressed components (struts) kept in equilibrium by a continuous network of tensioned cables. Unlike continuum approaches that rely on local homogenization, these discrete architectures capture "action at a distance" [Ingber, 1997]: the ability to transmit local mechanical signals across the entire structure through stress-hardened pathways, which can induce a global rearrangement of the entire structural lattice as a result of any local disturbance. This feature is essential for modeling non-affine deformations, such as snap-through and post-buckling instabilities, which are inherently lost in continuum theories [Coughlin and Stamenović, 1997, Xu et al., 2015, Lee and Terentjev, 2018].

Foundations and network geometry The application of this architectural principle to cell biology was pioneered by Ingber [1993, 1997]. He postulated that the cell stabilizes its shape not through bulk viscosity, but through a specific tensegrity force balance: a cytoskeleton where compressed microtubules (struts) are integrated with a tensioned actomyosin network (cables). From a rigorous mechanics perspective, this concept is grounded in the work of Calladine [1978], who first defined the conditions for self-stress in kinematic assemblies, a theory subsequently formalized for engineering systems by Motro [2003], Skelton [2009]. Building on these principles, Stamenović and Ingber [2002] and Paul et al. [2008] modeled the actin cytoskeleton as a discrete cable network. Crucially, Stamenović and Ingber [2002, 2009] mathematically demonstrated that the stiffness of such structures is linearly proportional to the internal pre-stress. This finding confirmed that adherent cells behave as pre-stressed structures, a fundamental property that simple continuum isotropic models fail to replicate naturally.

Modern computational frameworks and minimal units While early models were simple cable-strut assemblies, modern iterations have evolved into sophisticated frameworks that combine discrete and continuum elements. McGarry and Prendergast [2004] pioneered the hybrid finite element-tensegrity approach, embedding a discrete cytoskeletal network within a continuum cytoplasm and nucleus. This allowed for the simulation of complex cellular behaviors, such as variable compliance and strain hardening, that pure tensegrity models often oversimplify. Building on this, Bansod et al. [2018] introduced the Bendo-Tensegrity model, which accounts for the bending moments of microtubules, moving beyond the classical assumption of purely compressive struts to capture nonlinear stiffening. Recently, Sun et al. [2023, 2024] extended these discrete frameworks by coupling them with actomyosin activation dynamics, allowing the structure to exhibit autonomous contractility and reorientation under cyclic stretching.

However, increasing the number of elements often precludes analytical insight

into the fundamental mechanisms of stability. As highlighted by Skelton [2009], tensegrity principles are scale-independent; the mechanical response of a macroscopic network is often governed by the stability of its elementary units. Recognizing this, recent theoretical efforts have shifted back towards minimal tensegrity models (reduced-order systems) to isolate the precise conditions for cytoskeletal instability. In this context, Palumbo et al. [2018, 2022] demonstrated that complex mechanosensing behaviors (including the bifurcation between stability and collapse) can be effectively captured by a minimal tensegrity module. Unlike large-scale simulations, this reductionist approach allows for the analytical derivation of the equilibrium paths and buckling criteria that govern the cell's decision to reinforce or detach. This thesis adopts this minimal structural philosophy, utilizing an elementary tensegrity unit to mathematically derive the critical buckling conditions and effective cohesive laws that govern cell adhesion.

2.5 Modeling strategy and outline

The literature review reveals a dichotomy: continuum models capture global transport but often miss local structural instabilities, while discrete stochastic models capture molecular dynamics but lose the global cytoskeletal architecture. To bridge this gap, this thesis proposes a structural-energetic approach. Instead of solving kinetic equations of motion or viscous flow, we adopt a principle of energy minimization, positing that the cell seeks a mechanical equilibrium state that minimizes the total potential energy of the coupled cytoskeletal-adhesive system. To model the complex internal architecture, we utilize the minimal tensegrity unit introduced in Section 2.4.3: a reduced-order structure composed of compression struts (microtubules) stabilized by a continuous network of tensioned cables (actin). This framework is particularly suited for the current study because it naturally captures the non-linear phenomena identified in the state of the art: pre-stress stability and, crucially, buckling.

By reducing the cell to this elementary unit interacting with a substrate, we can analytically isolate the fundamental mechanisms of mechanotransduction, specifically, how structural instability drives the decision-making process during migration. Since our model is energetic rather than kinetic, we do not simulate the repetitive crawl of the cell over time, but rather the single contractile step that initiates motion.

2.5.1 Overview of chapters

The research in Part Part I is structured as follows:

- In Chapter 3, we introduce the mathematical framework for the discrete tensegrity model. We define the hyperelastic potentials for the cytoskeletal elements and the cohesive laws for the substrate, establishing the energy minimization framework. The chapter analyzes the model under various boundary conditions, progressing from the ideal symmetric case to the complex scenario involving adhesion damage. Crucially, this chapter derives the effective traction-separation laws that govern the cell-substrate interface.

- Finally, in Chapter 4, we upscale these findings by implementing the derived elasto-damaging laws within a continuum finite element model. This chapter investigates the interplay between cell contractility and substrate stiffness gradients, specifically focusing on the mechanisms governing the cell's positive and negative durotactic behavior.

3

A tensegrity-based unified framework

This chapter establishes a comprehensive mechanical framework designed to resolve the coupling between cytoskeletal stability and adhesive constraints. We derive a generalized discrete tensegrity model that integrates an asymmetric cytoskeletal architecture with nonlinear, elasto-damaging boundary conditions. By formulating the total potential energy for this comprehensive system, we establish a unified variational framework that allows us to explore distinct biological scenarios. These range from the coupling of actomyosin contraction, microtubule polymerization, and cytoskeletal buckling to the influence of cell polarization, substrate stiffness gradients, and adhesion failure, all of which can be rigorously isolated and analyzed as special cases. The structure of the analysis is organized as follows:

- Sec. 3.1 defines the kinematics for the most general tensegrity model: an asymmetric cytoskeletal unit coupled to nonlinear, elasto-damaging adhesions. We here introduce the unified variational framework, which encompasses all the specific sub-cases analyzed in the next sections.
- In Sec. 3.2, we study the cell contractility and the influence of microtubule polymerization by simplifying the model to a geometrically symmetric tensegrity structure with linear, elastic adhesions.
- In Sec. 3.3, to study the inherent polarized behavior of cells interacting with a substrate presenting a stiffness gradient, we specifically adopt an asymmetric tensegrity structure with linear elastic adhesion sites with different effective stiffnesses.
- Finally, in Sec. 3.4, we adopt a geometrically symmetric tensegrity structure and, by implementing elasto-damaging traction-separation laws for the cell-substrate interface, we explore their implications for positive and negative durotactic behavior.

3.1 Formulation of a generalized tensegrity unit

To capture the interplay between cytoskeletal architecture, structural instability, and adhesion mechanics, we formulate a generalized discrete tensegrity model. Un-

like continuum finite element approaches, which often smear out local instabilities, this discrete framework allows us to explicitly resolve the bifurcation behavior of the microtubule network and account for the entangled behavior of actomyosin contraction and microtubule polymerization.

3.1.1 Biophysical basis and topological reduction

The physiological basis for this abstraction is the adherent cell unit depicted in Figure 3.1. In its most general form, whether representing a whole cell or a local cytoskeletal unit, the biological system comprises two primary mechanical subsystems: the anchorage points (typically focal adhesion complexes connecting the internal cytoskeleton to the ECM, or in the case of the semi-cell unit, the central nucleus) and the cytoskeletal compartment (housing the actomyosin stress fiber bundles and microtubule struts)

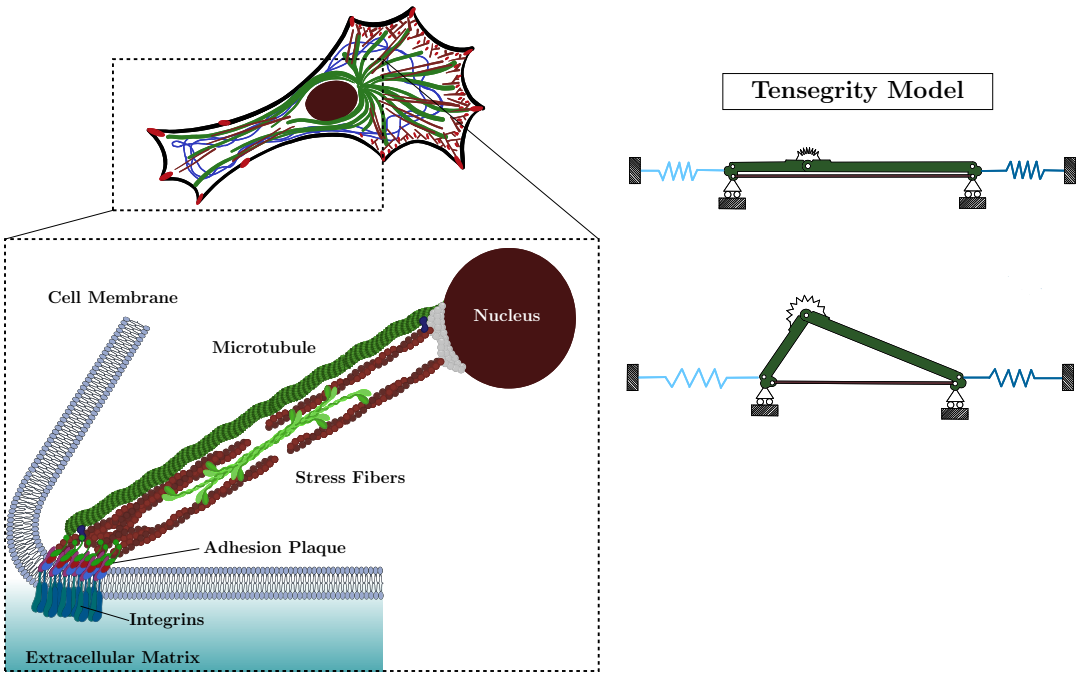

Figure 3.1: *Biological prototype and corresponding mechanical model. (Left) Schematic of an adherent cell highlighting the essential structural components: the nucleus, the cytoskeletal compartment (comprising actomyosin stress fibers and microtubules), and the focal adhesion complexes. (Right) The discrete tensegrity model derived from this biological topology, shown in both its reference undeformed state and the deformed equilibrium configuration.*

The cytoskeletal core: a two-element mechanism

In our proposed model, the topology of Figure 3.1 is abstracted into the minimal tensegrity system shown on the right of the same figure. This reduction

isolates the cytoskeletal core into two interacting components: a tension-bearing element representing the actomyosin motors and a compression-bearing element representing the microtubule network.

To exploit the tensegrity model to study the mechanosensitive implication of microtubule polymerization and buckling, and their concurrence with the actomyosin contractility, we homogenized the complex signaling cascades involved into macroscopic mechanical variables to create a tractable bio-chemo-mechanical system:

- Actomyosin contractility (Rho/ROCK): is captured by the pre-strain of the tensile cables.
- Microtubule dynamics (polymerization/motor transport): is homogenized into the inelastic pre-stretch of the strut elements. Following the observations of Bicek et al. [2009], we treat motor-driven anterograde transport and polymerization as mechanically equivalent forces that modify the effective reference length of the struts, driving them toward the buckling threshold.

Despite its topological simplicity, this two-element mechanism is capable of capturing the fundamental competition between the two primary drivers of cell motility: actomyosin contraction and microtubule polymerization. As illustrated in Figure 3.2, this allows us to identify two distinct regimes of instability:

1. **Contraction-driven buckling:** The instability is triggered by the active contraction of the tensile element [Murrell and Gardel, 2012]. Myosin motors reduce the stress-free length of the actin cables, generating a pulling force. If this force exceeds the critical load of the parallel microtubule, the strut buckles, and the cell undergoes significant contraction (Fig. 3.2, top).
2. **Polymerization-driven buckling:** The instability is triggered by the active elongation of the compressive element [Gudimchuk et al., 2020]. Following Bicek et al. [2009], we model the effect of polymerization and motor transport as an inelastic increase in the microtubule's reference length. This expansion is constrained by the actomyosin contraction and by the focal adhesions; when the resulting reaction force exceeds the critical threshold, the microtubule buckles internally (Fig. 3.2, bottom).

By unifying these biological drivers into a single energy minimization framework, we provide a rigorous mechanical basis for analyzing how these mechanisms coexist and influence cell mechanosensing.

The interface: phenomenological mapping of adhesion life cycle

While the cytoskeleton generates the active forces, the cell's mechanical response is governed by its boundary conditions, the focal adhesions. As detailed in Section 2.2, the focal adhesion is not a static tether but a dynamic structure governed by a specific life cycle: nucleation, reinforcement via the catch-bond mechanism, and eventual disassembly (turnover). Although the molecular landscape involving actin, integrins, talin, and vinculin is complex [De Pascalis and Etienne-Manneville, 2017], we adopt a heuristic interpretation of its macroscopic behavior.

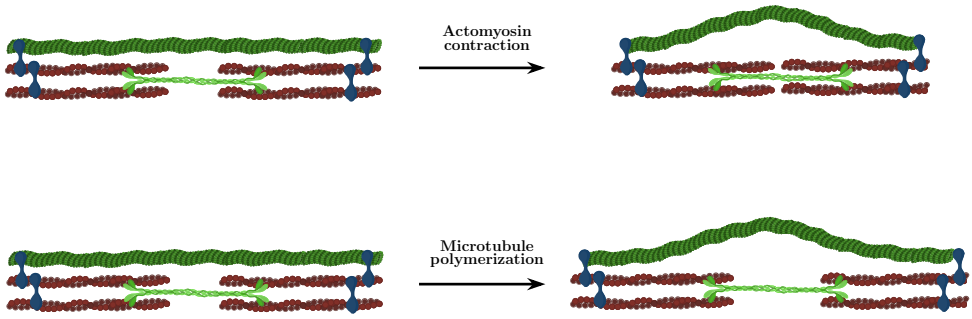

Figure 3.2: *The two-element mechanism governing the model's instability. (Top) Buckling driven by actomyosin contraction. (Bottom) Buckling driven by microtubule polymerization.*

We model the cell-substrate interface as a cohesive zone governed by an elastic-damaging law. This approach aggregates the interlaced chemomechanical mechanisms into a single scalar internal variable, the integrity parameter $\zeta \in [0, 1]$, which will be rigourously introduced in Sec. 3.1.4. The physical justification for

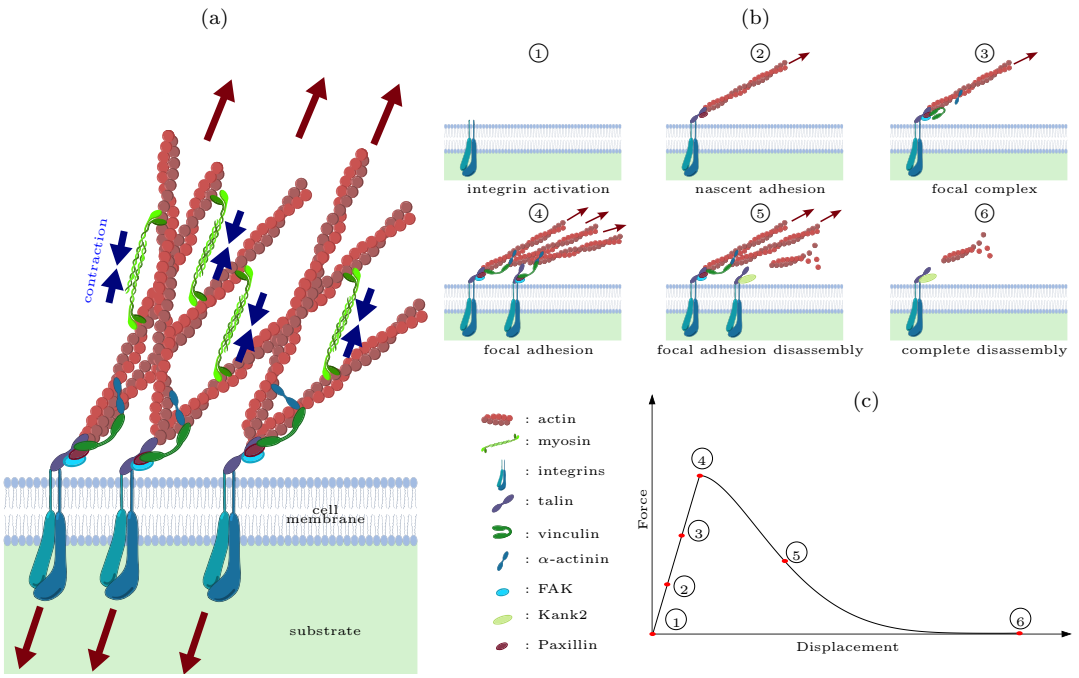

Figure 3.3: *Phenomenological mapping of the focal adhesion life cycle. (a) Key tension-sensitive proteins (modified after Cao et al. [2015] and De Pascalis and Etienne-Manneville [2017]). (b) The life cycle of the focal adhesion from nascent state to turnover. (c) The corresponding traction-displacement law adopted in the model, relating the biological stages to the mechanical integrity parameter ζ.*

this reduction is illustrated in Figure 3.3, which establishes a parallelism between the biological stages of the adhesion and our constitutive model:

- **Stage 1 (Integrin activation) → Elastic Loading:** The conformational switch of the integrin to an extended open state corresponds to the initial linear elastic loading phase.
- **Stages 2–4 (Maturation) → Peak Traction:** The maturation and eventually reinforcement via talin unfolding and vinculin binding correspond to the hardening phase, maintaining structural integrity ($\zeta \approx 1$) up to a critical yield threshold.
- **Stages 5–6 (Turnover) → Softening/Damage:** The disassembly of the complex is captured by the evolution of damage ($\dot{\zeta} < 0$), leading to vanishing traction capacity.

Durotaxis in a quasi-static framework

Another important aspect hereafter investigated is durotaxis. It is important to clarify the metric used to assess it in the context of the present thesis. In experimental biology, or kinetic modeling, durotaxis is often quantified by the migration velocity. But given the quasi-static nature of the adopted tensegrity model, the migration cannot be identified by a velocity vector but can be by the direction of the net centroidal displacement during a contraction cycle.

In order to investigate this substrate stiffness-driven mechanics in Secs. 3.3 and 3.4, the tensegrity system is anchored to the ECM by means of springs of different stiffness. Therefore, if the thermodynamic equilibrium configuration shifts the cell centroid towards the stiffer region, we define this as positive durotaxis. Conversely, a shift towards the softer region indicates negative durotaxis. By focusing on the magnitude and direction of this instantaneous displacement, we isolate the mechanical determinants of the decision-making process, specifically, how the contractile behavior is governed by the interplay between cytoskeletal polymerization and the progressive failure of adhesive links.

3.1.2 Kinematics of the asymmetric unit

We model the cell (or a representative cytoskeletal unit) as a 1D tensegrity structure (often referred to as a Hencky link-chain), as shown in Fig. 3.4, composed of two primary antagonistic elements:

1. **The Tensile Element:** representing the contractile actomyosin, which is modeled as a hyperelastic cable that can actively contract. This element carries tension but cannot sustain compression or bending.
2. **The Compressive Element:** representing the load-bearing component of the cytoskeleton, namely the microtubules, which are modeled as two hyperelastic bars connected by a central rotational spring (that mimics their bending stiffness) that can actively polymerize.

This discrete approximation captures the global buckling instability while maintaining analytical tractability.

Reference and current configurations

Let the reference configuration be defined by a stress-fiber bundle of length $2L_f$, and two microtubule elements composed of two rigid bars connected by a rotational hinge, where the hinge position divides the microtubule into two subunits of unequal lengths, L_t^h and L_t^s (denoted as 'hard' and 'soft' sides for consistency with the durotaxis analysis) as shown at the top of Fig. 3.4. To account for intrinsic cellular polarity and geometric irregularities, we introduce an asymmetry ratio η. In this initial configuration, we have that:

$$L_t^s = \eta L_t^h, \qquad \text{with} \qquad 2L_f = L_t^h + L_t^s = L_t^h(1+\eta). \tag{3.1}$$

Note that the asymmetry ratio $\eta \in]0, +\infty[$ and $\eta = 1$ recovers the perfectly symmetric geometry used in early stability analyses.

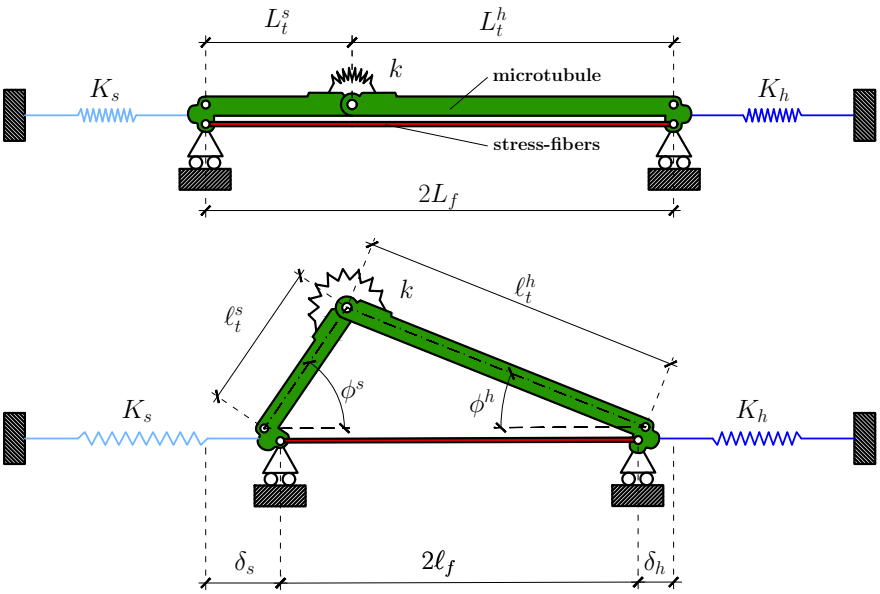

Figure 3.4: *Reference and deformed configuration of the asymmetric structural scheme adopted for the one-dimensional tensegrity model. Here the cell-focal adhesions-substrate connections are embedded within the equivalent springs of stiffness K_s, in light blue, and K_h, in dark blue, at the soft and hard parts of the substrate, respectively.*

Starting from this reference configuration, the system can reach the deformed configuration, shown at the bottom of Fig. 3.4, through active inelastic stretches $\lambda^* \in \mathbb{R}^+$. In particular,

- the microtubule, which can polymerize, experiences an inelastic pre-stretch $\lambda_t^* \geq 1$,
- the fiber bundles, which can contract, experience an inelastic pre-stretch $\lambda_f^* \leq 1$.

These pre-stretch lead the system to respond with elastic stretches, which are, $\hat{\lambda}_t^h$, $\hat{\lambda}_t^s$ and $\hat{\lambda}_f$, for the microtubules (hard and soft side) and the fiber bundles, respectively. Consistent with the finite strain framework, the deformation of both the fiber and the microtubule, which is made of an active inelastic part (remodeling) and a passive elastic part, turns out to be given via multiplicative superposition:

$$\lambda_f = \lambda_f^* \hat{\lambda}_f, \qquad \lambda_t^h = \lambda_t^* \hat{\lambda}_t^h. \qquad \lambda_t^s = \lambda_t^* \hat{\lambda}_t^s. \tag{3.2}$$

As a consequence of the inelastic pre-stretch, the system can deform and eventually buckle, as shown at the bottom of Fig. 3.4. In this deformed configuration, the current semi-length of the fiber bundle and the length of the microtubules are

$$\ell_f = L_f \lambda_f^* \hat{\lambda}_f \qquad \ell_t^h = L_t^h \lambda_t^* \hat{\lambda}_t^h. \qquad \ell_t^s = L_t^s \lambda_t^* \hat{\lambda}_t^s = \eta L_t^h \lambda_t^* \hat{\lambda}_t^s. \tag{3.3}$$

The microtubule's soft and hard side arms can rotate relative to the horizontal axis with angles ϕ_s and ϕ_h, respectively. By geometric compatibility, we have that

$$\ell_t^s \sin \phi_s = \ell_t^h \sin \phi_h \tag{3.4a}$$

$$2\ell_f = \ell_t^h \cos \phi_h + \ell_t^s \cos \phi_s, \tag{3.4b}$$

Replacing Eq. (3.3) into (3.4a), and exploiting basic trigonometric identities allow us to write

$$\cos \phi_s = \frac{\hat{\lambda}_t^h}{\eta \hat{\lambda}_t^s} f_1(\phi_h, \hat{\lambda}_t^h, \hat{\lambda}_t^s), \tag{3.5}$$

where

$$f_1(\phi_h, \hat{\lambda}_t^h, \hat{\lambda}_t^s) := \left[\frac{\eta^2 (\hat{\lambda}_t^s)^2}{(\hat{\lambda}_t^h)^2} - 1 + \cos^2 \phi_h \right]^{1/2}. \tag{3.6}$$

Substituting Eq. (3.3) into Eq. (3.4b) instead yields

$$2L_f \lambda_f^* \hat{\lambda}_f = L_t^h \lambda_t^* \hat{\lambda}_t^h \cos \phi_h + \eta L_t^h \lambda_t^* \hat{\lambda}_t^s \cos \phi_s. \tag{3.7}$$

Recalling Eq. (3.1), we can express the reference semi-length of the stress fiber as $L_f = L_t^h(1+\eta)/2$. This, together with (3.5), substituted into (3.7) gives

$$L_t^h (1+\eta) \lambda_f^* \hat{\lambda}_f = L_t^h \lambda_t^* \hat{\lambda}_t^h \cos \phi_h + \eta L_t^h \lambda_t^* \hat{\lambda}_t^s \left(\frac{\hat{\lambda}_t^h}{\eta \hat{\lambda}_t^s} f_1(\phi_h, \hat{\lambda}_t^h, \hat{\lambda}_t^s) \right). \tag{3.8}$$

Therefore, the incremental fibre stretch reads

$$\begin{aligned} \hat{\lambda}_f &= \frac{\lambda_t^* \hat{\lambda}_t^h}{\lambda_f^* (1+\eta)} \left(\cos \phi_h + f_1(\phi_h, \hat{\lambda}_t^h, \hat{\lambda}_t^s) \right) \\ &= \frac{\lambda_t^* \hat{\lambda}_t^h}{\lambda_f^* (1+\eta)} f_2(\phi_h, \hat{\lambda}_t^h, \hat{\lambda}_t^s), \end{aligned} \tag{3.9}$$

where

$$f_2(\phi_h, \hat{\lambda}_t^h, \hat{\lambda}_t^s) := f_1(\phi_h, \hat{\lambda}_t^h, \hat{\lambda}_t^s) + \cos\phi_h \tag{3.10}$$

Finally, we define the total cell contraction Δ, and by geometric compatibility we have:

$$\begin{aligned} \Delta &= \delta_s + \delta_h = 2(L_f - \ell_f) \\ &= 2L_f\left(1 - \lambda_f^*\hat{\lambda}_f\right) = L_t^h\left(1 + \eta - \lambda_t^*\hat{\lambda}_t^h f_2\right), \end{aligned} \tag{3.11}$$

where

$$\delta_s = \gamma\Delta, \qquad \delta_h = (1-\gamma)\Delta, \qquad \text{with } \gamma \in [0,\, 1] \tag{3.12}$$

are the displacements of the system edges at the soft and hard sides, respectively. Therefore, the total cell contraction, Δ, turns out to be partitioned into the displacements at the two ends, δ_s and δ_h through the parameter γ.

3.1.3 Constitutive models of the cytoskeleton

We assume that both microtubule and fiber elements follow an incompressible Neo-Hookean strain energy law. The strain energy densities for the fiber ($\mathcal{U}_f$) and the two microtubule segments ($\mathcal{U}_t^h$,$\mathcal{U}_t^s$) are given by:

$$\mathcal{U}_t^i = \frac{K_t L_t^i \lambda_t^*}{6}\left[(\hat{\lambda}_t^i)^2 + \frac{2}{\hat{\lambda}_t^i} - 3\right] \quad \text{for } i \in \{h, s\}, \tag{3.13a}$$

$$\mathcal{U}_f = \frac{K_f L_f \lambda_f^*}{6}\left[(\hat{\lambda}_f)^2 + \frac{2}{\hat{\lambda}_f} - 3\right], \tag{3.13b}$$

where $K_t = E_t A_t$ and $K_f = E_f A_f$ are the related axial stiffnesses, with E_t and E_f representing the Young moduli and A_t and A_f the cross-sectional areas. In order to solve the problem at hand, the energy density of the fiber can be rewritten in terms of the microtubule reference length and elastic stretches as follow:

$$\mathcal{U}_f = \frac{K_f L_t^h \lambda_f^*(1+\eta)}{12}\left\{\left[\frac{\lambda_t^*\hat{\lambda}_t^h}{\lambda_f^*(1+\eta)} f_2\right]^2 + \frac{2\lambda_f^*(1+\eta)}{\lambda_t^*\hat{\lambda}_t^h} f_2^{-1} - 3\right\}. \tag{3.14}$$

The rotational spring, representing the homogenized bending stiffness of the microtubule, is modeled with a logarithmic potential to ensure analytical tractability at large rotations [Palumbo et al., 2022]. The rotational angle to which the spring is subjected, recalling the implication of the geometric compatibility given by Eq.(3.5), is:

$$\Delta\phi = \phi_h + \phi_s = \phi_h + \arccos\frac{\hat{\lambda}_t^h}{\eta\hat{\lambda}_t^s} f_1\,. \tag{3.15}$$

Therefore the elastic energy of the rotational spring writes as:

$$\mathcal{U}_{sp} = -2\kappa \ln\left|\cos\left(\frac{\Delta\phi}{2}\right)\right|. \tag{3.16}$$

where $\kappa = \pi^2 B_t / L$ is the rotational stiffness constant, B_t being the bending stiffness of the microtubule groups.

Therefore, we can define the total energy of the cytoskeleton as the sum of all its basic components:

$$\Psi_{\text{cyto}}(\hat{\lambda}_t^h, \hat{\lambda}_t^s, \phi_h) = \mathcal{U}_t^s(\hat{\lambda}_t^s) + \mathcal{U}_t^h(\hat{\lambda}_t^h) + 2\mathcal{U}_f(\hat{\lambda}_t^h, \hat{\lambda}_t^s, \phi_h) + \mathcal{U}_{sp}(\hat{\lambda}_t^h, \hat{\lambda}_t^s, \phi_h). \quad (3.17)$$

3.1.4 Thermodynamics of the interface: the pseudo-elastic potential

The mechanical interaction between the tensegrity system and the adhesion interface is modeled as a cohesive interface governed by the thermodynamic principles of irreversible processes. We postulate the existence of a convex-concave pseudo-elastic energy potential Φ per unit area of the interface [Ortiz and Repetto, 1999], which depends on the interfacial sliding displacement δ_i (where $i \in \{s, h\}$ denotes the soft or hard boundary) and a scalar internal variable $\zeta_i \in [0, 1]$ representing the mechanical integrity of the adhesion complex.

Let the deformation history be discretized into a sequence of non-overlapping intervals $[t_n, t_{n+1}]$. The system dissipates energy as the adhesions undergo maturation and turnover. As shown by Benvenuti [2004], for damage processes that are monotonically increasing functions of the displacement field, the pseudo-elastic potential at the current state t_{n+1} can be expressed solely as a function of the current displacement and damage state:

$$\Phi_i(t_{n+1}) = \frac{1}{2}\zeta_i(t_{n+1}) K_i \, \delta_i^2(t_{n+1}) - \int_0^{\delta_i(t_{n+1})} \left.\frac{\partial \zeta_i}{\partial \tilde{\delta}}\right|_{\tilde{\delta}} \frac{1}{2} K_i \, \tilde{\delta}^2 d\tilde{\delta}. \quad (3.18)$$

Here, K_i is the effective initial stiffness of the adhesion complex (comprising the plaque, integrins, and substrate compliance), the derivation of which is detailed in Section 3.1.4. The integral term represents the inelastic work dissipated during the decohesion process. Figure 3.5a shows in black the typical shape of Φ.

The thermodynamic force conjugate to the displacement, is derived from the potential as [Evans, 1985a,b, Liu et al., 2007, Deshpande et al., 2008]:

$$t_i = \frac{d\Phi_i}{d\delta_i} = \zeta_i(\delta_i) K_i \delta_i. \quad (3.19)$$

This relation highlights that t_i is not purely elastic but is modulated by the current state of damage. As displayed in Figure 3.5b, the resulting force response exhibits a typical post-peak softening trend that leads to complete cell-substrate separation, consistent with the classical description of bond rupture by Bell [1978].

Damage evolution law

The evolution of the integrity parameter ζ_i is governed by a set of loading-unloading conditions valid for irreversible phenomena. We introduce the loading

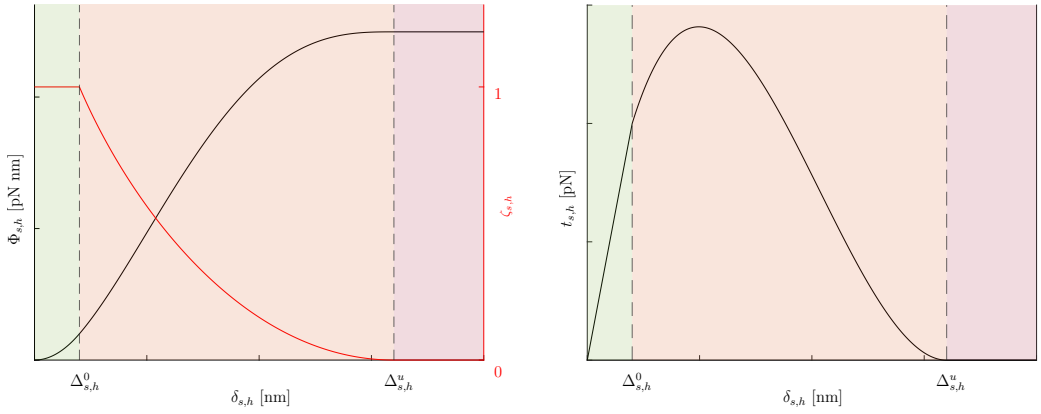

(a) **(b)**

Figure 3.5: *In figure a), the form of the considered cohesive pseudo-elastic energies for Φ_s and Φ_h is shown in black, while the profile representative of the mechanical integrity parameters ζ_s and ζ_h is plotted in red. The typical form of both the tractions t_s and t_h, which are conjugated to the potential, is plotted in figure b). The green, orange, and red domains correspond to the sound, damaged, and broken regimes, as indicated in Figure 4.1.*

function $g_i(\delta_i, \zeta_i)$ acting as a damage criterion. The evolution is governed by the standard Kuhn-Tucker conditions [Geers, 1997, Peerlings et al., 1996]:

$$g_i \leq 0, \qquad \dot{g}_i \geq 0, \qquad \dot{\zeta}_i \leq 0, \qquad g_i\,\dot{\zeta}_i = 0. \tag{3.20}$$

The solution of Eq. (3.20) leads to the following incremental form of the damage evolution process

$$\dot{\zeta}_i = h(\delta_i, \zeta_i), \tag{3.21}$$

which, after integration, yields the profile in red in Figure 3.5a.

Solving the incremental evolution problem (3.21) over a non-decreasing displacement history yields the specific profile for the integrity parameter:

$$\zeta_i(t_{n+1}) = \begin{cases} 1 & \text{if } \delta_i < \Delta_i^0 \quad \text{(Homeostatic)}, \\ \left(\dfrac{\Delta_i^0}{\delta_i}\right)^{\beta} \left(\dfrac{\Delta_i^u - \delta_i}{\Delta_i^u - \Delta_i^0}\right)^{\alpha} & \text{if } \Delta_i^0 \leq \delta_i < \Delta_i^u \quad \text{(Turnover)}, \\ 0 & \text{if } \delta_i \geq \Delta_i^u \quad \text{(Detached)}. \end{cases} \tag{3.22}$$

In this law, Δ_i^0 and Δ_i^u denote the activation and ultimate failure thresholds, respectively. The exponents α and β are phenomenological parameters that shape the softening tail, allowing the model to capture specific traction-separation behaviors observed in experiments. As shown in Figures 3.3c and 3.5b, this law allows us to capture the initial stiffening, the peak force transmission (the "clutch engagement"), and the subsequent softening characteristic of focal adhesion turnover.

Analytic evaluation of the energy. By substituting the explicit damage law (Eq. 3.22) into the energy definition (Eq. 3.18), we can evaluate the integral

term analytically. We first compute the derivative of the integrity parameter with respect to the displacement, $\partial\zeta/\partial\delta$, which yields:

$$\frac{\partial \zeta_i}{\partial \delta_i} = \begin{cases} 0 & \text{if } \delta_i < \Delta_i^0 \text{ or } \delta_i > \Delta_i^u, \\ -\zeta_i \left(\dfrac{\beta}{\delta_i} + \dfrac{\alpha}{\Delta_i^u - \delta_i} \right) & \text{if } \Delta_i^0 < \delta_i < \Delta_i^u. \end{cases} \tag{3.23}$$

Integrating this expression allows us to obtain the exact closed-form solution for the inelastic work contribution involving the hypergeometric function ${}_2F_1(a, b; c; x)$:

$$\int_0^{\delta_i} \left. \frac{\partial \zeta_i}{\partial \tilde{\delta}} \right|_{\tilde{\delta}} \frac{1}{2} K_i \, \tilde{\delta}^2 d\tilde{\delta} = \left[G_{\alpha\beta}(\tilde{\delta}) H_{\alpha\beta}(\tilde{\delta}) \right]_{\tilde{\delta}=\Delta_i^0}^{\tilde{\delta}=\delta_i}. \tag{3.24}$$

Here, the auxiliary functions $G_{\alpha\beta}$ and $H_{\alpha\beta}$ are defined as:

$$G_{\alpha\beta}(\tilde{\delta}) := \frac{K_i \, \zeta_i(\tilde{\delta}) \tilde{\delta}^2}{2(\beta-3)(\beta-2)\Delta_i^u} \left(1 - \frac{\tilde{\delta}}{\Delta_i^u} \right)^{-\alpha}, \tag{3.25a}$$

$$\begin{aligned} H_{\alpha\beta}(\tilde{\delta}) := & \alpha(\beta-2)\tilde{\delta} \; {}_2F_1 \left(1-\alpha, 3-\beta; 4-\beta; \frac{\tilde{\delta}}{\Delta_i^u} \right) \\ & + \beta(\beta-3)\Delta_i^u \; {}_2F_1 \left(-\alpha, 2-\beta; 3-\beta; \frac{\tilde{\delta}}{\Delta_i^u} \right) \end{aligned} \tag{3.25b}$$

It is important to remark that this integral term depends solely on the integration limits (the current displacement δ_i and the damage initiation threshold Δ_i^0). Consequently, this contribution is path-independent with respect to the loading envelope. This property ensures that the energy dissipated during the damage process is well-defined as a state function of the displacement, thereby preserving the validity of the potential energy minimization approach adopted for the equilibrium analysis.

Effective interface stiffness and constitutive parameters

To ensure biophysical fidelity, the mechanical properties of the interface are derived from a structural model of the Focal Adhesion (FA) plaque. We adopt the shear-lag model proposed by Cao et al. [2015], which treats the FA not as a single spring, but as a composite structure comprising the focal adhesion plaque, the integrin cluster, and the underlying substrate (see Figure 3.6).

The effective stiffness K_i of this specific chain is determined by the geometric and constitutive properties of its components. Generalizing the formulation by Cao et al. [2015], we express K_i as:

$$K_i = \frac{d_i(k_p + k_{\text{sub}})}{L_c} \left[\frac{L_p}{L_c} + 2\operatorname{csch}\left(\frac{L_p}{L_c} \right) + \left(\frac{k_p}{k_{\text{sub}}} + \frac{k_{\text{sub}}}{k_p} \right) \coth\left(\frac{L_p}{L_c} \right) \right]^{-1}, \tag{3.26}$$

where d_i is the integrin spacing, and L_c is the characteristic length of shear transfer, defined as:

$$L_c = d_i \sqrt{\frac{k_p k_{\text{sub}}}{k_i(k_p + k_{\text{sub}})}}. \tag{3.27}$$

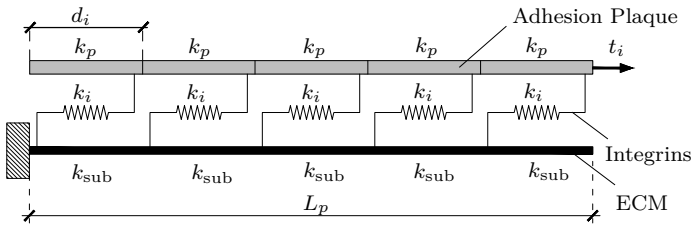

Figure 3.6: *Structural scheme adopted from [Cao et al., 2015] for the focal adhesion-extracellular matrix complex. The effective stiffness K_i is derived from the interplay between the plaque stiffness k_p, the integrin stiffness k_i, and the generic substrate stiffness k_{sub}.*

This formulation captures the non-linear dependency of the adhesion stiffness on the substrate compliance, a key factor in mechanosensing. As observed in Fig. 3.7, K_i exhibits a non-monotonic dependence on adhesion size, indicating an optimal length for force transmission.

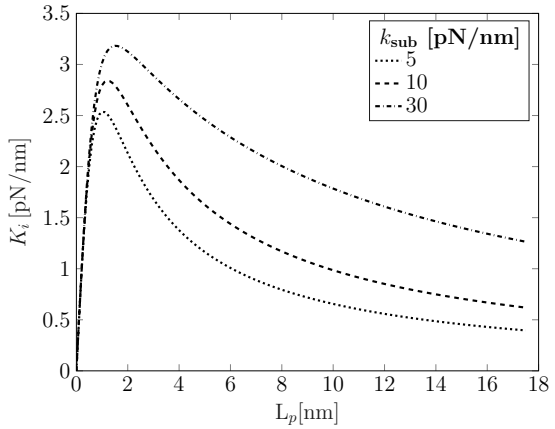

Figure 3.7: *The effective stiffness of a focal adhesion K_i as a function of its size L_p and ECM stiffness k_{sub}.*

3.1.5 Variational formulation and equilibrium

The mechanical state of the cell-substrate system is governed by the principle of minimum potential energy. We consider the total system comprising the cytoskeletal tensegrity structure and the two adhesive interfaces at the 'soft' (s) and 'hard' (h) boundaries. The total potential energy functional, defined over the set of generalized Lagrangian coordinates $\mathbf{q} = \{\gamma, \hat{\lambda}_t^s, \hat{\lambda}_t^h, \phi_h\}$, is given by:

$$\mathcal{P}(\gamma, \hat{\lambda}_t^s, \hat{\lambda}_t^h, \phi_h) = \Psi_{\text{cyto}}(\hat{\lambda}_t^s, \hat{\lambda}_t^h, \phi_h) + \Phi_s(\delta_s, \zeta_s) + \Phi_h(\delta_h, \zeta_h). \tag{3.28}$$

In this formulation, the interfacial displacements δ_s and δ_h are not independent variables but are kinematically determined by the generalized coordinates. Specifically, they are expressed as a partition of the total cell contraction Δ via the parameter γ (Eq. 3.12), while Δ itself is a function of the geometrical configuration

variables $(\hat{\lambda}_t^s, \hat{\lambda}_t^h, \phi_h)$ as defined in Eq. (3.11). Furthermore, the integrity parameters ζ_i depend on the displacement history δ_i, rendering the adhesion potentials fully dependent on the state of the cytoskeleton.

Stationarity and Equilibrium Conditions

The equilibrium configurations of the system correspond to the stationary points of the functional $\mathcal{P}$ with respect to the Lagrangian generalized coordinates. The first variation yields the following set of governing equations:

$$\frac{\partial \mathcal{P}}{\partial \gamma} = \frac{\partial \mathcal{P}}{\partial \hat{\lambda}_t^s} = \frac{\partial \mathcal{P}}{\partial \hat{\lambda}_t^h} = \frac{\partial \mathcal{P}}{\partial \phi_h} = 0. \tag{3.29}$$

These four nonlinear algebraic equations implicitly define the state of the system for a given level of contractility. The explicit form of this system depends on the specific geometric assumptions (e.g., symmetric vs. asymmetric cytoskeleton) and boundary conditions (e.g., rigid vs. elasto-damaging supports) considered. Consequently, the detailed derivation and solution of these equations will be addressed in the subsequent chapters, where each specific sub-case is analyzed.

3.1.6 Mechanochemical kinetics of focal adhesion growth

This section establishes the governing laws for the assembly and disassembly of the focal adhesion plaque as a function of the mechanical state. We adopt the thermodynamic framework for linear polymerizing systems proposed by Hill and Kirschner [1982], generalized here to account for the non-linear elasticity of the adhesion complex. While seminal applications of this theory [Shemesh et al., 2005, Cao et al., 2015, Palumbo et al., 2022] restricted the analysis to linear elastic materials, resulting in growth rates that depend linearly on mechanical force, we here relax this assumption. We treat the plaque as a Neo-Hookean material to capture the non-linear entropic elasticity characteristic of soft polymer networks under finite deformations.

Thermodynamics of monomer insertion

Let the focal adhesion be modeled as an aggregate of filaments with Young's modulus E_p and nominal cross-section A_p, subject to an axial tensile force F_p. The energetic cost of adding a monomer of reference length d_i to the aggregate depends on the mechanical work performed against this load. Following Hill and Kirschner [1982], the chemical potential μ_p of a monomer within the loaded filament is related to the force F_p via the Gibbs-Duhem relation:

$$d\mu_p = -l_m(F_p)\, dF_p = -L_m \lambda_p(F_p)\, dF_p, \tag{3.30}$$

where $l_m = L_m \lambda_p(F_p)$ is the current length of the monomer, L_m is the rest length of the monomer and λ_p is the axial stretch ratio. Integrating Eq. (3.30) from a stress-free state ($F_p = 0$) to the current loaded state yields the chemical potential of a bound monomer:

$$\mu_p(F_p) = \mu_p^0 - d_i \int_0^{F_p} \lambda_p(f)\, df, \tag{3.31}$$

where μ_p^0 represents the intrinsic chemical potential of the subunit in the absence of external force and assuming $L_m = d_i$. The driving force for polymerization is the difference in chemical potential between the bound state (μ_p) and the free cytosolic pool (μ_{free}):

$$\Delta\mu(F_p) = \mu_p(F_p) - \mu_{\text{free}} = \Delta\mu_0 - d_i \int_0^{F_p} \lambda_p(f)\, df, \tag{3.32}$$

where $\Delta\mu_0 = \mu_p^0 - \mu_{\text{free}}$. A negative difference ($\Delta\mu < 0$) favors assembly (growth), while a positive difference favors disassembly.

Constitutive law and approximation

We assume the plaque exhibits incompressible Neo-Hookean behavior. The stretch λ_p is related to the applied force F_p through the constitutive relation:

$$F_p = \frac{E_p A_p}{3}\left(\lambda_p - \frac{1}{\lambda_p^2}\right). \tag{3.33}$$

Inverting this relation analytically yields a complex expression for $\lambda_p(F_p)$. To facilitate the integration in Eq. (3.32), we approximate λ_p using a Taylor series expansion $\tilde{\lambda}_p(F_p)$ around the operational point of interest. This allows for a closed-form evaluation of the mechanical work term.

Growth rate kinetics

We assume that monomer exchange occurs primarily at the filament tips [Shemesh et al., 2005]. The local molecular flux j is modeled as linearly proportional to the thermodynamic driving force:

$$j(X) = -D\Delta\mu(X), \tag{3.34}$$

where $D > 0$ is a phenomenological kinetic coefficient. The total growth rate J of the adhesion plaque is the sum of the fluxes at its two boundaries: the proximal end ($X = 0$) and the distal end ($X = L_p$). From the shear-lag model (Sec. 3.1.4), the axial force varies along the plaque. We assume the proximal end is free ($F_p(0) = 0$) and the distal end bears the full cytoskeletal load. Thus, consistently with the thermodynamic force introduced in Eq. (3.19), we denote this boundary load for a specific adhesion site i as t_i ($F_p(L_p) = t_i$). Substituting these boundary conditions into Eq. (3.32):

- At the free end ($X = 0$):
$$\Delta\mu(0) = \Delta\mu_0.$$
- At the loaded end ($X = L_p$):
$$\Delta\mu(L_p) = \Delta\mu_0 - d_i \int_0^{t_i} \tilde{\lambda}_p(f)\, df.$$

The total growth flux $J = j(0) + j(L_p)$ becomes:

$$J(t_i) = -D\left[2\Delta\mu_0 - d_i \int_0^{t_i} \tilde{\lambda}_p(f)\, df\right]. \tag{3.35}$$

This relation explicitly couples the macroscopic force t_i generated by the actomyosin-microtubule system to the microscopic kinetics of focal adhesion remodeling.

3.1.7 Reduction to specific cases

The variational framework derived above describes the most general state of the coupled system. To isolate and analyze specific physical mechanismssuch as the role of cytoskeletal buckling versus the role of adhesion rupturewe reduce this generalized model to three sub-cases. These reductions are obtained by imposing constraints on the geometric asymmetry parameter (η) and the adhesion integrity variable (ζ).

- **The symmetric elastic case (Chapter 3.2)**.
  To establish the baseline mechanical stability of the cytoskeleton without the complexity of damage, we assume:
  - Symmetric geometry ($\eta = 1$). The tensegrity structure presents a geometric symmetric structure, with $L_t^s = L_t^h$.
  - Linear adhesion ($\zeta \equiv 1$). We restrict the analysis to the elastic regime ($\delta < \Delta^0$), assuming the focal adhesions operate below their activation threshold for remodeling.

- **The asymmetric elastic case (Chapter 3.3)**.
  To study how the geometric asymmetry of the cytoskeleton drives migration, we assume:
  - Asymmetric geometry ($\eta \neq 1$). We introduce a structural asymmetry in the tensegrity strut compartments, with $L_t^s \neq L_t^h$.
  - Linear adhesion ($\zeta \equiv 1$). The adhesions remain intact and behave linearly.

- **The symmetric elasto-damaging case (Chapter 3.4)**.
  To study how the adhesion failure influences the migration, we assume:
  - Symmetric geometry ($\eta = 1$). The structural core remains symmetric.
  - Elasto-damaging adhesion. We release the constraint on the integrity parameter. The damage thresholds are activated ($\delta > \Delta^0$), and ζ evolves according to the damage evolution law Eq. (3.22), allowing for adhesion maturation and turnover.

3.2 Mechanics of the symmetric cytoskeletal unit: influence of pre-strains and buckling

The general tensegrity model established in Chapter 3 is here specialized to the case of a symmetric cytoskeletal unit anchored by linear elastic adhesions. In particular, in this analysis we apply the devised system to study a cytoskeletal unit spanning from the focal adhesion to the cell nucleus. In particular, as shown in Fig. 3.1, the cytoskeletal network is physically linked to the extracellular substrate via the focal adhesion complex and internally to the cell nucleus. Mechanically, these anchorage points act as boundary conditions for the cytoskeletal forces. By focusing on a geometrically symmetric cytoskeletal core, we aim to isolate the intrinsic stability properties of the microtubule network, specifically the coupling between actomyosin pre-contraction and microtubule pre-compression, distinct from the effects of structural asymmetry.

3.2.1 Mechanical model formulation

In order to study the aforementioned cytoskeletal unit, and starting from the general tensegrity unit devised in Chap. 3, we performed the following simplification hypothesis:

1. **Geometric properties.** We assume the cytoskeletal unit, which is identified by the tensegrity model, to have $\eta = 1$. Thus, the reference lengths of the microtubules are equal ($L_t^s = L_t^h$).
2. **Adhesion properties.** The tensegrity unit is here supposed to be linked by means of linear elastic springs with $\zeta \equiv 1$. We assume the focal adhesions operate strictly within their linear regime ($\delta < \Delta^0$). In particular, one represents the focal adhesion-ECM complex of effective stiffness k_{eff} given by Eq. (3.26), and the other one represents the stiffness of the nucleus k_n.

Under these assumptions, the reference and deformed configurations are the ones represented in Fig. 3.8.

Reduced kinematics

The assumption of geometric symmetry ($\eta = 1$) significantly simplifies the system kinematics. We unify the reference lengths such that $L_t^s = L_t^h \equiv L_t$, and consequently $L_f = L_t \equiv L$. This symmetry extends to the orientation angles, $\phi_s = \phi_h \equiv \phi$, and the elastic microtubule pre-stretches, $\hat{\lambda}_t^h = \hat{\lambda}_t^s \equiv \hat{\lambda}_t$. Accordingly, the current microtubule semi-length is given by $\ell_t = L\lambda_t^*\hat{\lambda}_t$. Geometric compatibility requires that $\ell_f = \ell_t \cos\phi$, which reduces Eq. (3.9) to:

$$\hat{\lambda}_f = \frac{\lambda_t^*\hat{\lambda}_t \cos\phi}{\lambda_f^*}. \tag{3.36}$$

The total contractility, Δ, is defined as the sum of effective and nuclear components, $\delta_{\text{eff}} = \gamma\Delta$ and $\delta_n = (1-\gamma)\Delta$. This yields:

$$\Delta = 2L(1 - \lambda_t^*\hat{\lambda}_t \cos\phi). \tag{3.37}$$

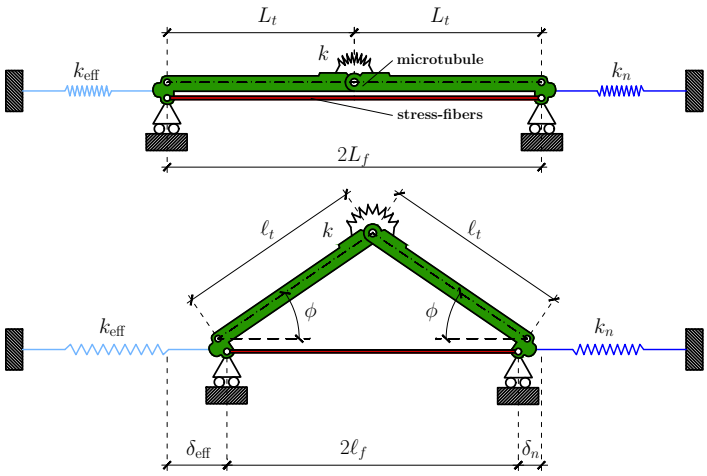

Figure 3.8: *Reference and deformed configuration of the symmetric structural scheme adopted for the one-dimensional tensegrity model. Here the cell-focal adhesion-substrate connection is embedded within the equivalent springs of stiffness k_{eff}, in light blue, while k_n, in dark blue, represents the stiffness of the nucleus.*

These reductions allow the potential energy of the microtubule and actomyosin components (Eqs. (3.13) and (3.14)) to be rewritten as:

$$\mathcal{U}_t = \frac{K_t L \lambda_t^*}{6}\left[(\hat{\lambda}_t)^2 + \frac{2}{\hat{\lambda}_t} - 3\right], \tag{3.38a}$$

$$\mathcal{U}_f = \frac{K_f L \lambda_f^*}{6}\left[\left(\frac{\lambda_t^* \hat{\lambda}_t \cos\phi}{\lambda_f^*}\right)^2 + \frac{2\lambda_f^*}{\lambda_t^* \hat{\lambda}_t \cos\phi} - 3\right]. \tag{3.38b}$$

Finally, the pseudo-elastic potentials for the focal adhesion-ECM and the nucleus (Eq. (3.18)) become fully elastic:

$$\Phi_{\text{eff}} = \frac{1}{2} k_{\text{eff}}\, \delta_{\text{eff}}^2 = 2k_{\text{eff}}\, \gamma^2 L^2 (1 - \lambda_t^* \hat{\lambda}_t \cos\phi)^2, \tag{3.39a}$$

$$\Phi_n = \frac{1}{2} k_n \delta_n^2 = 2k_n (1-\gamma)^2 L^2 (1 - \lambda_t^* \hat{\lambda}_t \cos\phi)^2. \tag{3.39b}$$

Governing equations

As a consequence of the assumed hypothesis and the derived reduced kinematics, the total potential energy of the system simplifies to a function of three independent Lagrangian parameters: the parameter γ, the microtubule elastic stretch $\hat{\lambda}_t$,

and the buckling angle ϕ. The reduced functional reads:

$$\mathcal{P}_{\text{sym}}(\gamma, \hat{\lambda}_t, \phi) = \Psi_{\text{cyto}}(\hat{\lambda}_t, \phi) + \Phi_{\text{eff}}(\gamma, \hat{\lambda}_t, \phi) + \Phi_n(\gamma, \hat{\lambda}_t, \phi) \tag{3.40}$$

where Ψ_{cyto} (Eq. (3.17)) reduces to

$$\Psi_{\text{cyto}}(\hat{\lambda}_t, \phi) = 2\mathcal{U}_t(\hat{\lambda}_t) + 2\mathcal{U}_f(\hat{\lambda}_t, \phi) + \mathcal{U}_{sp}(\phi). \tag{3.41}$$

Minimizing $\mathcal{P}_{\text{sym}}$ with respect to the state variables yields the governing equilibrium equations:

$$\frac{\partial \mathcal{P}_{\text{sym}}}{\partial \gamma} = \frac{\partial \mathcal{P}_{\text{sym}}}{\partial \hat{\lambda}_t} = \frac{\partial \mathcal{P}_{\text{sym}}}{\partial \phi} = 0. \tag{3.42}$$

First, stationarity with respect to the partition parameter γ recovers the standard series-spring relation:

$$\gamma = \frac{k_n}{k_{eff} + k_n}. \tag{3.43}$$

Next, the simultaneous stationarity with respect to the buckling angle ϕ and the microtubule elastic stretch $\hat{\lambda}_t$ leads to the coupled system:

$$\begin{aligned} &\sin\phi \Bigg\{ b \left[\frac{(\lambda_f^*)^2}{\lambda_t^* \hat{\lambda}_t \cos^2\phi} - \frac{(\lambda_t^*)^2 (\hat{\lambda}_t)^2 \cos\phi}{\lambda_f^*} \right] \\ &+ \frac{2\kappa}{\cos\phi} + 4L^2 A_k \lambda_t^* \hat{\lambda}_t (1 - \lambda_t^* \hat{\lambda}_t \cos\phi) \Bigg\} = 0, \end{aligned} \tag{3.44a}$$

$$\begin{aligned} &\left\{ a\lambda_t^* + \left[\frac{b}{\lambda_f^*} + 4L^2 A_k \right] (\lambda_t^*)^2 \cos^2\phi \right\} \hat{\lambda}_t^3 \\ &- 4L^2 A_k \lambda_t^* \cos\phi \, \hat{\lambda}_t^2 - a\lambda_t^* - \frac{b(\lambda_f^*)^2}{\lambda_t^* \cos\phi} = 0, \end{aligned} \tag{3.44b}$$

where we set

$$a := \frac{2K_t L_t}{3}, \qquad b := \frac{2K_f L_f}{3}, \qquad A_k = k_{eff}\, \gamma^2 + k_n (1-\gamma)^2.$$

Equation (3.44a) identifies the system's bifurcation behavior. The trivial solution $\phi = 0$ corresponds to the straight, unbuckled configuration where deformation is purely axial. Non-trivial solutions ($\phi \neq 0$, indicating buckling) emerge when the term inside the curly brackets vanishes:

$$b \left[\frac{(\lambda_f^*)^2}{\lambda_t^* \hat{\lambda}_t \cos^2\phi} - \frac{(\lambda_t^*)^2 (\hat{\lambda}_t)^2 \cos\phi}{\lambda_f^*} \right] + \frac{2\kappa}{\cos\phi} + 4L^2 A_k \lambda_t^* \hat{\lambda}_t (1 - \lambda_t^* \hat{\lambda}_t \cos\phi) = 0. \tag{3.45}$$

By substituting the geometric compatibility relation $\cos\phi = (\lambda_f^* \hat{\lambda}_f)/(\lambda_t^* \hat{\lambda}_t)$ (obtained from Eq. (3.36)) into the system, Eqs. (3.45) and (3.44b) can be decoupled

and recast as cubic polynomials in terms of the elastic stretches $\hat{\lambda}_f$ and $\hat{\lambda}_t$, respectively:

$$\left[b + 4L^2 A_k \lambda_f^*\right] \hat{\lambda}_f^3 - 4L^2 A_k \hat{\lambda}_f^2 - \frac{2\kappa}{\lambda_f^*}\hat{\lambda}_f - b = 0, \tag{3.46a}$$

$$\hat{\lambda}_t^3 + \frac{\lambda_f^*}{a\lambda_t^*\hat{\lambda}_f}\left\{4L^2 A_k(\hat{\lambda}_f)^2(\lambda_f^*\hat{\lambda}_f - 1) + b\left[(\hat{\lambda}_f)^3 - 1\right]\right\}\hat{\lambda}_t - 1 = 0. \tag{3.46b}$$

We first solve Eq. (3.46a) for the unknown fiber stretch $\hat{\lambda}_f$. Application of Cardano's formula yields the exact analytical root:

$$\hat{\lambda}_f = -\frac{a_2}{3a_3} + \sqrt[3]{-\frac{q_f}{2} + \sqrt{D_f}} + \sqrt[3]{-\frac{q_f}{2} - \sqrt{D_f}}, \tag{3.47}$$

where the discriminant D_f and coefficients are given by:

$$D_f = \frac{q_f^2}{4} + \frac{p_f^3}{27}, \qquad p_f = \frac{a_1}{a_3} - \frac{a_2^2}{3a_3^2}, \qquad q_f = \frac{a_0}{a_3} - \frac{a_1 a_2}{3a_3^2} + \frac{2a_2^3}{27a_3^3},$$
$$a_3 = b + 4L^2 A_k \lambda_f^*, \quad a_2 = -4L^2 A_k, \quad a_1 = -\frac{2\kappa}{\lambda_f^*}, \quad a_0 = -b.$$

Subsequently, using the determined value of $\hat{\lambda}_f$, the microtubule stretch $\hat{\lambda}_t$ is obtained by solving Eq. (3.46b). Since this equation lacks a quadratic term, the solution via Cardano's method simplifies to:

$$\hat{\lambda}_t = \sqrt[3]{-\frac{q_t}{2} + \sqrt{D_t}} + \sqrt[3]{-\frac{q_t}{2} - \sqrt{D_t}}, \tag{3.48}$$

with:

$$D_t = \frac{q_t^2}{4} + \frac{p_t^3}{27}, \qquad q_t = -1,$$
$$p_t = \frac{\lambda_f^*}{a\lambda_t^*\hat{\lambda}_f}\left\{4L^2 A_k(\hat{\lambda}_f)^2(\lambda_f^*\hat{\lambda}_f - 1) + b\left[(\hat{\lambda}_f)^3 - 1\right]\right\}.$$

With the elastic stretches $\hat{\lambda}_f$ and $\hat{\lambda}_t$ determined, the post-buckling geometry is fully resolved. The buckling angle ϕ and the total system displacement Δ are recovered as:

$$\phi = \arccos\left(\frac{\lambda_f^*\hat{\lambda}_f}{\lambda_t^*\hat{\lambda}_t}\right), \qquad \Delta = 2L(1 - \hat{\lambda}_f\lambda_f^*). \tag{3.50}$$

The critical condition for the onset of buckling corresponds to the limit $\phi \to 0$ (i.e., $\cos\phi \to 1$). This yields the explicit bifurcation criterion:

$$\lambda_f^*\hat{\lambda}_f = \lambda_t^*\hat{\lambda}_t. \tag{3.51}$$

From Eq. (3.51), one can deduce the critical threshold for either the contractile stretch λ_f^* (given a polymerization level) or the polymerization stretch λ_t^* (given a contraction level) required to trigger instability.

the traction force exerted on the focal adhesion complex is computed as:

$$t_{\text{eff}} = k_{\text{eff}}\,\delta_{\text{eff}} = k_{\text{eff}}\,\gamma\,2L(1 - \hat{\lambda}_f\lambda_f^*). \tag{3.52}$$

The kinematic predictions of this solution will be explored in the next Section across varying regimes of pre-stretch.

3.2.2 Numerical analysis of cytoskeletal stability

We investigate the equilibrium configurations of the cell-substrate system using the physiological parameters summarized in Table 3.1. The selected values characterize a representative cytoskeletal unit: a single microtubule strut coupled to a bundled assembly of actomyosin stress fibers. Consequently, the cross-sectional area A_f is significantly larger than that of a single filament, reflecting the bundling effect.

Param.	Description	Value	Ref.	Typical Range
L	MT and SF rest length	$20\,\mu$m	Fraldi et al. [2019]	$10-50\,\mu$m
L_p	Adhesion plaque length	*Variable*	Cao et al. [2015]	$1-5\,\mu$m
h_p	Plaque height	100 nm	Franz and Müller [2005]	$50-100$ nm
w_n	Plaque width	1000 nm	Franz and Müller [2005]	~ 1000 nm
d_i	Integrin spacing	100 nm	Cavalcanti-Adam et al. [2006]	100 nm
A_t	MT cross-section	$190\,\text{nm}^2$	Deguchi et al. [2006]	$190\,\text{nm}^2$
A_f	SF cross-section	$10^4\pi\,\text{nm}^2$	Deguchi et al. [2006]	$10^4\pi\,\text{nm}^2$
E_t	MT Young modulus	1.2 GPa	Fraldi et al. [2019]	1.2 GPa
E_f	SF Young modulus	1.45 MPa	Deguchi et al. [2006]	1.45 MPa
k_i	Integrin stiffness	5 pN/nm	Fisher et al. [1999]	5 pN/nm
k_p	Plaque stiffness	2.5 pN/nm	Banerjee and Marchetti [2012]	2.5 pN/nm
k_n	Nucleus stiffness	20 pN/nm	Mathur et al. [2007]	$10-50$ pN/nm
k_s	Substrate stiffness	10 pN/nm	Gentleman et al. [2003]	$10-100$ pN/nm
$\Delta\mu_0$	Ref. chem. potential	$250\,k_BT$	Nicolas et al. [2004]	$10-250\,k_BT$
B_t	MT bending stiffness	$215\,\text{nN}\,\mu\text{m}^2$	Brangwynne et al. [2006]	$0.02-215\,\text{nN}\,\mu\text{m}^2$

Table 3.1: *Geometric and constitutive parameters adopted for the numerical simulations.*

While previous studies largely restricted the analysis to the effects of actomyosin contractility alone [Palumbo et al., 2022], here we extend the investigation to the *coupled* regime. We assess the simultaneous effects of:

(i) active pre-contraction of the actomyosin bundle ($\lambda_f^* \leq 1$), and

(ii) active pre-polymerization of the microtubule ($\lambda_t^* \geq 1$).

The following sections demonstrate how the interplay between these two mechanisms determines the stability boundaries and the post-buckling behavior of the cell-inspired tensegrity system.

Kinematics of buckling and post-buckling response

This section analyzes the system's equilibrium configurations, specifically focusing on the transition from the straight ($\phi = 0$) to the buckled ($\phi \neq 0$) state. We examine how the interplay between actomyosin contractility (λ_f^*) and microtubule polymerization (λ_t^*) governs this instability, identifying the critical thresholds and quantifying the resulting elastic deformations.

Stability thresholds and bifurcation analysis To isolate the specific contribution of each active mechanism, we first restrict our analysis to independently applied inelastic pre-stretches. In this subsection, we investigate the stability thresholds triggered by

varying a single control parameter (either actomyosin contractility λ_f^* or microtubule polymerization λ_t^*) while maintaining the other component in its stress-free resting state ($\lambda^* = 1$).

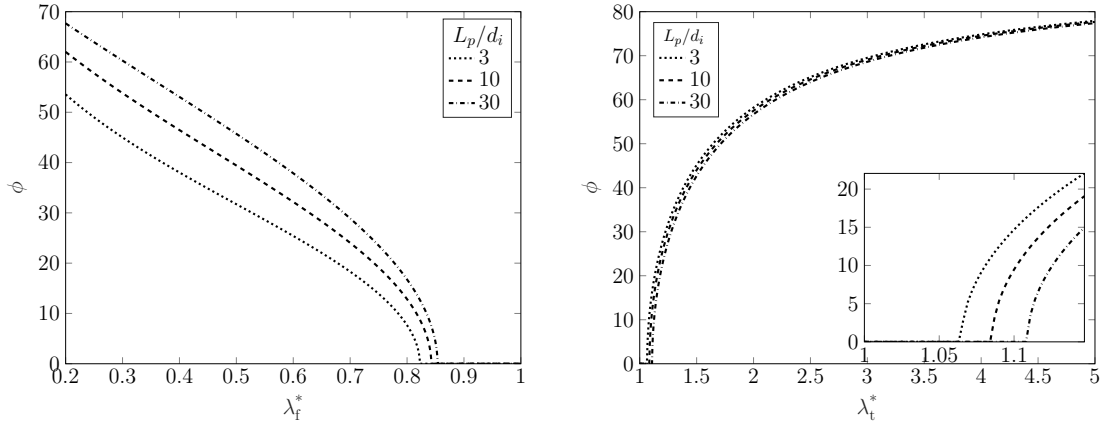

(a) **(b)**

Figure 3.9: *Bifurcation diagrams showing the equilibrium buckling angle ϕ driven by (a) increasing actomyosin contraction (decreasing λ_f^*) and (b) increasing microtubule polymerization (λ_t^*), for varying plaque lengths L_p/d_i.*

The onset of microtubule buckling is governed by the competition between the active pre-stretches and the stiffness of the focal adhesion complex. Fig. 3.9 presents the equilibrium buckling angle ϕ as a function of the inelastic pre-stretch for different values of the normalized plaque length L_p/d_i. We observe a classic bifurcation behavior:

- **Contractile-driven buckling.** For a fixed polymerization ($\lambda_t^* = 1$), buckling emerges only when the contractile pre-stretch drops below a critical threshold $\lambda_{f,cr}^*$, as shown in Fig. 3.9a.
- **Polymerization-driven buckling.** Conversely, for a fixed contraction ($\lambda_f^* = 1$), buckling is triggered when polymerization exceeds a critical extension $\lambda_{t,cr}^*$, as shown in Fig. 3.9b.

The sensitivity of these critical thresholds to the normalized plaque length L_p/d_i is reported in Figs. 3.10a and 3.10b. While both $\lambda_{f,cr}^*$ and $\lambda_{t,cr}^*$ exhibit a nonlinear dependence on normalized plaque length, they remain confined within narrow physiological ranges ($0.81 \leq \lambda_{f,cr}^* \leq 0.86$ and $1.06 \leq \lambda_{t,cr}^* \leq 1.14$). Notably, for mature focal adhesions ($L_p > 2d_i$), the critical values stabilize at approximately $\lambda_{f,cr}^* \approx 0.84$ and $\lambda_{t,cr}^* \approx 1.10$

We next examine the elastic stretches, $\hat{\lambda}_f$ and $\hat{\lambda}_t$, which quantify the elastic deformation of the filaments. Figures 3.11 and 3.12 show, respectively, the elastic stretch of the actomyosin bundle $\hat{\lambda}_f$ and of the microtubule $\hat{\lambda}_t$, as a function of the inelastic contraction λ_f^* and polymerization λ_t^*. These profiles reveal a fundamental decoupling effect in the post-buckling regime. In the straight configuration, the elastic stretches vary linearly with the applied inelastic pre-stretch λ^*. However, once buckling activates, a decoupled behavior emerges. The buckling acts as a mechanical fuse by which

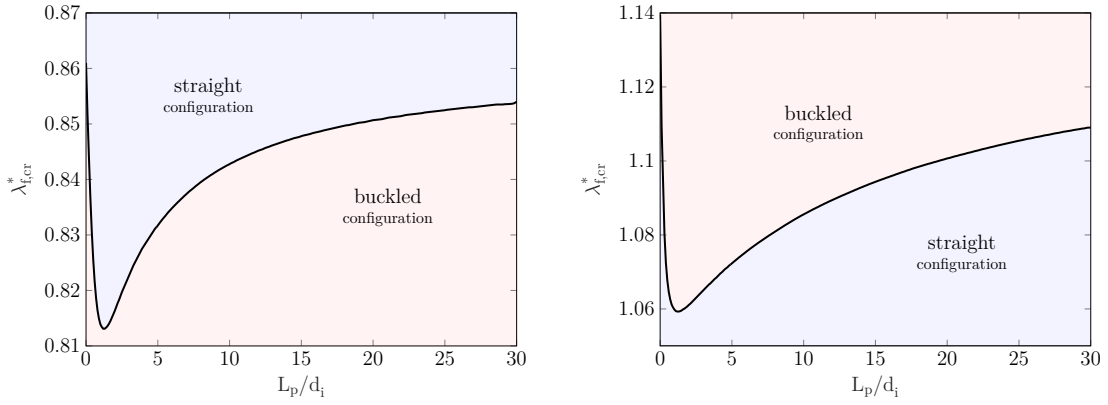

(a) **(b)**

Figure 3.10: *Critical stability thresholds for (a) contractility $\lambda^*_{f,cr}$ and (b) polymerization $\lambda^*_{t,cr}$ as functions of the normalized plaque length.*

- The actomyosin elastic stretch $\hat{\lambda}_f$ (Fig. 3.11) becomes highly nonlinear if buckling is contractile-driven but remains effectively constant if buckling is polymerization-driven.
- The microtubules' elastic stretch $\hat{\lambda}_t$ (Fig. 3.12), conversely, becomes highly nonlinear if polymerization-driven but remains insensitive if buckling is contractile-driven.

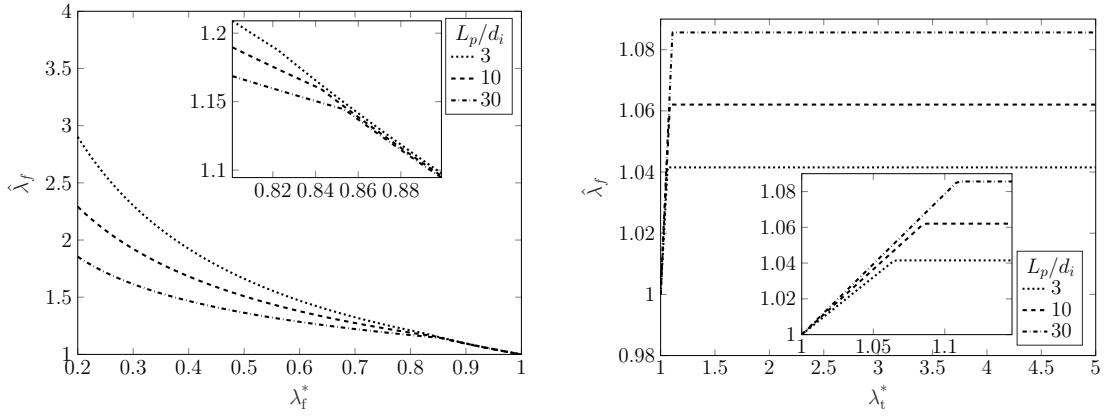

(a) **(b)**

Figure 3.11: *Elastic stretch of the actomyosin bundle $\hat{\lambda}_f$ versus (a) pre-contraction and (b) pre-polymerization for different L_p/d_i.*

This mechanism effectively caps the elastic stretch in the passive component (the one not subjected to inelastic pre-stretch), preventing further stress accumulation. Consequently, the active component is forced to accommodate the imposed deformation through geometric reconfiguration, leading to divergent behaviors:

- If the active component is the actomyosin fiber, when driven by pre-contraction, it exhibits a non-linear increase in elastic pre-stretch in the post-buckling regime

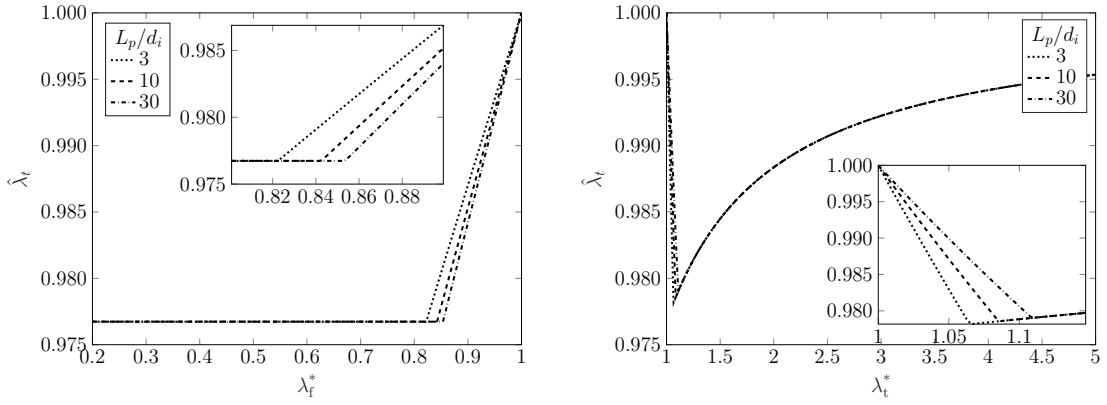

(a) **(b)**

Figure 3.12: *Elastic stretch of the microtubule $\hat{\lambda}_t$ versus (a) pre-contraction and (b) pre-polymerization.*

(Fig. 3.11a). On the other hand, the passive component (the microtubules), in the post-buckling regime, maintains the level of elastic stretch reached at the onset of the buckling (Fig. 3.12a.

- If the active components are the microtubules, when driven by pre-polymerization, they exhibit a non-linear relaxation at the onset of buckling, relieving the accumulated stretch via geometric reconfiguration (Fig. 3.12b). The passive component (the actomyosin fiber), on the other hand maintains the level of elastic stretch reached at the onset of the buckling (Fig. 3.11b).

Coupled effects of contraction and polymerization Finally, we investigate the realistic physiological scenario where both active mechanisms operate simultaneously. We simulate the coupled response by sweeping the pre-contraction λ_f^* across fixed levels of pre-polymerization λ_t^*, and vice versa, setting $L_p = 20d_i$.

Figures 3.13a and 3.13b display the resulting equilibrium buckling angles. These results demonstrate that the interaction between contractility and polymerization is highly synergistic. As shown in Fig. 3.13a, the presence of underlying pre-polymerization ($\lambda_t^* > 1$) fundamentally alters the stability landscape, shifting the bifurcation point significantly. This implies that polymerization sensitizes the system, allowing buckling to occur at much lower levels of contractility than would be required for a quiescent microtubule. Analogously, increasing levels of contractility can induce immediate buckling even at moderate polymerization levels (Fig. 3.13b), causing the system to bypass the straight configuration entirely.

The elastic stretches under combined loading (Figs. 3.14 and 3.15) reveal a nuanced behavior. While the onset of instability is synergistic, promoted by the simultaneous action of both mechanisms, the post-buckling elastic state retains the decoupled character observed in the independent analysis. Specifically, sweeping the contractility of the actomyosin fibers ($\lambda_f^* \in [0.2, 1]$) confirms that the actomyosin post-buckling elastic stretch $\hat{\lambda}_f$ is largely insensitive to the pre-polymerization level λ_t^* , as shown in Fig. 3.14a, which only affects the elastic stretch of the microtubules themselves $\hat{\lambda}_t$, as shown

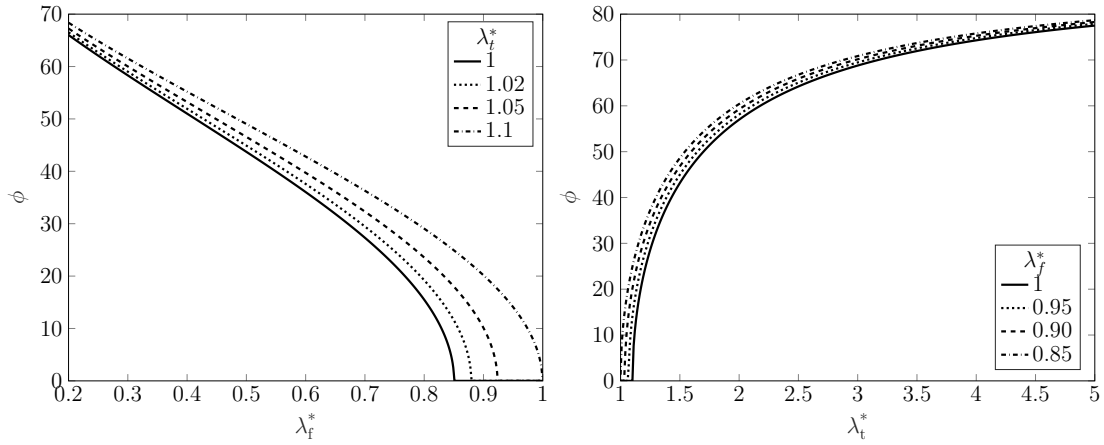

(a) **(b)**

Figure 3.13: *Combined pre-stretches: Buckling angle ϕ (a) as a function of the pre-contraction λ_f^* for distinct levels of pre-polymerization and (b) as a function of the pre-polymerization λ_t^* for distinct levels of pre-contraction, setting $L_p = 20d_i$.*

in Fig. 3.15a. Symmetrically, the microtubule post-buckling elastic stretch $\hat{\lambda}_t$ is insensitive to the pre-contraction levels λ_f^* (Fig. 3.15b), which only affects the post-buckling elastic stretch of the fibers themselves $\hat{\lambda}_f$, as shown in Fig. 3.14b.

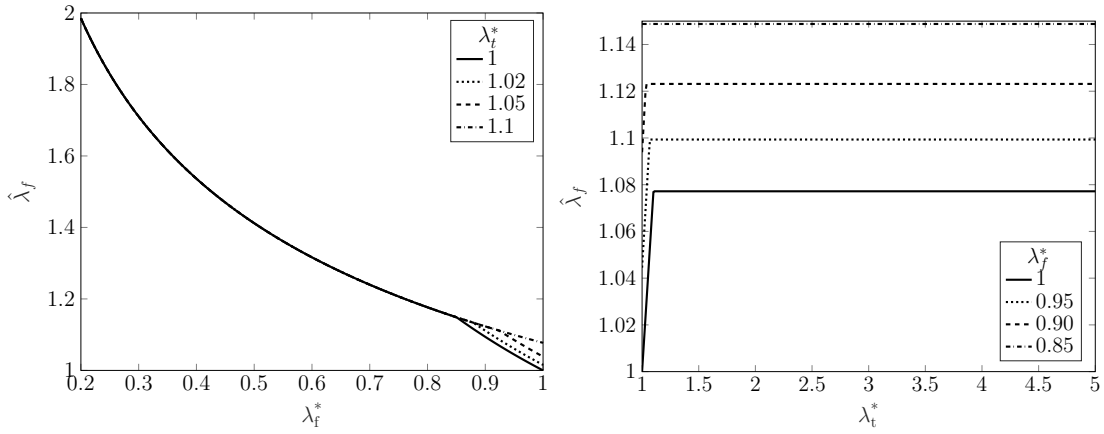

(a) **(b)**

Figure 3.14: *Combined pre-stretches: Elastic stretches of the actomyosin bundle $\hat{\lambda}_f$ (a) as a function of pre-contraction λ_f^* for distinct levels of pre-polymerization and (b) as a function of pre-polymerization λ_t^* for distinct levels of pre-contraction.*

3.2.3 Mechanical regulation of focal adhesion dynamics

In this section, we analyze the assembly and disassembly processes predicted by the model. The results presented hereafter confirm and complete the analysis previously reported by Palumbo et al. [2022], specifically extending the investigation to the coupled role of microtubules. According to the governing evolution equation (3.35), the

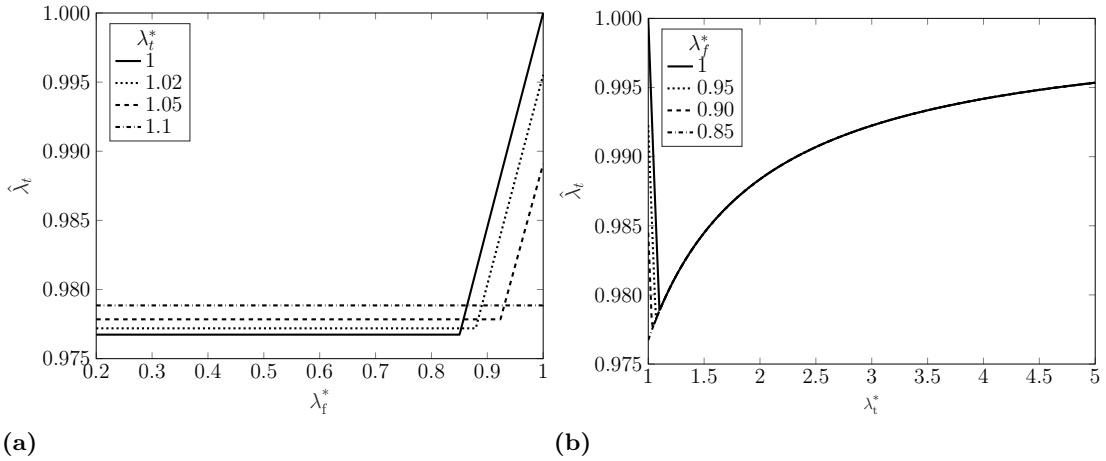

(a) **(b)**

Figure 3.15: *Combined pre-stretches: Elastic stretches of the microtubules $\hat{\lambda}_t$ (a) as a function of pre-contraction λ_f^* for distinct levels of pre-polymerization and (b) as a function of pre-polymerization λ_t^* for distinct levels of pre-contraction.*

adhesion plaque dynamics are driven by the mechanical load at the interface: tensile forces promote protein aggregation (assembly), while compressive forces induce dissociation (disassembly) [Tanaka and Kirschner, 1995, Hill, 1981, Heidemann and Buxbaum, 1994, Putnam et al., 2001, Geiger and Bershadsky, 2001]. In our framework, the driving force F_p acting on the plaque is the net mechanical load generated in response to the inelastic pre-stretches λ_f^* and λ_t^*, in the focal adhesion-ECM complex given by t_{eff} (Eq. (3.52)); therefore, $F_p = t_{\text{eff}}$. To capture the nonlinear response of the adhesion complex, we account for the finite elasticity of the plaque via a cubic expansion of the flux law. We have verified that for physiological force magnitudes (≈ 100 pN) and realistic stiffness k_p, the third-order expansion is sufficient to ensure convergence. The results presented hereafter highlight how increasing levels of actomyosin contraction and microtubule polymerization compete to regulate the plaque growth rate. Unless otherwise specified, the substrate stiffness is set to $K_s = 10$ pN/nm.

Combined effects on plaque assembly

We specifically investigate how the mechanosensitivity of the focal adhesion is modulated by the simultaneous action of actomyosin contractility and microtubule polymerization. Physically, polymerization acts as a disassembly driver: increasing the pre-polymerization level enhances the compressive force pushing on the focal adhesion-ECM complex, thereby increasing the negative component of the flux J (disaggregation). Conversely, actomyosin contractility acts as an assembly driver by exerting tension.

Figure 3.16a plots the net force F_p as a function of the actomyosin pre-stretch $\lambda_f^* \in [0.75, 1]$ for a fixed plaque length ($L_p = 1.4 d_i$) and for different values of the microtubule pre-stretch. We observe that increasing contractility (decreasing λ_f^*) monotonically increases the tensile load, promoting assembly. This effect is significantly amplified in the post-buckling regime, where the stiffness of the system drops, allowing for larger effective deformations.

Figure 3.16b illustrates the inverse scenario: the force F_p versus microtubule pre-

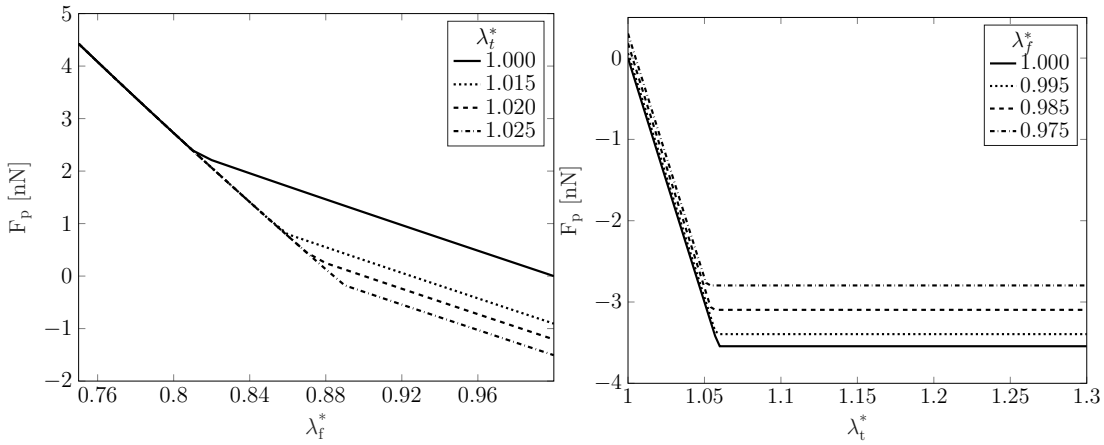

(a) **(b)**

Figure 3.16: *Combined pre-stretches: Force F_p (a) as a function of the actomyosin pre-contraction λ_f^* for distinct pre-polymerization levels, and (b) as a function of the microtubule pre-polymerization λ_t^* for distinct pre-contraction levels. The adhesion plaque length is set to $L_p = 1.4d_i$.*

stretch $\lambda_t^* \in [1, 1.3]$ for a fixed plaque length ($L_p = 1.4d_i$) and for different values of the actomyosin pre-contraction. Here, a critical saturation behavior emerges. Once microtubule buckling occurs, the mechanical force plateaus. This indicates that the microtubule component cannot transmit compressive loads beyond its critical buckling load. Consequently, buckling acts as a saturation mechanism for the disassembly signal, preventing the polymerization force from driving the plaque into unlimited disassembly.

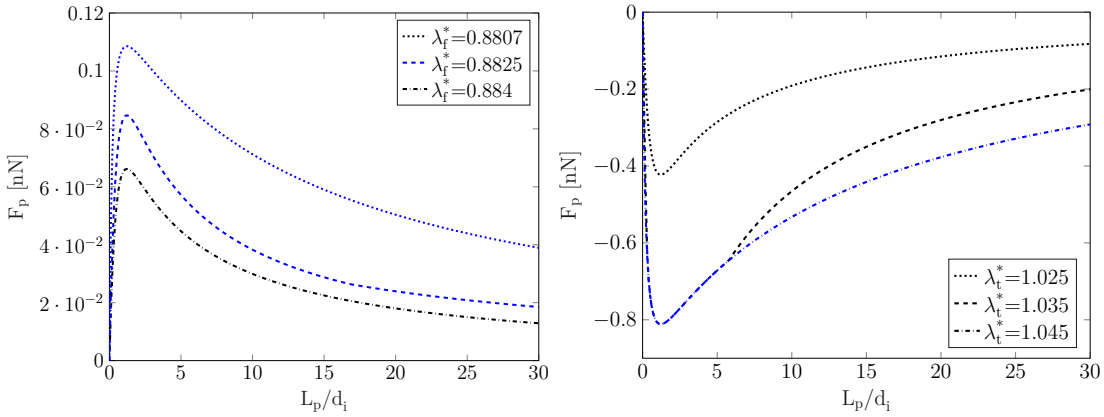

(a) **(b)**

Figure 3.17: *Force F_p as a function of normalized plaque length L_p/d_i (a) Contractile-dominant case (underlying $\lambda_t^* = 1.0222$). (b) Polymerization-dominant case (underlying $\lambda_f^* = 0.91$). Blue profiles indicate buckled configurations; black profiles indicate straight configurations.*

The mechanical force F_p is also intrinsically dependent on the size of the adhesion, as shown in Fig. 3.17a. Consistent with the mechanosensitive feedback assumed in

the model, an increase in contractility leads to a significant increase in the pulling force, enhancing the recruitment flux. Figure 3.17b depicts the scenario where pre-polymerization prevails. In this case, the force pushes against the adhesion, enhancing the disassembly. In both Figs. 3.17a and 3.17b, the profiles in blue and black correspond to buckled and straight configurations, respectively. The resulting protein fluxes J are

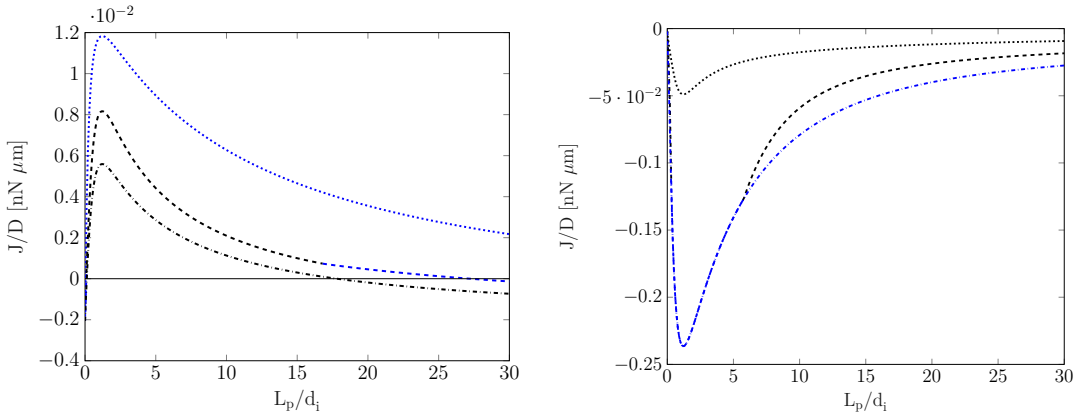

(a) **(b)**

Figure 3.18: *Comparison of growth laws for (a) varying inelastic pre-contraction λ_f^* and (b) varying pre-polymerization λ_t^*. Parameters correspond to those assumed in Figs. 3.17a and 3.17b.*

shown in Figs. 3.18a and 3.18b. The data confirm that positive tensile forces ($F_p > 0$) drive assembly ($J > 0$), while compressive forces ($F_p < 0$) induce disassembly ($J < 0$). These figures clearly recover the three regimes of plaque dynamics proposed by Cao et al. [2015] and observed experimentally [Cukierman et al., 2002]. Furthermore, these regimes resonate with the dynamics described by molecular motor-clutch models:

1. Nascent decay (frictional slippage). A newly nucleated plaque must overcome a critical size (related to $\Delta\mu^0$) to initiate growth. Below this size, the cluster lacks sufficient binding strength to transmit the cytoskeletal load, leading to disassembly (analogous to the frictional slippage regime in clutch models).

2. Stable growth (reinforcement). Beyond the critical size, the plaque elongates towards a stable equilibrium length, recruiting proteins to accommodate the increasing load.

3. Disassembly (homeostasis). Oversized plaques experience a negative flux and shrink back to the stable size, representing a homeostatic equilibrium where the cytoskeletal tension is balanced by the optimal number of bonds.

However, significantly high contractility levels can override this stability, leading to an unlimited assembly process where the force prevents the plaque from ever finding a stable equilibrium length.

Finally, Fig. 3.19b illustrates the physiological reality where the cell's net pre-strain results from the competition between these mechanisms. We plot the growth flux for varying pre-contraction levels combined with either a resting microtubule ($\lambda_t^* = 1$) or a slightly polymerized one ($\lambda_t^* = 1.002$, i.e., 2‰ stretch). Remarkably, even a minimal

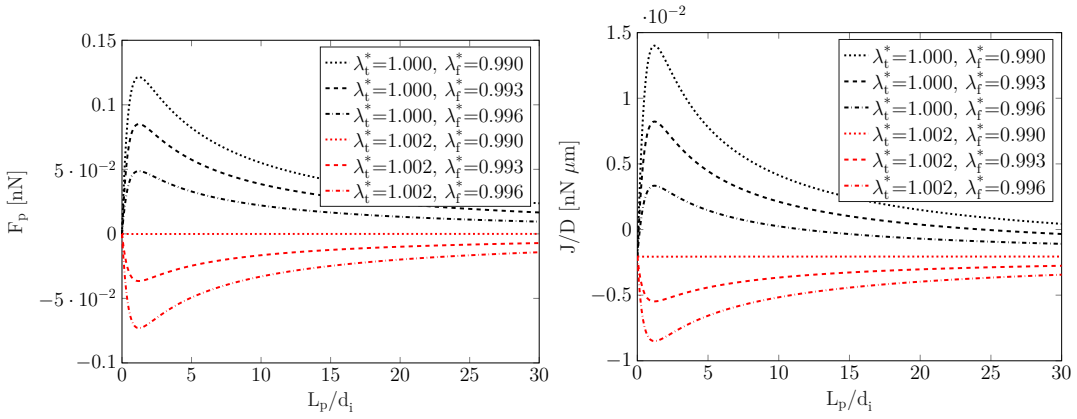

(a) **(b)**

Figure 3.19: *Combined pre-stretches: Force F_p (a) and aggregation or disaggregation flux (b) plotted as a function of the focal adhesion plaque length L_p normalized with respect to the integrin spacing d_i.*

pre-polymerization of 1–2‰ is sufficient to flip the system from an assembly regime to a disassembly regime, particularly at lower contractility levels. This suggests that the Focal Adhesion growth is highly frustrated: the assembly attempt driven by actomyosin can be easily negated by the compressive action of microtubules. Consequently, the same level of actomyosin contractility may promote growth in one context but fail to sustain the plaque if the microtubule polymerization slightly increases.

Influence of nonlinear growth kinetics

This section examines the implications of the mathematical structure assumed for the growth law. In the state-of-the-art literature, following the thermodynamic framework proposed by Hill [1981], the growth function is typically linearized under the assumption of small displacements [Shemesh et al., 2005]. However, limiting the expansion to the linear term restricts the validity of the model to the immediate vicinity of thermodynamic equilibrium. To extend the model to finite deformations, one might consider higher-order corrections. A crucial physical inconsistency arises if the expansion is truncated at the quadratic term ($J \propto F^2$). Since the quadratic term is even, it cannot distinguish between tensile and compressive forces. Physically, this would imply that large compressive forces could promote assembly in the same manner as tensile forces, violating the fundamental mechanosensitivity of the focal adhesion. Therefore, to capture the non-linear stiffening effects while preserving the directional sensitivity of the growth process (i.e., maintaining odd symmetry where $J(-F) \approx -J(F)$), the expansion must include the cubic term.

We verified the impact of these truncations in Fig. 3.20, which compares the growth flux J obtained using linear, quadratic, and cubic formulations for a fixed pre-polymerization of 5% and for two stiffnesses of the plaque k_p. It is evident that for plaque stiffness values $k_p < 1$ pN/nm, the non-linear contributions are significant and the quadratic approximation leads to erroneous flux predictions. To further quantify this deviation, Figs. 3.21a and 3.21b contrast the standard linear law (black profiles) against the proposed cubic growth law (red profiles, Eq. (3.35)). The discrepancy be-

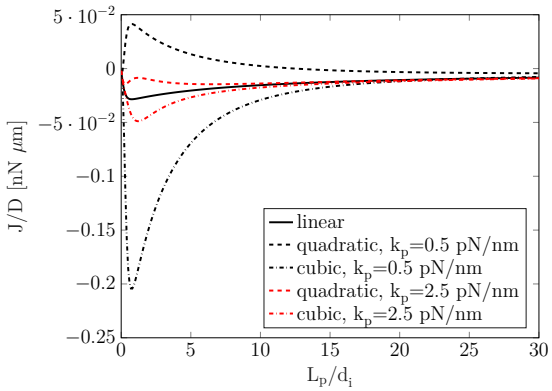

Figure 3.20: *Comparison of growth laws obtained by assuming linear, quadratic, and cubic forms of the flux function. Profiles are plotted for two values of plaque stiffness k_p, with fixed pre-stretches $\lambda_t^* = 1.025$ and $\lambda_f^* = 0.91$.*

comes pronounced in the regimes of high contractility or polymerization, confirming that a linear law underestimates the assembly flux under high tension and underestimates the disassembly flux under compression.

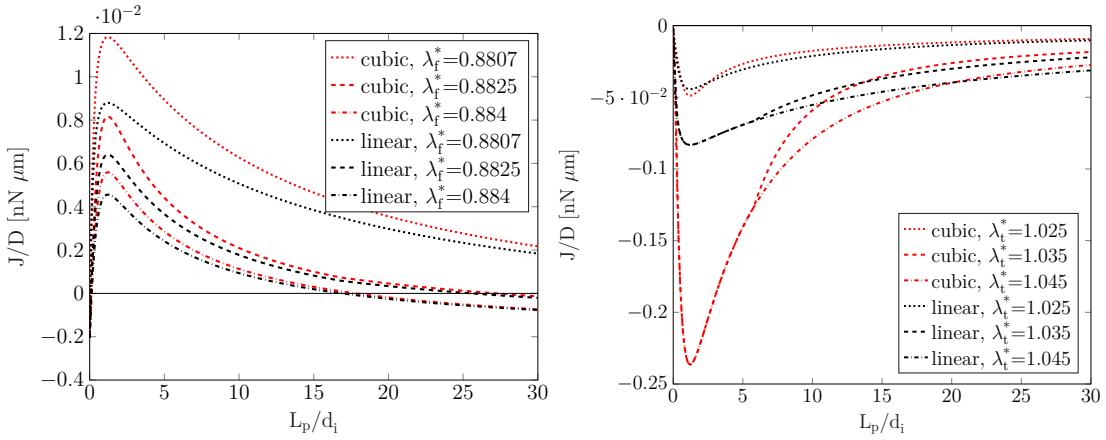

(a) **(b)**

Figure 3.21: *Comparison between the linearized growth law [Hill and Kirschner, 1982] (black profiles) and the non-linear cubic law proposed in Eq.* (3.35) *(red profiles). The evaluation is performed for (a) varying pre-contraction and (b) varying microtubule polymerization.*

Substrate stiffness and durotaxis

Finally, we briefly address the role of the extracellular environment. It is well-established that cells sense substrate rigidity, developing larger contractile forces on stiffer environments. Figure 3.22 illustrates the dependence of the growth flux on the substrate stiffness K_s. The model predicts that on softer substrates, the equilibrium stable length of the plaque is significantly reduced. Conversely, stiffer substrates support the formation of larger, more stable adhesions. This result provides a mechanistic confirmation

of durotaxis [Lo et al., 2000], where the adhesion complex grows more efficiently on rigid substrates because the stiffer environment allows for the development of higher isometric tension, which in turn drives the positive feedback loop of plaque assembly.

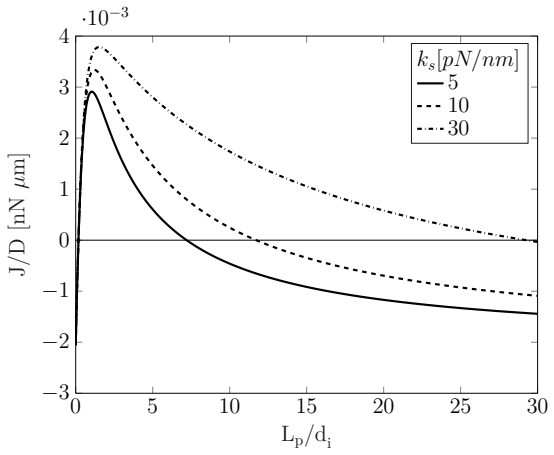

Figure 3.22: *Influence of the substrate stiffness K_s on the growth flux J, for fixed pre-stretches $\lambda_t^* = 1$ and $\lambda_f^* = 0.996$.*

3.2.4 Buckling sensitivity and adhesion equilibrium

The analytical framework developed in this section elucidates the competitive interplay between cytoskeletal architecture and focal adhesion dynamics. A key finding is the dramatic synergy between actomyosin contractility and microtubule polymerization in triggering structural instability. While our results indicate that independently applied pre-stretches must exceed relatively high thresholds (approximately 16% for contraction and 10% for polymerization) to induce buckling, their simultaneous action destabilizes the system at remarkably lower levels ($\approx 1\%$). This implies that the cell operates in a state of incipient instability, where small fluctuations in biochemical signaling (contractility or polymerization) can trigger large-scale geometric reconfiguration.

Crucially, our model identifies a homeostatic role for microtubules in regulating adhesion size. In the absence of polymerization, high contractility drives a runaway assembly process where the focal adhesion grows indefinitely, failing to reach a stable equilibrium. Our results demonstrate that the compressive load exerted by microtubule polymerization is necessary to counteract this tension, introducing a negative feedback loop that limits plaque growth. Thus, the physiological focal adhesion size is not determined by contractility alone, but by the thermodynamic equilibrium between the pulling force of the actin network and the pushing force of the microtubule struts.

Finally, the adoption of a non-linear (cubic) growth law reveals that the system is more responsive to mechanical cues than linear models suggest. This non-linearity amplifies the impact of mechanical stress on protein flux, providing a theoretical justification for the rapid assembly/disassembly rates observed in vivo during migration.

The limits of symmetry

Cell locomotion is an inherently polarized process driven by the spatial segregation of mechanical forces: protrusion at the leading edge and contraction at the trailing

edge [Recho et al., 2013]. The current model, while effectively capturing the autotactic regulation of adhesion size, is constrained by its geometric symmetry. It assumes a single contractile unit acting in parallel with a microtubule, without distinguishing between the cell front and rear. Consequently, it cannot reproduce the asymmetry of the cytoskeletal structure.

Therefore, the natural progression of this work is to extend the framework to a non-symmetric configuration. In the subsequent section, we relax the assumption of geometric symmetry to investigate how asymmetric buckling influences the kinematic response, particularly when coupled with differential adhesion stiffnesses at the cell boundaries.

3.3 Mechanics of the asymmetric cytoskeletal unit: influence of stiffness gradient

The general tensegrity framework established in Chapter 3 provided a rigorous basis for understanding the stability of cytoskeletal units coupled with elasto-damaging interfaces. In this section, we specialize this framework to address the mechanics of whole-cell locomotion, specifically examining the mechanosensing mechanisms underlying positive and negative durotaxis. While the previous chapter focused on a localized unit extending from the focal adhesion to the nucleus, the present analysis expands the scope to represent the integrated cytoskeleton anchored between two distinct substrate points. By building upon the intrinsic stability properties of the microtubule network, specifically the coupling between actomyosin pre-contraction and microtubule pre-polymerization analyzed in Chap. 3.2, we introduce two fundamental sources of asymmetry. First, following the findings of Théry et al. [2006], who demonstrated that the adhesive microenvironment governs the reproducible spatial organization of the nucleus and centrosome, we incorporate a structural asymmetry. This source of asymmetry is included via the parameter η that defines the positioning of the internal rotational hinge, which serves as a mechanical analog for the cell's polarized internal architecture. Second, we introduce asymmetric boundary conditions to simulate the external environment by means of substrate stiffness gradients.

3.3.1 Mechanical model formulation

To investigate the interplay between intracellular mechanics and extracellular environmental cues, we adapt the general tensegrity unit devised in Chapter 3. The model conceptualizes the cytoskeleton as a synergy between a compression-bearing, buckling-prone element (representing the microtubule network) and a tension-bearing element (representing the actomyosin stress fibers). This system is anchored to the extracellular matrix (ECM) through equivalent springs. To specifically analyze the influence of asymmetry on cell equilibrium and incipient motion, we impose the following specializations on the general model:

1. **Global geometric asymmetry.** Unlike the symmetric unit assumed in Chap. 3.2, we introduce the structural asymmetry ratio, $\eta \in]0, +\infty[$. Recalling the definition introduced in Chap. 3, this parameter defines the ratio between the reference lengths of the microtubule subunits relative to the soft (L_t^s) and hard (L_t^h) sides of

the cell, such that $\eta := L_t^s/L_t^h$. Consequently, the reference position of the buckling hinge is not necessarily central, reflecting the inherent polarity of a migrating cell.

2. **Linear adhesion and asymmetric boundaries.** We assume the focal adhesions operate strictly within their linear elastic regime. Referring to the integrity parameter ζ introduced in Chap. 3, we set $\zeta \equiv 1$ (no damage evolution) and assume deformations remain below the detachment threshold ($\delta < \Delta^0$). Crucially, the boundary conditions are asymmetric. The equivalent springs at the cell edges represent the combined stiffness of the focal adhesion and the local substrate. These are characterized by effective stiffnesses K_s and K_h (for the soft and hard substrate, respectively), derived according to the relations in Eq. (3.26). Note that, therein, the stiffness of the substrate k_{sub} is given by k_h or k_s in the case of hard and soft substrates, respectively.

Under these assumptions, the system is reduced to the configuration illustrated in Fig. 3.23. We recall that given the quasi-static nature of the adopted tensegrity model, the migration is not identified by a velocity vector but rather as the direction of the net centroidal displacement during a contraction cycle. The varying substrate stiffnesses induce differential boundary displacements. This net cellular displacement noted as Δ_N arises from the imbalance between the displacements δ_s and δ_h, and is computed as [Sunyer and Trepat, 2020]

$$\Delta_N = \delta_s - \delta_h. \tag{3.53}$$

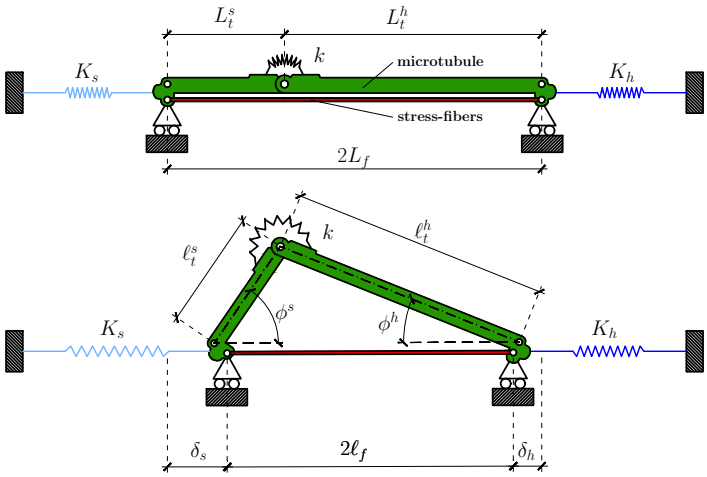

Figure 3.23: *Reference and deformed configuration of the asymmetric structural scheme adopted for the one-dimensional tensegrity model. Here the cell-focal adhesion-substrate connections are represented with the equivalent springs of stiffness K_s, in light blue, and K_h, in dark blue, for the soft and hard substrate, respectively.*

Reduced kinematics

The assumption of asymmetric geometry is aligned with the general tensegrity model presented in Chap. 3, therefore, all the kinematic quantities remain immutable. The assumptions about the linear adhesion instead lead to the simplification of both the soft and hard pseudo-elastic potential for the focal adhesion-ECM complexes, which become fully elastic:

$$\Phi_s = \frac{1}{2}K_s\delta_s^2, \qquad \Phi_h = \frac{1}{2}K_h\delta_h^2. \tag{3.54}$$

Recalling the total contraction Δ, given by Eqs. (3.11), and its partition into the soft and hard edge displacements shown in Eq. (3.11), the elastic potential energies can be written as

$$\Phi_s = \frac{1}{2}K_s\gamma^2\Delta^2 = \frac{1}{2}K_s\gamma^2\left[L_t^h\left(1+\eta-\lambda_t^*\hat{\lambda}_t^h f_2\right)\right]^2 \tag{3.55a}$$

$$\Phi_h = \frac{1}{2}K_h(1-\gamma)^2\Delta^2 = \frac{1}{2}K_h(1-\gamma)^2\left[L_t^h\left(1+\eta-\lambda_t^*\hat{\lambda}_t^h f_2\right)\right]^2. \tag{3.55b}$$

Governing equations

The total potential energy of the developed mechanical system gathering all the elastic energy contributions takes the form:

$$\mathcal{P}_{\text{asym}}(\gamma,\hat{\lambda}_t^s,\hat{\lambda}_t^h,\phi_h) = \Psi_{\text{cyto}}(\hat{\lambda}_t^s,\hat{\lambda}_t^h,\phi_h) + \Phi_s(\gamma,\hat{\lambda}_t^s,\hat{\lambda}_t^h,\phi_h) + \Phi_h(\gamma,\hat{\lambda}_t^s,\hat{\lambda}_t^h,\phi_h). \tag{3.56}$$

The solution of the problem associated with the vanishing of the first variation of $\mathcal{P}$ then provides the stationarity conditions of $\mathcal{P}_{\text{asym}}$ with respect to the Lagrangian parameters:

$$\frac{\partial\mathcal{P}_{\text{asym}}}{\partial\gamma} = \frac{\partial\mathcal{P}_{\text{asym}}}{\partial\hat{\lambda}_t^s} = \frac{\partial\mathcal{P}_{\text{asym}}}{\partial\hat{\lambda}_t^h} = \frac{\partial\mathcal{P}_{\text{asym}}}{\partial\phi_h} = 0. \tag{3.57}$$

The first stationarity equation readily gives

$$\gamma = \frac{K_h}{K_s+K_h}. \tag{3.58}$$

When computing the remaining stationarity conditions, the trivial solution associated with the path $\sin\phi_h = 0$ is obtained, which corresponds to straight configurations of the system. After discarding the trivial solution and substituting $L_t^s = \eta L_t^h$, into the expressions of Eq. (3.57), we obtain the equations governing the buckled system, which

are cast as follows:

$$
\begin{aligned}
&a_\eta \lambda_f^* f_3 \left[\frac{(\hat{\lambda}_t^h \lambda_t^*)^2}{(\lambda_f^*)^2(1+\eta)^2} f_2 - \frac{\lambda_f^*(1+\eta)}{\hat{\lambda}_t^h \lambda_t^*} \frac{1}{f_2^2} \right] - \\
&A_k (L_t^h)^2 \hat{\lambda}_t^h \lambda_t^* f_3 f_5 - \kappa \left(\frac{\hat{\lambda}_t^h \cos\phi_h}{\eta \hat{\lambda}_t^s f_1 f_4} + \frac{1}{\sin\phi_h} \right) \tan\frac{\Delta\phi}{2} = 0, \qquad (3.59a) \\
&a_\eta \lambda_f^* \left[-\frac{(\eta \hat{\lambda}_t^s \lambda_t^*)^2}{(\lambda_f^*)^2 \hat{\lambda}_t^h (1+\eta)^2} \frac{f_2}{f_1} + \frac{\hat{\lambda}_t^h (\lambda_t^* f_2)^2}{(\lambda_f^*)^2 (1+\eta)^2} - \frac{\lambda_f^*(1+\eta)}{(\hat{\lambda}_t^h)^2 \lambda_t^* f_2} + \frac{\lambda_f^*(1+\eta)(\eta \hat{\lambda}_t^s)^2}{(\hat{\lambda}_t^h)^4 \lambda_t^* f_1 f_2^2} \right] \\
&+ b\lambda_t^* \left[\hat{\lambda}_t^h - \frac{1}{(\hat{\lambda}_t^h)^2} \right] - \kappa f_4^{-1} \left[\frac{f_1}{\eta \hat{\lambda}_t^s} - \frac{\eta \hat{\lambda}_t^s}{(\hat{\lambda}_t^h)^2 f_1} \right] \tan\frac{\Delta\phi}{2} \\
&+ A_k (L_t^h)^2 \lambda_t^* \left[\frac{(\eta \hat{\lambda}_t^s)^2}{(\hat{\lambda}_t^h)^2 f_1} - f_2 \right] f_5 = 0, \qquad (3.59b) \\
&\frac{a_\eta \eta^2 \lambda_f^* \hat{\lambda}_t^s}{f_1} \left[\frac{(\lambda_t^*)^2 f_2}{(\lambda_f^*)^2 (1+\eta)^2} - \frac{\lambda_f^*(1+\eta)}{(\hat{\lambda}_t^h)^3 \lambda_t^* f_2^2} \right] \\
&+ b\eta \lambda_t^* \left[\hat{\lambda}_t^s - \frac{1}{(\hat{\lambda}_t^s)^2} \right] - \kappa f_4^{-1} \left[\frac{\eta}{\hat{\lambda}_t^h f_1} - \frac{\hat{\lambda}_t^h f_1}{\eta (\hat{\lambda}_t^s)^2} \right] \tan\frac{\Delta\phi}{2} \\
&- A_k (\eta L_t^h)^2 \hat{\lambda}_t^s \lambda_t^* f_5 (\hat{\lambda}_t^h f_1)^{-1} = 0. \qquad (3.59c)
\end{aligned}
$$

In the previous equations, f_3 and f_4 are functions of the Lagrangian parameters as follows:

$$
\begin{aligned}
f_3(\phi_h, \hat{\lambda}_t^h, \hat{\lambda}_t^s) &:= \frac{\cos\phi_h}{f_1(\phi_h, \hat{\lambda}_t^h, \hat{\lambda}_t^s)} + 1, \\
f_4(\phi_h, \hat{\lambda}_t^h, \hat{\lambda}_t^s) &:= \left[1 - \frac{(\hat{\lambda}_t^h)^2}{\eta^2 (\hat{\lambda}_t^s)^2} f_1(\phi_h, \hat{\lambda}_t^h, \hat{\lambda}_t^s)^2 \right]^{1/2}, \qquad (3.60) \\
f_5(\phi_h, \hat{\lambda}_t^h, \hat{\lambda}_t^s) &:= 1 + \eta - \hat{\lambda}_t^h \lambda_t^* f_2(\phi_h, \hat{\lambda}_t^h, \hat{\lambda}_t^s);
\end{aligned}
$$

however, the arguments have been dropped for conciseness. Finally, in Eqs. (3.59), the positions

$$
A_k := K_s \gamma^2 + K_h (1-\gamma)^2, \quad a_\eta := \frac{K_f L_t^h (1+\eta)}{3}, \quad b := \frac{K_t L_t^h}{3} \qquad (3.61)
$$

have been set and the relationship (3.15) has been exploited.

The system of three non-linear equations in the three unknowns ϕ_h, $\hat{\lambda}_t^h$, $\hat{\lambda}_t^s$ has been numerically solved by using the nonlinear systems solver *fsolve* available in Matlab©. Then, the angle ϕ_s and the displacement Δ have been computed via Eqs. (3.5) and (3.11), while δ_s and δ_h have been obtained through Eqs. (3.12) and (3.58).

Force on the focal adhesion plaque

Durotaxis manifests as a consequence of the fact that the cell contractility generates forces on the substrate, and these forces must be balanced either at the cell periphery or throughout the cell-substrate interface [Beedle and Roca-Cusachs, 2022].

Parameter	Description	Value	Source	Typical Value
L_f	SF rest length	20 μ m	Fraldi et al. [2019]	$10-50\mu$m
L_p	adhesion plaque rest length	variable	Cao et al. [2015]	up to few μm
h_p	plaque height	100 nm	Franz and Müller [2005]	50-100 nm
w_n	plaque width	1000 nm	Franz and Müller [2005]	1000 nm
d_i	integrin spacing	100 nm	Cavalcanti-Adam et al. [2006]	100 nm
A_t	MT rest cross-sectional area	190 nm^2	Deguchi et al. [2006], Kurachi et al. [1995]	$190nm^2$
A_f	SF rest cross-sectional area	$10^4\pi$ nm^2	Deguchi et al. [2006]	$10^4\pi$ nm^2
E_t	MT Young modulus	1.2 GPa	Fraldi et al. [2019]	$1.2GPa$
E_f	SF Young modulus	1.45 MPa	Deguchi et al. [2006]	$1.45MPa$
k_i	integrin stiffness	5 pN/nm	Fisher et al. [1999]	5 pN/nm
k_p	plaque stiffness	2.5 pN/nm	Banerjee and Marchetti [2012], Caille et al. [2002]	2.5 pN/nm
$\Delta\mu_0$	energy barrier for protein recruitment without mechanical load	250k$_B$ T	Nicolas et al. [2004]	10 k$_B$ T - 250 k$_B$ T
B_t	MT bending stiffness	$215\,nN\,\mu m^2$	Brangwynne et al. [2006]	$0.0215-215nN\,\mu m^2$

Table 3.2: *Adopted geometrical and constitutive parameters of the cell-equivalent model and corresponding realistic ranges. Herein, MT and SF identify the microtubule and the stress fiber, respectively.*

In the present model, the mechanical force exerted by the cell on the focal adhesion plaque is obtained for the soft and hard substrate as

$$\begin{aligned} t_s &= K_s\delta_s \\ t_h &= K_h\delta_h. \end{aligned} \tag{3.62}$$

Since the force at the two edges must be equal for equilibrium, we have that

$$F_p = t_s = t_h. \tag{3.63}$$

It can be drawn from Eqs.(3.62) and (3.63) that the plaque force F_p is proportional to both the stiffness of the focal adhesions-substrate complex (3.26), which also depends on the plaque length L_p, and the values of δ_s and δ_h computed through Eqs.(3.12), the latter being influenced by the asymmetry ratio η. The specific form taken by F_p and its relevance to the plaques attitude towards assembly and disassembly has been explored in Section 3.1.6.

3.3.2 Numerical analysis of cytoskeletal stability

The results shown in the forthcoming sections have been obtained by adopting the parameters in Tab.3.2. To systematically characterize the influence of the substrate stiffness gradient, we define the stiffness ratio $\chi = k_s/k_h$ (where $k_s \leq k_h$) and the average stiffness $k_{av} = (k_s + k_h)/2$. Consequently, the specific stiffness values at the soft and hard adhesion sites are uniquely determined by fixing χ and k_{av}.

Stability thresholds and parameter selection

For the subsequent analysis, it is crucial to identify the critical pre-strain thresholds, denoted as $\lambda^*_{f,cr}$ (critical contraction) and $\lambda^*_{t,cr}$ (critical polymerization), when the two pre-strains are applied independently. These values define the bifurcation points where the fundamental equilibrium path becomes unstable, triggering a switch from a straight to a buckled configuration. Figure 3.24 illustrates the dependence of these thresholds on the normalized plaque length L_p/d_i for varying degrees of geometric asymmetry η. It is important to note that the buckling mode is activated when the actomyosin contraction

is sufficiently strong ($\lambda_f^* < \lambda_{f,cr}^*$) or, conversely, when the polymerization stretch is sufficiently large ($\lambda_t^* > \lambda_{t,cr}^*$). The results indicate that the critical stretches are nonlinear functions of the adhesion size L_p. Furthermore, Figure 3.24 reveals that structural asymmetry exerts a stabilizing effect on the cytoskeleton. Specifically, increasing the asymmetry η leads to a decrease in $\lambda_{f,cr}^*$ and an increase in $\lambda_{t,cr}^*$. This implies that an asymmetric system requires higher levels of mechanical drive, either stronger contraction (lower λ_f^*) or more extensive polymerization (higher λ_t^*), to induce buckling compared to a symmetric configuration.

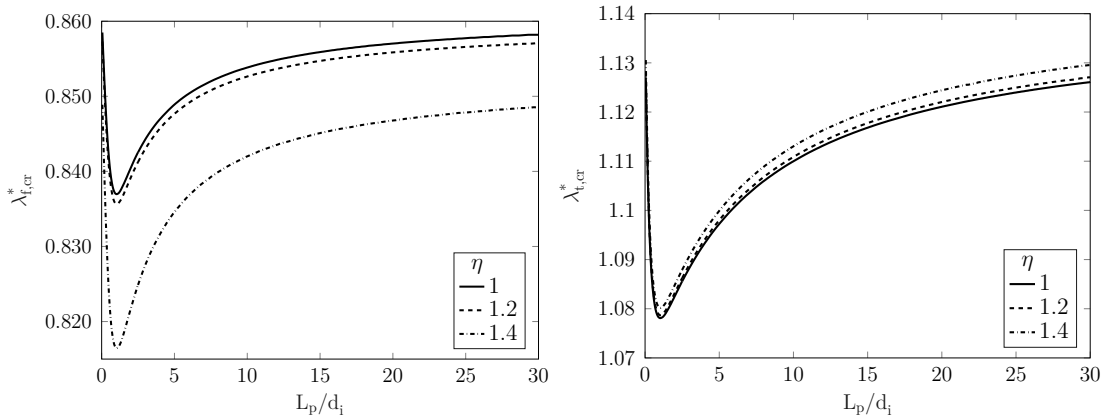

(a) **(b)**

Figure 3.24: *Profiles of the critical pre-strains $\lambda_{f,cr}^*$ (a) and $\lambda_{t,cr}^*$ (b) as a function of the normalized plaque length L_p/d_i. The curves refer to three different values of asymmetry η, with fixed stiffness parameters $\chi = 0.01$ and $k_{av} = 100$ pN/nm.*

Guided by these stability boundaries, we select the following pre-strain values for the applications presented in the forthcoming sections:

$$\lambda_f^* = 0.882 \quad \text{and} \quad \lambda_t^* = 1.1.$$

These values are chosen to be "pericritical," that is, sufficiently close to the theoretical bifurcation limits to ensure the system is capable of triggering the buckling instability.

The elastic response of the system to these imposed pre-stretches is depicted in Figure 3.25a. The incremental stretch of the actomyosin bundle, $\hat{\lambda}_f$ (Fig. 3.25aa), exhibits sensitivity to both the stiffness gradient χ and the geometric asymmetry η. In contrast, Figure 3.25b highlights a decoupling in the microtubule response: the elastic stretches of the microtubule subunits are strongly affected by the geometric asymmetry but remain virtually independent of the substrate stiffness gradient. This is evident by comparing the profiles of the soft-side subunit ($\hat{\lambda}_t^s$, black curves) and the hard-side subunit ($\hat{\lambda}_t^h$, red curves), which diverge significantly with η but show little variation with respect to χ.

3.3.3 Asymmetry-induced reversal of durotaxis

The present section assesses how the kinematics of the cell system depend on the interplay between geometrical asymmetry (η) and substrate stiffness gradients (χ), assuming a fixed adhesion plaque length L_p.

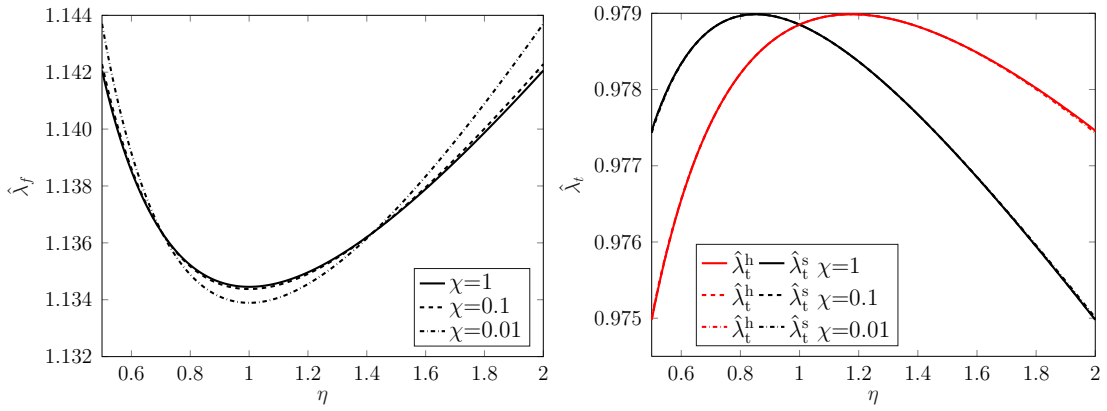

(a) **(b)**

Figure 3.25: *Elastic response of the cytoskeleton: (a) Incremental stretch of the acto-myosin bundle $\hat{\lambda}_f$; (b) Incremental stretches of the soft-side ($\hat{\lambda}_t^s$, black) and hard-side ($\hat{\lambda}_t^h$, red) microtubule subunits. All profiles are plotted as a function of the asymmetry ratio η for three different stiffness ratios χ, with $L_p = 2\,d_i$ and $k_{av} = 100$ pN/nm.*

Due to geometric compatibility and the off-centered position of the rotational hinge, the buckling angles at the cell edges (ϕ_s and ϕ_h) are generally distinct, as shown in Fig. 3.26, recovering the symmetric limit $\phi_s = \phi_h$ only when $\eta = 1$. This confirms that for the selected inelastic pre-stretches, these buckling angles remain virtually unaffected by the substrate stiffness gradient. In contrast, the translational displacements at the rear (δ_s) and front (δ_h) of the cell, and consequently the net displacement Δ_N, are strongly governed by both asymmetry and substrate stiffness. To quantify this, we computed

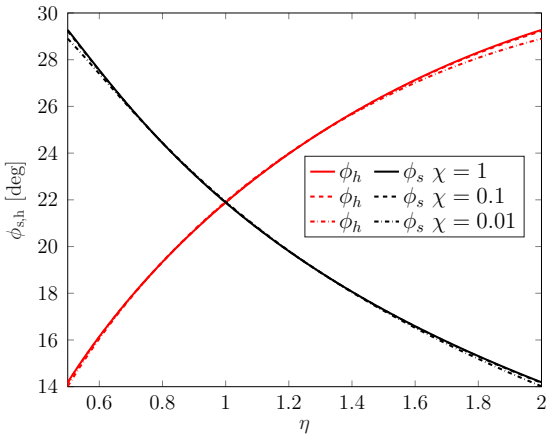

Figure 3.26: *Buckling angle of the soft-side (ϕ_s, black) and hard-side (ϕ_h, red) of the microtubule subunits. All profiles are plotted as a function of the asymmetry ratio η for three different stiffness ratios χ, with $L_p = 2\,d_i$ and $k_{av} = 100$ pN/nm.*

the displacements for a variable asymmetry ratio $\eta \in [0.5, 2]$ and varying stiffness ratios χ, while maintaining a constant average substrate stiffness $k_{av} = 100$ pN/nm. The pre-contraction and pre-polymerization levels were fixed at the operational values defined previously ($\lambda_f^* = 0.882, \lambda_t^* = 1.1$). Figure 3.27a reports the displacement profiles at

the soft side (δ_s, black) and hard side (δ_h, red). A key observation is that for a fixed average stiffness, the system achieves maximum local displacement at the symmetric configuration ($\eta = 1$). As the stiffness gradient increases (smaller χ), the magnitude of these displacements differs, but the peak remains centered at symmetry.

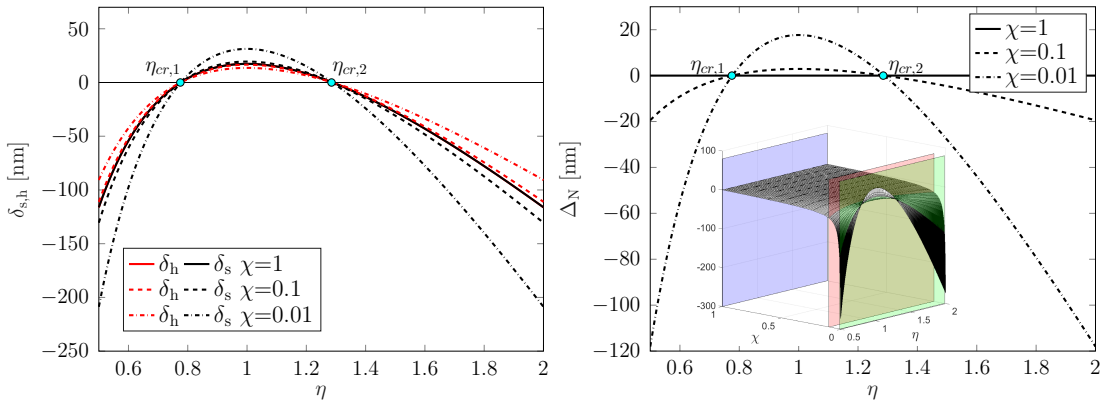

(a) **(b)**

Figure 3.27: *Kinematic response of the asymmetric unit: (a) Edge displacements at the soft (δ_s) and hard (δ_h) sides; (b) Net displacement Δ_N. Note that $\Delta_N > 0$ indicates positive durotaxis, while $\Delta_N < 0$ implies negative durotaxis. Curves correspond to three stiffness ratios χ, with $L_p = 2\,d_i$, $k_{av} = 100$ pN/nm, $\lambda_f^* = 0.882$, and $\lambda_t^* = 1.1$.*

Transition from positive to negative durotaxis

The macroscopic migratory behavior is captured by the net displacement Δ_N shown in Figure 3.27b. The profiles reveal that Δ_N vanishes not only at specific stiffness combinations but at two distinct critical asymmetry ratios, denoted as $\eta_{cr,1}$ and $\eta_{cr,2}$. These points mark the zero-crossing of the net displacement and define the stability boundaries of the durotactic process. This allows us to identify a specific domain of positive durotaxis:

- Positive durotaxis ($\Delta_N > 0$). Occurs when the asymmetry lies within the interval $\eta \in [\eta_{cr,1}, \eta_{cr,2}]$. Here, the cell migrates towards the stiffer substrate.
- Negative durotaxis ($\Delta_N < 0$). Occurs when the asymmetry falls outside this interval ($\eta < \eta_{cr,1}$ or $\eta > \eta_{cr,2}$). Here, the structural imbalance overcomes the stiffness gradient, causing the cell to migrate towards the softer side.

For the specific pre-strains adopted here ($\lambda_f^* = 0.882, \lambda_t^* = 1.1$), these critical transition points are identified as $\eta_{cr,1} = 0.775$ and $\eta_{cr,2} = 1.289$. To further highlight the dependence of migration on both asymmetry sources, namely geometry and substrate gradient, a three-dimensional surface plot of the system net displacement Δ_N in terms of the asymmetry ratios η and the substrate stiffness ratio χ can be appreciated in the inset figure of Figure 3.27b. The surface is intersected by three planes representing different gradient intensities:

- Green plane ($\chi = 0.01$): Strong stiffness gradient.

- Red plane ($\chi = 0.1$): Moderate gradient; the peak positive displacement decreases.
- Violet plane ($\chi = 1$): Homogeneous substrate (no gradient). Here, the profile becomes flat ($\Delta_N \approx 0$) as edge displacements are equal and opposite, resulting in neutral durotaxis.

Crucially, the analysis of Fig. 3.27 reveals that the critical values $\eta_{cr,1}$ and $\eta_{cr,2}$ are largely independent of the stiffness ratio χ. Indeed, the width of the positive durotaxis domain remains constant regardless of the steepness of the stiffness gradient. This invariance indicates that the boundaries of the durotactic transition are not dictated by the external gradient, but are intrinsic to the mechanical state of the cell. Consequently, the governing factors defining these critical thresholds lie in the internal cytoskeletal pre-stressspecifically the balance between actomyosin contractility and microtubule polymerizationwhich is the subject of the investigation in the following section.

3.3.4 Dependence of critical asymmetry on cytoskeletal pre-stress

To systematically study how the cytoskeletal state defines the boundaries of the durotactic regime, we investigate the dependence of the critical asymmetry ratios, $\eta_{cr,1}$ and $\eta_{cr,2}$, on the applied pre-strains. Analytically, the transition point where the system switches from positive to negative durotaxis corresponds to the condition where the total contraction of the system (defined previously in Eq. (3.11)) $\Delta = \delta_s + \delta_h = 0$. To compute these critical values, the equilibrium problem is reformulated as an inverse analysis. Instead of prescribing the geometric asymmetry η and solving for the kinematics, we impose the constraint $\Delta = 0$ and treat η as the unknown variable. Consequently, this constraint replaces the standard stationarity condition $\partial \mathcal{P}_{\text{asym}}/\partial\gamma = 0$ (from Eqs. (3.57)), allowing us to solve the system of non-linear equations for the four unknowns $(\eta, \hat{\lambda}_t^h, \hat{\lambda}_t^s, \phi_h)$ and directly determine the critical asymmetry η_{cr} as a function of the pre-strains.

The numerical solution to this inverse problem is visualized in Figure 3.28a. Here, the critical asymmetry ratio η_{cr} is plotted against the pre-contraction (λ_f^*) and pre-polymerization (λ_t^*) levels. To analyze the sensitivity of the system, we extract a 2D profile (Figure 3.28b) corresponding to the red plane in the 3D plot, where pre-polymerization is fixed to $\lambda_t^* = 1.1$. Figure 3.28b clearly delineates the domain of positive durotaxis, bounded by the two critical values. For the reference contraction $\lambda_f^* = 0.882$, we recover the previously identified limits $\eta_{cr,1} = 0.775$ and $\eta_{cr,2} = 1.289$. More importantly, the profile reveals a fundamental dependence on actomyosin activity:

- Stabilizing effect of contractility. As the pre-contraction level increases (i.e., λ_f^* decreases), the upper bound $\eta_{cr,2}$ increases while the lower bound $\eta_{cr,1}$ decreases. This widening of the interval $[\eta_{cr,1}, \eta_{cr,2}]$ implies that higher contractility makes the positive durotaxis mechanism more robust against geometric imperfections.
- Emergence of negative durotaxis. Conversely, as contractility weakens (approaching $\lambda_f^* \approx 0.89$), the interval narrows significantly, thus allowing negative durotaxis for asymmetry ratios higher than $\eta_{cr,2}$ or lower than $\eta_{cr,1}$.

If the pre-contraction is too low, the buckling instability does not occur, and durotaxis is not triggered.

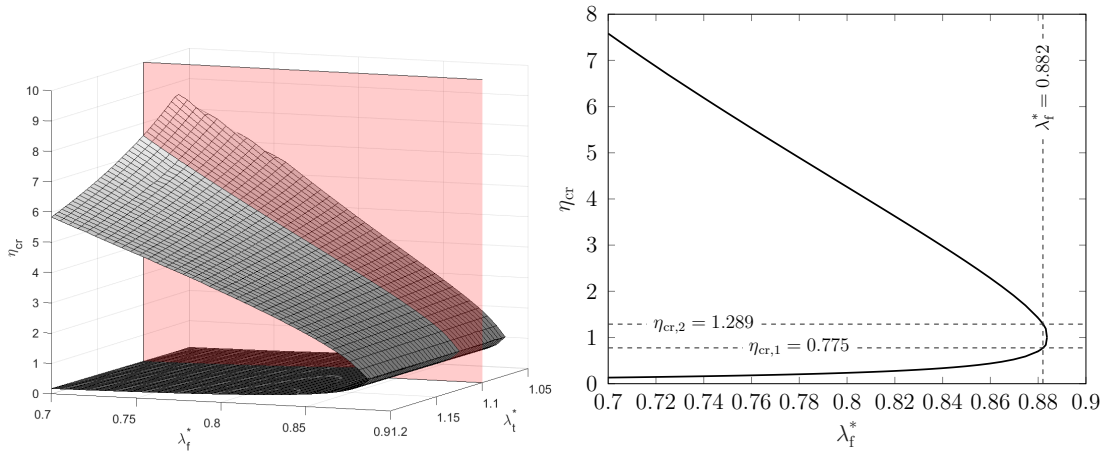

(a) **(b)**

Figure 3.28: *Critical values of η: (a) 3D surface map showing the critical asymmetry η_{cr} as a function of pre-strains λ_t^* and λ_f^*. (b) 2D cross-section at fixed $\lambda_t^* = 1.1$. The area between the curves represents the domain of positive durotaxis. Parameters: $L_p = 2d_i$, $k_{av} = 100$ pN/nm.*

This behavior highlights the competition between the internal forces. The system is subject to crosscurrent tendencies: actomyosin contraction generates a pulling force, while microtubule polymerization generates a pushing force. When the contractility is low, the pushing force becomes relatively dominant. In this regime, the system is on the verge of instability; even small perturbations in the system geometrical symmetry can tip the balance, causing the cell to move away from the stiff substrate (negative durotaxis). Thus, robust positive durotaxis is an emergent property of high actomyosin contractility counterbalancing the microtubule expansion.

3.3.5 Force transmission and plaque growth dynamics

We now investigate the response of the focal adhesion plaque to the simultaneous presence of geometric asymmetry and substrate stiffness gradients, specifically in terms of the transmitted forces and the resulting plaque growth flux.

Figures 3.29a and 3.29b display the force exerted on the plaque, F_p, and the corresponding net growth flux, J (as defined in Eq. (3.35)), as functions of the asymmetry ratio η. The results are computed for the established pre-strains ($\lambda_f^* = 0.882$, $\lambda_t^* = 1.1$) and varying stiffness ratios χ. Additionally, the inset in Figure 3.29b provides a three-dimensional visualization of the flux J/D as a function of both η and χ. The intersections of this surface with the planes $\chi = \{1, 0.1, 0.01\}$ correspond precisely to the 2D profiles plotted in the main figure.

A remarkable observation is that the symmetric configuration ($\eta = 1$) is consistently associated with positive fluxes ($J > 0$). This implies that a perfectly symmetric system is inherently in a non-equilibrium state characterized by continuous plaque assembly. Consequently, to achieve thermodynamic stability ($J = 0$), the system must depart from symmetry. This suggests that asymmetric buckling is not merely a mode of instability but a potential mechanism the cell can leverage to regulate focal adhesion stability. It

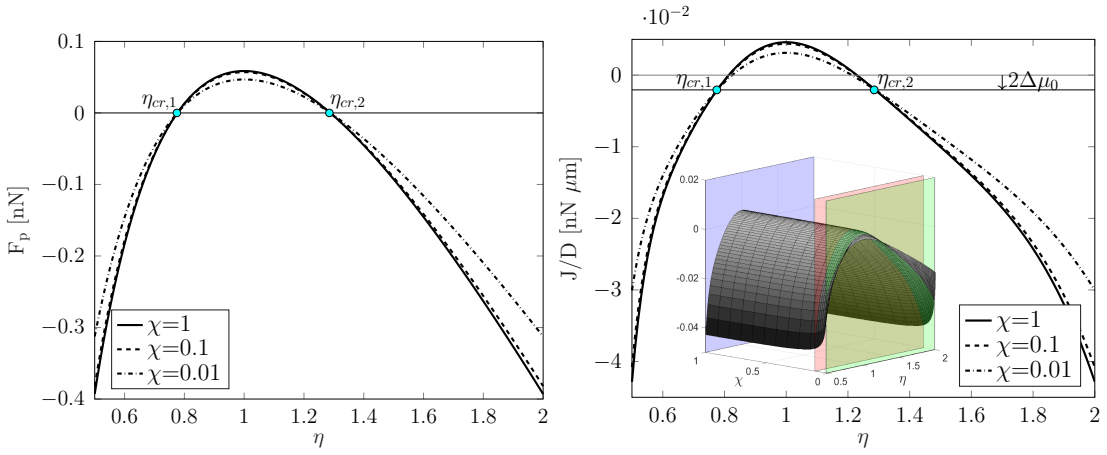

(a) **(b)**

Figure 3.29: *Force F_p (a) and net growth law $\bar{J}$ of the adhesion plaque (b) plotted as a function of the asymmetry ratio η. The curves refer to three different values of ratio χ and $k_{av} = 100$ pN/nm, setting $L_p = 2\,d_i$, with underlying pre-contraction $\lambda_f^* = 0.882$ and pre-polymerization $\lambda_t^* = 1.1$.*

is important to note that the conditions for mechanical neutrality (which correspond to $\Delta = 0$ and consequently $F_p = 0$) and chemical equilibrium ($J = 0$) do not coincide. Due to the chemical potential term $2\Delta\mu_0$ in the flux equation (Eq. (3.35)), the flux J is effectively shifted relative to the mechanical variables. Therefore, positive durotaxis, which implies a pulling force on the plaque, does not strictly imply plaque assembly in the case of an asymmetric configuration. As a result, the critical η-values where the net displacement vanishes ($\Delta_N = 0$) are distinct from the values where the net flux vanishes ($J = 0$). However, a consistent feature across all stiffness ratios χ is that the profiles of J intersect the theoretical baseline (shifted by $2\Delta\mu_0$) at the previously defined mechanical thresholds $\eta_{cr,1}$ and $\eta_{cr,2}$.

Regimes of stability and remodeling

The analysis of Figures 3.27b and 3.29b allows us to categorize the cell's behavior into three distinct regimes based on the asymmetry ratio. While the mechanical transition points $(\eta_{cr,1}, \eta_{cr,2})$ are independent of the stiffness gradient, the chemical equilibrium ($J = 0$) occurs at slightly different values. Nevertheless, these mechanical thresholds provide a useful framework for understanding the system's remodeling tendencies. Assuming the cell can adjust both its adhesion length L_p and its internal geometry η to seek equilibrium, we observe the following behavior:

$\eta < \eta_{cr,1}$ **(Negative flux regime).** The net flux J is negative. The plaque is thermodynamically unstable and is expected to disassemble. This disassembly will continue until the plaque either disappears entirely or reaches a new stable length where the flux vanishes. Alternatively, the cytoskeletal structure may undergo reconfiguration leveraging asymmetric buckling to increase the asymmetry ratio η, thereby moving the system closer to the equilibrium domain.

$\eta_{cr,1} \leq \eta \leq \eta_{cr,2}$ **(Mixed regime).** In this intermediate interval, the flux J transitions

from negative to positive and back. Consequently, the plaque will tend to remodel toward a specific length where assembly and disassembly are balanced. In this regime, the system may also stabilize by shifting the position of the rotational hinge (altering η) to find a zero-flux configuration.

$\eta > \eta_{cr,2}$ **(Negative flux regime).** Similar to the first regime, the flux J is negative, indicating a state of disassembly. The system will drive toward equilibrium either through depolymerization (reducing L_p) or by structurally adapting to decrease the asymmetry ratio η towards the stable central region.

3.3.6 Sensitivity to adhesion geometry and average stiffness

Current experimental protocols for addressing durotaxis typically characterize the mechanical behavior of adherent cells across substrates of variable average stiffness [Isomursu et al., 2022]. To provide results comparable with these state-of-the-art studies, we investigate the sensitivity of the model's mechanical response to the plaque length L_p and the average stiffness k_{av}.

As shown in Sec. 3.2.3, symmetric buckling over stiff substrates requires larger adhesion lengths to achieve stability compared to soft substrates [Benvenuti et al., 2022]. We extend this analysis below to consider the concurrent effects of asymmetrical buckling and stiffness gradients by varying L_p at a constant k_{av}. Subsequently, we examine the influence of k_{av} itself. Since the average stiffness alone is insufficient to describe a heterogeneous environment, this analysis is performed for varying stiffness ratios χ and asymmetry parameters η, thereby fully characterizing the substrate's mechanical landscape.

The influence of the plaque length on stability

We analyze the system behavior for three distinct geometric configurations: the symmetric reference case ($\eta = 1$) and two asymmetric configurations ($\eta = 1.2$ and $\eta = 1.4$), representing pre-critical and post-critical states based on our previous evaluations. Figures 3.30a and 3.30b illustrate the force exerted on the plaque (F_p) and the net growth flux (J/D) as functions of the normalized plaque length L_p/d_i. The plots assume a fixed average stiffness $k_{av} = 100$ pN/nm and compare three substrate conditions: uniform ($\chi = 1$) and graded ($\chi = 0.1, 0.01$), where lower χ values indicate sharper stiffness gradients.

The results demonstrate that both asymmetry and substrate gradients significantly alter the equilibrium conditions:

- **Effect of asymmetry.** On a uniform substrate ($\chi = 1$), the stable plaque length (where $J = 0$) decreases as the system becomes more asymmetric.
- **Effect of gradient.** For symmetric ($\eta = 1$) or slightly asymmetric ($\eta = 1.2$) systems, the presence of a stiffness gradient reduces the stable equilibrium length. Specifically, as the gradient intensifies (decreasing χ), the stable length shortens.

A different behavior emerges in the case of marked asymmetry ($\eta = 1.4$). In this regime, the growth flux remains consistently negative regardless of the stiffness ratio χ. This implies that highly asymmetric configurations prevent the plaque from ever reaching a stable equilibrium, inevitably leading to continuous disassembly or disappearance.

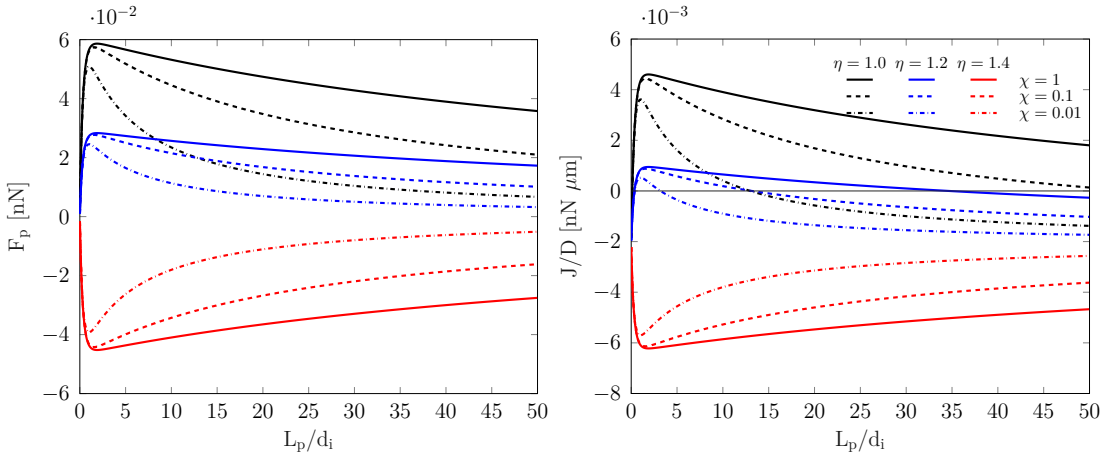

(a) (b)

Figure 3.30: *(a) Force exerted on the plaque F_p and (b) net growth flux J plotted as a function of the normalized plaque length L_p/d_i. Parameters: $k_{av} = 100$ pN/nm, $\lambda_f^* = 0.882$, $\lambda_t^* = 1.1$.*

Plaque force and growth depend on the average stiffness

To assess the interplay between the average substrate stiffness and the stiffness gradient, the plaque force and growth laws are plotted on a semi-logarithmic scale in Figures 3.31a and 3.31b, respectively. These profiles adopt the same χ and η values as the previous section while varying k_{av}.

The magnitude of the force F_p is an increasing function of the average stiffness k_{av}, eventually plateauing beyond a critical stiffness threshold. The growth flux J exhibits an analogous trend, with the primary difference being the shift in the zero-crossing point caused by the chemical potential barrier $2\Delta\mu_0$. This monotonic force-stiffness relationship aligns with experimental and analytical findings in the literature [He et al., 2014]. However, it stands in contrast to the biphasic behavior often observed in neurons, where force generation peaks at an optimal stiffness before declining [Elosegui-Artola et al., 2018, Isomursu et al., 2022]. Interestingly, glioma cells have been shown to exhibit a biphasic response that switches to a monotonic one when cytoskeletal reinforcement is engaged (or conversely, become biphasic upon talin depletion) [Isomursu et al., 2022], suggesting our model captures a regime of robust cytoskeletal reinforcement.

The dependency of F_p on k_{av} is strongly modulated by the geometric and gradient parameters. Specifically, the symmetric system on a homogeneous substrate ($\eta = 1, \chi = 1$) exerts the maximum absolute force on the plaque. Regarding the nature of the mechanical load, the analysis reveals that compressive forces decrease in magnitude as the stiffness gradient increases (lower χ). This indicates that plaques subjected to steep soft-to-hard gradients experience reduced compressive loading compared to those in homogeneous environments. Conversely, the tensile (pulling) forces generated during positive durotaxis are found to be attenuated in asymmetric systems ($\eta > 1$) relative to the symmetric configuration.

Regarding the protein flux, although the constant term $-2\Delta\mu_0$ decouples the mechanical force from the exact assembly rate, clear trends emerge. Pushing forces are invariably associated with plaque disassembly. Consistent with the force profiles, the

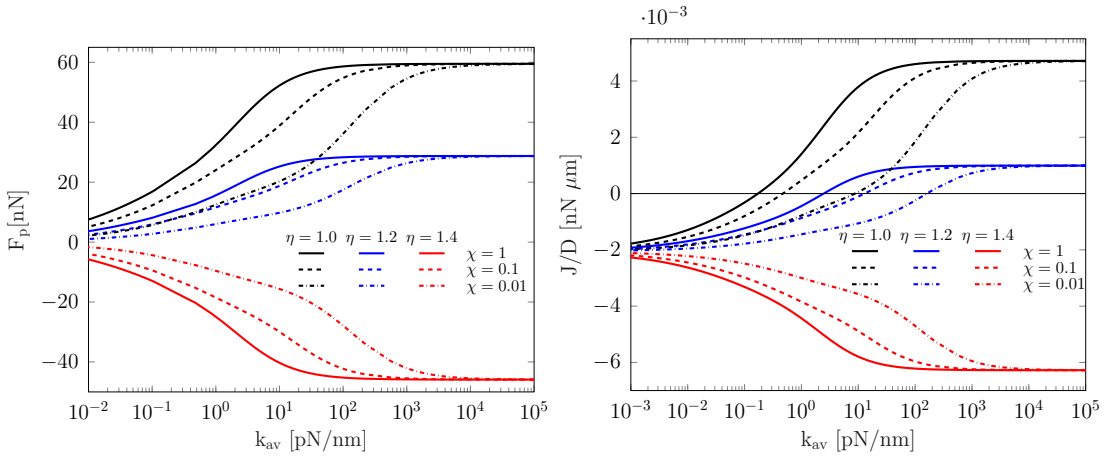

(a) **(b)**

Figure 3.31: *(a) Force of the adhesion plaque and (b) growth law of the adhesion plaque plotted as a function of the substrate average stiffness k_{av} in a semi-logarithmic plot. The curves have been obtained setting $L_p = 2\,d_i$, with underlying pre-contraction $\lambda_f^* = 0.882$, and pre-polymerization $\lambda_t^* = 1.1$.*

disassembly flux is weaker on high stiffness gradients than on homogeneous substrates. Conversely, for the assembly process (associated with positive fluxes), the rate intensifies on homogeneous substrates up to a saturation level of k_{av}. However, this assembly is attenuated in the presence of structural asymmetry.

In conclusion, this comparative analysis suggests that asymmetric buckling generally dampens plaque assembly, while high stiffness gradients and soft average substrates tend to mitigate plaque disassembly. Thus, the symmetric, homogeneous configuration represents the state of maximal mechanical activity, exhibiting the highest forces for both assembly and disassembly.

3.3.7 Implications for cell motility and mechanosensitivity

In the preceding analysis of symmetric configurations (Section 3.2), we established that the model predicts longer focal adhesion plaques on stiffer substrates compared to soft ones [Benvenuti et al., 2022]. That study further indicated that comparatively soft substrates allow for larger macroscopic cell displacements, thereby potentially favoring cell mobility.

The present Section extended these findings to asymmetric systems, revealing that in the positive durotaxis regime, asymmetric configurations stabilize at shorter plaque lengths than their symmetric counterparts. The relationship between focal adhesion size and cell speed is non-monotonic and cell-type dependent [Kim and Wirtz, 2013]; however, there is a consensus that focal adhesion size is a significant predictor of migration dynamics [Kim and Wirtz, 2013, Oakes et al., 2014]. Since smaller adhesions are typically associated with faster turnover rates and dynamic remodeling, our results suggest that structural asymmetry actively promotes locomotion. This effect is particularly pronounced on stiff substrates, where asymmetry significantly reduces the stable plaque length. Additionally, the finding that higher stiffness gradients correlate with shorter

focal adhesion complexes suggests that steep gradients may further enhance motility.

From a mechanical standpoint, structural asymmetry increases the threshold required for the onset of instability. Consequently, asymmetric systems require higher levels of pre-contraction or pre-polymerization to activate buckling compared to symmetric systems. Regarding force transmission, the symmetric system is associated with the highest anchorage forces. The observation that asymmetric systems exert lower peak forces on the plaque aligns with the hypothesis that symmetry breaking facilitates mobility, whereas perfect symmetry favors static, high-force adhesion.

Finally, the model highlights that both substrate stiffness and its gradient are governing determinants of focal adhesion stability. Crucially, the finding that plaques on soft substrates exhibit smaller growth fluxes compared to those on hard substrates aligns with the well-established experimental phenomenon of stiffness-dependent adhesion maturation [Prager-Khoutorsky et al., 2011, Balaban et al., 2001], and also with the molecular clutch hypothesis, which predicts that cytoskeleton-substrate links on compliant surfaces undergo rapid frictional slippage and fail to reinforce [Chan and Odde, 2008, Elosegui-Artola et al., 2016]. This agreement between our macroscopic tensegrity approach and molecular-level models suggests that the presented framework correctly captures the mechanics underlying stiffness sensing

The following section extends this framework by incorporating the elastic-damaging behavior of the focal adhesion-ECM link. This addition allows for the simulation of anchorage release once a critical displacement is reached, bridging the gap between the current static equilibrium analysis and the simulation of dynamic migration cycles.

3.4 Mechanics of the symmetric cytoskeletal unit: influence of elasto-damaging cell-substrate adhesion

In the previous chapter, we explored how structural asymmetry ($\eta \neq 1$) dictates cell migration when anchored to linear elastic substrates. In this final analysis, we invert the problem to isolate the role of the adhesive interface. We consider a geometrically symmetric cytoskeletal unit ($\eta = 1$) interacting with a mechanically evolving environment. Specifically, we revisit the general tensegrity framework and activate the elasto-damaging constitutive laws for the focal adhesions. This allows us to study the phenomenon of adhesion failure and detachment as a driver for motility. By maintaining structural symmetry, we aim to demonstrate that the cohesive failure of the focal adhesion, rather than intracellular polarity, is the fundamental mechanical mechanism driving positive and negative durotaxis. Furthermore, the discrete mechanistic insights derived from this lumped-parameter tensegrity model regarding the competition between contractility and adhesion failure serve as a foundational proof-of-concept. These results motivate the subsequent application of the elasto-damaging framework to a continuum model, allowing us to generalize these findings to a spatially distributed domain.

3.4.1 Mechanical model formulation

To analyze the interplay between cell symmetry and adhesive failure, we specialize the general tensegrity unit devised in Chapter 3 via the following specialization hypotheses:

1. **Geometric symmetry:** we assume the cell possesses no intrinsic structural

asymmetry, therefore we set the parameter $\eta = 1$. Consequently, the reference lengths of the microtubule subunits are identical ($L_t^s = L_t^h \equiv L_t$), as are the reference angles.

2. **Asymmetric elasto-damaging adhesions:** unlike the linear springs assumed in the previous chapter, here the focal adhesions are governed by the coupled damage-elasticity evolution laws defined in Sec. 3.1.4. The cell spans a stiffness gradient characterized by a soft substrate (K_s) and a hard substrate (K_h). Crucially, the integrity of these connections is not constant; the damage parameters ζ_s and ζ_h evolve independently based on the local displacement history.

Under these assumptions, the system is reduced to the configuration illustrated in Fig. 3.32.

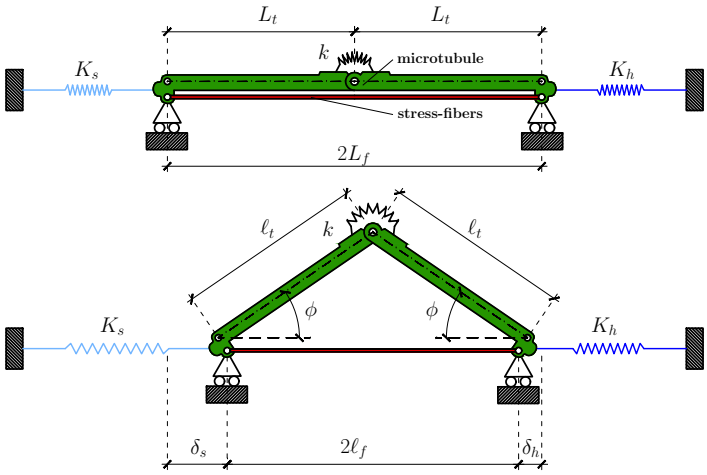

Figure 3.32: *Structural scheme adopted for the one-dimensional tensegrity model. Here the cell-focal adhesions-substrate connections are embedded within the equivalent springs of stiffness K_s, in light blue, and K_h, in dark blue, at the soft and hard parts of the substrate, respectively.*

Reduced kinematics

The assumption of geometric symmetry ($\eta = 1$) allows for the same kinematic reductions derived in Chapter 3.2 regarding the internal cytoskeletal components. We unify the reference lengths such that $L_t^s = L_t^h \equiv L_t$, implying $L_f = L_t \equiv L$. The internal symmetry ensures that the microtubule semi-lengths remain equal, $\ell_t = L\lambda_t^* \hat{\lambda}_t$, and the buckling angles satisfy $\phi_s = \phi_h \equiv \phi$. Consequently, the total contraction Δ is defined as:

$$\Delta = 2L(1 - \lambda_t^* \hat{\lambda}_t \cos\phi). \tag{3.64}$$

This global displacement Δ is partitioned into the displacements at the soft (δ_s) and hard (δ_h) interfaces via the parameter γ:

$$\delta_s = \gamma\Delta, \qquad \delta_h = (1-\gamma)\Delta. \tag{3.65}$$

However, unlike the previous chapters, the potential energies at the boundaries are not purely quadratic. They now depend on the damage state ζ. Using the definitions from the general model, the boundary potentials follow the pseudo-elastic potential of Eq. (3.18), which, after dropping the fictitious time parameter, is particularized for the soft and hard parts of the substrate:

$$\begin{aligned}\Phi_s(\delta_s,\zeta_s) &= \frac{1}{2}\zeta_s K_s\,\delta_s^2 - \int_0^{\delta_s} \left.\frac{\partial\zeta_s}{\partial\tilde{\delta}}\right|_{\tilde{\delta}} \frac{1}{2}K_s\,\tilde{\delta}^2 d\tilde{\delta}.\\ \Phi_h(\delta_h,\zeta_h) &= \frac{1}{2}\zeta_h K_h\,\delta_h^2 - \int_0^{\delta_h} \left.\frac{\partial\zeta_h}{\partial\tilde{\delta}}\right|_{\tilde{\delta}} \frac{1}{2}K_h\,\tilde{\delta}^2 d\tilde{\delta}.\end{aligned} \tag{3.66}$$

In these expressions, $\zeta_{s,h} \in [0,1]$ represents the integrity of the adhesion as defined in Eq. (3.22). This parameter evolves from 1 (intact) to 0 (fully detached) as the displacement exceeds the damage initiation threshold Δ_i^0 and approaches the ultimate failure threshold Δ_i^u. Furthermore, we recall that the integral term representing the dissipated energy can be expressed in a closed form involving the hypergeometric function, as specified in Eq. (3.24). The effective stiffnesses of the adhesion complexes, K_s and K_h, are given by Eq. (3.26) proposed by Cao et al. [2015].

Governing equations

The total potential energy of the system, $\mathcal{P}_{\text{dam}}$ is formulated as the sum of the symmetric cytoskeletal energy and the asymmetric, damage-dependent boundary energies. It is expressed as a function of the Lagrangian parameters and the damage state variables:

$$\mathcal{P}_{\text{dam}}(\gamma,\hat{\lambda}_t,\phi) = \Psi_{\text{cyto}}(\hat{\lambda}_t,\phi) + \Phi_s(\gamma,\hat{\lambda}_t,\phi) + \Phi_h(\gamma,\hat{\lambda}_t,\phi). \tag{3.67}$$

In this formulation, the interfacial displacements δ_s and δ_h are not independent coordinates but are kinematically determined by the generalized variables. Specifically, they act as a partition of the total cell contraction Δ governed by the parameter γ (Eq. (3.12)), while Δ itself is strictly a function of the geometrical configuration $(\hat{\lambda}_t,\phi)$. Crucially, the integrity parameters ζ_s and ζ_h are treated as irreversible state variables. They are defined by the maximum displacement encountered in the loading history, according to the evolution law derived in the general framework (Chapter 3). Consequently, the equilibrium configurations are identified by the stationarity of $\mathcal{P}_{\text{dam}}$ with respect to the kinematic parameters only:

$$\frac{\partial\mathcal{P}_{\text{dam}}}{\partial\gamma} = \frac{\partial\mathcal{P}_{\text{dam}}}{\partial\hat{\lambda}_t} = \frac{\partial\mathcal{P}_{\text{dam}}}{\partial\phi} = 0. \tag{3.68}$$

These stationarity conditions define the mechanical equilibrium for a fixed damage state. The system of three nonlinear equations in the three unknowns $\gamma,\phi,\hat{\lambda}_t$ was numerically solved using the nonlinear systems solver *fsolve* available in Matlab©.

Force on the focal adhesion plaque

In the context of elasto-damaging adhesions, the magnitude of the tensile force exerted by the cell on the focal adhesion plaques is modulated by the integrity of the adhesive bond. Accordingly, the tension at the soft (s) and hard (h) ends is given, through Eq. (3.19), by:

$$\begin{aligned} t_s &= \zeta_s(\delta_s) K_s \delta_s, \\ t_h &= \zeta_h(\delta_h) K_h \delta_h, \end{aligned} \tag{3.69}$$

where $\zeta_i \in [0, 1]$ is the integrity parameter defined in Eq. (3.22). Consistent with the path-independent nature of the adopted damage model, ζ_i is a state function determined solely by the current displacement relative to the damage initiation threshold Δ_i^0.

As in the linear case, the cytoskeletal unit must satisfy static equilibrium; therefore, the tensile forces at the opposing ends must balance:

$$F_p = t_s = t_h. \tag{3.70}$$

It is important to note that unlike the linear elastic scenario, the force F_p is now a nonlinear function of the displacement. The effective stiffness of the bond decreases as damage accumulates (decreasing ζ). Consequently, while the forces t_s and t_h must remain equal in magnitude, the resulting displacements δ_s and δ_h will differ significantly, driven not only by the substrate stiffness gradient but also by the differential damage evolution at the two ends. The specific functional form of F_p and its role in driving the plaques assembly or disassembly are analyzed in Section 3.1.6.

3.4.2 Numerical analysis of cytoskeletal stability

The results shown in the forthcoming sections have been obtained by adopting the parameters in Tab. 3.3. To systematically characterize the influence of the substrate stiffness gradient, we recall the definitions of stiffness ratio $\chi = k_s/k_h$ (where a lower χ indicates a steeper gradient) and average stiffness $k_{av} = (k_s + k_h)/2$. The specific substrate stiffnesses k_s and k_h are derived from these two invariants. Unless otherwise specified, the simulations assume a stiffness gradient of $\chi = 0.01$, an average stiffness of $k_{av} = 100$ pN/nm, and an adhesion plaque rest length of $L_p = 2d_i$.

Sensitivity of kinematics to elasto-damaging parameters

We first examine the kinematic response of the systemspecifically the net cellular displacement $\Delta_N = \delta_s - \delta_h$ and the individual nodal displacements as a function of increasing intracellular contractility (modeled via the inelastic pre-contraction λ_f^*). In this analysis, the microtubule pre-polymerization is fixed at $\lambda_t^* = 1$. For these simulations, the ultimate failure threshold is set to $\Delta_s^u = \Delta_h^u = 5$ μm for both substrates.

The results reveal that the direction of migration (positive vs. negative durotaxis) is governed by the sequence in which the adhesions sustain damage. We identify two distinct regimes:

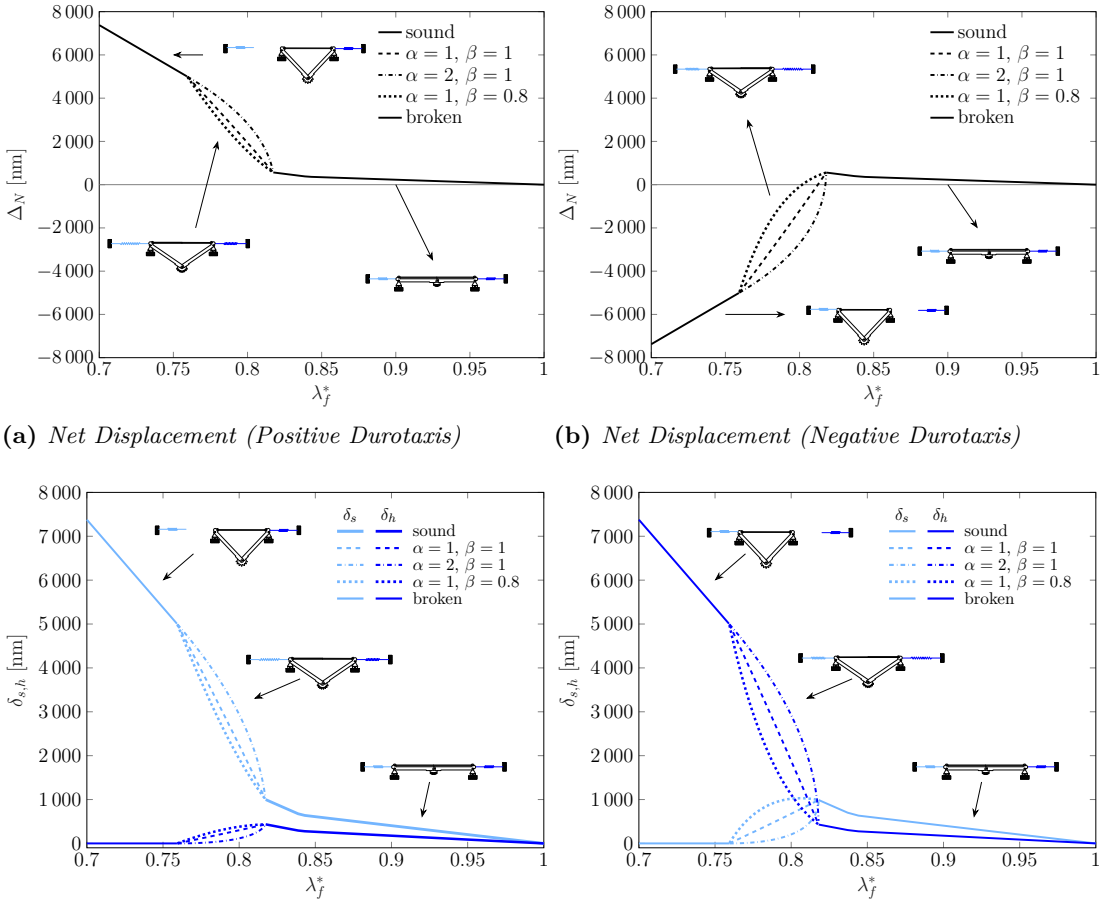

(a) *Net Displacement (Positive Durotaxis)*

(b) *Net Displacement (Negative Durotaxis)*

(c) *Nodal Displacements (Positive Durotaxis)*

(d) *Nodal Displacements (Negative Durotaxis)*

Figure 3.33: *Evolution of cellular kinematics as a function of the inelastic pre-contraction λ_f^* for three distinct damage evolution profiles defined by $(\alpha, \beta) \in \{(1,1),(2,1),(1,0.8)\}$. (a, c)* ***Positive durotaxis:*** *with symmetric thresholds ($\Delta_{s,h}^0 = 1\mu m$), the soft spring (light blue) reaches the damage threshold first, driving the net displacement Δ_N (a) toward the stiff side. (b, d)* ***Negative durotaxis:*** *with a reduced threshold on the hard side ($\Delta_h^0 = 430$ nm), damage initiates at the hard spring (dark blue) first, reversing the net displacement Δ_N (b) toward the soft side. Parameters: $L_p = 2d_i$, $k_{av} = 100$ pN/nm, $\chi = 0.01$, $\Delta^u = 5$ μm.*

Parameter	Description	Value	Source	Typical Range
L_f	SF rest length	$20\,\mu m$	Deguchi et al. [2006], Fraldi et al. [2019]	10–50 μm
L_p	adhesion plaque rest length	$200\,nm$	Caille et al. [2002], Franz and Müller [2005]	up to few μm
h_p	plaque height	$100\,nm$	Franz and Müller [2005]	50–100 nm
w_p	plaque width	$1\,\mu m$	Caille et al. [2002], Franz and Müller [2005]	$1000\,nm$
d_i	integrin spacing	$100\,nm$	Fisher et al. [1999], Cavalcanti-Adam et al. [2006]	$100\,nm$
A_t	MT rest cross-sectional area	$190\,nm^2$	Deguchi et al. [2006]	$190\,nm^2$
A_f	SF rest cross-sectional area	$10^4\pi\,nm^2$	Deguchi et al. [2006], Fraldi et al. [2019]	$10^4\pi\,nm^2$
E_t	MT Young modulus	$1.2\,GPa$	Kurachi et al. [1995], Deguchi et al. [2006]	$1.2\,GPa$
E_f	SF Young modulus	$1.45\,MPa$	Deguchi et al. [2006], Fraldi et al. [2019]	$1.45\,MPa$
k_i	integrin stiffness	$5\,pN/nm$	Fisher et al. [1999], Cavalcanti-Adam et al. [2006]	$5\,pN/nm$
k_p	plaque stiffness	$2.5\,pN/nm$	Caille et al. [2002], Banerjee and Marchetti [2012]	$2.5\,pN/nm$
$\Delta\mu_0$	energy barrier for protein recruitment without mechanical load	$250\,k_BT$	Nicolas et al. [2004]	10–250 k_BT
B_t	MT bending stiffness	$215\,nN\,\mu m^2$	Brangwynne et al. [2006]	0.0215–215 $nN\,\mu m^2$

Table 3.3: *Geometrical, mechanical, and energetic parameters adopted in the model, and corresponding typical ranges.*

Regime I: positive durotaxis (soft-side damage) This regime corresponds to the standard physiological case where the adhesion thresholds are symmetric ($\Delta_s^0 = \Delta_h^0 = 1$ μm). As the cell contracts, the soft substrate undergoes larger deformation than the hard substrate ($\delta_s > \delta_h$) to maintain force equilibrium. Consequently, the displacement δ_s reaches the damage initiation threshold Δ_s^0 first. This behavior is illustrated in Figures 3.33a and 3.33c. As damage accumulates on the soft side (light blue curve), the effective stiffness drops, causing the cell to lose its grip on the soft substrate while maintaining a stable anchor on the hard substrate. The resulting net displacement Δ_N is positive, indicating migration toward the stiff environment (positive durotaxis).

Regime II: negative durotaxis (hard-side damage) In this regime, we investigate the conditions required to reverse the migration direction. This is achieved by assuming the adhesion to the hard substrate is significantly more fragile than that to the soft substrate ($\Delta_h^0 = 430$ nm vs. $\Delta_s^0 = 1.5$ μm). As shown in Figures 3.33b and 3.33d, the hard-side displacement δ_h (dark blue) reaches its lower threshold Δ_h^0 before the soft side reaches Δ_s^0. Consequently, the hard adhesion degrades first. Once the hard anchor is compromised, the intact adhesion on the soft side pulls the cell back, resulting in a negative net displacement ($\Delta_N < 0$). This demonstrates that negative durotaxis (or mollitaxis) can emerge if the adhesion strength on the stiff substrate is pathologically low or chemically inhibited.

Evolutionary stages Analyzing Figures 3.33a and 3.33b in detail, we can identify three distinct stages in the system's response as the pre-contraction increases (i.e., as λ_f^* decreases from 1 to 0.7).

Stage 1: elastic response. Indicated by the continuous black line (approximately $\lambda_f^* \in]0.82, 1]$), this stage precedes the onset of damage ($\zeta_s = \zeta_h = 1$). Here, the system behaves as a linear elastic tensegrity structure. Due to the stiffness gradient, $\delta_s > \delta_h$, resulting in a naturally positive net displacement $\Delta_N > 0$. The system exhibits purely durotactic behavior driven by elastic equilibrium.

Stage 2: differential damage. In this interval ($\lambda_f^* \in]0.76, 0.82[$), damage initiates at one of the adhesions. In the positive durotaxis case (Fig. 3.33a), the soft spring damages first ($\zeta_s < 1, \zeta_h = 1$). As the soft adhesion weakens, the net displacement Δ_N increases sharply. This is confirmed by Figure 3.33c, where δ_s grows significantly

while δ_h relaxes toward zero. Conversely, in the negative durotaxis case (Fig. 3.33b), the hard spring damages first ($\zeta_s = 1, \zeta_h < 1$). The net displacement Δ_N decreases and eventually becomes negative. Figure 3.33d shows δ_h increasing while δ_s vanishes, indicating the cell is losing its grip on the hard substrate and being pulled toward the soft side. The branching lines in these plots correspond to the specific damage evolution parameters α and β which influence the damage law of Eq. (3.22).

Stage 3: adhesion failure. The final stage occurs when the displacement at the damaged end reaches the ultimate failure threshold Δ^u. As will be discussed in the following section, once an adhesion fully detaches ($\zeta \to 0$), the cytoskeletal unit loses its ability to sustain tension. Consequently, the elastic recoil causes traction forces to vanish at both ends.

In conclusion, the tensegrity model equipped with elasto-damaging springs demonstrates that both positive and negative durotaxis are consistent equilibrium solutions. The specific migratory direction is determined by the interplay between the substrate stiffness gradient and the damage thresholds Δ^0 and Δ^u of the adhesive complex.

Tractions and growth fluxes

The mechanical and biochemical consequences of the damage process are analyzed in Figure 3.34, which plots the traction forces $t_{s,h}$ and the growth fluxes $J_{s,h}/D$ as functions of the nodal displacements δ_s (light blue) and δ_h (dark blue).

Traction behavior The traction profiles (Figs. 3.34a and 3.34b) reveal the interplay between damage and equilibrium. In the case of positive durotaxis (Fig. 3.34a), the response is characterized by two distinct phases:

- Elastic phase ($\delta_s < \Delta_s^0$). Both springs behave elastically, with traction increasing linearly with displacement.
- Damage phase ($\delta_s \geq \Delta_s^0$). Once the threshold is exceeded, the soft adhesion enters the damage regime. Its traction capacity decreases along a softening branch, the steepness of which is governed by the evolution parameters α and β. Crucially, to satisfy static equilibrium ($t_h = t_s$), the hard spring, which remains undamaged, is forced to reduce its force. Consequently, the hard spring unloads, retracing its linear elastic path downwards (dark blue line).

In the case of negative durotaxis (Fig. 3.34b), the behavior is inverted: the hard spring reaches its threshold Δ_h^0 first and undergoes softening, forcing the intact soft spring to unload elastically.

Growth flux and disassembly The evolution of the focal adhesion size is governed by the growth fluxes $J_{s,h}$, displayed in Figures 3.34c and 3.34d. As defined in Eq. (3.35), the growth rate is driven by the competition between the chemical potential barrier $2\Delta\mu_0$ (which opposes growth) and the mechanical work performed by the traction forces (which promotes growth). Consequently, the flux profiles strictly mirror the traction behavior. Initially, as tension t increases, the mechanical work term in Eq. (3.35) grows, driving the flux to positive values ($J > 0$) and causing adhesion assembly. However, as damage initiates and the traction force drops along the softening branch, the mechanical driving force diminishes. When the tension falls below a critical level, the chemical

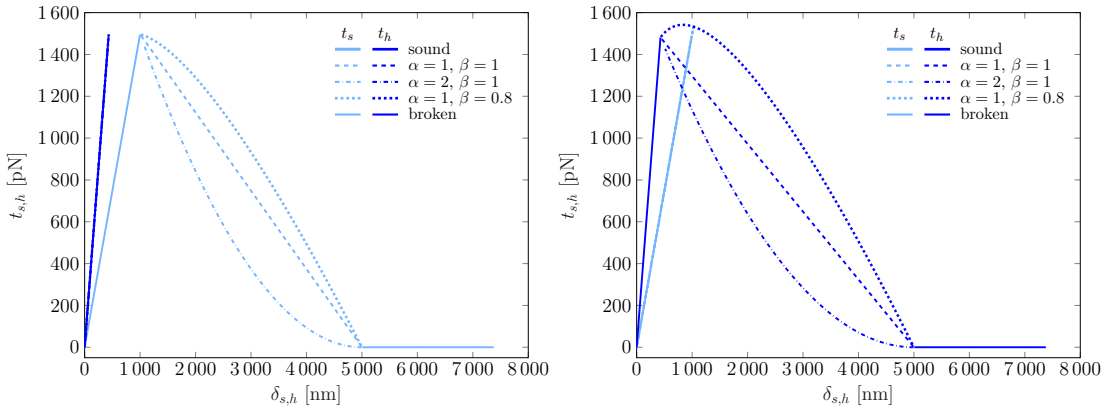

(a) *Traction Force (Positive Durotaxis)*

(b) *Traction Force (Negative Durotaxis)*

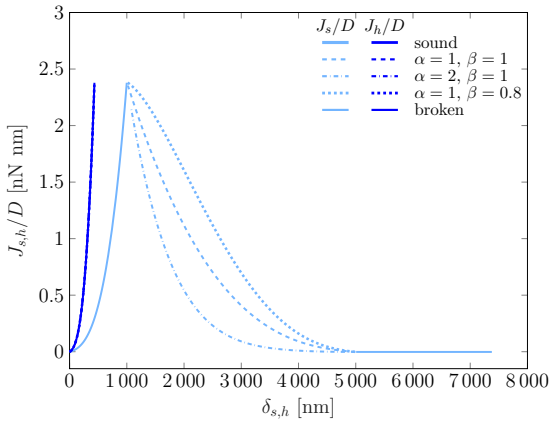

(c) *Growth Flux (Positive Durotaxis)*

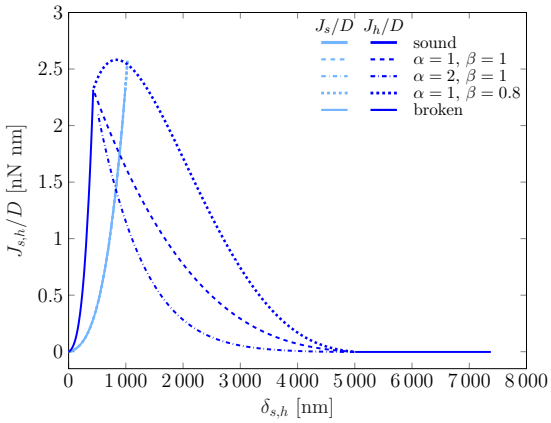

(d) *Growth Flux (Negative Durotaxis)*

Figure 3.34: *Evolution of traction forces $t_{s,h}$ (a, b) and growth fluxes $J_{s,h}/D$ (c, d) versus nodal displacements $\delta_{s,h}$. (a, c)* ***Positive durotaxis:*** *the soft spring (light blue) reaches the damage threshold first. Its traction follows a softening path, forcing the hard spring (dark blue) to unload elastically. (b, d)* ***Negative durotaxis:*** *the hard spring (dark blue) reaches the damage threshold first, undergoing softening, while the soft spring (light blue) unloads. The curve styles correspond to the damage parameters (α, β) defined in Figure 3.33.*

potential barrier dominates, causing the flux to turn negative ($J < 0$). This result highlights a key feature of the model: focal adhesions do not grow unconditionally. Instead, mechanical damage triggers a reduction in tension that inevitably leads to the disassembly of the plaque.

3.4.3 Implications of elasto-damaging adhesion

The analysis of the one-dimensional tensegrity system elucidates the critical role of adhesion integrity in governing cytoskeletal stability. A primary implication of the proposed model is its ability to capture the transition from positive to negative durotaxis through a purely mechanical framework. The results demonstrate that this reversal is not arbitrary but is strictly governed by the differential damage evolution at the cell-substrate interfaces. Specifically, positive durotaxis is identified as the physiological baseline where the adhesion to the soft substrate reaches its damage threshold first ($\delta_s > \Delta_s^0$), necessitating a migration toward the stiffer environment to maintain equilibrium. Conversely, negative durotaxis emerges as a mechanically consistent solution when the adhesion to the hard substrate is physically compromised ($\Delta_h^0 \ll \Delta_s^0$), causing it to fail first. Furthermore, the incorporation of a softening traction-separation law resolves the physical inconsistency often encountered in linear elastic models, where adhesion size is predicted to grow indefinitely with substrate stiffness. By linking the growth flux to the mechanical integrity of the bond, the present model ensures that focal adhesion growth is bounded. The emergence of a post-peak softening branch in the flux profile (Fig. 3.34c) reflects the physical reality of disassembly: as the adhesive bond degrades, the driving force for polymerization vanishes, preventing unrealistic force accumulation. These local mechanisms, identified within the simplified 1D unit, provide the physical basis for understanding how local damage drives global cellular migration.

4

A continuum model of a contractile cell with elasto-damaging adhesion

In the previous chapter, we utilized a reduced-order tensegrity model to identify the fundamental mechanochemical mechanisms governing cell stability. That framework successfully highlighted the role of synergistic instability and the thermodynamic competition between contraction and polymerization. However, the one-dimensional nature of the tensegrity unit limits its predictive capacity regarding complex geometric phenomena. Specifically, the discrete model enforces a global force balance that cannot capture spatial localization. In a 1D chain, rupture at one end instantly unloads the entire system. In contrast, real cells exhibit localized stress concentrations, where focal adhesion failure may occur at the leading edge while the trailing edge remains stable, or vice versa [Plotnikov et al., 2012]. Furthermore, a continuum approach is required to account for three-dimensional effects such as the continuous distribution of traction forces. Therefore, in this Chapter, we translate the elasto-damaging adhesive law developed in Chap. 3 into a continuum model with boundary conditions that simulate the degrading nature of the adhesions. We propose a finite-strain continuum formulation to investigate how the interplay between cytoskeletal contractility and substrate stiffness gradients drives the macroscopic phenomenon of durotaxis.

4.1 Continuum formulation in the presence of substrate mechanical gradients

Cell contractility is a ubiquitous driver of locomotion [Oakes et al., 2014, Murrell et al., 2015], acting in concert with lamellipodium protrusion and the disassembly of adhesions [Lauffenburger and Horwitz, 1996, Serpelloni et al., 2021]. While contractility can be isotropic (e.g., cell rounding) or localized (e.g., cytokinesis), in the context of migration, it serves to break symmetry [Erlich et al., 2022]. By generating tension against the substrate, the actomyosin network allows the cell to interrogate its mechanical environment. Consequently, the cell is modeled as a continuum body adhering to a substrate (Fig. 4.1). The active contractile behavior of the actomyosin cytoskeleton (Figure 4.1a) is introduced into the continuum model as an isotropic active pre-stretch tensor. To investigate durotaxis, the substrate is divided into two distinct regions: a soft region and a hard region. This configuration imposes a sharp mechanical gradient at the interface to which the cell adheres.

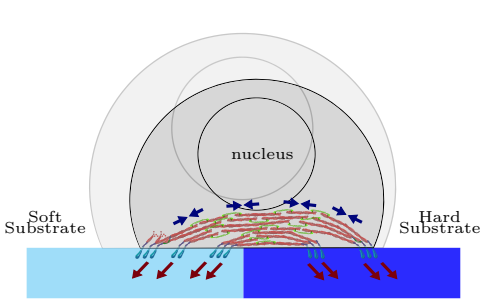

(a) *Contractile cell with myosin motors*

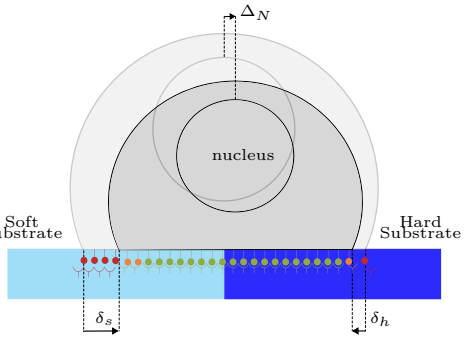

(b) *Equivalent contractile cell with elastic-damaging connections*

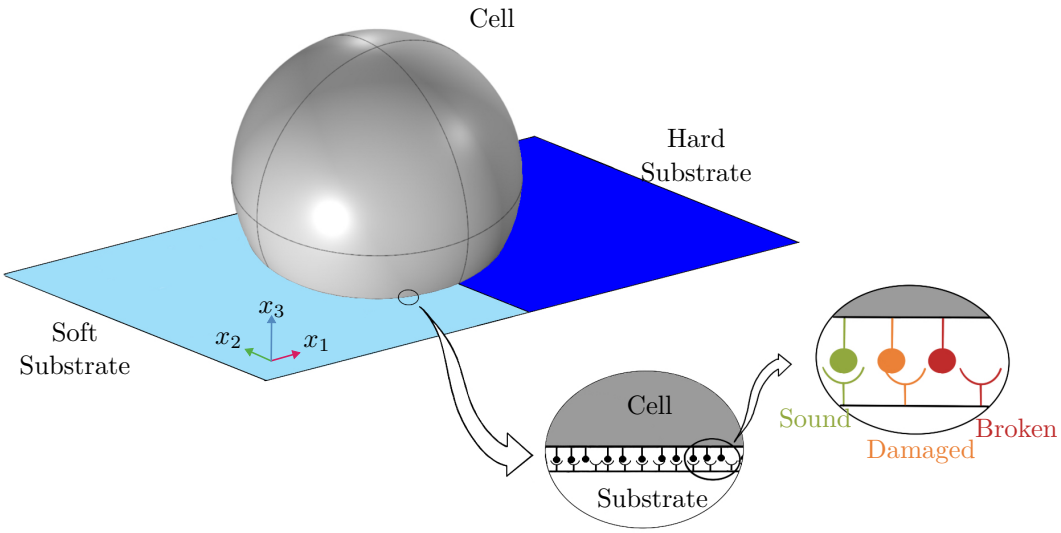

(c) *Three-dimensional model with cell-substrate connectors*

Figure 4.1: *The cell placed on a substrate with a mechanical gradient and anchored to the substrate through the focal adhesions and contracting due to the actomyosin activity (Figure a) is modeled using an equivalent continuum model with elastic-damaging connections of spatially variable stiffness to account for the mechanical gradients (Figure b). This is a case of positive durotaxis, as the cell system moves towards the hard part of the substrate. Figure c) displays a sketch of the cell on the substrate with the reference axes and the layer of mechanical links between the cell and the substrate. Sound links are plotted in green, while the damaged and broken ones are indicated in orange and red, respectively.*

The mechanical behavior of the focal adhesion complex, encompassing integrins, talin, and the extracellular matrix, is homogenized into a nonlinear traction-separation law acting at the interface. Following the damage mechanics framework introduced in Sec. 3.1.4, the state of the adhesive interface is visualized in Figures 4.1b and 4.1c as:

- **Sound links** (Green). Adhesions operating within the elastic regime.
- **Damaged links** (Orange). Adhesions undergoing softening/degradation due to excessive strain.
- **Broken links** (Red). Adhesions that have failed and carry no load.

4.1.1 Kinematics of durotaxis

We focus on the sliding displacements $\boldsymbol{\delta}$ at the cell-substrate interface (the x_1-x_2 plane). For any point on the contact surface, an effective equivalent displacement δ is defined as the Euclidean norm of the sliding vector $\boldsymbol{\delta} = \{\delta_1, \delta_2\}^T$ [Deshpande et al., 2008, Ortiz and Pandolfi, 1999]:

$$\delta = |\boldsymbol{\delta}| = \sqrt{\delta_1^2 + \delta_2^2}. \tag{4.1}$$

To quantify the global migration tendency and to define the traction-separation law, we analyze the sliding magnitudes associated with the soft (s) and hard (h) regions of the substrate. Variables pertaining to these regions are denoted by the subscripts s and h, respectively. Figure 4.1b, which shows the diametric slice of the hemispherical cell (Fig. 4.1c), illustrates the interplay between the internal isotropic contractile pre-stretch, the external stiffness gradient, and the damage induced by the sliding deformations. Recalling the net cell displacement $\Delta_N = \delta_s - \delta_h$ defined for the tensegrity model, we interpret it here analogously as the difference between the representative sliding magnitudes on the soft and hard sides. Consistent with the analysis performed in Chap. 3, we distinguish two regimes:

- **Positive durotaxis ($\Delta_N > 0$).** The sliding on the soft side (δ_s) exceeds that on the hard side (δ_h). The cell effectively loses its grip on the soft substrate while maintaining anchorage on the hard substrate, resulting in a net translocation toward the stiffer region. This regime is characterized by the failure of the highly stressed links on the soft side.
- **Negative durotaxis ($\Delta_N < 0$).** The sliding on the hard side exceeds that on the soft side. Here, the stronger anchorage is paradoxically on the soft substrate (due to the preservation of integrity), and the cell migrates toward the compliant region. This regime concludes with the failure of the links on the hard substrate.

4.2 Finite elasticity and mechanical balance equations

Actomyosin contractility is modeled here not as an active stress [Erlich et al., 2022], but as an active change of the reference configuration (active strain). As discussed in [Palumbo et al., 2022, Benvenuti et al., 2022, 2023], applying a pre-stretch rather than a pre-stress allows the system to naturally find its equilibrium state compatible with the boundary conditions.

We adopt a finite strain kinematics framework [Holzapfel, 2000]. The total deformation gradient $\mathbf{F}$, mapping points from the stress-free reference configuration $\mathcal{B}_0$ to the current deformed configuration $\mathcal{B}_t$ (Fig. 4.2), is defined as [Rausch and Kuhl, 2013]:

$$\mathbf{F}(\mathbf{X},t) = \nabla \mathbf{x} \equiv \nabla \boldsymbol{\varphi}(\mathbf{X},t) \tag{4.2}$$

with components $F_{ij} = \frac{\partial x_i}{\partial X_j}$, where $\mathbf{x} = \boldsymbol{\varphi}(\mathbf{X},t)$. To account for contractility, $\mathbf{F}$ is multiplicatively decomposed into an active inelastic part ($\mathbf{F}^*$) and a passive elastic part ($\mathbf{F}_e$):

$$\mathbf{F} = \mathbf{F}_e \mathbf{F}^*. \tag{4.3}$$

Here, $\mathbf{F}^*$ represents the isotropic contractile shortening of the stress-free state (the "actomyosin contraction"), mapping $\mathcal{B}_0$ to a fictitious intermediate configuration $\mathcal{B}^*$. The elastic deformation gradient $\mathbf{F}_e$ subsequently maps $\mathcal{B}^*$ to $\mathcal{B}_t$, accommodating the compatibility with the boundary conditions (Figure 4.2).

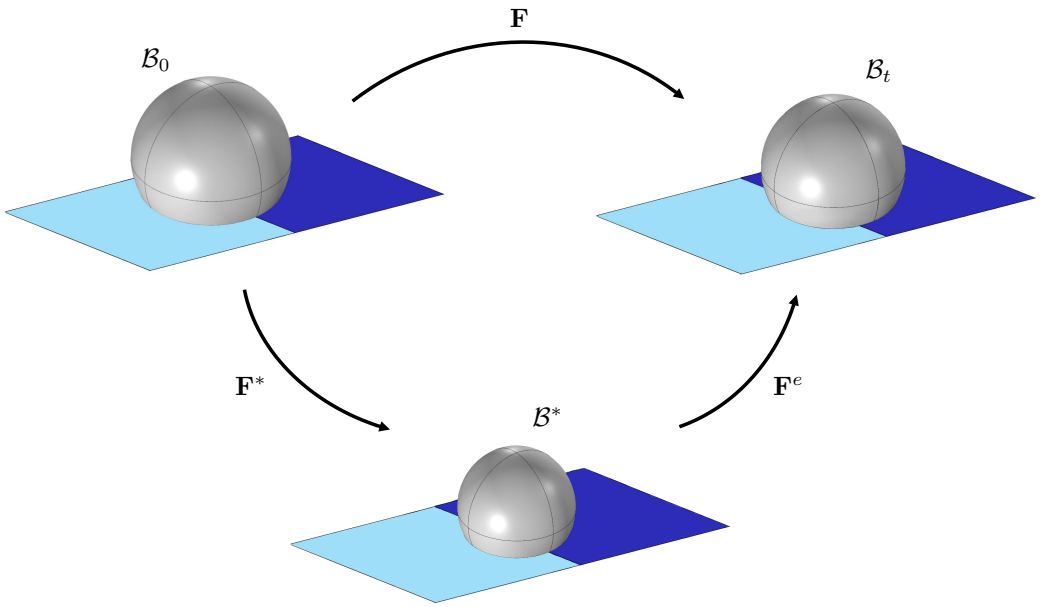

Figure 4.2: *Kinematics of the pre-stretched cell. The total strain tensor maps the initial configuration $\mathcal{B}_0$ into the deformed configuration $\mathcal{B}_t$, it can be multiplicatively decomposed as $\mathbf{F} = \mathbf{F}^e\mathbf{F}^*$. The inelastic deformation gradient $\mathbf{F}^*$ initially maps the reference configuration $\mathcal{B}_0$ into an intermediate fictitious configuration $\mathcal{B}^*$ and the elastic deformation gradient $\mathbf{F}^e$, subsequently maps the intermediate into the deformed configuration.*

The Cauchy stress $\boldsymbol{\sigma}(\mathbf{x},t)$ acting on the spatial configuration is related to the first Piola-Kirchhoff stress $\mathbf{P}$ acting on the reference configuration by the standard push-forward operation [Ogden, 2003, Holzapfel, 2000]:

$$\boldsymbol{\sigma} = J^{-1}\mathbf{P}\mathbf{F}^{*T}\mathbf{F}^{eT}, \quad \text{with} \quad J = \det(\mathbf{F}). \tag{4.4}$$

where ds is the surface element of normal $\mathbf{n}(\mathbf{x},t)$ in the spatial configuration and dS_0 the surface element of normal $\mathbf{N}_0(\mathbf{X})$ in the reference configuration. The mechanical response of the cell bulk is governed by the hyperelastic strain energy density $\mathcal{W}$.

The second Piola-Kirchhoff stress $\mathbf{S}$ in the reference configuration is derived from the elastic stress $\mathbf{S}^e$ (defined in the intermediate configuration) via the pull-back operation [Rodriguez et al., 1994]:

$$\mathbf{S} = 2\frac{\partial \mathcal{W}}{\partial \mathbf{C}} = \mathbf{F}^{*-1}\mathbf{S}^e\mathbf{F}^{*-T}, \quad \text{with} \quad \mathbf{S}^e = 2\frac{\partial \mathcal{W}}{\partial \mathbf{C}_e}. \tag{4.5}$$

Assuming quasi-static conditions (negligible inertial effects), the principle of virtual power states that the internal power equals the power expended by external forces. In order to distinguish between the traction exerted on the soft ($\mathbf{t}_s$) and hard substrates ($\mathbf{t}_h$) the external surface of the cell can be expressed as $\partial\hat{\mathcal{B}}_0 \equiv \partial\mathcal{B}_0 \setminus \partial\mathcal{B}_{0,s} \bigcup \partial\mathcal{B}_{0,h}$. Neglecting body forces, the power functional $\mathcal{P}$ is written as [Ortiz and Pandolfi, 1999]:

$$\mathcal{P} = \int_{\mathcal{B}_0} \mathbf{P} : \dot{\mathbf{F}}\, dV_0 + \int_{\partial\mathcal{B}_{0,s}} \mathbf{t}_s \cdot \dot{\boldsymbol{\varphi}}\, dS_0 + \int_{\partial\mathcal{B}_{0,h}} \mathbf{t}_h \cdot \dot{\boldsymbol{\varphi}}\, dS_0, \tag{4.6}$$

where $\mathbf{P}$ is work-conjugated to the rate of the deformation gradient $\dot{\mathbf{F}}$, and the tractions $\mathbf{t}_s$ and $\mathbf{t}_h$ perform work on the rates of displacement $\dot{\boldsymbol{\varphi}}$ at the cell-substrate cohesive interfaces $\partial\mathcal{B}_{0,s}$ and $\partial\mathcal{B}_{0,h}$, respectively.

The first variation of $\mathcal{P}$ leads to the required governing equilibrium equations:

$$\nabla_0 \cdot \mathbf{P} = \mathbf{0} \qquad \text{in } \mathcal{B}_0, \tag{4.7a}$$

$$\mathbf{P}\mathbf{N}_0 = \mathbf{0} \qquad \text{on } \partial\hat{\mathcal{B}}_0, \tag{4.7b}$$

$$\mathbf{P}\mathbf{N}_0 = \mathbf{t}_s \qquad \text{on } \partial\mathcal{B}_{0,s}, \tag{4.7c}$$

$$\mathbf{P}\mathbf{N}_0 = \mathbf{t}_h \qquad \text{on } \partial\mathcal{B}_{0,h}. \tag{4.7d}$$

In Section 4.3, the relationship $\mathbf{P} = \mathbf{F}^e\mathbf{S}^e\mathbf{F}^{*-T}$ [Ogden, 2003] will be exploited.

4.2.1 A traction-separation law for cell-substrate adhesion

To bridge the gap between the discrete tensegrity model and the continuum formulation, we generalize the traction-separation law and the adhesion growth flux, originally introduced in Chapter 3, to the three-dimensional continuum setting.

The mechanical interaction at the interface is governed by a cohesive law derived from the pseudo-elastic potential (Eq. (3.18)). As detailed in Sec. 3.1.4, the scalar force magnitude transmitted by a single focal adhesion-substrate complex is given by:

$$t_i(\mathbf{X}) = \frac{d\Phi_i}{d\delta_i} = \zeta_i(\mathbf{X}) K_i \delta_i(\mathbf{X}),$$

where the subscript $i \in \{s, h\}$ denotes the soft or hard region. Consequently, the traction force vector exerted by a single focal adhesion group is expressed as:

$$\mathbf{t}_i(\mathbf{X}) = \frac{t_i(\mathbf{X})}{\delta_i(\mathbf{X})}\boldsymbol{\delta_i}(\mathbf{X}) = \zeta_i(\mathbf{X}) K_i \boldsymbol{\delta}_i(\mathbf{X}). \tag{4.8}$$

The damage variable $\zeta_i(\mathbf{X})$, which accounts for the degradation of the link, is defined as:

$$\zeta_i(\mathbf{X}) = \begin{cases} 1 & \text{if } \delta_i(\mathbf{X}) < \Delta_i^0, \\ \left(\dfrac{\Delta_i^0}{\delta_i(\mathbf{X})}\right)^{\beta} \left(\dfrac{\Delta_i^u - \delta_i(\mathbf{X})}{\Delta_i^u - \Delta_i^0}\right)^{\alpha} & \text{if } \Delta_i^0 \le \delta_i(\mathbf{X}) < \Delta_i^u, \\ 0 & \text{if } \delta_i(\mathbf{X}) \ge \Delta_i^u. \end{cases}$$

Here, $\Delta^0_{s,h}$ and $\Delta^u_{s,h}$ represent the activation and failure displacements, respectively, while α and β are phenomenological parameters governing the softening profile.

4.2.2 Growth rate of the focal adhesion plaque

The remodeling of the focal adhesion is governed by the mechanochemical kinetics detailed in Sec. 3.1.6, where we described the adhesion plaque as a Neo-Hookean material [Palumbo et al., 2022, Benvenuti et al., 2022, 2023]. As established in the thermodynamic framework [Hill and Kirschner, 1982], the energy cost of inserting a monomer depends on the work done against the mechanical load. Therefore, the focal adhesions elongate in the direction of the cell body [Hoffmann and Schwarz, 2013], by recruiting monomers when pulled and releasing monomers when pushed.

To evaluate the growth rate, we first identify the force vector $\mathbf{f}_p$ acting on an individual adhesion plaque is the reaction to the traction vector $\mathbf{t}_i$ exerted by the cell boundary:

$$\mathbf{f}_p(\mathbf{X}) = -\mathbf{t}_i(\mathbf{X}) = -\zeta_i(\mathbf{X}) K_i \boldsymbol{\delta}_i(\mathbf{X}), \qquad \text{with } \mathbf{X} \in \partial\mathcal{B}_{0,i}. \tag{4.9}$$

We therefore define the scalar force magnitude f_p as:

$$f_p(\mathbf{X}) = |\mathbf{f}_p(\mathbf{X})| = \zeta_i(\mathbf{X}) K_i \boldsymbol{\delta}_i(\mathbf{X}). \tag{4.10}$$

Substituting this magnitude into the thermodynamic flux relation derived in Sec. 3.1.6 yields:

$$J(f_p) = -D \left[2\Delta\mu_0 - d_i \int_0^{f_p(\mathbf{X})} \tilde{\lambda}_p(f)\, df \right]. \tag{4.11}$$

Here, d_i is the monomer reference length, $\Delta\mu_0$ is the chemical potential difference in the stress-free state, and $\tilde{\lambda}_p(f)$ is the stretch ratio of the Neo-Hookean filament approximated via Taylor expansion. This relation explicitly couples the macroscopic force generated by cell contractility to the microscopic kinetics of adhesion remodeling.

4.3 Finite element implementation and validation

The continuum framework was implemented in COMSOL Multiphysics©. Extending the thermomechanical small-strain analysis of Shenoy et al. [2016] to the finite deformation regime, the cell is modeled as a compressible Neo-Hookean material. The strain energy density $\mathcal{W}$ is decoupled into isochoric (shape-changing) and volumetric (volume-changing) contributions [Simo and Taylor, 1991, Holzapfel, 2000]:

$$\mathcal{W} = \frac{\overline{\mu}}{2}(\overline{I_1} - 3) + \frac{\overline{K}}{4}\left(J_e^2 - 1 - 2\ln J_e\right), \tag{4.12}$$

where $\overline{I}_1 = \mathrm{tr}(\overline{\mathbf{C}}_e)$ is the first invariant of the isochoric elastic right Cauchy-Green tensor, defined as $\overline{\mathbf{C}}_e = J_e^{-2/3}\mathbf{C}_e$, and $J_e = \det(\mathbf{F}_e)$ is the elastic volume ratio. The effective bulk modulus $\overline{K}$ and shear modulus $\overline{\mu}$ are derived from the chemo-mechanical parameters proposed by Shenoy et al. [2016]:

$$\overline{K} = \frac{1}{3}\frac{3K\beta_s - 1}{\beta_s - \alpha_v}, \qquad \overline{\mu} = \frac{1}{2}\frac{2\mu\beta_s - 1}{\beta_s - \alpha_d} \tag{4.13}$$

Here, β_s represents the chemical stiffness, while α_v and α_d are the volumetric and deviatoric chemo-mechanical feedback parameters, respectively. For the simulations, we assume $\beta_s = 2.77$ kPa^{-1}, α_v= 2.33 kPa^{-1}, and $\alpha_d = 2.33$ kPa^{-1} [Shenoy et al., 2016].

The constitutive response is computed via the second Piola-Kirchhoff stress $\mathbf{S}$. Using the chain rule on the decoupled energy density, $\mathbf{S}$ is given by [Rausch and Kuhl, 2013]:

$$\mathbf{S} = 2\frac{\partial \mathcal{W}}{\partial \mathbf{C}} = \mathbf{F}^{*-1}\left[J_e^{-2/3}\mathbb{P}^e : \overline{\mathbf{S}^e} + J_e\frac{\partial \mathcal{W}_{vol}(J_e)}{\partial J_e}\mathbf{C}_e^{-1}\right]\mathbf{F}^{*-T}, \tag{4.14}$$

where $\overline{\mathbf{S}^e} = 2\,\partial \mathcal{W}_{iso}(\overline{I_1})/\partial\overline{\mathbf{C}_e}$ and $\mathbb{P}^e = \mathbb{I} - 1/3(\mathbf{C}_e^{-1}\otimes\mathbf{C}_e)$ is the fourth order projection tensor.

The active actomyosin contractility is introduced via the isotropic pre-stretch tensor:

$$\mathbf{F}^* = \lambda^*\mathbf{I}, \tag{4.15}$$

where the scalar $\lambda^* < 1$ governs the intensity of the contraction.

4.3.1 Localization of traction forces

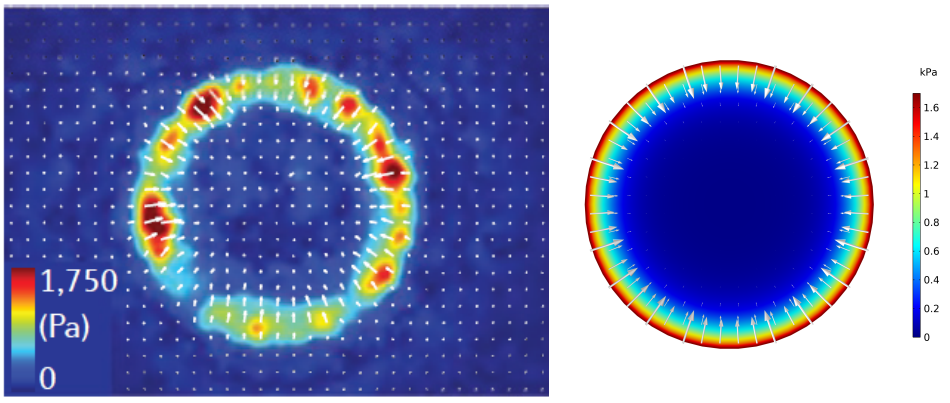

(a) **(b)**

Figure 4.3: *Traction stress and magnitude for a circular cell, reproduced with Authors' permission after [Murrell et al., 2015] (a). Contour plot of the traction considering a homogeneous substrate with $K_s = K_h = 5$ nN/nm and a pre-stretch $\lambda_f^* = 0.85$ (b).*

To validate the continuum formulation, we simulated a cell adhering to a homogeneous substrate and compared the resulting traction field with experimental data reported by Murrell et al. [2015] for fibroblasts. The cell geometry is modeled as a disk with area $A = 1600\,\mu$m^2 (Radius $R \approx 22.6\,\mu$m). The material properties are set to a Young's modulus $E = 5.4$ kPa and Poisson coefficient $\nu = 0.43$. A homogeneous distribution of springs beneath the cell has been assumed on a substrate with $K_s = K_h = 5$ nN/nm. The disk is subjected to a pre-stretch $\lambda_f^* = 0.85$. As shown in Figure 4.3, the continuum model correctly captures the spatial localization of traction forces. Consistent with experimental observations (Fig. 4.3a), the numerical results (Fig. 4.3b) reveal that stresses are not uniformly distributed but concentrate within a thin circumferential layer at the cell periphery. This result justifies the geometric simplification adopted in subsequent simulations, where the explicit modeling of adhesive interactions is confined to the outer circumferential ring (see Fig. 4.5).

4.3.2 The contractility tensor and polarization

To bridge our finite-strain formulation with the chemo-mechanical framework of Shenoy et al. [2016], we evaluate the effective contractility tensor $\boldsymbol{\rho}$ corresponding to the input pre-stretch $\mathbf{F}^*$. This tensor describes the chemical free energy of myosin recruitment and provides a measure of cell polarization. Specifically, the eigenvalues and eigenvectors of $\boldsymbol{\rho}$ predict the cell polarization and the orientation of stress fibers. Generalizing the theory to finite strains, we evaluate $\boldsymbol{\rho}$ as:

$$\boldsymbol{\rho} = \mathbf{F}^{*-1}\left[2J_e^{-2/3}\mathbb{P}^e : \frac{\partial \mathcal{W}_{iso,\rho}(\overline{I_1})}{\partial \overline{\mathbf{C}_e}} + J_e \frac{\partial \mathcal{W}_{vol,\rho}(J_e)}{\partial J_e}\mathbf{C}_e^{-1}\right]\mathbf{F}^{*-T}, \tag{4.16}$$

where $\mathcal{W}_{iso,\rho}(\overline{I_1}) = \overline{\mu_\rho}/2(\overline{I_1} - 3)$, $\mathcal{W}_{vol,\rho} = \overline{K}_\rho/4(J_e^2 - 1 - 2\ln J_e)$ and $\overline{K_\rho}$ and $\overline{\mu_\rho}$ are the bulk and shear effective moduli for motor density, defined following Shenoy et al. [2016]:

$$\overline{K_\rho} = \frac{1}{3}\frac{3K\alpha_v - 1}{\beta_s - \alpha_v}, \qquad \overline{\mu_\rho} = \frac{1}{2}\frac{2\mu\alpha_d - 1}{\beta_s - \alpha_d}. \tag{4.17}$$

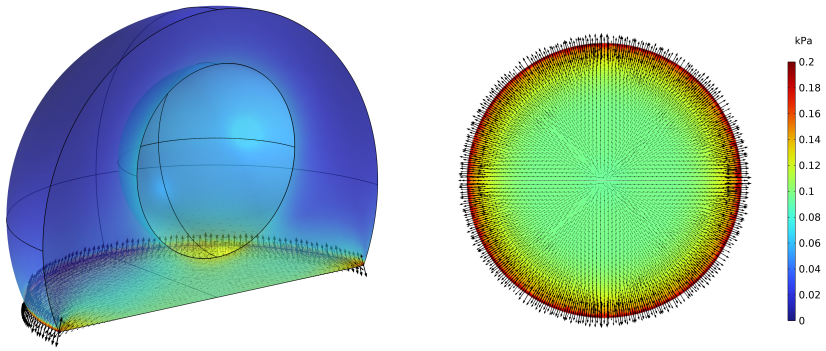

(a) **(b)**

Figure 4.4: *Transparent three-dimensional view of cell hemisphere (a), and bottom view (b) of the contractility parameter η (4.18) for a cell adherent to a homogeneous substrate with $K_s = K_h = 3$ nN/nm subjected to pre-stretch $\lambda_f^* = 0.95$. The black arrows represent the distribution of the analogous of the myosin motors polarization orientation computed as the eigenvector associated to the maximum eigenvalue of $\boldsymbol{\rho}$. The cell has a radius of 10 μm, nucleus radius R_n of 4.7 μm with bulk modulus $K = 0.833$ kPa, and shear modulus $\mu = 0.385$ kPa.*

To quantify the degree of polarization, we introduce the scalar measure η, defined as half the difference between the maximum (ρ_1) and minimum (ρ_3) principal eigenvalues of the contractility tensor:

$$\eta = \frac{1}{2}(\rho_1 - \rho_3). \tag{4.18}$$

This scalar provides a measure of the magnitude of motor polarization.

We modeled the cell as a hemisphere ($R = 10\,\mu$m) with bulk modulus $K = 0.833$ kPa and shear modulus $\mu = 0.385$ kPa. The nucleus was treated as a linear elastic inclusion ($R_n = 4.7\,\mu$m, $E_n = 1.2$ kPa, $\nu_n = 0.3$). Applying an isotropic pre-stretch of

$\lambda^* = 0.95$ yields the results shown in Figure 4.4. The black arrows, corresponding to the principal eigenvector of $\boldsymbol{\rho}$, indicate the predicted polarization direction of myosin motors. Crucially, the model reveals that even with an isotropic active input, the geometric boundary conditions induce a strong polarization of the internal stress field, aligning with the observed organization of stress fibers. The localization of maximum contractility and motor alignment near the cell periphery further validates the assumption made in Section 4.3.1. Consequently, for computational efficiency in subsequent simulations, the full bed of springs is replaced by a defined cohesive interaction zone confined to a circumferential ring of width $2\,\mu$m (Figure 4.5).

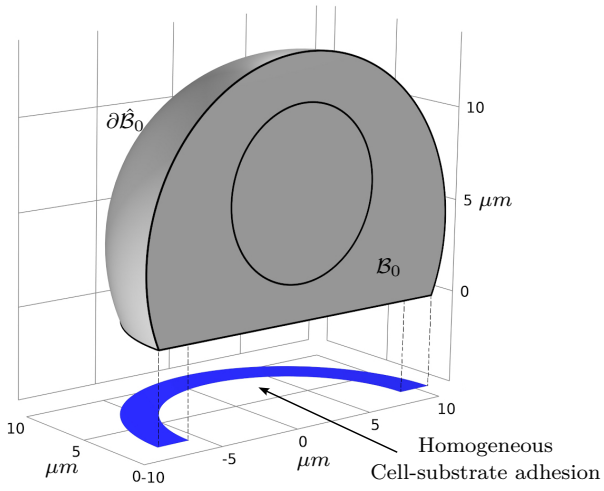

Figure 4.5: *Geometry of the hemispherical cell with radius R=10 μm. The location of the underlying cell-substrate cohesive springs is confined to a thin circumferential layer of 2 μm.*

4.3.3 Optimal stiffness

A critical prediction of this elasto-damaging framework is the non-monotonic relationship between substrate stiffness and traction force. While classical linear models suggest that traction increases monotonically with stiffness before plateauing [He et al., 2014], the existence of an optimal stiffness for maximal traction is a well-established phenomenon in mechanobiology [Chan and Odde, 2008, Elosegui-Artola et al., 2016, Sáez and Venturini, 2023]. This biphasic behavior, where traction increases up to an optimum before decreasing, has been extensively characterized in neurons and famously verified in glioma cells by Isomursu et al. [2022]. Our model phenomenologically captures this softening-like force-stiffness profile. To investigate this, we performed a parametric study using the material properties $K = 0.833$ kPa and $\mu = 0.385$ kPa. To isolate the effect of interface compliance, the traction-separation law was systematically varied for each substrate stiffness as shown in Figure 4.6a. Specifically, the peak adhesive force and failure displacement (Δ^u) were held constant, while the activation displacement (Δ^0) was varied. This procedure modifies the initial stiffness of the interface while maintaining a constant ultimate adhesive capacity. The results, presented in Figure

4.6b, demonstrate the emergence of a biphasic trend. We observe an optimal substrate stiffness range where the cell exerts maximum traction. Furthermore, as the internal contraction level increases (lower λ^*), this optimal stiffness interval shifts towards the left (softer substrates), highlighting the non-linear coupling between intracellular contractility and extracellular mechanics in the mechanosensing process.

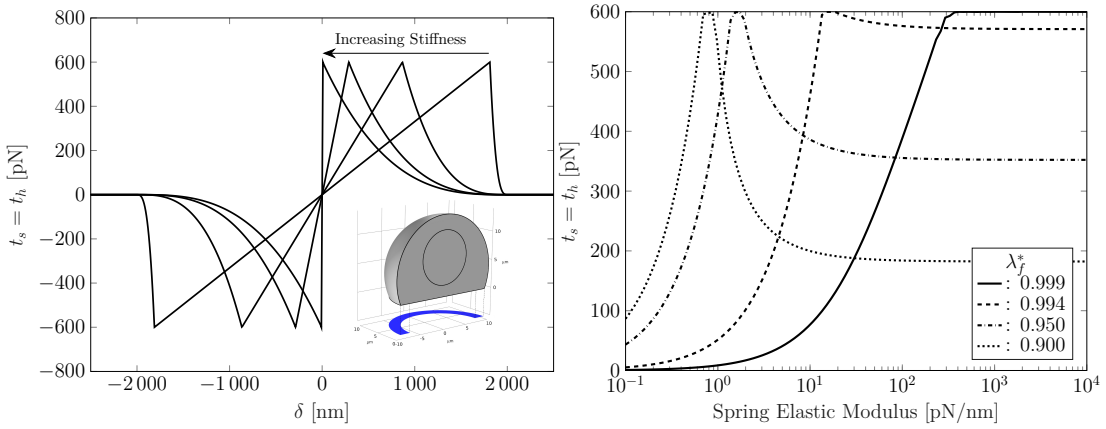

(a) **(b)**

Figure 4.6: *In Figure a), the force-displacement laws related to the cell-substrate interface for different substrate stiffness values are reported at constant peak force. Figure b) displays the maximum force exerted by the cell versus substrate stiffness for different contractile pre-stretch levels in a semilogarithmic scale. The material parameters are bulk modulus $K = 0.833$ kPa, shear modulus $\mu = 0.385$ kPa.*

4.3.4 Validation against traction-displacement data

Force-displacement laws provide critical insight into the biophysical processes of mechanically stimulated tissues and single cells. However, establishing these laws requires the rigorous calibration of biophysical parameters and the identification of appropriate modeling assumptions [Nguyen and Gu, 2016]. While numerous experiments have unraveled the complex chemo-mechanical mechanisms governing cell-substrate interactions, measuring simultaneous traction forces and displacements of living cells in a realistic biological environment remains challenging. Consequently, robust experimental datasets suitable for identifying mechanobiology-based force-displacement laws are rare. Among the available data, adhesive shear forces and detachment have been measured in living chondrocytes and bacteria [Nguyen and Gu, 2016, Alam et al., 2019], while Oakes et al. [2014] successfully mapped the substrate displacement and traction stresses of cells on gels of varying shear moduli, effectively decoupling the effects of substrate stiffness, cell morphology, and focal adhesions. To validate the predictive capabilities of the present framework, the elastic stiffness of the traction-separation law at the cell-substrate interface was identified by comparison with the experimental dataset of Oakes et al. [2014]. In their study, Oakes et al. [2014] measured the tractions exerted by fibroblasts, revealing a strict relationship between the total cell deformation work, cell spread area, and geometry, while noting that the number of focal adhesions and substrate stiffness had a secondary effect on the total force magnitude. For the numerical comparison,

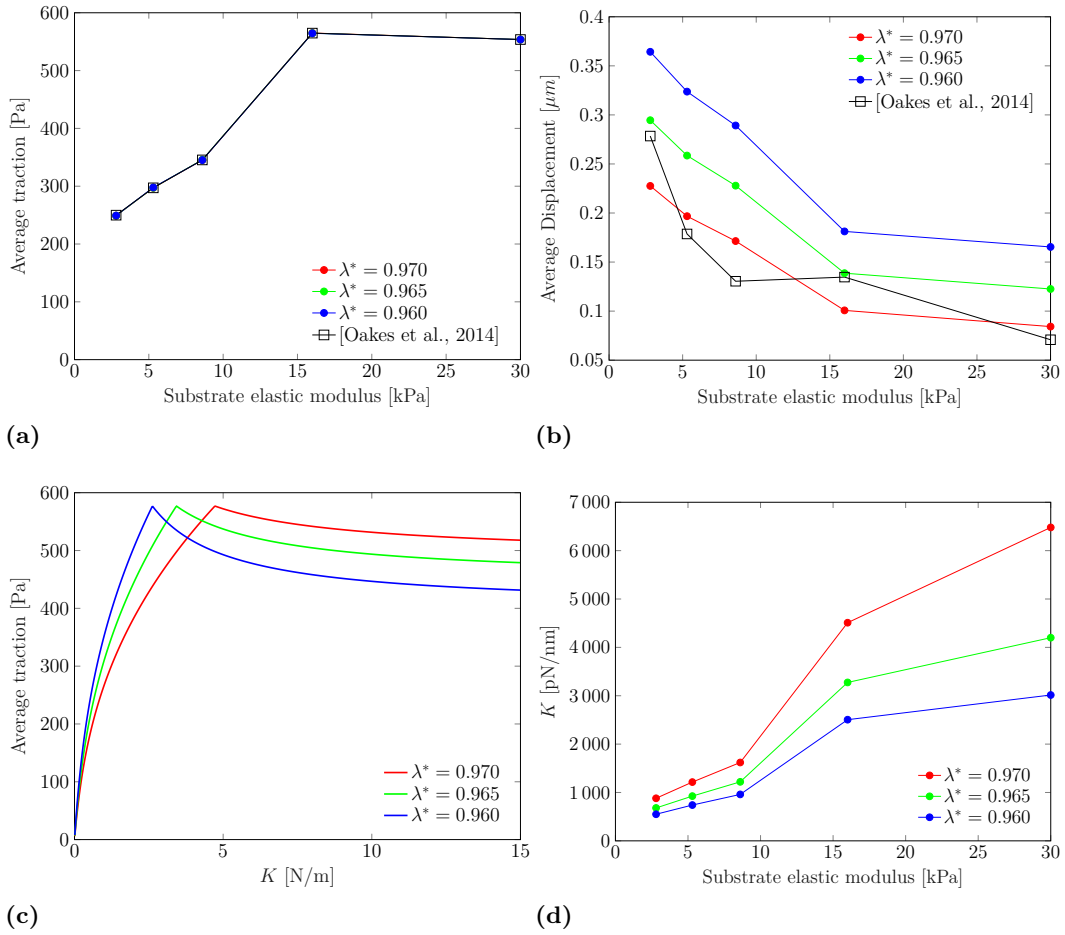

Figure 4.7: *The pre-stretch values have been identified based on Oakes et al. [2014] experimentally measured average tractions for variable substrate elastic modulus E (a). The corresponding average displacements computed with the present model in Figure b) consistently captures the experimental data. The consequent average traction versus the cohesive law stiffness is nonlinear with a peak for certain stiffness values (c). The non-decreasing relationship between $K_s = K_h = K$ and the substrate Young modulus E is also shown in Figure d).*

we adopted the material properties reported in the experiment: a cell Young's modulus $E = 5.4$ kPa and Poisson's ratio $\nu = 0.43$. Consistent with the continuum hypothesis [Bell, 1978], we assume the adhesion groups form a continuous distribution, where the resultant force is the product of the discrete group forces and their surface density. The calibration procedure was performed by selecting three representative pre-stretch values (λ^*) to simulate varying contractility levels. For each substrate stiffness and contractility level, the stiffness of the cohesive interface law ($K_s = K_h = K$) was iteratively adjusted until the computed average traction matched the experimental values reported by Oakes et al. [2014] (Figure 4.7a). The average traction was calculated by integrating the traction magnitude along the boundary and normalizing by the adhesion area. This procedure yielded the calibration curve shown in Figure 4.7d, which establishes the required relationship between the macroscopic substrate modulus (kPa) and the microscopic interface stiffness (pN/nm) for our elasto-damaging law. To validate this calibration, we compared the average displacements predicted by the model against the experimental counterparts (Figure 4.7b). The close agreement demonstrates that, once the interface stiffness is properly calibrated to match traction data, the model correctly captures the kinematic response (displacements) of the cell. Finally, Figure 4.7c displays the constitutive behavior of the model, plotting the average traction against the interface stiffness K. The results indicate that the assumption of a softening traction profile is robust and necessary to simultaneously satisfy both the traction and displacement constraints imposed by the experimental data.

4.3.5 Mechanical gradient effects

Whereas in Section 4.3 the substrate was assumed to be homogeneous, this section investigates the response to a mechanical gradient. The cell is modeled on a substrate that is equally split into a hard and a soft region, as shown in Fig. 4.8. The effect of this gradient on the cell's directional migration, whether towards the stiff or soft part, is assessed through a series of computational experiments. By varying the critical displacement and force thresholds of the cohesive laws governing the interface, we demonstrate that the model can recover both positive durotaxis and negative durotaxis (often referred to as mollitaxis).

Cell contractility and durotactic attitude

A cell of radius $R = 10$ μm has been modeled. The cell is positioned such that it is bisected by the substrate discontinuity: one hemisphere of the cell body adheres to the soft region, while the other adheres to the hard region. The cohesive zone is restricted to a circumferential layer of width $R/5$. Figures 4.9a and 4.9b show in dark and light blue the assumed traction-sliding laws of the hard and soft spring, while the red curves indicate the mechanical integrity parameter $\zeta_{s,h}$ evolution. The elastic stiffnesses of the cohesive law for the soft and hard parts are set to $K_s = 5$ pN/nm and $K_h = 10$ pN/nm, respectively.

Positive durotaxis The case of positive durotaxis, where the cell migrates towards the hard part of the substrate, is recovered using the parameters in Figure 4.9a. Here, the initial and final damage thresholds are identical for both sides ($\Delta^0_{s,h} = 0.1$ μm and $\Delta^u_{s,h} = 1$ μm). The results are summarized in Table 4.1, which displays the traction

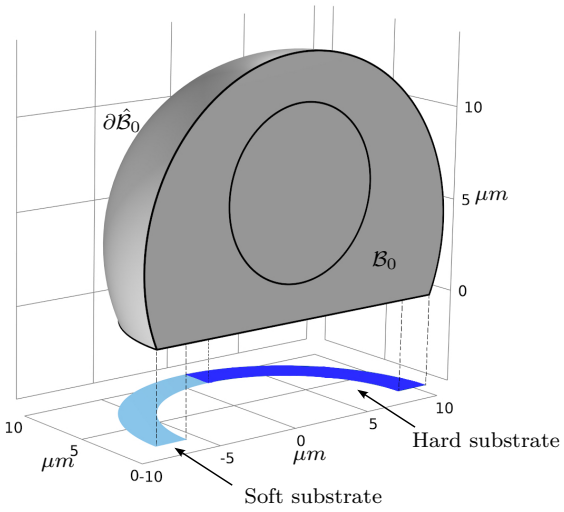

Figure 4.8: *The figure shows one hemisphere of the cell of radius $R = 10$ μm. The underlying soft and hard parts of the cell-substrate cohesive zone are restricted to a thin circumferential layer of 2 μm.*

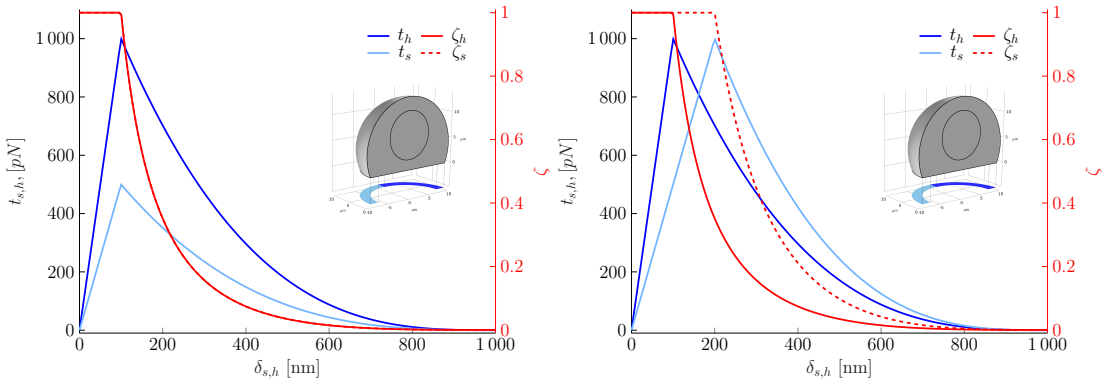

(a) **(b)**

Figure 4.9: *The figure shows the force- (a) and displacement-based (b) traction-sliding laws adopted to detect both positive and negative durotactic attitudes. The initial and final damaging thresholds are $\Delta^0_{s,h} = 100$ nm and $\Delta^u_{s,h} = 1$ μm, respectively (a), and $\Delta^0_h = 100$ nm, $\Delta^0_h = 200$ nm and $\Delta^u_{s,h} = 1000$ nm, respectively (b). The light blue and dark blue curves correspond to $K_s = 5$ pN/nm and $K_h = 10$ pN/nm, respectively. Finally, the red curves represent the mechanical integrity parameters $\zeta_{s,h}$.*

forces, the damage integrity parameter, and the positive part of the growth flux $\langle J \rangle$ ($\langle \cdot \rangle$ indicates the Macaulay brackets). The columns correspond to increasing contractility (from 2% to 10% inelastic contraction). At the lowest contraction level ($\lambda^* = 0.98$), the cell exerts maximum traction on the hard side (black arrows), which remains mechanically sound (blue zone in the integrity parameter plot). Conversely, the soft side begins to suffer damage. Crucially, the growth flux $\langle J \rangle$ is everywhere positive, though it is higher on the hard side. As the pre-contraction increases, the damage on the soft side evolves further, eventually disconnecting that hemisphere from the substrate. Consequently, the cell becomes anchored solely to the hard part, driving migration in that direction.

Negative durotaxis (mollitaxis) Positive durotaxis can invert into negative durotaxis if the adhesion dynamics are altered such that damage initiates earlier on the hard side. To simulate this, we adopted the laws in Figure 4.9b: the initial damage threshold on the hard side ($\Delta_h^0 = 0.1$ μm) is half that of the soft side ($\Delta_s^0 = 0.2$ μm), while the ultimate failure limits remain identical ($\Delta_s^u = \Delta_h^u = 1$ μm). Table 4.2 illustrates the transition from positive to negative durotaxis with increasing contractility. For a low pre-contraction (2%), the system still favors the hard side. However, as soon as the contractility reaches a critical level (e.g., $\lambda^* = 0.96$), the behavior reverses. The high stiffness of the hard springs causes traction forces to rise rapidly, reaching the lower damage threshold Δ_h^0 and degrading the bonds. In contrast, the compliant soft springs stretch without exceeding their higher activation threshold, maintaining integrity. As a result, the cell anchors itself to the soft part while disconnecting from the hard part, exhibiting a clear negative durotactic behavior.

Table 4.1: *The table illustrates the conventional durotaxis instance in terms of traction exerted by the cell on the substrate (in the first row), the damage integrity parameter in the second row, and the positive part of the growth flux in the third row. The contractility increases when moving from left to right. All the plots represent the bottom view of the cell.*

λ^*	0.98	0.96	0.94	0.90
Tractions $t_{s,h}$	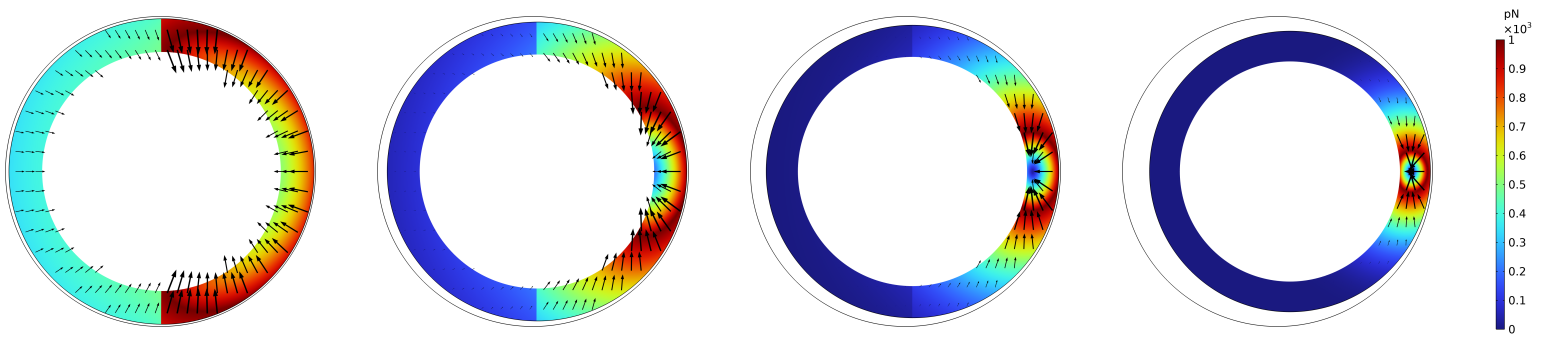			
Integrity Parameter $\zeta_{s,h}$	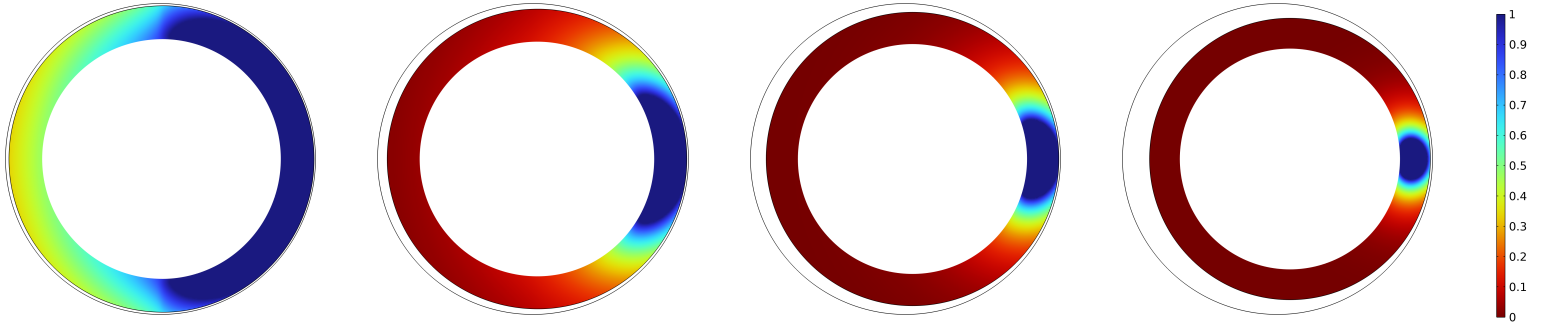			
Growth Flux $\langle J_{s,h}\rangle/D$	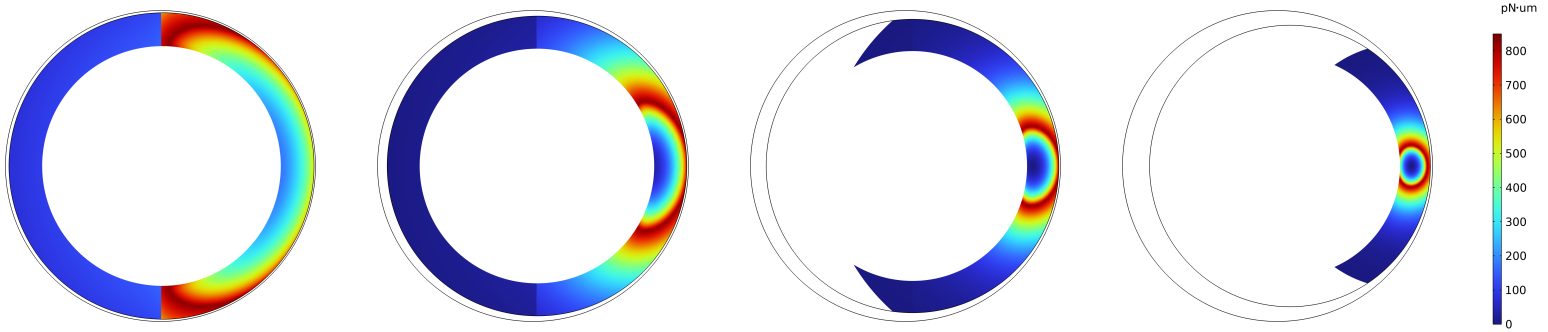			

Table 4.2: *The table collects a series of figures illustrating the reversal of positive durotaxis into negative durotaxis. The contour maps in the first row display the force exerted by the cell on the substrate, the damage integrity parameter in the second row, and the positive part of the growth flux in the last row. The contractility increases when moving from left to right. All the plots represent the bottom view of the cell.*

λ^*	0.98	0.96	0.94	0.90
Tractions $t_{s,h}$	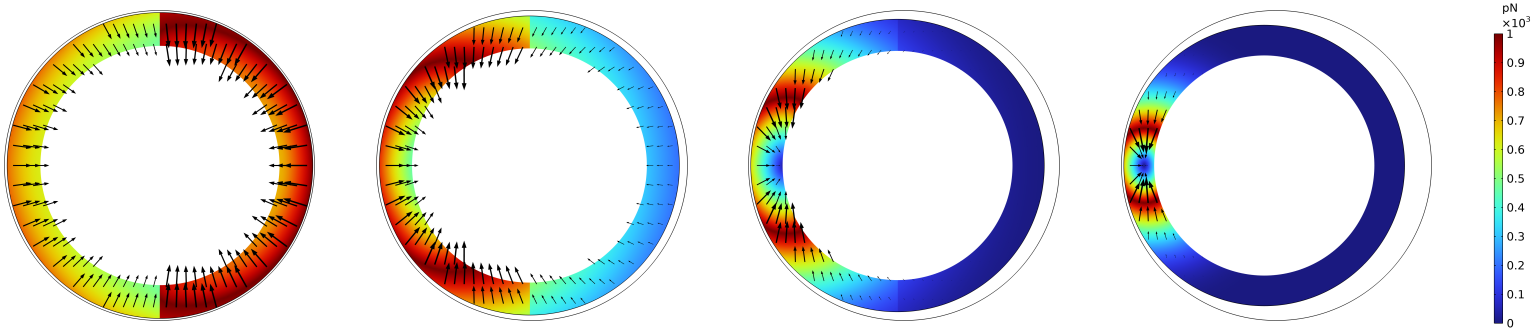			
Integrity Parameter $\zeta_{s,h}$	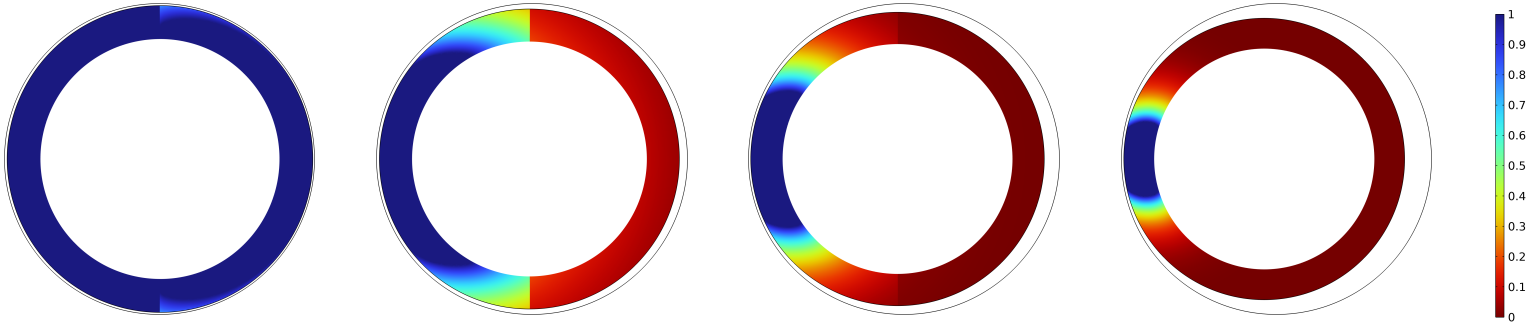			
Growth Flux $\langle J_{s,h}\rangle/D$	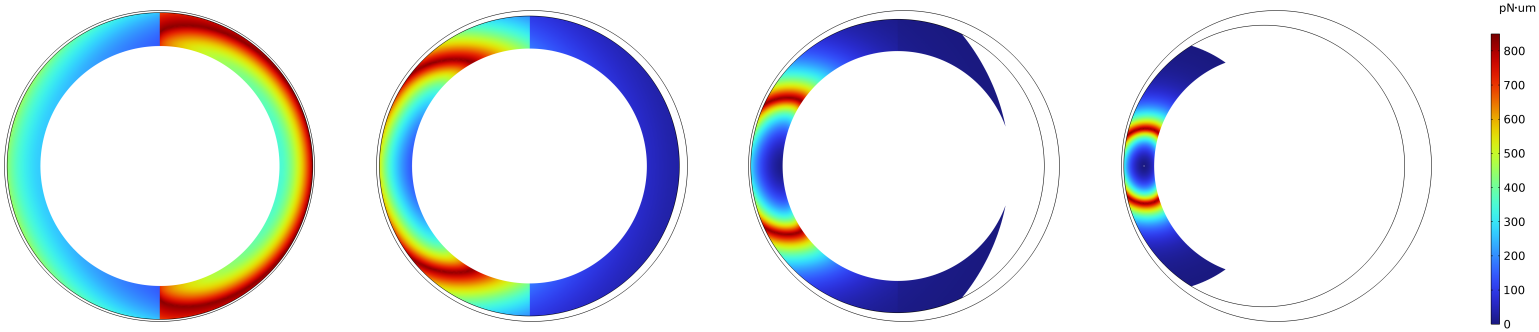			

4.4 Concluding remarks on the continuum framework

The computational analysis presented in this chapter highlights the capability of the proposed elasto-damaging cohesive law to capture complex mechanosensing phenomena.

First, the fully three-dimensional finite element implementation successfully captured the spatial distribution of traction forces. The results reveal a localization of focal adhesions at the boundary of the cell-substrate interface, a finding that is consistent with experimental measurements and demonstrates the model's ability to handle realistic geometries.

Second, the analysis provides a mechanistic explanation for the reversal of positive durotaxis into negative durotaxis. It has been shown that these distinct regimes are governed by different failure modes:

- In the positive durotactic regime, damage activates and propagates primarily on the soft part of the substrate, causing the cell to anchor to the stiff edge.
- In the negative durotactic regime, the behavior reverses; damage initiates at the hard springs (due to lower thresholds or excessive force accumulation), leading to detachment from the stiff substrate and migration towards the compliant region.

Third, the framework recovers the existence of an optimal stiffness range for maximal traction generation [Elosegui-Artola et al., 2018, Isomursu et al., 2022, Sáez and Venturini, 2023]. This biphasic response contrasts with the monotonically increasing dependence assumed by linear elastic models [He et al., 2014]. The model suggests that this optimum arises from the competition between contractility and adhesion integrity: on sufficiently stiff substrates, high traction forces eventually trigger the damage threshold, limiting the maximum force the cell can sustain.

Finally, the thermodynamic growth flux was shown to follow a softening post-peak branch. This result concurs with the biological evidence that focal adhesion plaque growth is self-limiting and saturates, unlike the endless growth suggested by purely linear traction-separation laws.

Part II

A Mechanical Model of Tissue Engulfment

The computational framework presented in this Part of the thesis was developed within the *Hiperlife* library. The core numerical implementation of the CutFEM method within this library is attributed to the developer Santos Oliván et al. [2021] and to the doctoral work of Pau Blanco Dorca. However, the specific application of this method to the problem of tissue invasion, including the formulation of the governing equations and the coupling of elastocapillarity with active degradation, was conceived and implemented by the candidate under the supervision of the co-supervisor, Professor Marino Arroyo Balaguer.

Specifically, the candidate's contributions to this Part of the thesis are:

- **Model formulation and implementation.** The candidate derived the continuum equations for the mechanical system and implemented these specific weak forms into the Hiperlife environment.
- **Code development.** While the underlying CutFEM architecture pre-existed, the candidate contributed to the debugging and refinement of the method to ensure stability in the large-deformation regime required for this specific investigation.
- **Simulations and analysis.** All numerical simulations, parameter sweeps, and the subsequent post-processing and physical interpretation of the results were performed solely by the candidate.

Finally, regarding the computational efficiency highlighted as a key outcome of this work, the high performance results from the synergy between the robust CutFEM architecture developed by Santos Oliván et al. [2021] and Pau Blanco Dorca and the specific implementation choices made by the candidate to optimize the solver convergence for this problem.

5

Introduction to Part II: dynamics of tissue engulfment

Part II of this thesis investigates the dynamics of tissue engulfment, a process fundamental to both embryonic development and cancer progression. In this introductory chapter, we bridge the gap between biological observation and physical theory. We begin by reviewing the biological context of collective migration and invasion, followed by an analysis of the "active droplet" analogy often used to describe these phenomena. Finally, we present the computational framework developed in this work and outline the structure of the following chapter.

5.1 Biological context: from collective migration to invasion

In the extensive spectrum of biological processes, distinct from individual cell migration, a phenomenon known as collective cell migration arises [Friedl, 2004, Friedl and Wolf, 2009]. In this context, the physiochemical processes regulating the movement of a single cell are preserved but are organized and synchronized at a supracellular level. This leads to the behavior of the group of cells acting as a singular organism [Hidalgo-Carcedo et al., 2011, Tambe et al., 2011]. While collective migration is prevalent throughout embryogenesis, resulting in the development of tissues and organs, a specific and critical sub-category of this behavior is known as *invasion*.

In various biological scenarios, active cellular tissues initially adhere to the fibrous extracellular matrix (ECM) and subsequently penetrate to become (partially) engulfed within it. This process is observed in branching morphogenesis, angiogenesis, hair follicle development, and embryo implantation [Andrew and Ewald, 2010, Barrasa-Ramos et al., 2022, Fitzgerald et al., 2008, Villeneuve et al., 2024, Staun-Ram and Shalev, 2005, Cheung et al., 2013, Dvir et al., 2015]. Crucially, it is also a fundamental hallmark of invasive tumor types.

During these motions, the cell group structurally modifies the tissue by reshaping it through basal membrane deposition and the secretion of enzymes, such as matrix metalloproteases (MMPs) [Friedl and Gilmour, 2009]. These enzymes locally degrade the surrounding matrix, mechanically facilitating invasion by creating paths of least resistance or by altering the local tension and fiber orientation of the ECM [Egeblad et al., 2010]. Consequently, the resulting engulfment can arise from two distinct mechanisms: the elastic deformation of the ECM caused by active tensions within the cellular tissue,

akin to elastocapillarity [Shi et al., 2022, Kristal-Muscal et al., 2013], or the chemical degradation of the ECM [Friedl and Alexander, 2011]. Often, the process involves a complex combination of both. However, the distinct roles and interplay of active traction, elastocapillary forces, and degradation mechanisms at the cell-ECM interface are frequently blurred. Despite morphological similarities, the mechanical condition of the ECM may differ significantly depending on which mechanism dominates.

5.2 The active droplet analogy and modeling challenges

To investigate the mechanical aspects of this problemspecifically the metastatic spread of cancer and embryo implantationthis Part of the thesis models the large-scale collective engulfment of tissue into a substrate. To do so, the analogy of a cell or cell cluster as an active liquid droplet is employed. This modeling choice is powerful and physically justified by the fact that cell-cell adhesions and cortical tension generate an effective surface tension, analogous to a liquid droplet [Ryan et al., 2001]. This “cell as a droplet" behavior is well-supported in the literature, having been observed in the wetting of epithelial tissues [Pérez-González et al., 2019], the spreading of spheroidal aggregates [Douezan et al., 2011], and the dimples generated by human colon carcinoma cell colonies into soft hydrogels [Shi et al., 2022]. Furthermore, the importance of surface tension is established in tissue differentiation during embryonic development [Foty et al., 1996], in the mechanosensitivity and fate of mesenchymal stem cells (MSC) [Razafiarison et al., 2018], and in the endocytosis of nanoparticles [Zhang et al., 2015, Yi and Gao, 2016, Shen et al., 2019].

However, modeling this process presents significant computational challenges. The application of previously developed discrete tensegrity models is computationally prohibitive for simulating the thousands of cells involved in a tissue. Conversely, while simpler continuum models are successful for modeling a single cell and its elasto-damaging adhesion, their formulations are often too simplistic to capture the complex, large-scale interface mechanics of an entire tissue that is simultaneously deforming and degrading the substrate.

5.3 Proposed framework and outline

Therefore, to model tissue invasion, a more robust continuum approach is required. We examine these scenarios by specializing and applying the continuum mathematical model for an active fluid proposed by Cicconofri et al. [2024]. The devised framework treats the entire tissue collective as a single “active droplet" acting over a hyperelastic solid matrix that can undergo localized erosion. The mechanics of the active droplet are framed within the physics of elastocapillarity, where the tissue’s surface tension competes with the substrate’s elasticity.

To account for possible ECM degradation, the formulation is grounded in a rigorous variational formulation of irreversible thermodynamics [Onsager, 1931, Arroyo et al., 2018, Cicconofri et al., 2024]. The numerical implementation of this problem is non-trivial, inheriting the complexities of computational elastocapillarity, namely the interplay between fluid-structure interaction and multi-phase flow, augmented by the difficulty of particle removal from the solid interface due to degradation. The resulting two-moving-interface problem is explored using an advanced numerical method

(a hybrid fitted-CutFEM technique) capable of accurately tracking both the tissue-substrate and tissue-external environment boundaries as they evolve. This relies on non-conforming meshes, the phase-field method to describe immiscible fluid evolution, and a Nitsche-Onsager variational formulation to consistently introduce boundary conditions and thermodynamic forces driving the degradation.

Chapter 6 is structured to logically progress from fundamental physical principles to complex tissue-substrate interactions:

- In Secs. 6.1–6.2, we begin by reviewing wetting theory and elastocapillarity, followed by a derivation of Onsager's variational principle, first applied to Stokes flow and then generalized for the current multiphysics problem.
- In Secs. 6.3–6.4, we construct the variational framework incrementally, first formulating the interfacial dynamics for a non-degrading substrate and subsequently extending the model to account for localized degradation driven by thermodynamic forces.
- In Secs. 6.5–6.6, we detail the numerical implementation and present a comprehensive set of simulations. These experiments validate the model against benchmarks and quantify the competition between mechanical indentation and degradation.
- Finally, in Sec. 6.7, we present the specific findings of the invasion model.

6

Mechanical model of tissue engulfment

6.1 Elastocapillarity

Elastocapillarity refers to the ability of capillary forces to induce deformations of an elastic material in contact with fluids. The effect of those forces is observable across a wide range of length scales in several natural and artificial systems [Duprat and Stone, 2015], and is governed by the surface stresses acting at the interfaces of the fluid components and the bulk elasticity of the solid.

The molecular origins of surface tension, which dramatically influence the mechanics of soft solids, stem from the cohesive forces among liquid molecules. A molecule within the bulk of a liquid possesses a cohesive energy derived from its interactions with neighboring molecules. Conversely, molecules at an interface are not entirely surrounded by other molecules, leading to a reduction in cohesive energy and an increase in free energy, which is proportional to the interfacial area. Therefore, for the fluids, we can define the surface energy as an energy penalty per unit area, mathematically defined as the excess of free energy $\mathcal{F}$ associated with an increase of area A, while keeping temperature T, volume V, and number of moles n constant

$$\gamma = \left(\frac{\partial \mathcal{F}}{\partial A}\right)_{T,V,n}. \tag{6.1}$$

This surface energy gives rise to a surface stress $\boldsymbol{\Upsilon}$, that opposes the increase of area. For simple liquids, this tensor is isotropic, meaning it can be written as $\boldsymbol{\Upsilon} = \Upsilon \mathbf{I}$, where $\mathbf{I}$ is the identity tensor and Υ is a scalar magnitude called the surface tension. Furthermore, in simple liquids, the magnitude of the surface tension is equal to the surface free energy per unit area ($\Upsilon = \gamma$). This equivalence leads to the common interchangeability of their names [de Gennes et al., 2004]. However, this property is not valid for solids, for which in general $\gamma \neq \Upsilon$ and Υ is not necessarily isotropic [Shuttleworth, 1950].

To study and characterize the phenomena where surface stresses are important, a well-known characteristic physical scale known as the *elastocapillarity length* is introduced. It is defined as $l = \gamma/E$, the ratio between the surface tension γ and the Young modulus of the substrate E. At physical scales significantly larger than the elastocapillarity length ($L \gg \gamma/E$), bulk elasticity dominates, and the influence of surface stresses is minimal. However, for systems with a characteristic size on the order of, or smaller than, the elastocapillarity length, the impact of surface stresses becomes predominant and leads to significant deformations in the solid.

Given that this chapter intends to investigate the engulfment of active tissue into a fibrous extracellular matrix, we focus on the foundational wetting theory [Young, 1805, Dupré, 1869, Neumann, 1894]. In the study of three-phase contact lines, Young [1805] demonstrated that in a droplet interacting with a rigid solid substrate, as the one represented in Fig. 6.1a, the contact angle θ is independent of the far-field boundary conditions, but it solely depends on the interfacial energy of the different surfaces. In particular, the thermodynamic equilibrium at the contact line is described by the Young-Dupré relation [Dupré, 1869]:

$$\gamma_{lv} \cos\theta = \gamma_{sv} - \gamma_{sl}, \tag{6.2}$$

which relates the contact angle to the surface energies of the liquid-vapor γ_{lv}, solid-vapor γ_{sv}, and solid-liquid γ_{sl} interfaces. Subsequently, Neumann [1894] investigated the interaction between three immiscible fluids, as the one depicted in figure 6.1b. In this scenario, unlike the rigid solid case, all interfaces are deformable. Consequently, the equilibrium is no longer defined by a single horizontal projection as in equation (6.2), but by the vector balance of surface stresses at the contact line, as represented in the zoom of Fig. 6.1b, known as Neumann's triangle:

$$\Upsilon_{12} \cdot \mathbf{t}_{12} + \Upsilon_{13} \cdot \mathbf{t}_{13} + \Upsilon_{23} \cdot \mathbf{t}_{23} = 0, \tag{6.3}$$

where Υ_{ij} and $\mathbf{t}_{ij}$ are the surface stress tensor and tangent vector of the interface between phases i and j, respectively.

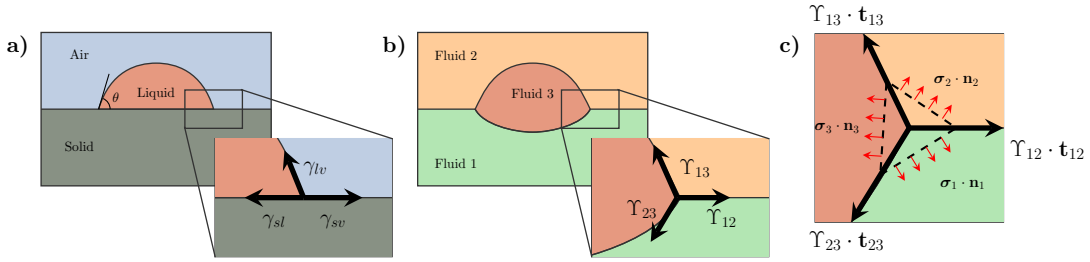

Figure 6.1: *a) Droplet interacting with a solid substrate: the contact angle θ depends on the surface energies and is given by the Young-Dupré law. b) Equilibrium shape of the interaction between three fluids where the contact line and the orientation of the three interfaces are determined by the force balance given by Neumann's triangle. c) Force balance on a small test volume around the contact line in the case of a soft solid substrate, where $\boldsymbol{\sigma}_{1,2,3}$ are the Cauchy stress tensors of the three phases. Reproduced from Style et al. [2017]*

Although Eqs. (6.2) and (6.3) effectively characterize fluid-solid and fluid-fluid interactions, researchers found that the wetting of soft solids was inadequately represented by either description and requires a unified description. This discrepancy arises because the surface tension of the liquid droplet exerts a capillary force strong enough to deform a soft substrate, creating a "wetting ridge" at the contact line. In these cases, the geometry of the contact line at the equilibrium can be obtained by a force balance around the triple point, as represented in Fig. 6.1c, that requires both surface stresses and bulk elasticity. Thus, we have the following balance equation

$$\int_{L_1} \boldsymbol{\sigma}_1 \cdot \mathbf{n}_1 \, dL + \int_{L_2} \boldsymbol{\sigma}_2 \cdot \mathbf{n}_2 \, dL + \int_{L_3} \boldsymbol{\sigma}_3 \cdot \mathbf{n}_3 \, dL + \Upsilon_{12} \cdot \mathbf{t}_{12} + \Upsilon_{13} \cdot \mathbf{t}_{13} + \Upsilon_{23} \cdot \mathbf{t}_{23} = 0. \tag{6.4}$$

Here, the first three terms represent the bulk elastic response (integrated over the boundary L_i of the i-th media's control volume), and the second three terms represent the capillary forces.

Consequently, the behavior of the system will be governed by the ratio between the characteristic size of the system R (which could be the radius of the droplet) and the elastocapillarity length $l = \gamma_{lv}/E$. If the substrate is sufficiently stiff ($R \gg l$), the deformation is negligible, and the contact angle follows the Young-Dupré law. Conversely, if the substrate is extremely soft ($R \ll l$), solid surface tension dominates bulk elasticity, and the contact line behaves like a fluid-fluid interface governed by Neumann's triangle. In the intermediate case of fluids interacting with soft substrates, as the one depicted in Figs. 6.1c and 6.2b, Style et al. [2013] demostrated that while the global droplet shape depends on its macroscopic size, the geometry of the wetting ridge is determined locally by elastocapillarity (Fig. 6.2a). Specifically, for large droplets where $R \gg l$, the wetting ridge shows a deformation negligible relative to the droplet size, resulting in an apparent contact angle consistent with rigid substrates. However, for microscopic droplets, with $R \ll l$, the soft solid exhibits a fluid-like behavior, with its shape dictated entirely by interfacial forces. This demonstrates a key principle of elastocapillarity: by simply altering the length scale R relative to the elastocapillarity length l, a soft solid can exhibit a range of behavior spanning from rigid-like to fluid-like.

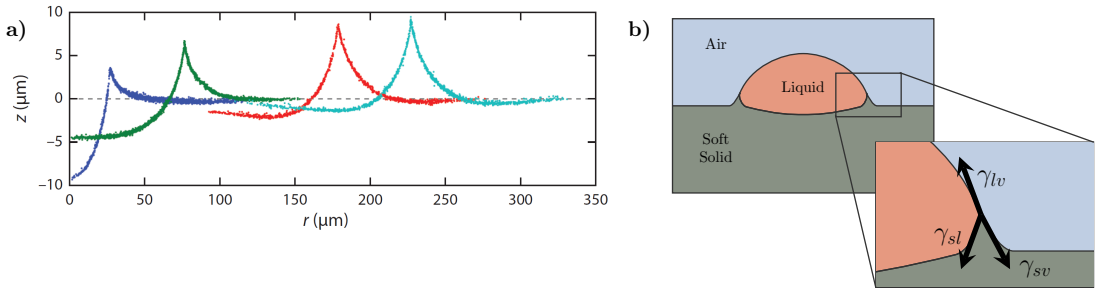

Figure 6.2: *a) Experimental data for glycerol droplets of different radii on a 50μm soft silicone gel substrate. b) Wetting of a droplet on a soft solid substrate. Reproduced with permission from Style et al. [2013]*

6.2 Onsager's variational formalism

In order to derive the equations behind the physics governing the interaction of an active tissue with an elastic matrix, we employ Onsager's variational formalism of irreversible thermodynamics. This emergent variational modeling framework is well-suited for the description of dissipative dynamics in soft matter and biological systems. It allows us to create complex models coupling multiple physics and guarantees the compliance with the second law of thermodynamics [Doi, 2011, 2015, Peletier, 2014, Arroyo et al., 2018]. Introduced by Onsager [1931], this principle is an extension of Rayleigh's least energy dissipation principle. It establishes a connection between the principle of microscopic reversibility and the symmetry properties of the evolution equation that regulate the macroscopic scale of irreversible processes. Despite the fact that Onsager's relation is typically used in the context of linear irreversible thermodynamics [Prigogine, 1967], it can be derived from a more general variational principle applicable to fully nonlinear

settings [Doi, 2011]. This characteristic allowed the application of this principle in a variety of different contexts spanning from study of hydrodynamics, such as in the immiscible two-phase flows [Qian et al., 2006, Xu and Qian, 2017], or in the diffusion and reaction-diffusion equation of multicomponent solutions [Doi, 2011, Wang et al., 2020], to biological frameworks, as in the lipid membrane dynamics [Arroyo and DeSimone, 2009, Rahimi and Arroyo, 2012, Peco et al., 2013], in the modelling of growth tissues [Ackermann and Ben Amar, 2023, Cicconofri et al., 2024], or in the study of nematic fluids [Mirza et al., 2025] or to the study of solid mechanics.

In Sec. 6.2.1 we introduce Onsager's variational principle through its application to a discrete dissipative system, and we show the differences with respect to the principle of least energy dissipation. This introduction provides the basic features of Onsager's variational principle, which will be formalized in Sec. 6.2.2 where an abstract statement about the principle is provided. The systematic way in which Onsager's principle allows us to derive the equations for complex systems will be employed throughout the chapter.

6.2.1 Onsager's variational principle for discrete dissipative systems

Since Onsager's variational principle extends Rayleigh's principle of least energy dissipation, we will initially present the latter in order to derive the former. Let us examine the movement of rigid particles in a viscous fluid [Doi, 2011]. Particularly, we examine particles that are subjected to potential forces, assuming that their motion occurs in an incompressible Stokes flow (i.e., in the limit of zero Reynolds number). Therefore, we can note with $X = (X_1, X_2, ..., X_n)$ the generalized coordinates describing the state of the particles where n is the number of degrees of freedom of our system. In this setting, the particles' motion is determined by imposing that the sum of the forces acting on them is zero. First of all, we have the generalized potential forces, acting on the particles, conjugate to X_i, induced by the potential energy $U(X)$

$$F_i = -\frac{\partial U(X)}{\partial X_i}. \tag{6.5}$$

Letting $\dot{X}_i$ be the generalized velocity, i.e., the rate at which the state of the particles changes, and recalling that on a particle moving in a Newtonian fluid experiences a frictional force, we can write the second kind of forces as

$$F_{Hi} = -\sum_j \xi_{ij}\dot{X}_j, \tag{6.6}$$

where ξ_{ij} are the frictional coefficients, which can be obtained by solving the equations in Stokesian hydrodynamics, and they lead to the so-called Lorentz reciprocal relation [Happel and Brenner, 1965]

$$\xi_{ij} = \xi_{ji}, \qquad \text{and} \qquad \sum_{i,j} \xi_{ij}\dot{X}_i\dot{X}_j \geq 0 \quad \text{for any } \dot{X}_i. \tag{6.7}$$

Thus, they are symmetric and positive definite.

The balances of forces are then

$$\sum_j \xi_{ij}\dot{X}_j = -\frac{\partial U(X)}{\partial X_i}, \tag{6.8}$$

from which we can obtain the time evolution equation for x_i

$$\dot{X}_i = -\sum_j \xi_{ij}^{-1} \frac{\partial U(X)}{\partial X_j}, \tag{6.9}$$

The friction coefficients ξ_{ij} and the potential U are both functions of x_i, as noted by Doi [2011]. Consequently, (6.9) is a nonlinear function in the generalized coordinates. The time evolution equation (6.8), can be cast into a variational principle using the reciprocal relation (6.7). In particular, we can define Φ as a quadratic function of $\dot{X}$ which represent the work that the particles exert on the fluid per unit time

$$\Phi = \sum_{i,j} \xi_{ij} \dot{X}_i \dot{X}_j, \tag{6.10}$$

and $\dot{U}$ as a linear function of $\dot{X}_i$ which is the rate of change of the potential energy

$$\dot{U} = \sum_i \frac{\partial U}{\partial X_i} \dot{X}_i. \tag{6.11}$$

Therefore, we can introduce the Rayleighian, defined as

$$\mathcal{R} = \mathcal{D} + \dot{U} = \frac{1}{2} \sum_{i,j} \xi_{ij} \dot{X}_i \dot{X}_j + \sum_i \frac{\partial U}{\partial X_i} \dot{X}_i \tag{6.12}$$

where $\mathcal{D} = 1/2\, \Phi$ is called energy dissipation function. From the principle of least energy dissipation, we can now obtain the force balance equation (6.8) from the stationarity of the Rayleighian with respect to $\dot{X}_i$

$$\frac{\partial \mathcal{R}}{\partial \dot{X}_i} = 0. \tag{6.13}$$

This is the hydrodynamic variational principle in its most general form. The reciprocity of ξ_{ij} and its positive definiteness are the cornerstones of this variational principle. These enable the construction of the strictly convex scalar function Φ, with the existence and uniqueness of the minimizer, ensuring stability.

The fundamental contribution of Onsager in this field allowed the extension of the above Rayleigh's principle to the study of irreversible processes. In particular, he noticed that the following form, which is referred to as Onsager's kinetic equation, can be utilized to represent a multitude of physics problems

$$\dot{X}_i = \sum_j L_{ij} \frac{\partial S(X)}{\partial X_j}. \tag{6.14}$$

This equation describes the evolution of the state of a system where x_i are the set of variables describing the non-equilibrium state of the system, $S(X)$ is the system entropy, and L_{ij} are the phenomenological kinetic coefficients. Taking advantage of the time-reversal symmetry, i.e., the microscopic reversibility, of microscopic fluctuations at equilibrium, Onsager [1931] proved the reciprocity of the phenomenological coefficients

$$L_{ij} = L_{ji}\,, \tag{6.15}$$

which enables the kinetic equation (6.14) to be expressed in the form of a variational principle, as is done in the principle of least energy dissipation. This leads to the so-called Onsager's variational principle, where the system's evolution is determined by the minimization of the following Rayleighian.

$$\tilde{\mathcal{R}} = \frac{1}{2}\sum_{i,j} L_{ij}^{-1}\dot{X}_i\dot{X}_j - \sum_i \frac{\partial S}{\partial X_i}\dot{X}_i. \tag{6.16}$$

In particular, the two terms represent half of the irreversible and the full reversible entropy changes of the system, respectively. Irreversible processes that evolve at a finite speed and subsequently dissipate energy, thereby creating entropy, are associated with the former. Conversely, quasi-static reversible processes are associated with the latter. In the case of an isothermal system, this principle reduces to the hydrodynamic variational principle, and the Rayleighian, which will be minimized, assumes the following form

$$\tilde{\mathcal{R}} = \mathcal{D} + \dot{\mathcal{F}} = \frac{1}{2}\sum_{i,j} \xi_{ij}\dot{X}_i\dot{X}_j + \sum_i \frac{\partial \mathcal{F}}{\partial X_i}\dot{X}_i\,, \tag{6.17}$$

where $\dot{\mathcal{F}}$ is the rate of change of the free energy $\mathcal{F}$ of the system. In the same fashion, Onsager's kinetic equation for an isothermal system becomes

$$\dot{X}_i = -\sum_j \xi_{ij}^{-1}\frac{\partial \mathcal{F}}{\partial X_j} \tag{6.18}$$

By examining the equations (6.12) and (6.17), it is evident that their structures are similar. However, they differ significantly in that in (6.17), x_i denotes general coordinates that specify the non-equilibrium state, and the potential energy U is replaced by the free energy $\mathcal{F}$.

Process variables

In many cases, the energy dissipation function $\mathcal{D}$ and the rate of change of the free energy $\dot{\mathcal{F}}$ are not easily obtained as a function of the time derivative of the state variable $\dot{X}_i$. In particular, the energy dissipation function $\mathcal{D}$ is easily expressed as a function of other variables v_i called process variables. These process variables are related to $\dot{X}_i$ through the so-called process operator $P(X)$ [Peletier, 2014] by means of the following expression:

$$\dot{X}_i = \sum_j P_{ij}V_j. \tag{6.19}$$

The matrix P_{ij} is not necessarily square; in fact, the number of process variables V_j may differ from the number of state variables X_i. Additionally, its coefficients may be a function of the state variables. Then the energy dissipation function can be written as

$$\mathcal{D} = \frac{1}{2}\sum_{i,j} \xi_{ij}V_iV_j. \tag{6.20}$$

Consequently, the Rayleighian is given by

$$\mathcal{R} = \frac{1}{2}\sum_{i,j} \xi_{ij}V_iV_j + \sum_{i,j}\frac{\partial \mathcal{F}}{\partial X_i}P_{ij}V_j \tag{6.21}$$

whose minimization gives

$$V_i = -\sum_{j,k} \xi_{ij}^{-1} \frac{\partial \mathcal{F}}{\partial X_k} P_{kj}. \tag{6.22}$$

Recalling the expression (6.19) involving the process operator, we can obtain the kinetic equations

$$\dot{X}_i = -\sum_j L_{ij} \frac{\partial \mathcal{F}}{\partial X_j} \qquad \text{where} \qquad L_{ij} = \sum_{l,k} P_{ik} P_{jl} \xi_{kl}^{-1} \tag{6.23}$$

The coefficients L_{ij} satisfy the reciprocal relation and the positive definiteness.

Constraints

If the process variables V_i are subjected to a set of constraints, we can still prove the fulfillment of the reciprocal relation. Given m constraints of the form

$$\sum_i C_i^{(p)} V_i = 0 \qquad p = 1, ..., m \tag{6.24}$$

we can include them in the Rayleighian

$$\mathcal{R} = \frac{1}{2} \sum_{i,j} \xi_{ij} V_i V_j + \sum_{i,j} \frac{\partial \mathcal{F}}{\partial X_i} P_{ij} V_j - \sum_p \lambda^{(p)} \sum_i C_i^{(p)} V_i \tag{6.25}$$

where $\lambda^{(p)}$ are Lagrange multipliers. The minimization of the above Rayleighian with respect to the process variables gives

$$V_j = -\sum_{m,k} \xi_{jk}^{-1} P_{mk} \frac{\partial \mathcal{F}}{\partial X_m} + \sum_{p,k} \lambda^{(p)} \xi_{jk}^{-1} C_k^{(p)}. \tag{6.26}$$

Plugging this expression inside (6.24) and solving for $\lambda^{(p)}$ gives us

$$\lambda^{(q)} = \sum_p (A^{-1})_{qp} \sum_m b_m^{(p)} \frac{\partial \mathcal{F}}{\partial X_m} \tag{6.27}$$

where we have defined

$$b_m^{(p)} = \sum_{i,k} P_{ij} \xi_{jk}^{-1} C_k^{(p)} \qquad A_{pq} = \sum_{i,j} C_i^{(p)} \xi_{ij}^{-1} C_j^{(q)}$$

Substituting back $\lambda^{(p)}$ into (6.26), and recalling (6.19) we can obtain the following kinetic coefficients

$$L_{ij} = \sum_{l,k} P_{ik} P_{jl} \xi_{kl}^{-1} - \sum_{p,q} b_i^{(p)} b_j^{(q)} (A^{-1})_{pq}. \tag{6.28}$$

We can finally infer that also in this case the kinetic coefficients satisfy the reciprocal relations.

6.2.2 Generalization of Onsager's principle

The Onsagers variational principle introduced in the previous section through its application to Stokes flow can be stated here in an abstract form [Peletier, 2014, Arroyo et al., 2018]. Objective of this section is to conceptualize the procedure outlined by Onsager's principle in order to apply it to more complex problems.

Maintaining the same notation of the previous section, we denote the state variables of the system as $X(t)$, the process variables as V, the system free energy as $\mathcal{F}(X)$, and a dissipation potential as $\mathcal{D}(V;X)$, where '$(V;X)$' means that the main dependence is on V but there may be some parametric dependence on X. We highlight here that $\mathcal{D}$ does not need to be quadratic in V [Edelen, 1972, Mielke et al., 2016], but it should satisfy the following thermodynamical requirements: $\mathcal{D}$ should be nonnegative, $\mathcal{D}(0,X)=0$, and it should be a convex function in V. In addition, we define the potential $\mathcal{W}(V;X)$ accounting for the externally supplied power such that $\mathcal{W}(V;X) = -F(X)V$ where $F(X)$ are external/active generalized forces. Analogously to the the last paragraph of the previous section, we also suppose that the process variables are linearly constrained by

$$\mathbb{C}(X)V = 0. \tag{6.29}$$

As stated in the previous section paragraph about the process operators, we have that the process variables V, may not be simply the time derivative of the state variables $\dot{X}$. For this reason, we related the two descriptions through a process operator which linearly act on the process variables.

$$\dot{X} = P(X)V. \tag{6.30}$$

In order to form the Rayleighian, we need to obtain the rate of change of the free energy $\dot{\mathcal{F}}$, which follows from the chain rule and from (6.30)

$$\dot{\mathcal{F}}(X,\partial_t X) = D\mathcal{F}(X)\,\partial_t X = D\mathcal{F}(X)\,P(X)V, \tag{6.31}$$

where $D\mathcal{F}(X)$ is the derivative of the free energy. We can form the Rayleighian as

$$\mathcal{R}(V;X) = D\mathcal{F}(X)\,P(X)V - F(X)V + \mathcal{D}(V;X). \tag{6.32}$$

Onsager's variational principle then asserts that the system will evolve such that

$$V = \underset{W}{\operatorname{argmin}}\,\mathcal{R}(W;X), \qquad \text{subjected to} \quad \mathbb{C}(X)W = 0. \tag{6.33}$$

This constrained dynamics, as seen in Sec. 6.2.1 leads to kinematic coefficients that satisfy the reciprocal relation and can be equivalently formulated as a stationary saddle point of the Lagrangian

$$\mathcal{L}(V,\Lambda;X) = D\mathcal{F}(X)\,P(X)\,V - F(X)\,V + \mathcal{D}(V;X) + \Lambda\cdot\mathbb{C}(X)\,V \tag{6.34}$$

where Λ are Lagrange multipliers. Once the process variables V are obtained from the minimization of the Lagrangian, we can finally recover the state variables $X(t)$ through the time integration of equation (6.30).

In order to demonstrate that Onsager's variational principle is thermodynamically consistent by construction, it is necessary to demonstrate that the first-order optimality condition guarantees energy conservation and the second-order optimality condition

guarantees non-negative entropy production. Let us examine the first-order optimality condition. The stationarity condition $\delta_\Lambda \mathcal{L} = 0$ results in $\mathbb{C}(X)V = 0$, while the stationarity condition $\delta_V \mathcal{L} = 0$ leads to the dynamical equilibrium equation

$$D\mathcal{F}(X)\, P(X) + D_V \mathcal{D}(V; X) - F(X) + \Lambda \cdot \mathbb{C}(X) = 0. \tag{6.35}$$

This equation establishes a balance between thermodynamic driving forces, dissipative forces, external/active forces, and constraint forces. This ensures the stability of the system at equilibrium, where all the forces balance out. Multiplying equation (6.35) by the actual V along the dissipative dynamics and rearranging the terms

$$D\mathcal{F}(X)\, P(X)V = -D_V \mathcal{D}(V; X)V + F(X)V - \Lambda \cdot \mathbb{C}(X)V. \tag{6.36}$$

We can now recall equations (6.31) and (6.24) to obtain the following energy balance, which relates the rate of change of the free energy, the power dissipated in irreversible processes, and the external/active power input

$$\dot{\mathcal{F}}(X) = -D_V \mathcal{D}(V; X)V + F(X)V. \tag{6.37}$$

After demonstrating that energy balance is guaranteed in the stationary condition, it is necessary to examine second-order optimality. The stationary point of the Rayleighian, in order to be a minimum, requires that the dissipation potential $\mathcal{D}(V; X)$ is convex in V. This implies that the first-order Taylor Expansion at any point is a global underestimator of the function. Recalling the requirement that $\mathcal{D}(0; X) = 0$ we obtain

$$0 = \mathcal{D}(0; X) \geq \mathcal{D}(V; X) + D_V \mathcal{D}(V; X)(0 - V), \tag{6.38}$$

recalling that $\mathcal{D}(V; X) \geq 0$ by assumption, we can obtain that

$$\mathcal{D}(V; X) \geq D_V \mathcal{D}(V; X)\, V \geq 0. \tag{6.39}$$

We can finally deduce that $\mathcal{D}$ is convex, and we acknowledge that the second inequality is an entropy production inequality for irreversible processes. Indeed, Eq. (6.39) along with Eq. (6.36), for a "homogeneous" system with $\mathcal{W}(V; X) = 0$, shows that

$$\dot{\mathcal{F}} \leq 0 \tag{6.40}$$

Therefore, due to the fact that the free energy decays along the dynamics, we can infer that $\mathcal{F}$ is a Lyapunov function of the dynamics. This shows that Onsager's principle is consistent with the second law of thermodynamics by construction as long as $\mathcal{D}$ it satisfies the requirements listed above. It is worth mentioning that the notion of stability fulfilled by Onsager's principle is stated in a fully non-linear setting without assuming a quadratic form of the dissipation potential. For quadratic dissipation potentials, we can simplify the above equations, observing that the power dissipated is twice the dissipation potential $D_V \mathcal{D}(V; X)\, V = 2\mathcal{D}(V; X)$.

In conclusion, this approach can be used to model irreversible processes where inertia can be neglected and the dissipative forces can be derived from a dissipation potential. Then, starting from the construction of the Rayleighian $\mathcal{R}$, obtained as a sum of elementary energetic and dissipative components, we can obtain the governing equation of the system by minimizing $\mathcal{R}$ with respect to the process variables. The variational approach generates a natural time discretization that can be used to create variational time integrators for computational purposes. Additionally, this method is not based upon the formulation of the strong form of the problem and can be easily discretized using finite elements.

6.3 Binary-fluid-solid interfacial mechanics

In this Section we present the mathematical formulation of the model for the study of the interaction of a binary fluid with an elastic matrix. The proposed formulation, based on Onsager's variational formalism of irreversible thermodynamics, will disregard the localized degradation at the tissue-elastic matrix interface, which will be introduced as an additional complexity in Sec. 6.3. The simplified model introduced in this Section will serve as a valuable tool for validating both the formulation and the numerical model. The results obtained will be compared with analytical results and experimental data found in literature in Secs. 6.6.1, 6.6.2, 6.6.3, and 6.6.4.

As previously stated in Chap. 5, the phenomena of wetting and elastocapillarity play a crucial role in biology. For this reason, with the proposed model, we aim to reproduce two types of problems illustrated in Figs. 6.3a and 6.3b, addressing the wetting of a tissue, intended as an active fluid droplet, on a rigid substrate and the elastocapillarity effect arising in the presence of a soft solid substrate, respectively. In particular, building upon the basic concepts of elastocapillarity introduced in Sec. 6.1, the active tissue as a droplet engulfing the fibrous extracellular matrix is studied through a key set of simplifying assumptions based on the fluid limit. We assume that the magnitude of the surface stress (Υ) is equal to the surface free energy per unit area (γ) for all fluid components. Crucially, we apply this same simplification, $\Upsilon = \gamma$, for the soft solid matrix at the solid-tissue interface and the solid-external medium interface for the purposes of this initial investigation. This approach inherently neglects the full complexity described by the Shuttleworth relation ($\Upsilon \neq \gamma$) for the solid, which provides the thermodynamic link between stress and strain on a solid surface. A rigorous extension of this model would involve relaxing this assumption and incorporating the full Shuttleworth relation for the solid matrix.

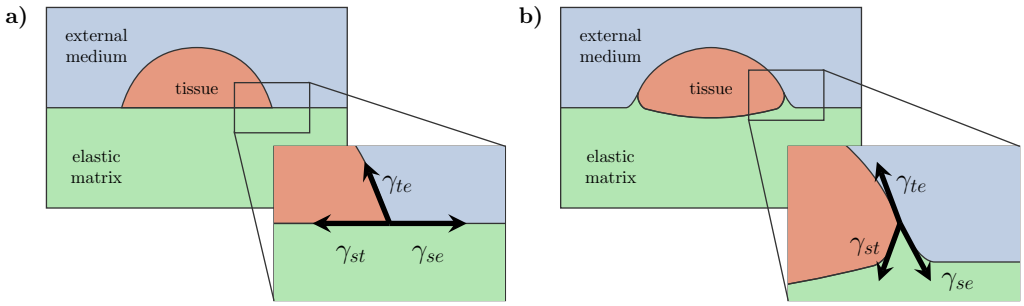

Figure 6.3: *a) Wetting of a tissue on a rigid substrate. b) Elastocapillarity effect arising in the interaction of the tissue with a soft substrate*

Because of the complexity and non-linearity of multi-phase fluid-structure interaction (FSI) problems, analytical solutions are challenging to derive and feasible only under strict simplifications [Style and Dufresne, 2012]. Consequently, numerical analysis must be utilized. To achieve this goal in the next Sections we are going to introduce the kinematics of the system, which will be subsequently framed into the Nitsche-Onsager variational formalism and finally, numerically solved through an immersed finite element method.

6.3.1 Kinematics without localized degradation

We consider the system depicted in Fig. 6.4 consisting of an elastic matrix symbolizing a substrate or an extracellular matrix, overlaid by a binary fluid, which in the context of biology can be seen as an active tissue such as an organoid surrounded by an external medium. In the reference configuration, the domains occupied by the binary fluid and the elastic matrix are $\Omega_f^{\mathrm{r}} \subset \mathbb{R}^3$ and $\Omega_{\mathrm{e}}^{\mathrm{r}} \subset \mathbb{R}^3$, respectively. Their generic deformed configuration at time $t > 0$, are denote as $\Omega_f(t) \subset \mathbb{R}^3$ for the fluids and $\Omega_{\mathrm{e}}(t) \subset \mathbb{R}^3$ for the elastic matrix domains. To tackle the binary nature of the fluid domain, we define a phase field order parameter $\phi_0(\mathbf{X})$ for $\mathbf{X} \in \Omega_f^{\mathrm{r}}$ and $\phi(\mathbf{x}, t)$ for $\mathbf{x} \in \Omega_f$ in the reference and deformed configurations, respectively. The ordering parameter smoothly varies across the interface Γ^{r} from $\phi_0 = -1$ inside the active tissue to $\phi_0 = 1$ in the external medium, as shown in the bottom part of Fig. 6.4. The interface between the two fluids is therefore approximated as a diffuse interface with a small finite thickness ε.

We describe the deformation of each of the two media by their corresponding deformation maps $\boldsymbol{\Psi}(\cdot, t) : \Omega_f^{\mathrm{r}} \to \Omega_f(t)$ and $\boldsymbol{\varphi}(\cdot, t) : \Omega_{\mathrm{e}}^{\mathrm{r}} \to \Omega_{\mathrm{e}}(t)$ We can introduce the

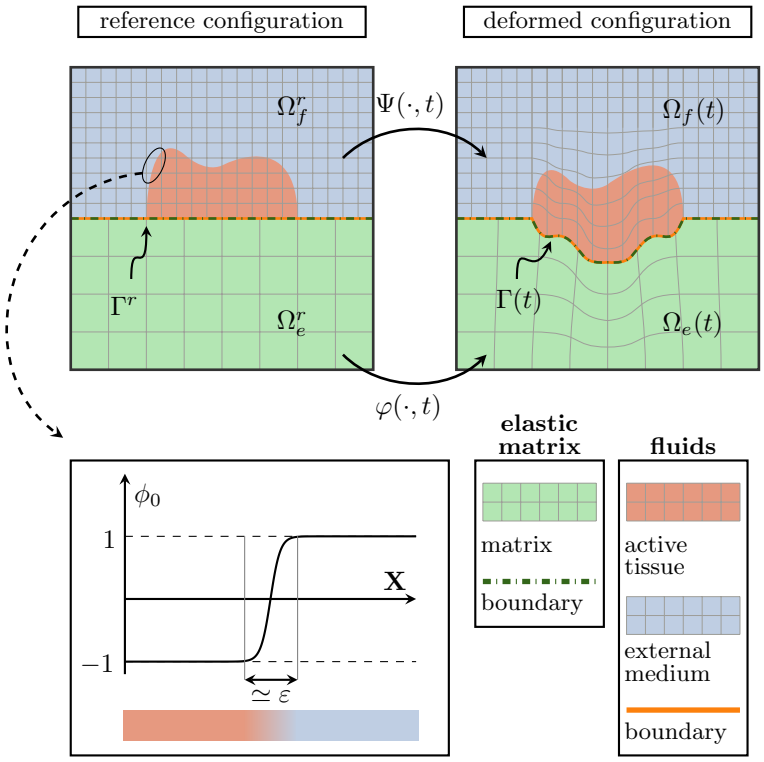

Figure 6.4: *Reference and deformed configuration of the binary-fluid-solid system. The reference binary-fluid and solid domains Ω_f^r and Ω_e^r are mapped by Ψ and φ into their deformed configurations $\Omega_f(t)$ and $\Omega_e(t)$, respectively. The binary fluid interface is obtained through a phase field approach where the order parameter in the reference configuration ϕ_0 is represented in the bottom part of the figure. The width of the interface is noted by ε*

Eulerian velocity of the external matrix as

$$\partial_t \boldsymbol{\varphi} \circ \boldsymbol{\varphi}^{-1}(\mathbf{x}, t) = \partial_t \boldsymbol{\varphi} \left(\boldsymbol{\varphi}^{-1}(\mathbf{x}, t), t \right) \qquad \text{for } \mathbf{x} \in \Omega_{\mathrm{e}}(t), \tag{6.41}$$

and of the binary fluid, for which we introduce the symbol $\mathbf{v}$

$$\mathbf{v}(\mathbf{x}, t) = \partial_t \Psi \circ \Psi^{-1}(\mathbf{x}, t) = \partial_t \Psi \left(\Psi^{-1}(\mathbf{x}, t), t \right) \qquad \text{for } \mathbf{x} \in \Omega_f(t). \tag{6.42}$$

The interface in the reference configuration, hence at $t = 0$, can be defined as $\Gamma^{\mathrm{r}} = \Gamma(0) = \partial\Omega_f^{\mathrm{r}} = \partial\Omega_{\mathrm{e}}^{\mathrm{r}}$. Assuming a no-gap, no-overlap condition at the interface between the two domains, we have that the mappings of the interface Γ^{r} between the two domains must coincide; therefore,

$$\Gamma(t) = \Psi(\Gamma^{\mathrm{r}}, t) = \boldsymbol{\varphi}(\Gamma^{\mathrm{r}}, t). \tag{6.43}$$

The no-gap no-overlap condition, stated by Eq. (6.43), is weaker than the no-slip condition, which requires the continuity of the velocity of the particle at the interface. Indeed, it imposes only the continuity of the normal component of the velocity at the interface between the two media. If we take $\boldsymbol{\gamma}^{\mathrm{r}}(\mathbf{s})$ to be a parametrization of the interface Γ^{r} with $\mathbf{s}$ parametric coordinates, then Eq. (6.43) imposes that $\Psi \circ \boldsymbol{\gamma}^{\mathrm{r}}$ and $\boldsymbol{\varphi} \circ \boldsymbol{\gamma}^{\mathrm{r}}$ are parametrizations of the deformed interface $\Gamma(t)$. This implies that for any $\boldsymbol{x} \in \Gamma(t)$ there exist two distinct parametric coordinates $\boldsymbol{s}$ and $\boldsymbol{s}^*$ in the parametrized reference surface $\boldsymbol{\gamma}^{\mathrm{r}}$ such that

$$\boldsymbol{x} = \Psi(\boldsymbol{\gamma}^{\mathrm{r}}(\boldsymbol{s}), t) = \boldsymbol{\varphi}(\boldsymbol{\gamma}^{\mathrm{r}}(\boldsymbol{s}^*), t). \tag{6.44}$$

The relation between the two parametric coordinates $\boldsymbol{s}$ and $\boldsymbol{s}^*$ may be time dependent, $\mathbf{s}^* = \boldsymbol{\xi}(\mathbf{s}, t)$ which implies that the time derivative of Eq. (6.44), using the chain rule, can be cast as

$$\mathbf{v}(\boldsymbol{x}, t) = \partial_t \boldsymbol{\varphi} \circ \boldsymbol{\varphi}^{-1}(\mathbf{x}, t) + D\boldsymbol{\varphi}(\boldsymbol{\gamma}^{\mathrm{r}}(\boldsymbol{s}^*), t) D\boldsymbol{\gamma}^{\mathrm{r}}(\boldsymbol{s}^*) \partial_t \boldsymbol{\xi}(\mathbf{s}, t), \tag{6.45}$$

where we used the symbol D to denote the derivative of the maps between points in space. The second term of the right-hand side is tangential to Γ as a consequence of the fact that $D\boldsymbol{\gamma}^{\mathrm{r}}(\boldsymbol{s}^*)\partial_t \boldsymbol{\xi}(\mathbf{s}, t)$ is tangential to Γ^{r}. Therefore, if we multiply Eq. (6.45) by the normal to the interface $\mathbf{n}(\mathbf{x}, t)$ pointing towards $\Omega_{\mathrm{e}}(t)$, we obtain that over $\Gamma(t)$

$$\mathbf{n} \cdot (\mathbf{v} - \partial_t \boldsymbol{\varphi} \circ \varphi^{-1}) = 0. \tag{6.46}$$

In conclusion, this suggests that we have continuity of the normal component of the velocity at the interface. For what concerns instead the tangential component, we have that the relative tangential motion between the two domains is allowed and leads to the definition of the slip interfacial velocity as

$$\mathbf{v}^{\parallel} = \boldsymbol{\Pi}(\mathbf{v} - \partial_t \boldsymbol{\varphi} \circ \boldsymbol{\varphi}^{-1}) \tag{6.47}$$

where $\boldsymbol{\Pi} = \mathbf{I} - \mathbf{n}(\mathbf{x}, t) \otimes \mathbf{n}(\mathbf{x}, t)$ is the projection tensor on the tangent plane on $\Gamma(t)$, and $\mathbf{I}$ is the identity tensor.

6.3.2 Onsager's variational formulation

To describe the dynamics of sessile droplets on a substrate, we adopt Onsager's variational formalism of irreversible thermodynamics. Therefore, the time evolution of the system follows from the minimization of the Rayleighian functional. In the present formulation, the state variables are the deformation map of the elastic matrix $\boldsymbol{\varphi}$, the position of the interface $\Gamma(t)$ and the phase field ϕ. The process variables, characterizing the evolution of the system and with respect to which the problem must be minimized, are the velocity of the elastic matrix $\partial_t\boldsymbol{\varphi}$, the fluid velocity $\mathbf{v}$, and the sliding velocity $\mathbf{v}^{\parallel}$. Therefore, in order to apply Onsager's principle, we need to identify the expressions of the free energies, dissipation potentials, and power inputs involved in the problem in terms of the defined state and process variables.

Free energies

The free energy of the elastic matrix domain is given by the sum of the elastic energy of the matrix and the surface energy of the binary-fluid-solid interface

$$\mathcal{F}_{\mathrm{e}}[\boldsymbol{\varphi},\Gamma,\phi] = \int_{\Omega_{\mathrm{e}}^{\mathrm{r}}} W(\nabla_{\mathrm{r}}\boldsymbol{\varphi})dV_{\mathrm{r}} + \int_{\Gamma(t)} T(\phi)dS, \tag{6.48}$$

where ∇_{r} represents the differentiation with respect to the reference domain coordinates, $W(\nabla_{\mathrm{r}}\boldsymbol{\varphi})$ is the strain energy density of the hyperelastic solid matrix, $\nabla_r\boldsymbol{\varphi}$ is the deformation gradient, and T is the surface tension between the fluids and the solid. Due to the multiphase nature of the fluid domain, the surface tension is a function of the phase field, defined as $T = T(\phi) = {}^{(1-\phi)}/_{2}\,\gamma_{st} + {}^{(1+\phi)}/_{2}\,\gamma_{se}$.

Another energetic contribution to the free energy of the system is given by the free energy of the phase field, which is given by a Landau functional [Du et al., 2004, Wang, 2005]

$$\mathcal{F}_{\phi}[\phi] = \int_{\Omega_f} \frac{3}{2\sqrt{2}}\sigma\left(\frac{1}{4\epsilon}(\phi^2-1)^2 + \frac{\epsilon}{2}\left|\nabla\phi\right|^2\right)dV\,, \tag{6.49}$$

where ∇ represents the differentiation with respect to the spatial (current) domain coordinates, ϵ is the thickness of the interface and $\sigma = \gamma_{te}$ is the interfacial energy per unit area, which in the present study represents the surface tension between the active fluid and the external medium. In particular, the first term of this functional is the classical double-well potential and the second one is the interfacial energy, which penalizes sharp changes in ϕ.

Then the total free energy of the system is given by

$$\mathcal{F}[\boldsymbol{\varphi},\boldsymbol{\psi},\Gamma] = \mathcal{F}_{\mathrm{e}}[\boldsymbol{\varphi},\Gamma,\phi] + \mathcal{F}_{\phi}[\phi] \tag{6.50}$$

Dissipation potential

The dissipation mechanisms taken into account are the viscous dissipations that take place in the active tissue and the external medium, as well as the dissipation associated with the relative motion of the fluid and the solid due to the slip interfacial velocity. The dissipation potential adopted is thus

$$\mathcal{D}_f[\mathbf{v},\mathbf{v}^{\parallel}] = \frac{\mu(\phi)}{4}\int_{\Omega_f}\left|\nabla\mathbf{v}+\nabla\mathbf{v}^{\mathrm{T}}\right|^2 dV + \int_{\Gamma} d\left(\mathbf{v}^{\parallel}\right)dS \tag{6.51}$$

where $\mu(\phi)$ is the viscosity of the fluid domain, which depends linearly on the phase field order parameter $\mu(\phi) = {}^{(1-\phi)}/_{2}\mu_{\mathrm{t}} + {}^{(1+\phi)}/_{2}\mu_{\mathrm{e}}$ with μ_{t} and μ_{e} viscosities of the tissue and external medium, respectively. Furthermore, in Eq. (6.51), we have that $d\left(\mathbf{v}^{\parallel}\right)$ is the dissipation density per unit interface area for which we consider a quadratic potential of the form

$$d\left(\mathbf{v}^{\parallel}\right) = \frac{\xi^{\parallel}}{2}\left|\mathbf{v}^{\parallel}\right|^{2} \tag{6.52}$$

where $\xi^{\parallel}$ is the parallel friction coefficient.

We disregard for now viscous or poroelastic dissipations that may occur in the external matrix, which can be considered in the future advancement of the current model.

Power input

In the absence of body forces or external forces, we assume that the activity of the system is restricted to the interface and can be introduced in the formulation through the power input functional

$$\mathcal{W}[\mathbf{v}^{\parallel}] = -\int_{\Gamma} \mathbf{f}_{a}^{\parallel} \cdot \mathbf{v}^{\parallel} dS \tag{6.53}$$

where $\mathbf{f}_{a}^{\parallel}$ represents an active force inducing tangential slip, which can be understood as an active crawling force applied by the tissue in order to glide or rotate over a substrate [Palamidessi et al., 2019].

Constraints

Finally, we introduce a constraint functional to impose the incompressibility of the fluids and the jump in the parallel component of the velocity at the solid-fluids interface, which is given by

$$\mathcal{C}[\partial_t\boldsymbol{\varphi}, \mathbf{v}, \mathbf{v}^{\parallel}] = -\int_{\Omega_f} p(\nabla \cdot \mathbf{v}) dV - \int_{\Gamma} \boldsymbol{\lambda} \cdot \left[\boldsymbol{\Pi}\left(\mathbf{v} - \frac{\partial \boldsymbol{\varphi}}{\partial t}\right) - \mathbf{v}^{\parallel}\right] dS \tag{6.54}$$

where p and $\boldsymbol{\lambda}$ are Lagrange multipliers.

Rayleighian and Lagrangian

Onsager's variational formalism, employed to obtain the dissipative dynamics of a sessile droplet interacting with a substrate, as elucidated in Section 6.2, requires the formation of the Rayleighian as the sum of the rate of change of the free energies, the dissipation potentials, and the power input functional as follows:

$$\mathcal{R}[\partial_t\boldsymbol{\varphi}, \mathbf{v}, \mathbf{v}^{\parallel}] = \frac{d}{dt}\mathcal{F}_{\mathrm{e}}[\partial_t\boldsymbol{\varphi}, \mathbf{v}] + \frac{d}{dt}\mathcal{F}_{\phi}[\mathbf{v}] + \mathcal{D}_f[\mathbf{v}, \mathbf{v}^{\parallel}] + \mathcal{W}[\mathbf{v}^{\parallel}]. \tag{6.55}$$

The governing equations can thus be obtained from the minimization of the Rayleigh functional subjected to the constraints defined by the constrain functional $\mathcal{C}[\partial_t\boldsymbol{\varphi}, \mathbf{v}, \mathbf{v}^{\parallel}]$. In conclusion, the dynamic of the system can be obtained by extremizing the Lagrangian

$$\mathcal{L}[\partial_t\boldsymbol{\varphi}, \mathbf{v}, \mathbf{v}^{\parallel}, p, \boldsymbol{\lambda}] = \mathcal{R}[\partial_t\boldsymbol{\varphi}, \mathbf{v}, \mathbf{v}^{\parallel}] + \mathcal{C}[\partial_t\boldsymbol{\varphi}, \mathbf{v}, \mathbf{v}^{\parallel}, p, \boldsymbol{\lambda}] \tag{6.56}$$

6.3.3 Variational derivation of the governing equations

In order to determine the constrained dynamics of the system, requiring the stationarity of the Lagrangian specified in Eq. (6.56), it is essential to derive the rate of change of the free energies of the elastic matrix, the surface energy of the binary-fluid-solid interface, and the phase field.

Rate of change of the free energies

Starting from the rate of change of the free energy of the elastic matrix given by the first term of Eq. (6.48), and applying the chain rule, we obtain

$$\frac{d}{dt}\int_{\Omega_{\mathrm{e}}^{\mathrm{r}}} W(\nabla_{\mathrm{r}}\boldsymbol{\varphi})dV_r = \int_{\Omega_{\mathrm{e}}^{\mathrm{r}}} \partial_t W(\nabla_{\mathrm{r}}\boldsymbol{\varphi})dV_{\mathrm{r}} = \int_{\Omega_{\mathrm{e}}^{\mathrm{r}}} \mathbf{P}_{\mathrm{e}} : \nabla_{\mathrm{r}}\,\partial_t\boldsymbol{\varphi}\,dV_{\mathrm{r}} \tag{6.57}$$

where $\mathbf{P}_{\mathrm{e}}$ is the first Piola-Kirchhoff stress tensor. Integrating by parts,

$$\frac{d}{dt}\int_{\Omega_{\mathrm{e}}^{\mathrm{r}}} W(\nabla_{\mathrm{r}}\boldsymbol{\varphi})dV_r = -\int_{\partial\Omega_{\mathrm{e}}^{\mathrm{r}}} \left(\mathbf{P}_{\mathrm{e}}^T\,\partial_t\boldsymbol{\varphi}\right)\cdot\mathbf{n}_r\,dS_{\mathrm{r}} - \int_{\Omega_{\mathrm{e}}^{\mathrm{r}}} (\nabla_r\cdot\mathbf{P}_{\mathrm{e}})\cdot\,\partial_t\boldsymbol{\varphi}\,dV_{\mathrm{r}} \tag{6.58}$$

where the minus sign in the first term comes from the fact that the normal $\mathbf{n}^{\mathrm{r}}$ points inside the $\Omega_{\mathrm{e}}^{\mathrm{r}}$. Recalling that $\mathbf{P}_{\mathrm{e}} = J\boldsymbol{\sigma}_{\mathrm{e}}\mathbf{F}^{-T}$, the identity $\nabla_r\cdot\mathbf{P}_{\mathrm{e}} = J\nabla\cdot\boldsymbol{\sigma}_{\mathrm{e}}$, and Nanson's formula $\mathbf{n}dS = J\mathbf{F}^{-T}\mathbf{n}_r\,dS_r$ we obtain

$$\frac{d}{dt}\int_{\Omega_{\mathrm{e}}^{\mathrm{r}}} W(\nabla_{\mathrm{r}}\boldsymbol{\varphi})dV_r = -\int_{\partial\Omega_{\mathrm{e}}^{\mathrm{r}}} \left(J\mathbf{F}^{-1}\boldsymbol{\sigma}_{\mathrm{e}}\,\partial_t\boldsymbol{\varphi}\right)\cdot\mathbf{n}_r\,dS_{\mathrm{r}} - \int_{\Omega_{\mathrm{e}}^{\mathrm{r}}} J(\nabla\cdot\boldsymbol{\sigma}_{\mathrm{e}})\cdot\,\partial_t\boldsymbol{\varphi}\,dV_{\mathrm{r}}. \tag{6.59}$$

Writing all the integrals in the spatial configuration gives us the final expression for the rate of change of the free energy

$$\frac{d}{dt}\int_{\Omega_{\mathrm{e}}^{\mathrm{r}}} W(\nabla_{\mathrm{r}}\boldsymbol{\varphi})dV_r = -\int_{\Gamma(t)} \partial_t\boldsymbol{\varphi}\circ\boldsymbol{\varphi}^{-1}\cdot\boldsymbol{\sigma}_{\mathrm{e}}\mathbf{n}\,dS - \int_{\Omega_{\mathrm{e}}(t)} (\nabla\cdot\boldsymbol{\sigma}_{\mathrm{e}})\cdot\partial_t\boldsymbol{\varphi}\circ\boldsymbol{\varphi}^{-1}\,dV. \tag{6.60}$$

In order to determine the rate of change of surface energy at the binary-fluid-solid interface, we apply the integration by parts formula on the surface, as discussed in Finn [1986], we recover the contributions of the variable surface tension and the curvature,

$$\frac{d}{dt}\int_{\Gamma(t)} T(\phi)dS = \int_{\Gamma(t)} \left(\nabla_\Gamma T\cdot\mathbf{v} + 2HT(\mathbf{v}\cdot\mathbf{n})\right)dS, \tag{6.61}$$

where H is the mean curvature and $\nabla_\Gamma(\bullet) = \nabla(\bullet) - \mathbf{n}(\mathbf{n}\cdot\nabla(\bullet))$ is the spatial gradient ∇ projected onto the tangential plane to Γ. The first term corresponds to the Marangoni force tangential to the interface and the second one to the Laplace pressure acting normal to it.

Ultimately, regarding the rate of change of the phase-field free energy, we recall that the phase field is advected in accordance with the kinetic condition:

$$\frac{\partial\phi}{\partial t} = -\mathbf{v}\cdot\nabla\phi. \tag{6.62}$$

The rate of change of the phase field free energy is given by the time derivative of the integral over the moving domain $\Omega_f(t)$

$$\frac{d}{dt}\mathcal{F}_\phi = \frac{d}{dt}\int_{\Omega_f(t)} \frac{3}{2\sqrt{2}}\sigma\left(\frac{1}{4\epsilon}(\phi^2-1)^2 + \frac{\epsilon}{2}\left|\nabla\phi\right|^2\right)dV = \frac{d}{dt}\int_{\Omega_f(t)} f_\phi\,dV, \tag{6.63}$$

where we denoted the energy density integrand as f_ϕ. Applying the Reynolds transport theorem, we obtain

$$\frac{d}{dt}\mathcal{F}_\phi = \int_{\Gamma(t)} f_\phi \mathbf{v}\cdot\mathbf{n} dS + \int_{\Omega_f(t)} \frac{\delta f_\phi}{\delta\phi}\frac{\partial\phi}{\partial t}\, dV. \tag{6.64}$$

The variational derivative in the second term corresponds to the chemical potential $\hat{\mu}$, which using the Euler-Lagrange operator, can be expressed as

$$\hat{\mu} = \frac{\delta\mathcal{F}_\phi}{\delta\phi} = \frac{\partial f_\phi}{\partial\phi} - \nabla\cdot\left(\frac{\partial f_\phi}{\partial(\nabla\phi)}\right) = \frac{3}{2\sqrt{2}}\sigma\left(\frac{1}{\epsilon}\phi(\phi^2-1) - \epsilon\nabla^2\phi\right) \tag{6.65}$$

By substituting this equation into (6.64) and invoking the kinematic condition (6.62), we derive the final form for the rate of change of the phase-field free energy

$$\frac{d}{dt}\mathcal{F}_\phi[\mathbf{v}] = \int_{\Gamma(t)} f_\phi \mathbf{v}\cdot\mathbf{n} dS - \int_{\Omega_f(t)} \hat{\mu}\nabla\phi\cdot\mathbf{v}\, dV. \tag{6.66}$$

Governing equations

Gathering all the terms of the Lagrangian together, we have

$$\begin{aligned}\mathcal{L}\left[\partial_t\boldsymbol{\varphi}, \mathbf{v}, \mathbf{v}^{\parallel}, p, \boldsymbol{\lambda}\right] =& \frac{d}{dt}\mathcal{F}_e\left[\partial_t\boldsymbol{\varphi}, \mathbf{v}\right] + \frac{d}{dt}\mathcal{F}_\phi\left[\mathbf{v}\right] + \mathcal{D}_f\left[\mathbf{v}, \mathbf{v}^{\parallel}\right] \\ &+ \mathcal{W}\left[\mathbf{v}^{\parallel}\right] + \mathcal{C}\left[\partial_t\boldsymbol{\varphi}, \mathbf{v}, \mathbf{v}^{\parallel}, p, \boldsymbol{\lambda}\right].\end{aligned} \tag{6.67}$$

Dropping the dependency of the Lagrangian and exploiting the complete form of all associated terms yields

$$\begin{aligned}\mathcal{L} =& -\int_{\Gamma(t)} \partial_t\boldsymbol{\varphi}\cdot\boldsymbol{\sigma}_{\mathrm{e}}\mathbf{n}\, dS - \int_{\Omega_{\mathrm{e}}(t)} (\nabla\cdot\boldsymbol{\sigma}_{\mathrm{e}})\cdot\partial_t\boldsymbol{\varphi}\, dV \\ &+ \int_{\Gamma(t)} (\nabla_\Gamma T\cdot\mathbf{v} + 2HT(\mathbf{v}\cdot\mathbf{n}))\, dS + \int_{\Gamma(t)} f_\phi\mathbf{v}\cdot\mathbf{n} dS \\ &- \int_{\Omega_f(t)} \hat{\mu}\nabla\phi\cdot\mathbf{v}\, dV + \frac{\mu(\phi)}{4}\int_{\Omega_f(t)} \left|\nabla\mathbf{v} + \nabla\mathbf{v}^{\mathrm{T}}\right|^2 dV \\ &+ \int_{\Gamma(t)} \frac{\xi^{\parallel}}{2}\left|\mathbf{v}^{\parallel}\right|^2 dS - \int_{\Gamma(t)} \mathbf{f}_a^{\parallel}\cdot\mathbf{v}^{\parallel}\, dS - \int_{\Omega_f(t)} p(\nabla\cdot\mathbf{v})\, dV \\ &- \int_{\Gamma(t)} \boldsymbol{\lambda}\cdot\left[(\mathbf{v} - \partial_t\boldsymbol{\varphi}) - \mathbf{v}^{\parallel}\right] dS.\end{aligned} \tag{6.68}$$

Stationarity of the Lagrangian (6.68) with respect to $\partial_t\boldsymbol{\varphi}$ leads to the balance of linear momentum in the bulk $\Omega_e(t)$

$$\nabla\cdot\boldsymbol{\sigma}_e = 0 \qquad \text{in } \Omega_e(t), \tag{6.69}$$

and to the condition

$$-\boldsymbol{\sigma}_e\mathbf{n} + \boldsymbol{\lambda} = 0 \qquad \text{on } \Gamma(t). \tag{6.70}$$

Stationarity with respect to $\mathbf{v}$ leads to the balance of linear momentum in the bulk $\Omega_f(t)$

$$\nabla\cdot\boldsymbol{\sigma}_f + \hat{\mu}\nabla\phi = 0 \qquad \text{in } \Omega_f(t), \tag{6.71}$$

where $\boldsymbol{\sigma}_f = \mu(\nabla\mathbf{v} + \nabla\mathbf{v}^T) - p\mathbf{I}$ and to the condition

$$\boldsymbol{\sigma}_f\mathbf{n} - \boldsymbol{\lambda} + f_\phi\mathbf{n} + \nabla_\Gamma T(\phi) + 2T(\phi)H\mathbf{n} = 0 \qquad \text{on } \Gamma(t). \tag{6.72}$$

Adding Eqs. (6.70) and (6.72) lead to the force balance at the interface

$$\boldsymbol{\sigma}_e\mathbf{n} - \boldsymbol{\sigma}_f\mathbf{n} = f_\phi\mathbf{n} + \nabla_\Gamma T(\phi) + 2T(\phi)H\mathbf{n} \qquad \text{on } \Gamma(t), \tag{6.73}$$

which states that the jump in the traction across the interface is balanced by the capillary force arising from wetting gradients and from the phase-field energy density.

Stationarity with respect to $\mathbf{v}^{\|}$ leads to

$$\boldsymbol{\Pi}\boldsymbol{\sigma}_f\mathbf{n} + \nabla_\Gamma T(\phi) = \boldsymbol{\Pi}\boldsymbol{\sigma}_e\mathbf{n} = -\xi^{\|}\mathbf{v}^{\|} + \mathbf{f}_a^{\|} \qquad \text{on } \Gamma(t), \tag{6.74}$$

which express the force balance tangential to the interface.

6.4 Binary-fluid-solid interfacial mechanics: degradation

Analogous to the scenario presented in Sec. 6.3.1, we examine the system illustrated in Fig. 6.5, comprising an elastic matrix representing a substrate or extracellular matrix, overlaid by a binary fluid, which, in a biological context, may be interpreted as an active tissue, such as an organoid, enveloped by an external medium. In this case, we want to take into account the possibility of the active tissue degrading the substrate. In order to describe the kinematics of this degradation, we considered the reference configuration of the elastic matrix domain as time-dependent. This assumption carries the idea that the set of reference material particles is changing during the evolution of the system [Ateshian, 2007, Garikipati, 2009]. The results of the competition between the degradation and the indentation will be shown in Sec. 6.6.5.

6.4.1 Kinematics with localized degradation

In accordance with the notation established in Sec. 6.3.1, we will restate similar terminology here for convenience. The reference domain occupied by the binary fluid is denoted by $\Omega_f^{\mathrm{r}} \subset \mathbb{R}^3$. Conversely, the reference domain occupied by the external matrix may exhibit localized degradation at the matrixtissue interface and thus be denoted by $\Omega_{\mathrm{e}}^{\mathrm{r}}(t) \subset \mathbb{R}^3$. The deformed domains occupied by the binary fluid and the elastic matrix are denoted by $\Omega_f(t) \subset \mathbb{R}^3$ and $\Omega_{\mathrm{e}}(t) \subset \mathbb{R}^3$, respectively. The binary nature of the fluid domain is achieved by employing a phase field with an order parameter ranging between -1 and 1 while moving from the active tissue to the external medium, as illustrated in Fig. 6.5. Specifically, we have $\phi_0(\mathbf{X})$ for $\mathbf{X} \in \Omega_f^{\mathrm{r}}$ and $\phi(\mathbf{x}, t)$ for $\mathbf{x} \in \Omega_f$ in the reference and deformed configurations, respectively. The interface between the two fluids is therefore approximated as a diffuse interface with a small finite thickness ε.

We describe the deformation of each of the two media by their corresponding deformation maps $\Psi(\cdot, t) : \Omega_f^{\mathrm{r}} \to \Omega_f(t)$ and $\varphi(\cdot, t) : \Omega_{\mathrm{e}}^{\mathrm{r}}(t) \to \Omega_{\mathrm{e}}(t)$

In the case of degradation, $\partial\Omega_{\mathrm{e}}^{\mathrm{r}}(t)$ and $\partial\Omega_f^{\mathrm{r}}$ do not coincide for $t > 0$, hence making the definition Γ^{r} presented in Sec. 6.3.1 inaccurate. Resorting to the no-gap no-overlap condition, we can still define the actual interface $\Gamma(t)$ as

$$\Gamma(t) = \partial\Omega_f(t) = \partial\Omega_{\mathrm{e}}(t), \tag{6.75}$$

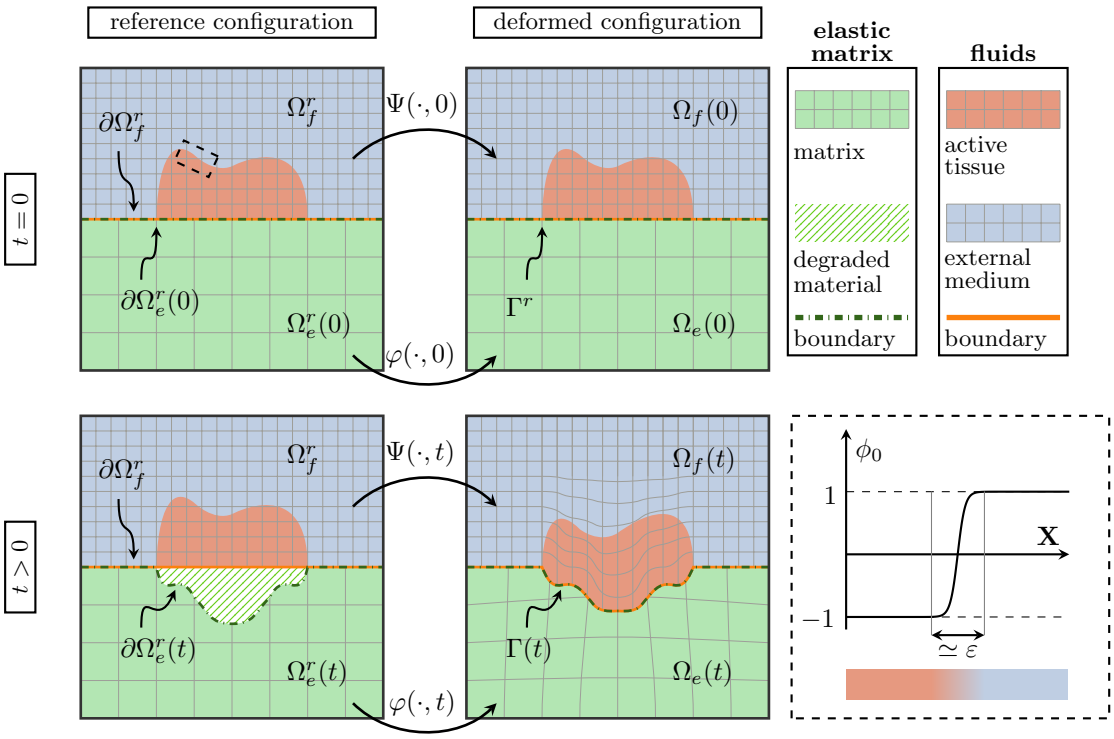

Figure 6.5: *Reference and deformed configuration of the binary-fluid-solid system with degradation of the elastic matrix. The reference binary-fluid Ω_f^r and solid $\Omega_e^r(t)$ domains are mapped by Ψ and φ into their deformed configurations $\Omega_f(t)$ and $\Omega_e(t)$, respectively. The binary fluid interface is obtained through a phase field approach where the order parameter in the reference configuration ϕ_0 is represented in the bottom right part of the figure. The width of the interface is noted by ε*

and by continuity of the deformation maps we can infer that

$$\Gamma(t) = \boldsymbol{\psi}(\partial\Omega_f^{\mathrm{r}}, t) = \boldsymbol{\varphi}(\partial\Omega_{\mathrm{e}}^{\mathrm{r}}(t), t). \tag{6.76}$$

If we define a parametrization $\boldsymbol{\gamma}_f^{\mathrm{r}}(\mathbf{s})$ of the fixed surface $\partial\Omega_f^{\mathrm{r}}$, we have that the mapping of this parametrization $\boldsymbol{\psi}(\boldsymbol{\gamma}_f^{\mathrm{r}}(\mathbf{s}), t)$ is a parametrization of the deformed interface $\Gamma(t)$, which turns out to be a material interface for the binary-fluid domain. We can thus note the normal component of the velocity of this material surface as

$$v_\Gamma = \mathbf{n} \cdot \mathbf{v}. \tag{6.77}$$

On the other hand, if we introduce a parametrization of the surface $\partial\Omega_{\mathrm{e}}^{\mathrm{r}}(t)$ that is time-dependent, it also will be time-dependent $\boldsymbol{\gamma}_{\mathrm{e}}^{\mathrm{r}}(\mathbf{s}, t)$. Recalling Eq. (6.76) we can inferred that a parametrization of the deformed configuration can be expressed as

$$\boldsymbol{\gamma}(\mathbf{s}, t) = \boldsymbol{\psi}(\boldsymbol{\gamma}_f^{\mathrm{r}}(\mathbf{s}), t) = \boldsymbol{\varphi}(\boldsymbol{\gamma}_{\mathrm{e}}^{\mathrm{r}}(\mathbf{s}, t), t). \tag{6.78}$$

Applying the chain rule, we obtain again the normal component of the velocity of the interface as

$$v_\Gamma(\mathbf{x}, t) = \mathbf{n}(\mathbf{x}, t) \cdot \partial_t \boldsymbol{\gamma}(\mathbf{s}, t) = \mathbf{n}(\mathbf{x}, t) \cdot \left[D\boldsymbol{\varphi}(\mathbf{x}^{\mathrm{r}}, t)\, \partial_t \boldsymbol{\gamma}_{\mathrm{e}}^{\mathrm{r}}(\mathbf{s}, t) + \partial_t \boldsymbol{\varphi}(\mathbf{x}^{\mathrm{r}}, t) \right], \tag{6.79}$$

where $\mathbf{x} = \boldsymbol{\gamma}(\mathbf{s}, t)$ and $\mathbf{x}^{\mathrm{r}} = \boldsymbol{\gamma}_{\mathrm{e}}^{\mathrm{r}}(\mathbf{s}, t)$. If we know combine the two equation for v_Γ, we find that the normal component of the velocity of the material particles at the interface is discontinuous

$$\mathbf{n}(\mathbf{x}, t) \cdot (\mathbf{v} - \partial_t \boldsymbol{\varphi}(\mathbf{x}^{\mathrm{r}}, t)) = \mathbf{n} \cdot D\boldsymbol{\varphi}(\mathbf{x}^{\mathrm{r}}, t)\, \partial_t \boldsymbol{\gamma}_{\mathrm{e}}^{\mathrm{r}}(\mathbf{s}, t). \tag{6.80}$$

We note the relative normal velocity as

$$v_{\mathrm{d}}(\mathbf{x}, t) = \mathbf{n} \cdot D\boldsymbol{\varphi}(\mathbf{x}^{\mathrm{r}}, t)\, \partial_t \boldsymbol{\gamma}_{\mathrm{e}}^{\mathrm{r}}(\mathbf{s}, t), \tag{6.81}$$

therefore, Eq (6.80) can be written as

$$v_{\mathrm{d}} = \mathbf{n} \cdot \left(\mathbf{v} - \partial_t \boldsymbol{\varphi} \circ \boldsymbol{\varphi}^{-1} \right) \tag{6.82}$$

The subscript 'd' stands for 'degradation' and v_{d} is called degradation velocity or d-velocity. In particular, we assume that the degradation velocity $v_{\mathrm{d}} = v_{\mathrm{d}}(\mathbf{x}, t) = {}^{(1-\phi(\mathbf{x},t))}/_{2}\, \bar{v}_{\mathrm{d}}(\mathbf{x}, t)$ is non-zero only at the interface between the tissue and the elastic matrix. In the present work we only explore the cases of $v_{\mathrm{d}} = 0$, which corresponds to the formulation of Sec. 6.3.1, and $v_{\mathrm{d}} > 0$ which corresponds to the case of degradation of the matrix here explored. Indeed, looking at Eq. (6.82) we can interpret a positive degradation velocity as a flow of the external matrix inside the fluid domain in a sort of degradation of the matrix itself. If we note with $\mathbf{n}^{\mathrm{r}}$ the unit normal to $\partial\Omega_{\mathrm{e}}^{\mathrm{r}}(t)$ pointing into the elastic matrix, we can also define the Lagrangian d-velocity, which correspond to the normal velocity of the boundary of the elastic matrix reference domain, as

$$V_{\mathrm{d}}(\mathbf{x}^{\mathrm{r}}, t) = \mathbf{n}^{\mathrm{r}}(\mathbf{x}^{\mathrm{r}}, t) \cdot \partial_t\, \boldsymbol{\gamma}_{\mathrm{e}}^{\mathrm{r}}(\mathbf{s}, t). \tag{6.83}$$

With this definition we can rewrite Eq. (6.81) as

$$v_{\mathrm{d}}(\mathbf{x}, t) = \left[\mathbf{n} \cdot D\boldsymbol{\varphi}(\mathbf{x}^{\mathrm{r}}, t)\, \mathbf{n}^{\mathrm{r}}(\mathbf{x}^{\mathrm{r}}, t) \right]\, V_{\mathrm{d}}(\mathbf{x}^{\mathrm{r}}, t), \tag{6.84}$$

which, recalling Nanson's formula, $\det(D\boldsymbol{\varphi})D\boldsymbol{\varphi}^{-T}\mathbf{n}^{\mathrm{r}}\,dS_{\mathrm{r}} = \mathbf{n}\,dS$ with dS_{r} and dS the area measure on $\partial\Omega_{\mathrm{e}}^{\mathrm{r}}(t)$ and $\Gamma(t)$, respectively, we can obtain the relation

$$v_{\mathrm{d}}\,dS = V_{\mathrm{d}}\,J\,dS_r, \tag{6.85}$$

where $J = \det(D\boldsymbol{\varphi})$. This equation relates the jump in the normal component of the velocity due to the degradation between the reference and deformed configurations. In conclusion, the velocity field at the binary-fluid-solid interface is discontinuous both in the tangential component and in the normal component, as seen in Eqs. (6.47) and (6.82), due to slippage and degradation, respectively. We can therefore write that

$$\mathbf{v} - \partial_t\boldsymbol{\varphi}\circ\boldsymbol{\varphi}^{-1} = v_{\mathrm{d}}\mathbf{n} + \mathbf{v}^{\parallel} \qquad \text{on } \partial\Omega_e^r(t), \tag{6.86}$$

which expresses the jump of the velocity at the binary-fluid-solid interface.

6.4.2 Onsager's variational formulation

To describe the dynamics of an organoid on a substrate, we adopt Onsager's variational formalism of irreversible thermodynamics. Therefore, the time evolution of the system follows from the minimization of the Rayleighian functional. In the present formulation, the state variables are the deformation map of the elastic matrix $\boldsymbol{\varphi}$ and the position of the interface $\Gamma(t)$. The process variables, characterizing the evolution of the system and with respect to which the problem must be minimized, are the elastic matrix velocity $\partial_t\boldsymbol{\varphi}$, the fluid velocity $\mathbf{v}$, the sliding velocity $\mathbf{v}^{\parallel}$ defined in Sec 6.3.1, and the degradation velocity v_{d}. Therefore, in order to apply Onsager's principle, we need to identify the expressions of the free energies, dissipation potentials, and power inputs involved in the problem in terms of the defined state and process variables.

Free energies

The free energy of the elastic matrix domain is given by the sum of the elastic energy of the matrix and the surface energy of the binary-fluid-solid interface

$$\mathcal{F}_{\mathrm{e}}[\boldsymbol{\varphi},\Gamma,\phi] = \int_{\Omega_{\mathrm{e}}^{\mathrm{r}}(t)} W(\nabla_{\mathrm{r}}\boldsymbol{\varphi})dV_{\mathrm{r}} + \int_{\Gamma(t)} T dS, \tag{6.87}$$

where $W(\nabla_{\mathrm{r}}\boldsymbol{\varphi})$ is the strain energy density of the hyperelastic solid matrix,$\nabla_{\mathrm{r}}\boldsymbol{\varphi}$ is the deformation gradient, and $T = T(\phi) = {}^{(1-\phi)}/_{2}\,\gamma_{st} + {}^{(1+\phi)}/_{2}\,\gamma_{se}$ is the surface tension between the fluids and the solid.

Another energetic contribution to the free energy of the system is given by the free energy of the phase field, which is given by a Landau functional [Du et al., 2004, Wang, 2005]

$$\mathcal{F}_{\phi}[\phi] = \int_{\Omega_f(t)} \frac{3}{2\sqrt{2}}\sigma\left(\frac{1}{4\epsilon}(\phi^2-1)^2 + \frac{\epsilon}{2}\left|\nabla\phi\right|^2\right)dV, \tag{6.88}$$

where ϵ is the thickness of the interface and $\sigma = \gamma_{te}$ is the interfacial energy per unit area, which in the present study it represents the surface tension between the active fluid and the external medium. In particular, the first term of this functional is the classical double-well potential, and the second one is the interfacial energy, which penalizes sharp changes in ϕ.

Then the total free energy of the system is given by

$$\mathcal{F}[\boldsymbol{\varphi},\boldsymbol{\psi},\Gamma] = \mathcal{F}_{\mathrm{e}}[\boldsymbol{\varphi},\Gamma] + \mathcal{F}_{\phi}[\phi]. \tag{6.89}$$

Dissipation potential

The dissipation mechanisms taken into account are the viscous dissipations, which take place in the active tissue and in the external medium, as well as the dissipation associated with the relative motion of the fluids and the solid due to slip and degradation. The dissipation potential adopted is thus

$$\mathcal{D}_f[\mathbf{v}, \mathbf{v}^{\parallel}, v_{\mathrm{d}}] = \frac{\mu(\phi)}{4} \int_{\Omega_f(t)} \left|\nabla \mathbf{v} + \nabla \mathbf{v}^{\mathrm{T}}\right|^2 dV + \int_{\Gamma(t)} d\left(v_{\mathrm{d}}, \mathbf{v}^{\parallel}\right) dS, \tag{6.90}$$

where $\mu(\phi) = {}^{(1-\phi)}\!/_{2}\mu_{\mathrm{t}} + {}^{(1+\phi)}\!/_{2}\mu_{\mathrm{e}}$ is the viscosity of the fluid domain, which depends linearly on the phase-field order parameter, and where μ_{t} and μ_{e} denote the viscosities of the tissue and external medium, respectively. Furthermore, in Eq. (6.51), we have that $d\left(v_{\mathrm{d}}, \mathbf{v}^{\parallel}\right)$ is the dissipation density per unit interface area for which we consider a quadratic potential of the form

$$d\left(v_{\mathrm{d}}, \mathbf{v}^{\parallel}\right) = \frac{\xi^{\perp}}{2} v_{\mathrm{d}}^2 + \frac{\xi^{\parallel}}{2} \left|\mathbf{v}^{\parallel}\right|^2, \tag{6.91}$$

where $\xi^{\perp}$ and $\xi^{\parallel}$ are the perpendicular and parallel friction coefficients, respectively.

We disregard for now viscous or poroelastic dissipations that may occur in the external matrix, which can be considered in the future advancement of the current model.

Power input

In the absence of body forces or external forces, we assume that the activity of the system is restricted to the interface and can be introduced in the formulation through the power input functional

$$\mathcal{W}[\mathbf{v}^{\parallel}, v_{\mathrm{d}}] = -\int_{\Gamma(t)} \mathbf{f}_a^{\parallel} \cdot \mathbf{v}^{\parallel} dS - \int_{\Gamma(t)} f_{\mathrm{d}}\, v_{\mathrm{d}} dS, \tag{6.92}$$

where $\mathbf{f}_a^{\parallel}$ represents an active force inducing tangential slip and f_{d} is a generalized force power-conjugate to v_{d} [Gurtin, 1999, Abeyaratne and Knowles, 2006]. We call f_{d} as degradation force, or d-force, and we assume that its sign must be positive in order to induce positive degradation velocity. As already explained in Sec. 6.3.1, $\mathbf{f}_a^{\parallel}$ is a force that can induce the sliding of the tissues over the elastic matrix. but due to the fact that the object of this thesis is to study the degradation process, we are going to leave its definition unspecified.

Constraints

Finally, we introduce a constraint functional to impose the incompressibility of the fluids and the jump in the parallel component of the velocity at the solid-fluids interface, which is given by

$$\begin{aligned}\mathcal{C}[\partial_t \boldsymbol{\varphi}, \mathbf{v}, \mathbf{v}^{\parallel}, v_{\mathrm{d}}, p, \boldsymbol{\lambda}, \lambda_n] = &-\int_{\Omega_f(t)} p(\nabla \cdot \mathbf{v}) dV - \int_{\Gamma(t)} \lambda_n \left[\mathbf{n} \cdot (\mathbf{v} - \partial_t \boldsymbol{\varphi}) - v_{\mathrm{d}}\right] dS \\ &- \int_{\Gamma(t)} \boldsymbol{\lambda} \cdot \left[\boldsymbol{\Pi}\left(\mathbf{v} - \partial_t \boldsymbol{\varphi}\right) - \mathbf{v}^{\parallel}\right] dS,\end{aligned} \tag{6.93}$$

where p, λ_n and $\boldsymbol{\lambda}$ are Lagrange multipliers with $\boldsymbol{\lambda}$ tangential to $\Gamma(t)$.

Rayleighian and Lagrangian

To obtain the dissipative dynamics of an active tissue that deforms and degrades a soft substrate via Onsager's variational formalism, the Rayleighian is defined as the sum of the rate of change of the free energy, the dissipation potential, and the power input functional:

$$\mathcal{R}[\partial_t\boldsymbol{\varphi}, \mathbf{v}, \mathbf{v}^{\parallel}, v_{\mathrm{d}}] = \frac{d}{dt}\mathcal{F}_{\mathrm{e}}[\partial_t\boldsymbol{\varphi}, \mathbf{v}, v_{\mathrm{d}}] + \frac{d}{dt}\mathcal{F}_{\phi}[\mathbf{v}] + \mathcal{D}_f[\mathbf{v}, \mathbf{v}^{\parallel}, v_{\mathrm{d}}] + \mathcal{W}[\mathbf{v}^{\parallel}, v_{\mathrm{d}}]. \tag{6.94}$$

The governing equations can thus be obtained from the minimization of the Rayleigh functional subjected to the constraints defined by the constrain functional $\mathcal{C}[\partial_t\boldsymbol{\varphi}, \mathbf{v}, \mathbf{v}^{\parallel}, v_{\mathrm{d}}]$. In conclusion, the dynamic of the system can be obtained by extremizing the Lagrangian

$$\mathcal{L}[\partial_t\boldsymbol{\varphi}, \mathbf{v}, \mathbf{v}^{\parallel}, v_{\mathrm{d}}, p, \boldsymbol{\lambda}, \lambda_n] = \mathcal{R}[\partial_t\boldsymbol{\varphi}, \mathbf{v}, \mathbf{v}^{\parallel}, v_{\mathrm{d}}] + \mathcal{C}[\partial_t\boldsymbol{\varphi}, \mathbf{v}, \mathbf{v}^{\parallel}, v_{\mathrm{d}}, p, \boldsymbol{\lambda}, \lambda_n]. \tag{6.95}$$

6.4.3 Variational derivation of the governing equations

In order to determine the constrained dynamics of the system, requiring the stationarity of the Lagrangian specified in Eq. (6.95), it is essential to derive the rate of change of the free energies of the elastic matrix, the surface energy of the binary-fluid-solid interface, and the phase field.

Rate of change of the free energies

Starting from the rate of change of the free energy of the elastic matrix given by the first term of Eq. (6.87), and applying the Reynolds transport theorem and the chain rule, we obtain

$$\frac{d}{dt}\int_{\Omega_{\mathrm{e}}^{\mathrm{r}}(t)} W(D\boldsymbol{\varphi})dV_r = \int_{\Omega_{\mathrm{e}}^{\mathrm{r}}(t)} \partial_t W(D\boldsymbol{\varphi})dV_{\mathrm{r}} - \int_{\partial\Omega_{\mathrm{e}}^{\mathrm{r}}(t)} W(D\boldsymbol{\varphi})\partial_t\boldsymbol{\gamma}_{\mathrm{e}}^{\mathrm{r}}\cdot\mathbf{n}^{\mathrm{r}}dS_{\mathrm{r}}, \tag{6.96}$$

where the minus sign comes from the fact that the normal $\mathbf{n}^{\mathrm{r}}$ points inside the $\Omega_{\mathrm{e}}^{\mathrm{r}}(t)$. Recalling Eq. (6.83), Eq. (6.96) can be recast as

$$\frac{d}{dt}\int_{\Omega_{\mathrm{e}}^{\mathrm{r}}(t)} W(D\boldsymbol{\varphi})dV_r = \int_{\Omega_{\mathrm{e}}^{\mathrm{r}}(t)} \mathbf{P}_{\mathrm{e}} : \nabla_{\mathrm{r}}\,\partial_t\boldsymbol{\varphi}\,dV_{\mathrm{r}} - \int_{\partial\Omega_{\mathrm{e}}^{\mathrm{r}}(t)} V_{\mathrm{d}}W(D\boldsymbol{\varphi})\,dS_{\mathrm{r}}, \tag{6.97}$$

where ∇_{r} represents the differentiation with respect to the reference domain coordinates, and $\mathbf{P}_{\mathrm{e}}$ is the first Piola-Kirchhoff stress tensor. Integrating by parts the first term,

$$\begin{aligned}\frac{d}{dt}\int_{\Omega_{\mathrm{e}}^{\mathrm{r}}(t)} W(D\boldsymbol{\varphi})dV_r = &-\int_{\partial\Omega_{\mathrm{e}}^{\mathrm{r}}(t)} \left(\mathbf{P}_{\mathrm{e}}^T\,\partial_t\boldsymbol{\varphi}\right)\cdot\mathbf{n}_r\,dS_{\mathrm{r}} - \int_{\Omega_{\mathrm{e}}^{\mathrm{r}}(t)} (\nabla_r\cdot\mathbf{P}_{\mathrm{e}})\cdot\,\partial_t\boldsymbol{\varphi}\,dV_{\mathrm{r}} \\ &- \int_{\partial\Omega_{\mathrm{e}}^{\mathrm{r}}(t)} V_{\mathrm{d}}W(D\boldsymbol{\varphi})\,dS_{\mathrm{r}}.\end{aligned} \tag{6.98}$$

Recalling that $\mathbf{P}_{\mathrm{e}} = J\boldsymbol{\sigma}_{\mathrm{e}}\mathbf{F}^{-T}$, the identity $\nabla_r\cdot\mathbf{P}_{\mathrm{e}} = J\nabla\cdot\boldsymbol{\sigma}_{\mathrm{e}}$, and Nanson's Formula $\mathbf{n}dS = J\mathbf{F}^{-T}\mathbf{n}_r\,dS_r$ we obtain

$$\begin{aligned}\frac{d}{dt}\int_{\Omega_{\mathrm{e}}^{\mathrm{r}}(t)} W(\nabla_{\mathrm{r}}\boldsymbol{\varphi})dV_r = &-\int_{\partial\Omega_{\mathrm{e}}^{\mathrm{r}}(t)} \left(J\mathbf{F}^{-1}\boldsymbol{\sigma}_{\mathrm{e}}\,\partial_t\boldsymbol{\varphi}\right)\cdot\mathbf{n}_r\,dS_{\mathrm{r}} - \int_{\Omega_{\mathrm{e}}^{\mathrm{r}}(t)} J(\nabla\cdot\boldsymbol{\sigma}_{\mathrm{e}})\cdot\,\partial_t\boldsymbol{\varphi}\,dV_{\mathrm{r}} \\ &- \int_{\partial\Omega_{\mathrm{e}}^{\mathrm{r}}(t)} V_{\mathrm{d}}W(\nabla_{\mathrm{r}}\boldsymbol{\varphi})\,dS_{\mathrm{r}},\end{aligned} \tag{6.99}$$

which, together with Eq. (6.85), allows us to write all the integrals in the spatial configuration as

$$\frac{d}{dt}\int_{\Omega_{\mathrm{e}}^{\mathrm{r}}(t)} W(\nabla_{\mathrm{r}}\boldsymbol{\varphi})dV_r = -\int_{\Gamma(t)} \partial_t\boldsymbol{\varphi}\circ\boldsymbol{\varphi}^{-1}\cdot\boldsymbol{\sigma}_{\mathrm{e}}\mathbf{n}\,dS - \int_{\Omega_{\mathrm{e}}(t)}(\nabla\cdot\boldsymbol{\sigma}_{\mathrm{e}})\cdot\partial_t\boldsymbol{\varphi}\circ\boldsymbol{\varphi}^{-1}\,dV - \int_{\Gamma(t)} v_{\mathrm{d}}\frac{W(\nabla_{\mathrm{r}}\boldsymbol{\varphi}\circ\boldsymbol{\varphi}^{-1})}{J\circ\boldsymbol{\varphi}^{-1}}\,dS. \tag{6.100}$$

As pointed out in the case of the interaction of a binary fluid with a solid domain, without degradation, we have that the rate of change of surface energy is given by (6.61) here reposted for ease of reading

$$\frac{d}{dt}\int_{\Gamma(t)} T(\phi)dS = \int_{\Gamma(t)} \left(\nabla_\Gamma T\cdot\mathbf{v} + 2HT(\mathbf{v}\cdot\mathbf{n})\right)dS. \tag{6.101}$$

Finally, in the same fashion, we can obtain the rate of change of the phase-field free energy, already obtained in Eq. (6.66), here reposted for ease of reading

$$\frac{d}{dt}\mathcal{F}_\phi[\mathbf{v}] = \int_{\Gamma(t)} f_\phi\mathbf{v}\cdot\mathbf{n}dS - \int_{\Omega_f(t)}\hat{\mu}\nabla\phi\cdot\mathbf{v}\,dV, \tag{6.102}$$

where $\hat{\mu}$ is the chemical potential and f_ϕ the energy density integrand of Eq. (6.88).

Governing equations

Gathering all the terms of the Lagrangian together, we have

$$\begin{aligned}\mathcal{L}\left[\partial_t\boldsymbol{\varphi},\mathbf{v},\mathbf{v}^{\parallel},v_{\mathrm{d}},p,\boldsymbol{\lambda},\lambda_n\right] =& \frac{d}{dt}\mathcal{F}_e\left[\partial_t\boldsymbol{\varphi},\mathbf{v},v_{\mathrm{d}}\right] + \frac{d}{dt}\mathcal{F}_\phi\left[\mathbf{v}\right] + \mathcal{D}_f\left[\mathbf{v},\mathbf{v}^{\parallel},v_{\mathrm{d}}\right] \\ &+ \mathcal{W}\left[\mathbf{v}^{\parallel},v_{\mathrm{d}}\right] + \mathcal{C}\left[\partial_t\boldsymbol{\varphi},\mathbf{v},\mathbf{v}^{\parallel},v_{\mathrm{d}},p,\boldsymbol{\lambda},\lambda_n\right].\end{aligned} \tag{6.103}$$

Dropping the dependency of the Lagrangian and exploiting the complete form of all associated terms yields

$$\begin{aligned}\mathcal{L} =& -\int_{\Gamma(t)}\partial_t\boldsymbol{\varphi}\cdot\boldsymbol{\sigma}_{\mathrm{e}}\mathbf{n}\,dS - \int_{\Omega_{\mathrm{e}}(t)}(\nabla\cdot\boldsymbol{\sigma}_{\mathrm{e}})\cdot\partial_t\boldsymbol{\varphi}\,dV \\ &- \int_{\Gamma(t)} v_{\mathrm{d}}\frac{W(\nabla_{\mathrm{r}}\boldsymbol{\varphi})}{J}\,dS + \int_{\Gamma(t)}\left(\nabla_\Gamma T\cdot\mathbf{v} + 2HT(\mathbf{v}\cdot\mathbf{n})\right)dS \\ &+ \int_{\Gamma(t)} f_\phi\mathbf{v}\cdot\mathbf{n}dS - \int_{\Omega_f(t)}\hat{\mu}\nabla\phi\cdot\mathbf{v}\,dV \\ &+ \frac{\mu(\phi)}{4}\int_{\Omega_f(t)}\left|\nabla\mathbf{v}+\nabla\mathbf{v}^{\mathrm{T}}\right|^2 dV + \int_{\Gamma(t)}\frac{\xi^\perp}{2}v_{\mathrm{d}}^2 + \frac{\xi^{\parallel}}{2}\left|\mathbf{v}^{\parallel}\right|^2 dS \\ &- \int_{\Gamma(t)}\mathbf{f}_a^{\parallel}\cdot\mathbf{v}^{\parallel}\,dS - \int_{\Gamma(t)} f_{\mathrm{d}}\,v_{\mathrm{d}}\,dS - \int_{\Omega_f(t)} p(\nabla\cdot\mathbf{v})\,dV \\ &- \int_{\Gamma(t)}\lambda_n\left[\mathbf{n}\cdot(\mathbf{v}-\partial_t\boldsymbol{\varphi}) - v_{\mathrm{d}}\right]dS - \int_{\Gamma(t)}\boldsymbol{\lambda}\cdot\left[\boldsymbol{\Pi}\left(\mathbf{v}-\partial_t\boldsymbol{\varphi}\right) - \mathbf{v}^{\parallel}\right]dS.\end{aligned} \tag{6.104}$$

Stationarity of the Lagrangian (6.104) with respect to $\partial_t\boldsymbol{\varphi}$ leads to the balance of linear momentum in the bulk $\Omega_e(t)$

$$\nabla\cdot\boldsymbol{\sigma}_e = 0 \qquad \text{in } \Omega_e(t), \tag{6.105}$$

and to the condition

$$-\boldsymbol{\sigma}_e\mathbf{n} + \lambda_n\mathbf{n} + \boldsymbol{\lambda} = 0 \qquad \text{on } \Gamma(t). \tag{6.106}$$

Stationarity with respect to $\mathbf{v}$ leads to the balance of linear momentum in the bulk $\Omega_f(t)$

$$\nabla \cdot \boldsymbol{\sigma}_f + \hat{\mu}\nabla\phi = 0 \qquad \text{in } \Omega_f(t), \tag{6.107}$$

where $\boldsymbol{\sigma}_f = \mu(\nabla\mathbf{v} + \nabla\mathbf{v}^T) - p\mathbf{I}$ and to the condition

$$\boldsymbol{\sigma}_f\mathbf{n} - \lambda_n\mathbf{n} - \boldsymbol{\lambda} + f_\phi\mathbf{n} + \nabla_\Gamma T(\phi) + 2T(\phi)H\mathbf{n} = 0 \qquad \text{on } \Gamma(t). \tag{6.108}$$

Adding Eqs. (6.106) and (6.108) lead to the force balance at the interface,

$$\boldsymbol{\sigma}_e\mathbf{n} - \boldsymbol{\sigma}_f\mathbf{n} = f_\phi\mathbf{n} + \nabla_\Gamma T(\phi) + 2T(\phi)H\mathbf{n} \qquad \text{on } \Gamma(t), \tag{6.109}$$

which states that the jump in the traction across the interface is balanced by the Laplace pressure, by the Marangoni forces and by the force exerted by the tissue-external medium surface. Recalling that $\boldsymbol{\lambda}$ is tangential to $\Gamma(t)$, we may identify the Lagrange multipliers as

$$\lambda_n = \mathbf{n} \cdot \boldsymbol{\sigma}_e\mathbf{n} = \mathbf{n} \cdot \boldsymbol{\sigma}_f\mathbf{n} + f_\phi\mathbf{n} + 2T(\phi)H\mathbf{n} \tag{6.110a}$$

$$\boldsymbol{\lambda} = \boldsymbol{\Pi}\boldsymbol{\sigma}_f\mathbf{n} + \nabla_\Gamma T(\phi) = \boldsymbol{\Pi}\boldsymbol{\sigma}_e\mathbf{n}. \tag{6.110b}$$

Stationarity with respect to $\mathbf{v}^{\parallel}$ leads force balance tangential to the interface

$$\boldsymbol{\Pi}\boldsymbol{\sigma}_f\mathbf{n} + \nabla_\Gamma T(\phi) = \boldsymbol{\Pi}\boldsymbol{\sigma}_e\mathbf{n} = -\xi^{\parallel}\mathbf{v}^{\parallel} + \mathbf{f}_a^{\parallel} \qquad \text{on } \Gamma(t). \tag{6.111}$$

Finally, stationarity with respect to v_d provide an additional equation for the generalised force balance conjugate to the degradation given by

$$-\frac{W}{J} + \xi^{\perp}v_\mathrm{d} - f_\mathrm{d} + \lambda_n = 0 \qquad \text{on } \Gamma(t) \tag{6.112}$$

Introducing for convenience the notation $f_\mathrm{d} = \xi^{\perp}v_\mathrm{d}^*$ with v_d^* the force-free degradation velocity and substituting (6.110a)

$$v_\mathrm{d} = v_\mathrm{d}^* - \frac{1}{\xi^{\perp}}\left(\mathbf{n} \cdot \boldsymbol{\sigma}_e\mathbf{n} - \frac{W}{J}\right) \qquad \text{on } \Gamma(t). \tag{6.113}$$

6.4.4 Generalize force balance conjugate to the d-velocity: characteristics

In equation 6.113, between brackets on the right-hand side, we recognize a thermodynamic Eshelby-like driving force $f_{th} = \mathbf{n} \cdot \boldsymbol{\sigma}\mathbf{n} - W/J$, typical of configurational mechanics [Gurtin, 1999, Abeyaratne and Knowles, 2006]. Although this expression has been obtained under the simplifying assumptions of constant active force (or eqivalently constant v_d^*) and quadratic dissipation, it provides insights on the general structure of the constitutive relation governing the dynamics of degradation/deposition.

We can interpret v_d^* as the force-free d-velocity, assuming that the elastic matrix does not thermodynamically oppose or favor degradation/deposition. The thermodynamic force is composed of the normal component of the traction normal to the interface minus the elastic energy per unit actual volume. Assuming that in a stress-free configuration $W = 0$, then

- Compression $f_{th} < 0$ favors degradation since removal of material release the elastic energy

  1. by the kinetic effect of pulling the elastic matrix towards the interface, thereby reducing compression, and,
  2. by removing material that was storing elastic energy.

- Under tension, the two terms in f_{th} have opposite signs. Because at small strains traction depends linearly on deformation, whereas W depends quadratically on deformation, we expect that at least for moderate tension, the traction term dominates $f_{th} > 0$. Hence, tension opposes degradation since removal of matrix material further stretches it.

6.5 Numerical implementation

Modeling fluid-structure interaction subjected to large deformations and coupled with a two-phase flow problem presents significant numerical challenges. In this scenario, standard numerical techniques like the finite element method, which rely on boundary-fitted meshes, become impractical. Maintaining a good mesh quality without distorted elements requires the continuous generation of new boundary-fitted meshes, which leads to prohibitively expensive computations. To overcome these limitations, our approach resorts to a hybrid fitted-CutFEM technique. This framework is built around the moving non-material interface between the fluid and the solid, which separates the computational domain into two subdomains. In our model, the subdomain corresponding to the solid is discretized using the Cut Finite Element Method (CutFEM), while the surrounding fluid subdomain is meshed with a body-fitted unstructured mesh. The choice of the cutFEM for the solid and the body-fitted mesh for the fluids was dictated by the fact that we wanted to allow large deformations and topological changes arising from the possible degradation of the matrix in the former while keeping accurate local refinement at the two-phase fluid interface, whose evolution is governed by a phase field, in the latter.

The unfitted component of our model, CutFEM [Burman et al., 2015], belongs to a broad family of methods that embed geometry in a non-conforming background mesh, including IBM [Peskin, 2002], XFEM [Moës et al., 1999], IFEM [Zhang et al., 2004]. To address the well-known challenge of ill-conditioning arising from small cut cells in our CutFEM discretization, we employ a cell aggregation-based stabilization technique (agFEM) [Badia et al., 2018b]. Finally, continuity conditions across the interface between the fitted and unfitted subdomains are weakly enforced using Nitsche's method [Nitsche, 1971], which preserves the symmetry of the formulation and combines the geometric flexibility of CutFEM with the efficiency of a body-fitted discretization.

In the development of this section, we outline all the aspects involved in the numerical implementation of our model. We begin in Sec. 6.5.1 by reformulating the variational principle with a Nitsche formulation to weakly impose interface conditions. Sec. 6.5.2 then details the variational time integrator scheme adopted for time discretization. Finally, Sec. 6.5.3 presents the fully discrete spatial formulation, detailing the hybrid fitted-CutFEM technique, the aggregation-based stabilization method, and the procedure for integrating cut elements.

6.5.1 Nitsche's formulation in Onsager's variational formalism

The variational principle for the fluid-structure interaction problem is reformulated here using Nitsche's method. Originally proposed by Nitsche [1971], this technique provides a straightforward method for weakly addressing Dirichlet boundary conditions on non-conforming interfaces without employing Lagrange multipliers. We begin by modifying the Lagrangians previously defined in Eqs. (6.104) and (6.68), corresponding to the scenarios with and without degradation of the elastic matrix, respectively. The constraints on the system, which were previously established through the Lagrange multipliers p, $\boldsymbol{\lambda}$, and λ_n, are now relaxed. Specifically, the fluid's incompressibility is handled using a penalty term. The interfacial kinematic conditions are enforced through the penalty functional, along with the Nitsche consistency integrals, which ensure that the original interface conditions are satisfied exactly, thereby avoiding the consistency errors inherent to pure penalty approaches. For brevity, the following derivation is presented only for the case with solid degradation. The non-degrading case can be recovered by simply setting the degradation velocity $v_\mathrm{d} = 0$. Therefore, Eq. (6.104) is recast as

$$\begin{aligned}\mathcal{N}\left[\partial_t\boldsymbol{\varphi}, \mathbf{v}, \mathbf{v}^{\parallel}, v_\mathrm{d}\right] =& \frac{d}{dt}\mathcal{F}_e\left[\partial_t\boldsymbol{\varphi}, \mathbf{v}, v_\mathrm{d}\right] + \frac{d}{dt}\mathcal{F}_\phi\left[\mathbf{v}\right] + \mathcal{D}_f\left[\mathbf{v}, \mathbf{v}^{\parallel}, v_\mathrm{d}\right] \\ &+ \mathcal{W}\left[\mathbf{v}^{\parallel}, v_\mathrm{d}\right] + \frac{\lambda}{2}\int_{\Omega_f}\left(\mathrm{tr}\left(\nabla\mathbf{v}\right)\right)^2\, dV \\ &+ \frac{\beta^{\perp}}{2}\int_{\Gamma(t)}\left[(\mathbf{v}-\partial_t\boldsymbol{\varphi})\cdot\mathbf{n} - v_\mathrm{d}\right]^2 dS - \int_{\Gamma(t)} t_n\left[(\mathbf{v}-\partial_t\boldsymbol{\varphi})\cdot\mathbf{n} - v_\mathrm{d}\right] dS \\ &+ \frac{\beta^{\parallel}}{2}\int_{\Gamma(t)}\left|\boldsymbol{\Pi}(\mathbf{v}-\partial_t\boldsymbol{\varphi}) - \mathbf{v}^{\parallel}\right|^2 dS - \int_{\Gamma(t)}\mathbf{t}\cdot\left[\boldsymbol{\Pi}(\mathbf{v}-\partial_t\boldsymbol{\varphi}) - \mathbf{v}^{\parallel}\right] dS\end{aligned} \tag{6.114}$$

where $t_n = \mathbf{T}\cdot\mathbf{n}$ and $\mathbf{t} = \boldsymbol{\Pi}\mathbf{T}$ are the normal and tangential traction components at the interface. Specifically, we can define a one-parameter family of functionals $\mathcal{N}_\zeta$ by considering $\mathbf{T} = \zeta\boldsymbol{\sigma}_e\mathbf{n} + (1-\zeta)(\boldsymbol{\sigma}_f\mathbf{n} - L\nabla\phi)$ with $\zeta \in [0,1]$. These functionals lead to different Euler-Lagrange equations, but all of them are consistent with the exact solutions. In particular, if the force balance at the interface is as given by Eq. (6.109), then $\mathbf{T} = \boldsymbol{\sigma}_e\mathbf{n}$. Regarding instead the $\beta^{\perp}$ and $\beta^{\parallel}$, these are often called in literature "stabilization parameters" or "penalty parameters," chosen large enough to ensure the stability of the formulation [Hansbo, 2005, Sanders et al., 2012, Du et al., 2020]. If we assume that both the perpendicular and parallel stabilization parameters are equal, i.e. $\beta = \beta^{\perp} = \beta^{\parallel}$, we obtain

$$\begin{aligned}\mathcal{N}\left[\partial_t\boldsymbol{\varphi}, \mathbf{v}, \mathbf{v}^{\parallel}, v_\mathrm{d}\right] =& \frac{d}{dt}\mathcal{F}_e\left[\partial_t\boldsymbol{\varphi}, \mathbf{v}, v_\mathrm{d}\right] + \frac{d}{dt}\mathcal{F}_\phi\left[\mathbf{v}\right] + \mathcal{D}_f\left[\mathbf{v}, \mathbf{v}^{\parallel}, v_\mathrm{d}\right] \\ &+ \mathcal{W}\left[\mathbf{v}^{\parallel}, v_\mathrm{d}\right] + \frac{\lambda}{2}\int_{\Omega_f}\left(\mathrm{tr}\left(\nabla\mathbf{v}\right)\right)^2\, dV \\ &+ \frac{\beta}{2}\int_{\Gamma(t)}\left[(\mathbf{v}-\partial_t\boldsymbol{\varphi}) - (v_\mathrm{d}\mathbf{n} + \mathbf{v}^{\parallel})\right]^2 dS \\ &- \int_{\Gamma(t)}\mathbf{T}\cdot\left[(\mathbf{v}-\partial_t\boldsymbol{\varphi}) - (v_\mathrm{d}\mathbf{n} + \mathbf{v}^{\parallel})\right] dS.\end{aligned} \tag{6.115}$$

Making the Nitsche-Lagrangian $\mathcal{N}$ stationary with respect to $\partial_t\boldsymbol{\varphi}$, leads to the fol-

lowing equation on the interface $\Gamma(t)$

$$-\boldsymbol{\sigma}_e\mathbf{n} - \beta\left[(\mathbf{v} - \partial_t\boldsymbol{\varphi}) - (v_\mathrm{d}\mathbf{n} + \mathbf{v}^\parallel)\right] + \mathbf{T} = 0 \qquad \text{on } \Gamma(t). \tag{6.116}$$

Making $\mathcal{N}$ stationary with respect to $\mathbf{v}$, leads to the following equation on $\Gamma(t)$

$$\boldsymbol{\sigma}_f\mathbf{n} + f_\phi\mathbf{n} + \nabla_\Gamma T(\phi) + 2T(\phi)H\mathbf{n} + \beta\left[(\mathbf{v} - \partial_t\boldsymbol{\varphi}) - (v_\mathrm{d}\mathbf{n} + \mathbf{v}^\parallel)\right] - \mathbf{T} = 0 \qquad \text{on } \Gamma(t). \tag{6.117}$$

If we add together Eqs. (6.116) and (6.117), as we already saw in Sec. 6.4.3, we recover the force balance at the interface given in Eq. (6.109). Making $\mathcal{N}$ stationary with respect to $\mathbf{v}^\parallel$ yield

$$\xi^\parallel\mathbf{v}^\parallel - \mathbf{f}_a^\parallel + \beta^\parallel\left[\boldsymbol{\Pi}(\mathbf{v} - \partial_t\boldsymbol{\varphi}) - \mathbf{v}^\parallel\right] + \mathbf{t} = 0 \qquad \text{on } \Gamma(t), \tag{6.118}$$

which recalling that $\mathbf{t} = \boldsymbol{\Pi}\mathbf{T} = \boldsymbol{\Pi}\boldsymbol{\sigma}_e\mathbf{n}$ can be recast as

$$\xi^\parallel\mathbf{v}^\parallel - \mathbf{f}_a^\parallel - \beta^\parallel\left[\boldsymbol{\Pi}(\mathbf{v} - \partial_t\boldsymbol{\varphi}) - \mathbf{v}^\parallel\right] + \boldsymbol{\Pi}\boldsymbol{\sigma}_e\mathbf{n} = 0 \qquad \text{on } \Gamma(t), \tag{6.119}$$

or

$$(\xi^\parallel + \beta^\parallel)\mathbf{v}^\parallel = \mathbf{f}_a^\parallel + \beta^\parallel\left[\boldsymbol{\Pi}(\mathbf{v} - \partial_t\boldsymbol{\varphi})\right] - \boldsymbol{\Pi}\boldsymbol{\sigma}_e\mathbf{n} \qquad \text{on } \Gamma(t). \tag{6.120}$$

Finally, making $\mathcal{N}$ stationary with respect to v_d, we obtain

$$\xi^\perp v_\mathrm{d} - f_\mathrm{d} + \beta^\perp\left[(\mathbf{v} - \partial_t\boldsymbol{\varphi})\cdot\mathbf{n} - v_\mathrm{d}\right] + t_n = 0 \qquad \text{on } \Gamma(t), \tag{6.121}$$

which recalling that $t_n = \mathbf{T}\cdot\mathbf{n} = \mathbf{n}\cdot\boldsymbol{\sigma}_e\mathbf{n}$ can be recast as

$$\xi^\perp v_\mathrm{d} - f_\mathrm{d} - \frac{W}{J} - \beta^\perp\left[(\mathbf{v} - \partial_t\boldsymbol{\varphi})\cdot\mathbf{n} - v_\mathrm{d}\right] + \mathbf{n}\cdot\boldsymbol{\sigma}_e\mathbf{n} = 0 \qquad \text{on } \Gamma(t), \tag{6.122}$$

or

$$(\xi^\perp + \beta^\perp)v_\mathrm{d} = f_\mathrm{d} - \frac{W}{J} + \beta^\perp(\mathbf{v} - \partial_t\boldsymbol{\varphi})\cdot\mathbf{n} - \mathbf{n}\cdot\boldsymbol{\sigma}_e\mathbf{n} \qquad \text{on } \Gamma(t). \tag{6.123}$$

From Eqs. (6.123) and (6.120), we can therefore express v_d and $\mathbf{v}^\parallel$ as functions of the process variables $\partial_t\boldsymbol{\varphi}$ and $\mathbf{v}$. Therefore, the Onsager's variational principle reduces to

$$\{\partial_t\boldsymbol{\varphi}, \mathbf{v}\} = \underset{\{\partial_t\boldsymbol{\varphi}, \mathbf{v}\}}{\operatorname{argmin}}\,\mathcal{N}\left[\boldsymbol{\varphi}, \boldsymbol{\psi}; \partial_t\boldsymbol{\varphi}, \mathbf{v}\right]. \tag{6.124}$$

6.5.2 Time discretization

The primary approach for time discretization of partial differential equations involves discretizing the governing equations derived from Onsager's variational principle obtained in Section 6.4.3. Nevertheless, the variational principle for dynamics offers an alternative approach that involves the discretization of the variational principle itself, given in Eq. (6.33). This type of time integrator, which is based on the discretization of the variational principle, is termed *variational time integrator* and is frequently employed in the context of Hamiltonian systems [Lew et al., 2004]. We employed a first-order variational time integrator for Onsager's principle, which ensures that $\mathcal{F}$ is a Lyapunov functional of the dynamics, which results in the stability of the resulting discrete dynamics.

Utilizing the established notation for Onsager's variational principle as presented in Section 6.2.2, we obtained that in the dynamics of the sessile droplet, and also in the dynamics of the active tissue, the process variables can be obtained as time derivatives of the state vasiable as $\partial_t X = V$. Considering a time discretization characterized by a time grid $(t^1, ..., t^N)$, we approximate $V^n = V(t^n)$ with a backward difference

$$V^n \approx \frac{X^{n+1} - X^n}{\Delta t^n}, \tag{6.125}$$

where $X^n = X(t^n)$ and $\Delta t^n = t^{n+1} - t^n$. We can therefore approximate the dissipation potential and the power as

$$\mathcal{D}(V; X) \approx \mathcal{D}\left(\frac{X^{n+1} - X^n}{\Delta t^n}; X^n\right), \qquad \mathcal{W}(V; X) \approx \mathcal{W}\left(\frac{X^{n+1} - X^n}{\Delta t^n}; X^n\right). \tag{6.126}$$

For what concern instead the rate of change of the free energy, rather than resorting to an expression like $\dot{\mathcal{F}} \approx D\mathcal{F} \cdot {}^{(X^{n+1}-X^n)}/_{\Delta t^n}$ we consider a first-order finite difference of the form

$$\dot{\mathcal{F}}(X, \partial_t X) \approx \frac{\mathcal{F}(X^{n+1}) - \mathcal{F}(X^n)}{\Delta t^n}. \tag{6.127}$$

This approach ensures that $\mathcal{F}$ is a Lyapunov functional of the dynamics and retains its full nonlinearity. We can define the discrete Rayleighian as

$$\mathcal{R}\left(X^{n+1}; X^n\right) = \frac{\mathcal{F}(X^{n+1})}{\Delta t^n} + \mathcal{D}\left(\frac{X^{n+1} - X^n}{\Delta t^n}; X^n\right) + \mathcal{W}\left(\frac{X^{n+1} - X^n}{\Delta t^n}; X^n\right). \tag{6.128}$$

Where we have ignored the term ${}^{\mathcal{F}(X^n)}/_{\Delta t^n}$, which is irrelevant from the variational point of view. Therefore the discrete form of the variational principle in Eq. (6.33) is

$$X^{n+1} = \underset{X}{\operatorname{argmin}} \mathcal{R}\left(X; X^n\right). \tag{6.129}$$

To prove that $\mathcal{F}$ is a Lyapunov functional of the dynamics, we consider an homogeneous problem with $\mathcal{W}(X; V) = 0$, and we evaluate the Rayleighian at X^{n+1}

$$\mathcal{R}\left(X^{n+1}; X^n\right) = \frac{\mathcal{F}(X^{n+1})}{\Delta t^n} + \mathcal{D}\left(\frac{X^{n+1} - X^n}{\Delta t^n}; X^n\right), \tag{6.130}$$

and X^n

$$\mathcal{R}\left(X^n; X^n\right) = \frac{\mathcal{F}(X^n)}{\Delta t^n} + \mathcal{D}\left(0; X^n\right) = \frac{\mathcal{F}(X^n)}{\Delta t^n}. \tag{6.131}$$

From the discrete variational principle in Eq. (6.129), we know that X^{n+1} minimizes $\mathcal{R}$, therefore $\mathcal{R}\left(X^{n+1}; X^n\right) - \mathcal{R}\left(X^n; X^n\right) \leq 0$. This leads us to

$$0 \geq \mathcal{R}\left(X^{n+1}; X^n\right) - \mathcal{R}\left(X^n; X^n\right) \tag{6.132}$$

$$= \frac{\mathcal{F}(X^{n+1}) - \mathcal{F}(X^n)}{\Delta t^n} + \mathcal{D}\left(\frac{X^{n+1} - X^n}{\Delta t^n}; X^n\right) \tag{6.133}$$

$$\geq \frac{\mathcal{F}(X^{n+1}) - \mathcal{F}(X^n)}{\Delta t^n}, \tag{6.134}$$

where we have used the fact that by assumption $\mathcal{D}(V;X) \geq 0$. Eq.(6.132) therefore results in

$$\mathcal{F}(X^{n+1}) \leq \mathcal{F}(X^n), \tag{6.135}$$

which finally proves that $\mathcal{F}$ is a Lyapunov functional of the discrete dynamics. We observe that the discretization of $\dot{\mathcal{F}}$ through the difference $\mathcal{F}(X^{n+1}) - \mathcal{F}(X^n)$ means that the time-step Δt^n is constrained not by stability but by accuracy and the solvability of the non-linear problem.

Considering the time discretization described above, we can discretize the time evolution of the system given by Eq. (6.124) in a general non-uniform grid $(t^1, ..., t^N)$, with $\Delta t^n = t^{n+1} - t^n$ and $n = 0, ..., N-1$. The Nitsche-Lagrangian $\mathcal{N}$ then becomes

$$\begin{aligned}\mathcal{N}^n\left[\boldsymbol{\varphi}, \boldsymbol{\psi}; \boldsymbol{\varphi}^n, \boldsymbol{\psi}^n\right] = \frac{\mathcal{F}_e\left[\boldsymbol{\varphi}\right]}{\Delta t^n} + \frac{\mathcal{F}_\phi\left[\boldsymbol{\varphi}\right]}{\Delta t^n} + \mathcal{D}_f\left[\frac{\boldsymbol{\psi} - \boldsymbol{\psi}^n}{\Delta t^n}; \boldsymbol{\psi}^n\right] \\ + \mathcal{W}\left[\frac{\boldsymbol{\varphi} - \boldsymbol{\varphi}^n}{\Delta t^n}, \frac{\boldsymbol{\psi} - \boldsymbol{\psi}^n}{\Delta t^n}; \boldsymbol{\varphi}^n, \boldsymbol{\psi}^n\right] + \mathcal{C}\left[\frac{\boldsymbol{\varphi} - \boldsymbol{\varphi}^n}{\Delta t^n}, \frac{\boldsymbol{\psi} - \boldsymbol{\psi}^n}{\Delta t^n}; \boldsymbol{\varphi}^n, \boldsymbol{\psi}^n\right],\end{aligned} \tag{6.136}$$

where $\mathcal{C}$ includes the penalty term for the incompressibility constraint of the fluid domain and the interfacial kinematic conditions addressed with the Nitsche consistency integrals along with the penalty term as seen in Eq. (6.114). Therefore the discreate time evolution of $\boldsymbol{\varphi}$ and $\boldsymbol{\psi}$ can be obtained by the Onsager's variational principle

$$\left\{\boldsymbol{\varphi}^{n+1}, \boldsymbol{\psi}^{n+1}\right\} = \underset{\boldsymbol{\varphi}, \boldsymbol{\psi}}{\operatorname{argmin}} \mathcal{N}^n\left[\boldsymbol{\varphi}, \boldsymbol{\psi}; \boldsymbol{\varphi}^n, \boldsymbol{\psi}^n\right]. \tag{6.137}$$

6.5.3 The finite element spaces

This section details the spatial discretization of the continuum model presented in Sec. 6.3 and 6.4, establishing the final computational model. The transition from the continuous to the discrete form is achieved in several steps. We first introduce the hybrid fitted-CutFEM framework, defining the mesh configurations and the corresponding finite element spaces. Subsequently, we address the main numerical challenges inherent to this unfitted approach: the stabilization technique for small cut cells and the method for numerical integration over their complex geometries. The section concludes with the presentation of the fully discretized governing equations. The formulation will be carried out in a two-dimensional setting and subsequently transformed into an axisymmetric one.

Computational domain

The continuum domain $\Omega \subset \mathbb{R}^d$, where $d = \{2, 3\}$ is the spatial dimensionality, at any time t is partitioned into a solid domain, $\Omega_e(t)$, and a fluid domain, $\Omega_f(t)$, such that $\Omega = \Omega_e(t) \cup \Omega_f(t)$. The two domains are separated by the non-material moving-fluid solid interface $\Gamma(t) = \partial\Omega_e(t) \cap \partial\Omega_f(t)$ as represented in the left part of Fig. 6.6. To discretize the system, we employ a hybrid meshing strategy that treats the fluid and solid domains with distinct approaches. The adopted decomposition is illustrated in Fig.6.6b, and the complete computational domain is represented in Fig.6.6c. The fluid domain, $\Omega_f(t)$, is discretized using a conforming, body-fitted unstructured mesh of d-simplexes, denoted

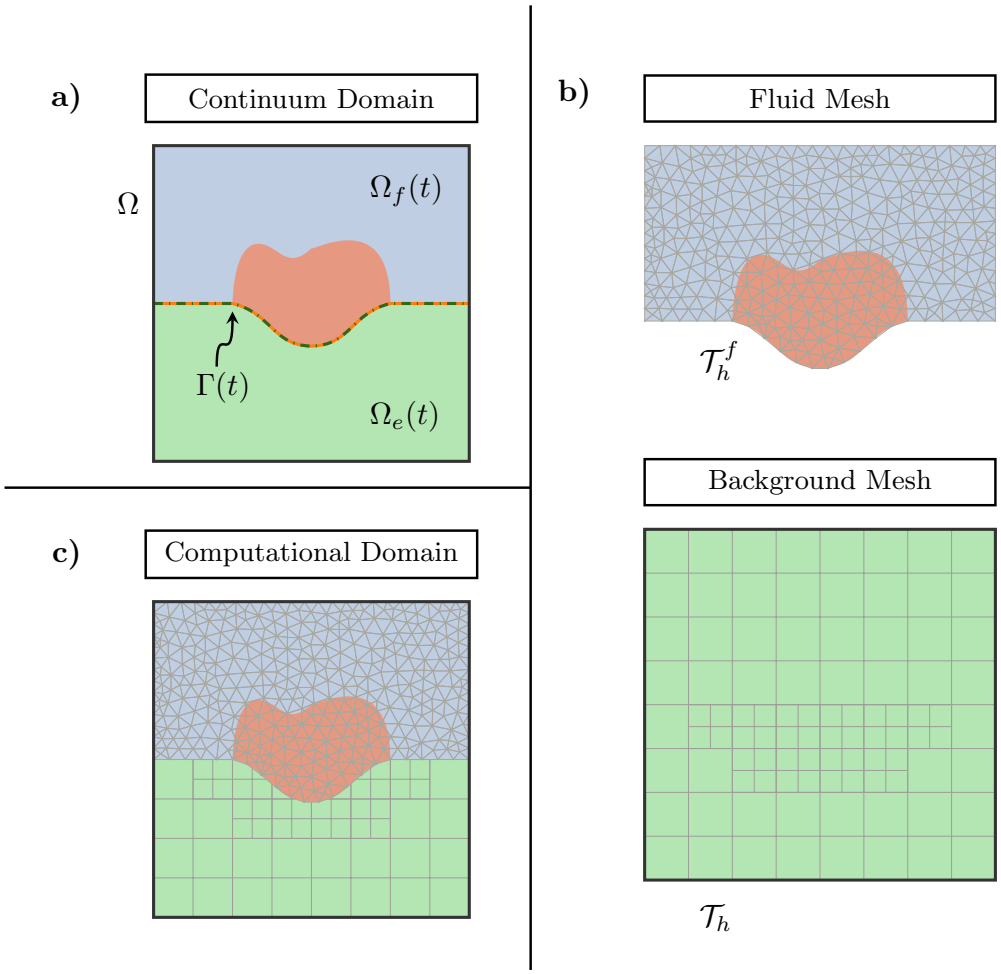

Figure 6.6: *Schematic of the hybrid fitted-unfitted discretization process. a) Continuum domain Ω composed of the solid $\Omega_e(t)$ and the fluid $\Omega_f(t)$. b) Generated meshes: a body-fitted mesh for the fluid $\mathcal{T}_h^f$ and a non-conforming background grid for the immersed solid $\mathcal{T}_h$. c) Computational domain, representing the union of the fitted fluid mesh and the active elements of the unfitted solid mesh.*

as $\mathcal{T}_h^f$. The facets of this mesh align with the fluid-solid interface $\Gamma(t)$, as illustrated in Fig. 6.6b. In contrast, the solid domain, $\Omega_e(t)$, is handled with an unfitted approach, where it is immersed in a background mesh that tessellates the entire domain Ω, and it is denoted as $\mathcal{T}_h$. This is a structured non-conforming adaptive mesh of hypercubes (d-cubes), with a dynamic tree-based refinement (quadtree/octree), as illustrated in Fig. 6.6b. A crucial 2:1 balance condition is enforced, meaning the refinement level of any two adjacent cells can differ by at most one [Badia et al., 2020]. This requirement, which is a prerequisite for the subsequently introduced aggregation technique [Badia et al., 2018b,a, 2021], guarantees smooth mesh gradation and simplifies the constraints for hanging nodes, ensuring their dependence solely on completely resolved nodes rather than other hanging nodes.

Let T be a generic cell in the background mesh $T \in \mathcal{T}_h$. As is common in the unfitted methods, we define the set of *active elements* for the solid discretization, $\mathcal{T}_h^{\text{act}}$, as the subset of the background cells

$$\mathcal{T}_h^{\text{act}} = \{T \in \mathcal{T}_h : T \cap \Omega_e(t) \neq \emptyset\}. \tag{6.138}$$

Conversely, we can also define the set of *inactive elements*, $\mathcal{T}_h^{\text{inact}}$, as the subset of all the background cells that are completely outside the solid domain:

$$\mathcal{T}_h^{\text{inact}} = \{T \in \mathcal{T}_h : T \cap \Omega_e(t) = \emptyset\}. \tag{6.139}$$

These inactive elements do not contribute to the system of equations and are thus computationally ignored and excluded from the assembly process. Therefore, $\{\mathcal{T}_h^{\text{act}}, \mathcal{T}_h^{\text{inact}}\}$ is a partition of $\mathcal{T}_h$, as shown in Fig. 6.7a. For any cell T we can now define the volume (or area) fraction as $\eta_T := |T \cap \Omega_e(t)|/|T|$, where $|\cdot|$ denotes the measure (i.e., area in 2D or volume in 3D), and we also introduce a user-defined parameter $\eta_0 \in (0, 1]$, which represents the threshold value of volume (or area) fraction under which an element is considered ill-posed. Therefore, we can partition the set of active elements $\mathcal{T}_h^{\text{act}}$ into two subsets, namely the set of well-posed cells represented by $\mathcal{T}_h^W$ for which $\eta_T \geq \eta_0$, and the set of ill-posed cells $\mathcal{T}_h^I$ for which $0 < \eta_T < \eta_0$. The partition $\{\mathcal{T}_h^W, \mathcal{T}_h^I\}$ of the active set $\mathcal{T}_h^{\text{act}}$ is represented in Fig. 6.7b.

Multi-parent aggregation technique

To resolve the numerical instabilities caused by the ill-posed elements $\mathcal{T}_h^I$, we employ a multi-parent aggregation technique inspired by the Aggregation Finite Element Method (agFEM) of Badia et al. [2018b,a, 2021]. While standard agFEM creates a partition of the mesh into disjoint "macro-elements," our approach introduces a more flexible coupling where an ill-posed cell is stabilized by a set of well-posed neighbor elements.

To properly define this multi-parent aggregation technique, we first introduce the *optimal candidate root set map*, $S : \mathcal{T}_h^{\text{act}} \to 2^{\mathcal{T}_h^W}$, which associates to each active cell $T \in \mathcal{T}_h^{\text{act}}$. a set of well-posed optimal root cells $S(T) \in 2^{\mathcal{T}_h^W}$. This multi-parent relationship is established by a modified cell aggregation algorithm, which iteratively assigns parents to ill-posed cells. The algorithm is as follows:

1. All the well-posed cells $T \in \mathcal{T}_h^W$ are marked as "touched" and assigned themselves as their own root optimal candidate, i.e. $S(T) = \{T\}$. All the ill-posed cells $T \in \mathcal{T}_h^I$ are marked as "untouched."

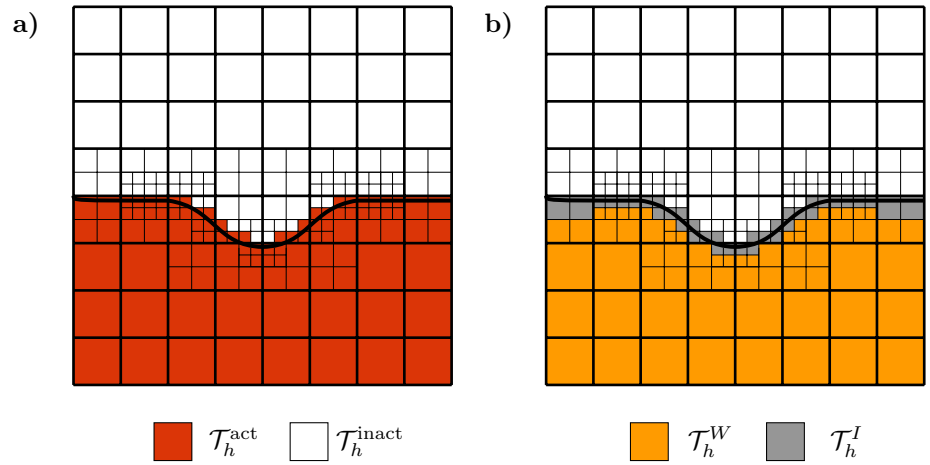

Figure 6.7: *Classification of the background mesh elements. a) The background mesh $\mathcal{T}_h$ is partitioned into active ($\mathcal{T}_h^{act}$) and inactive ($\mathcal{T}_h^{inact}$) elements. b) The active set $\mathcal{T}_h^{act}$ is further subdivided into the sets of well-posed ($\mathcal{T}_h^{W}$) and ill-posed ($\mathcal{T}_h^{I}$) cells.*

2. For each "untouched" cell T, we identify a set of adjacent, already "touched" candidate neighbors, $\mathcal{L}(T)$. This set contains all the touched cells T' that share a facet F with T whose intersection with the physical domain of the solid matrix is non-empty ($F \cap \Omega_e(t) \neq \emptyset$).

3. We construct the set of all possible root candidates for the untouched cell T, denoted as $\mathcal{U}(T)$, as the union of all the parent set of all its "touched" neighbors:

$$\mathcal{U}(T) = \bigcup_{T' \in \mathcal{L}(T)} S(T'). \tag{6.140}$$

4. Using the *closest root cell criterion* from Badia et al. [2021], we identifies the optimal root candidates as

$$S(T) = \underset{T^* \in \mathcal{U}(T)}{\operatorname{argmin}}\ \tilde{d}(T, T^*) \tag{6.141}$$

This expression returns the set of all the root candidates that achieve the minimum distance between the ill-posed element T and the root candidate T^*, defined as

$$\tilde{d}(T, T^*) \doteq \frac{\max\limits_{\gamma \in \mathcal{F}^0_{T^*},\, \delta \in \mathcal{F}^0_T} \|\mathbf{x}^\gamma - \mathbf{x}^\delta\|_\infty}{\max\limits_{\gamma,\, \gamma' \in \mathcal{F}^0_{T^*}} \|\mathbf{x}^\gamma - \mathbf{x}^{\gamma'}\|_\infty}, \tag{6.142}$$

where $\mathcal{F}^0_T$ denotes the sets of vertices of T,$\mathcal{F}^0_{T^*}$ denotes the sets of vertices of T^*, $\mathbf{x}^\bullet$ the coordinates of vertex $\bullet$, and $\|\cdot\|_\infty$ the infinity norm.

5. We mark as touched all the cells for which we identified their optimal root candidates set.

6. We repeat steps 2 to 5 until all the cells $T \in \mathcal{T}_h^{\text{act}}$ have their optimal root candidates set.

The output of this aggregation scheme is the parent set map, S, which associates at each active element $T \in \mathcal{T}_h^{\text{act}}$ the set of well-posed optimal root cells $S(T) \in 2^{\mathcal{T}_h^W}$. The iterative nature of the devised aggregation strategy is depicted in Fig. 6.8.

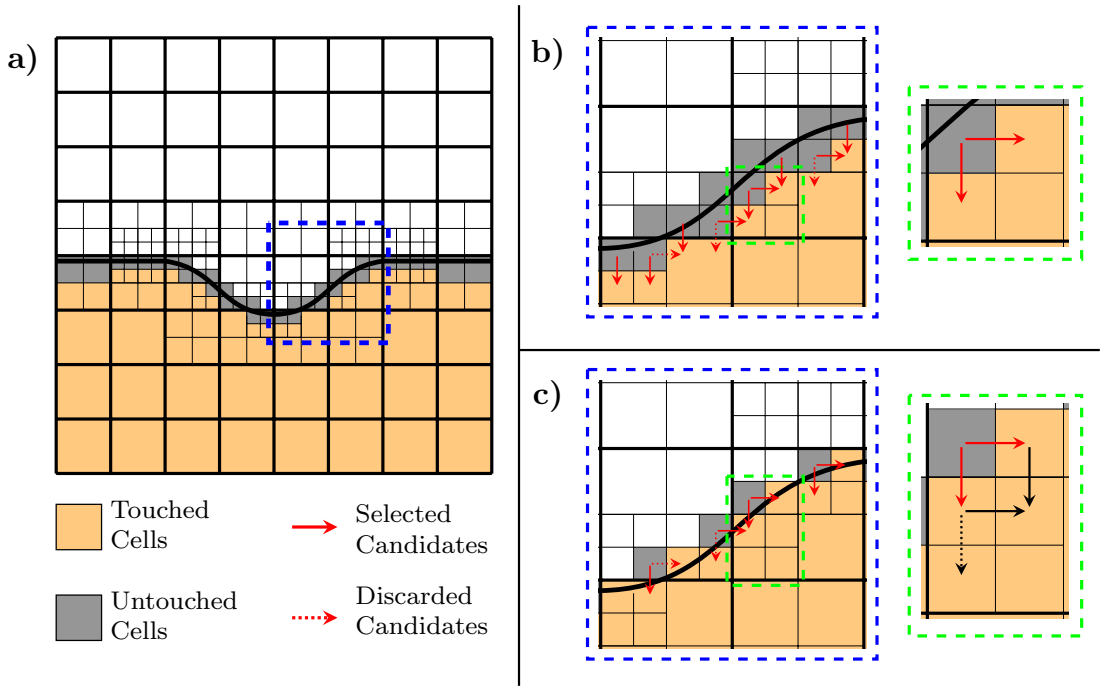

Figure 6.8: *Multi-parent iterative aggregation scheme. a) The process begins with the well-posed cells $\mathcal{T}_h^W$ marked as "touched" and the ill-posed cells $\mathcal{T}_h^I$ marked as "untouched." b) First aggregation iteration (Zoom). "Untouched" cells adjacent to the initial "touched" cells are aggregated. The green frame highlights the case of multi-parent aggregation, where an ill-posed cell is assigned two parent cells. c) Second aggregation iteration (Zoom). The aggregation process is repeated with the second layer of "untouched" cells. The green frame shows an "untouched" cell, whose neighbors were aggregated in the previous iteration. The process is repeated until the complete "touching" of all the active cells.*

Boundary conditions

As established, the continuum domain Ω can be partitioned into the elastic matrix, $\Omega_e(t)$, and fluid, $\Omega_f(t)$, subdomains. The boundaries of these subdomains are classified as either external, where essential (Dirichlet) conditions are prescribed, or as the internal fluid-solid interface. In particular, as shown in Fig. 6.9, we denote the Dirichlet boundary for the solid and for the fluid as Γ_D^e and Γ_D^f, respectively. The solid-fluid interface, as already specified, is denoted as $\Gamma(t)$.

The essential boundary conditions prescribed on the external boundary Γ_D^e and Γ_D^f, are imposed strongly. This is achieved by directly constraining the finite element function spaces, as detailed in the following section. On the other hand, the continuity and kinematic conditions on the moving fluid-solid interface, $\Gamma(t)$ are enforced weakly using the Nitsche's method, as presented in Sec. 6.5.1. This provides the flexibility needed to couple the two different mesh types.

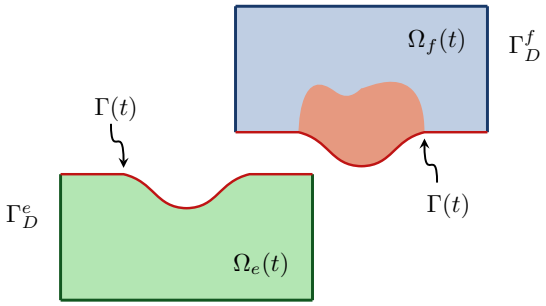

Figure 6.9: *Continuum domain subdivision, showing the partitioning of the boundary into the external Dirichlet boundary for the elastic matrix (Γ_D^e) and fluid (Γ_D^f), and the internal fluid-solid interface ($\Gamma(t)$).*

Hybrid fitted-aggregated finite element space

The system of equations is going to be discretized into a global finite element space $\mathcal{V}_h$, which is constructed from two different spaces: one for the elastic matrix domain, $\mathcal{V}_h^e$, and one for the fluid domain, $\mathcal{V}_h^f$. The essential (Dirichlet) boundary conditions, introduced in the previous section, are here imposed strongly by enforcing them directly into the definition of the finite element spaces. For the sake of simplicity, the formulation is presented for a generic scalar-valued field, but it can be straightforwardly generalized to a vector-valued field by considering each of its components separately.

The finite element space for the fluid domain. $\mathcal{V}_h^f$, is a standard continuous Galerkin space of linear polynomials defined on the body-fitted mesh of d-simplices $\mathcal{T}_h^f$. The union of the elements in this mesh forms the discrete fluid domain $\Omega_h^f = \bigcup_{T\in\mathcal{T}_h^f} T$. This space is constrained to satisfy the essential boundary conditions on Γ_D^f. The resulting finite element space is therefore:

$$\mathcal{V}_h^f = \{v_h \in C^0(\Omega_h^f) : v_h|_T \in \mathcal{P}^1(T), \forall\, T \in \mathcal{T}_h^f, \text{ and } v_h = g_h^f \text{ on } \Gamma_D^f\}, \tag{6.143}$$

where $\mathcal{P}^1(T)$ is the space of linear polynomials on an element T and g_h^f is a suitable finite element interpolant of the boundary data function g^f defined on Γ_D^f.

The finite element space for the elastic matrix, $\mathcal{V}_h^e$, is defined on the active part of the background mesh, $\mathcal{T}_h^{\text{act}}$. Its construction is more sophisticated than that for the fluid domain, as it must satisfy three types of constraints: continuity across hanging nodes, stabilization via the multi-parent aggregation technique, and the prescribed essential boundary conditions on Γ_D^e. Following the framework of Badia et al. [2021], we begin by defining an initial unconstrained finite element space of linear polynomials on the active mesh:

$$\mathcal{V}_h^{e,\text{uc}} = \{v_h \in L^2(\Omega_h^e) : v_h|_T \in \mathcal{Q}^1(T), \forall\, T \in \mathcal{T}_h^{\text{act}}\}, \tag{6.144}$$

where $\Omega_h^e = \bigcup_{T\in\mathcal{T}_h^{\text{act}}} T$ is the discrete solid domain and $\mathcal{Q}^1(T)$ the space of bilinear (or trilinear for $d = 3$) polynomials defined on T. The functions in this initial space $\mathcal{V}_h^{e,\text{uc}}$ are generally discontinuous and do not satisfy the required stability or boundary conditions. To construct the final, stable, and continuous solid space, $\mathcal{V}_h^e$, we apply two sequential sets of linear constraints to the DOFs of $\mathcal{V}_h^{e,\text{uc}}$. This two-step process ensures that the different types of constraints are applied without conflict, as will be detailed next.

Given that $\mathcal{T}_h$ is a non-conforming 2:1 balance tree-based mesh, the intersection between adjacent cells is either a full facet of both cells or a full facet of the more refined cell, which corresponds to a portion of a facet of the coarser cell as shown in Fig. 6.10a. We adopt the formal geometric properties from Assumption 2.1 of Badia et al. [2021]. The presence of these non-conforming intersections requires a partition of the degrees of freedom (DOFs) associated with the active mesh, $\mathcal{T}_h^{\text{act}}$, which we denote with Σ, into two disjoint sets:

- the set of *free* DOFs Σ^{F}, which are not constrained by neighboring cells
- the set of *hanging* DOFs Σ^{H}, whose values will be constrained by the free DOFs of the adjacent coarser cell to ensure continuity.

The partition of the DOFs $\Sigma = \Sigma^{\text{F}} \cup \Sigma^{\text{H}}$ into free and hanging sets, illustrated in Fig. 6.10b, allows for the construction of a continuous, or conforming, finite element space. To enforce continuity, the value of each hanging DOF, v_h^σ for $\sigma \in \Sigma^{\text{H}}$, is constrained to be an interpolation of the DOFs of the adjacent coarser cell. We call the set of free DOFs on the coarser cell that constrain a hanging DOF σ the set of *master* DOFs, denoted $\mathcal{M}_\sigma^H \subset \Sigma^F$. The constraint is a linear relation of the form:

$$v_h^\sigma = \sum_{\sigma'\in\mathcal{M}_\sigma^{\text{H}}} C_{\sigma\sigma'}^{\text{H}} v_h^{\sigma'} \quad \forall\, \sigma \in \Sigma^{\text{H}}, \tag{6.145}$$

where the interpolation weights are given by the values of the master basis functions evaluated at the hanging node's location, i.e., $C_{\sigma\sigma'}^{\text{H}} = N^{\sigma'}(\mathbf{x}^\sigma)$. The standard conforming finite element space, denoted by $\mathcal{V}_h^{e,\text{conf}}$, can now be defined as the subspace of $\mathcal{V}_h^{e,\text{uc}}$ whose functions satisfy all the hanging node constraints:

$$\mathcal{V}_h^{e,\text{conf}} = \{v_h \in \mathcal{V}_h^{e,\text{uc}} : v_h^\sigma = \sum_{\sigma'\in\mathcal{M}_\sigma^{\text{H}}} C_{\sigma\sigma'}^{\text{H}} v_h^{\sigma'} \text{ for all } \sigma \in \Sigma^{\text{H}}\}. \tag{6.146}$$

The conforming space $\mathcal{V}_h^{e,\text{conf}}$ remains numerically unstable due to the presence of the ill-posed cut cells. To resolve this, we introduce a final set of constraints derived from our multi-parent aggregation scheme, which define the stable aggregated finite element

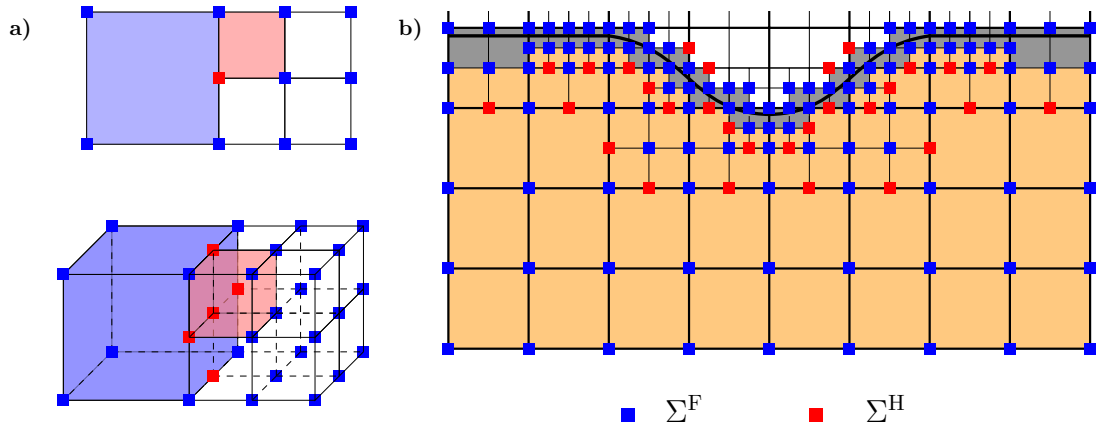

Figure 6.10: *Non-conforming mesh geometry and the resulting DOF partition. a) Intersection between two adjacent non-conforming cells in 2D and 3D, which creates hanging nodes. b) The corresponding partition of the degrees of freedom (DOFs) on the active mesh, $\mathcal{T}_h^{act}$, into the set of free DOFs (Σ^F) and hanging DOFs (Σ^H)*

space, $\mathcal{V}_h^{e,\mathrm{agg}}$, as a subset of $\mathcal{V}_h^{e,\mathrm{conf}}$. The construction of this stable space requires constraining the DOFs associated with the previously defined ill-posed cells, $\mathcal{T}_h^I$, to the DOFs associated with well-posed cells $\mathcal{T}_h^W$. To formalize this, we introduce a finer partition of all the DOFs, Σ. We first classify the DOFs into well-posed Σ^{W} or ill-posed Σ^{I} depending on if they have local support in at least one well-posed cell or not, respectively. We then subdivide these sets based on whether the DOFs are free or hanging, collectively obtaining the partition $\Sigma = \Sigma^{\mathrm{W,F}} \cup \Sigma^{\mathrm{W,H}} \cup \Sigma^{\mathrm{I,F}} \cup \Sigma^{\mathrm{I,H}}$, illustrated in Fig. 6.11. To ensure the dependencies between constrained degrees of freedom are hierarchical and free of circular references, we adopt the criteria from Definition 2.3 of Badia et al. [2021]. This definition provides the conditions that a DOF σ has to meet in order to belongs to $\Sigma^{\mathrm{W,F}}$. Therefore, in the aggregate finite element space, the

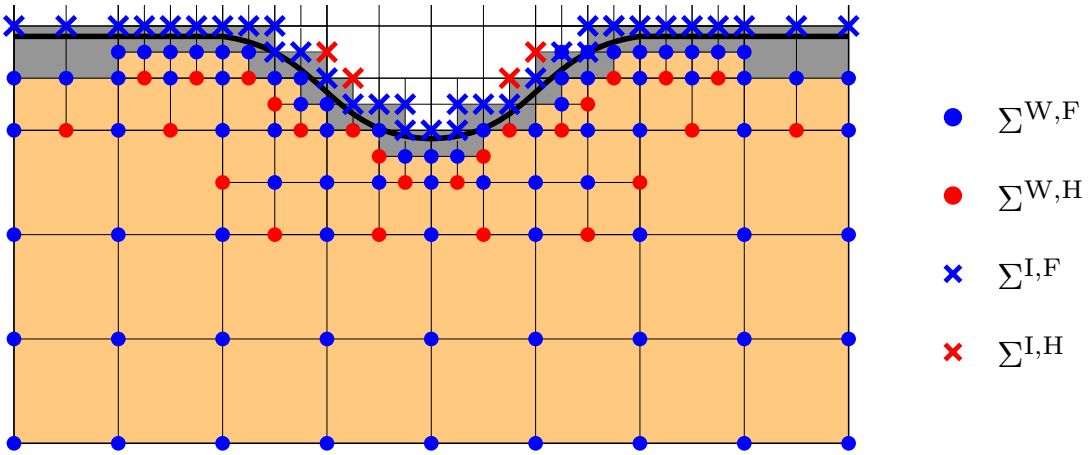

Figure 6.11: *Complete partition of the degrees of freedom (DOFs). The DOFs are first classified as well-posed or ill-posed, represented with circle or cross markers, and then further subdivided into free and hanging sets, graphically distinguished with the color blue and red, respectively.*

only independent degrees of freedom are the well-posed, free DOFs, $\Sigma^{\mathrm{W,F}}$. All other DOFs, which we collect into the set of constrained DOFs $\Sigma^{\mathrm{C}} = \Sigma^{\mathrm{W,H}} \cup \Sigma^{\mathrm{I,F}} \cup \Sigma^{\mathrm{I,H}}$, must be expressed as linear combinations of the independent DOFs in $\Sigma^{\mathrm{W,F}}$. The specific form of these linear constraints is adapted from the framework of Badia et al. [2021] to incorporate our multi-parent aggregation technique. Given a constrained DOF $\sigma \in \Sigma^{\mathrm{C}}$, we define its linear constraint based on which subset it belongs to:

- Well-Posed Hanging DOF
  If $\sigma \in \Sigma^{\mathrm{W,H}}$, it is constrained by the hanging nodes interpolation rule. In particular, as specified in the derivation of Eq. (6.145) for the creation of the conforming space $\mathcal{V}_h^{e,\mathrm{conf}}$, we identify the set of master DOFs $\mathcal{M}_\sigma^{\mathrm{H}} \subset \Sigma^{\mathrm{W,F}}$. Thus, given $v_h \in \mathcal{V}_h^{e,\mathrm{nc}}$ and $\sigma \in \Sigma^{\mathrm{W,H}}$, the constraint is then the standard continuity-enforcing relation:
  $$v_h^\sigma = \sum_{\tilde{\sigma} \in \mathcal{M}_\sigma^{\mathrm{H}}} C_{\sigma\tilde{\sigma}}^{\mathrm{H}} v_h^{\tilde{\sigma}} \quad \forall\, \sigma \in \Sigma^{\mathrm{W,H}} \tag{6.147}$$
  where $C_{\sigma\tilde{\sigma}}^{\mathrm{H}} = N^{\tilde{\sigma}}(\mathbf{x}^\sigma)$ are the interpolation weights and $N^{\tilde{\sigma}}$ is the Lagrangian basis function for the master DOF $\tilde{\sigma}$ evaluated at $\mathbf{x}^\sigma$.

- Ill-Posed Free DOF
  If $\sigma \in \Sigma^{\mathrm{I,F}}$, we must define its aggregation constraint by resolving all dependencies down to the set of well-posed, free DOFs. First, we identify the set of parent cells for σ by composing the parent set map $S : \mathcal{T}_h^{\mathrm{act}} \to 2^{\mathcal{T}_h^W}$ with an *ownership* map, $T^{\mathrm{own}} : \Sigma^{\mathrm{I,F}} \to \mathcal{T}_h^I$ which for any ill-posed DOFs returns a possible ill-posed cell T containing it [Verdugo et al., 2019]. We can now formally define the set of aggregated DOFs for σ, denoted $\mathcal{N}_\sigma^{\mathrm{ag}}$ as the union of all the DOFs located on the parent cells of σ:
  $$\mathcal{N}_\sigma^{\mathrm{ag}} = \bigcup_{T^{\mathrm{p}} \in K(\sigma)} \mathcal{I}(T^{\mathrm{p}}) \tag{6.148}$$
  where $\mathcal{I}(T^{\mathrm{p}})$ is the set of global DOFs associated with the parent cell T^{p}. In general, since K is defined in the power set of $\mathcal{T}_h^{\mathrm{W}}$, $\mathcal{N}_\sigma^{\mathrm{ag}}$ it can be composed of both free and hanging, well-posed DOFs. Due to the fact that we want to express the aggregation constraints as a linear combination of well-posed free DOFs, and since all $T^{\mathrm{p}} \in K(\sigma)$ are in $\mathcal{T}_h^{\mathrm{W}}$, we introduce the partition $\mathcal{N}_\sigma^{\mathrm{ag}} = \mathcal{N}_\sigma^{\mathrm{ag,F}} \cup \mathcal{N}_\sigma^{\mathrm{ag,H}}$, with $\mathcal{N}_\sigma^{\mathrm{ag,F}} \doteq \mathcal{N}_\sigma^{\mathrm{ag}} \cap \Sigma^{\mathrm{W,F}}$ and $\mathcal{N}_\sigma^{\mathrm{ag,H}} \doteq \mathcal{N}_\sigma^{\mathrm{ag}} \cap \Sigma^{\mathrm{W,H}}$. Recalling the case of well-posed hanging DOFs, we have that the set of masters of $\mathcal{N}_\sigma^{\mathrm{ag,H}}$ is given by $\bigcup_{\sigma' \in \mathcal{N}_\sigma^{\mathrm{ag,H}}} \mathcal{M}_{\sigma'}^H$. Therefore we can define the set of master DOFs of $\sigma \in \Sigma^{\mathrm{I,F}}$ as:
  $$\mathcal{M}_\sigma^{\mathrm{ag}} \doteq \mathcal{N}_\sigma^{\mathrm{ag,F}} \cup \left(\bigcup_{\sigma' \in \mathcal{N}_\sigma^{\mathrm{ag,H}}} \mathcal{M}_{\sigma'}^H \right). \tag{6.149}$$
  The two sets composing $\mathcal{M}_\sigma^{\mathrm{ag}}$ are not necessarily disjoint. Therefore, given $v_h \in \mathcal{V}_h^{e,\mathrm{conf}}$ and $\sigma \in \Sigma^{\mathrm{I,F}}$, the aggregation constraints can be written as a linear combination of well-posed DOF associated to σ
  $$v_h^\sigma = \sum_{\tilde{\sigma} \in \mathcal{M}_\sigma^{\mathrm{ag}}} C_{\sigma\tilde{\sigma}}^{\mathrm{A}} v_h^{\tilde{\sigma}}. \tag{6.150}$$

The final, composed weights, $C^{\mathrm{A}}_{\sigma\tilde{\sigma}}$, result from the composition of the aggregation and hanging node constraints. For a master DOF $\tilde{\sigma} \in \mathcal{M}^{\mathrm{ag}}_{\sigma}$, this final weight is given by the expression:

$$C^{\mathrm{A}}_{\sigma\tilde{\sigma}} = C^{\mathrm{ag}}_{\sigma\tilde{\sigma}} + \sum_{\sigma' \in \mathcal{N}^{\mathrm{ag,H}}_{\sigma} \text{ s.t. } \tilde{\sigma} \in \mathcal{M}^{\mathrm{H}}_{\sigma'}} C^{\mathrm{ag}}_{\sigma\sigma'} C^{\mathrm{H}}_{\sigma'\tilde{\sigma}}. \tag{6.151}$$

This formula combines the influence of the direct aggregation masters (C^{ag}) and the masters inherited from the hanging nodes (C^{H}). The aggregation weights C^{agg} form the basis of our discrete extension operator. For any constrained DOF σ_{c} and a DOF σ_{p} in its parent set $\mathcal{N}^{\mathrm{ag}}_{\sigma_{\mathrm{c}}}$, the weight is defined as:

$$C^{\mathrm{ag}}_{\sigma_{\mathrm{c}}\sigma_{\mathrm{p}}} = \begin{cases} \frac{N^{\sigma_{\mathrm{p}}}(\mathbf{x}^{\sigma_{\mathrm{c}}})}{n_p(\sigma_{\mathrm{c}})} & \text{if } \sigma_{\mathrm{p}} \in \mathcal{N}^{\mathrm{ag,F}}_{\sigma_{\mathrm{c}}} \\ 0 & \text{if } \sigma_{\mathrm{p}} \in \mathcal{N}^{\mathrm{ag,H}}_{\sigma_{\mathrm{c}}} \end{cases}, \tag{6.152}$$

where $n_p(\sigma_{\mathrm{c}}) = |K(\sigma_{\mathrm{c}})|$ is the total number of parent cells for σ_{c}. The denominator acts as a normalization factor, averaging the contributions from each parent cell to ensure a stable extension.

- Ill-Posed Hanging DOF
  If a DOF σ is both ill-posed and hanging ($\sigma \in \Sigma^{\mathrm{I,H}}$), the constraints are applied hierarchically. The primary constraint is the continuity-enforcing one due to the hanging node, which expresses σ in terms of its master DOFs, $\mathcal{M}^{H}_{\sigma}$. The final expression is then obtained by the composition of all subsequent dependencies.

  To formalize this, we partition the initial master set $\mathcal{M}^{H}_{\sigma}$ into its well-posed and ill-posed components, $\mathcal{M}^{H}_{\sigma} \cap \Sigma^{\mathrm{W,F}}$ and $\mathcal{M}^{H}_{\sigma} \cap \Sigma^{\mathrm{I,F}}$, respectively. The ill-posed masters must themselves be resolved down to a set of well-posed, free DOFs. By applying the logic from the previous case to each $\sigma' \in \mathcal{M}^{H}_{\sigma} \cap \Sigma^{\mathrm{I,F}}$, we obtain their respective master sets $\mathcal{M}^{\mathrm{ag}}_{\sigma'}$. Therefore, the final, resolved master set for σ, denoted $\mathcal{M}^{\mathrm{H,ag}}_{\sigma}$, is the union of the original well-posed masters and the resolved masters of the ill-posed ones:

$$\mathcal{M}^{\mathrm{H,ag}}_{\sigma} = \left(\mathcal{M}^{H}_{\sigma} \cap \Sigma^{\mathrm{W,F}}\right) \cup \left(\bigcup_{\sigma' \in \mathcal{M}^{H}_{\sigma} \cap \Sigma^{\mathrm{I,F}}} \mathcal{M}^{\mathrm{ag}}_{\sigma'} \right). \tag{6.153}$$

  The final constraint for σ is a linear combination of the DOFs in this resolved set:

$$v^{\sigma}_{h} = \sum_{\tilde{\sigma} \in \mathcal{M}^{\mathrm{H,ag}}_{\sigma}} C^{\mathrm{H,ag}}_{\sigma\tilde{\sigma}}\, v^{\tilde{\sigma}}_{h}. \tag{6.154}$$

  The final, composed weights $C^{\mathrm{H,ag}}_{\sigma\tilde{\sigma}}$, are found by combining the initial hanging node constraints with the aggregation constraints. The expression for the weight that a master DOF $\tilde{\sigma} \in \mathcal{M}^{\mathrm{H,ag}}_{\sigma}$, has on σ is:

$$C^{\mathrm{H,ag}}_{\sigma\tilde{\sigma}} = C^{\mathrm{H}}_{\sigma\tilde{\sigma}} + \sum_{\sigma' \in \mathcal{M}^{\mathrm{H}}_{\sigma} \cap \Sigma^{\mathrm{I,F}}} C^{\mathrm{H}}_{\sigma\sigma'} C^{\mathrm{A}}_{\sigma'\tilde{\sigma}}, \tag{6.155}$$

  where $C^{\mathrm{H}}_{\sigma\sigma'}$ is the initial hanging node weight (defined as zero if $\tilde{\sigma} \notin \left(\mathcal{M}^{H}_{\sigma} \cap \Sigma^{\mathrm{W,F}}\right)$), and $C^{\mathrm{A}}_{\sigma'\tilde{\sigma}}$ is the composed aggregation weight for the ill-posed free DOF $\sigma' \in \mathcal{M}^{H}_{\sigma} \cap \Sigma^{\mathrm{I,F}}$ (defined as zero if $\tilde{\sigma} \notin \bigcup_{\sigma' \in \mathcal{M}^{H}_{\sigma} \cap \Sigma^{\mathrm{I,F}}} \mathcal{M}^{\mathrm{ag}}_{\sigma'}$), as resolved in Eq. (6.152).

Having defined the constraints for all subsets of dependent DOFs, we can now formally define the final, stable finite element space for the solid domain. First, we unify the notation. For any constrained DOF $\sigma \in \Sigma^{\mathrm{C}}$, we define its master set $\mathcal{M}_\sigma$ and its corresponding constraint coefficients $C_{\sigma\sigma'}$ based on its classification:

$$\mathcal{M}_\sigma \doteq \begin{cases} \mathcal{M}_\sigma^{\mathrm{H}} & \text{if } \sigma \in \Sigma^{\mathrm{W,H}} \\ \mathcal{M}_\sigma^{\mathrm{ag}} & \text{if } \sigma \in \Sigma^{\mathrm{I,F}} \\ \mathcal{M}_\sigma^{\mathrm{H,ag}} & \text{if } \sigma \in \Sigma^{\mathrm{I,H}} \end{cases} \qquad C_{\sigma\sigma^*} \doteq \begin{cases} C_{\sigma\sigma*}^{\mathrm{H}} & \text{if } \sigma \in \Sigma^{\mathrm{W,H}} \\ C_{\sigma\sigma*}^{\mathrm{A}} & \text{if } \sigma \in \Sigma^{\mathrm{I,F}} \\ C_{\sigma\sigma*}^{\mathrm{H,ag}} & \text{if } \sigma \in \Sigma^{\mathrm{I,H}} \end{cases} . \tag{6.156}$$

Adopting this unified notation, the aggregated finite element space, $\mathcal{V}_h^{e,\mathrm{ag}}$, is defined as the subspace of the initial unconstrained space that satisfies all internal (hanging) and aggregation constraints:

$$\mathcal{V}_h^{e,\mathrm{ag}} = \{v_h \in \mathcal{V}_h^{e,\mathrm{uc}} : v_h^\sigma = \sum_{\sigma^* \in \mathcal{M}_\sigma} C_{\sigma\sigma^*} v_h^{\sigma^*} \text{ for all } \sigma \in \Sigma^{\mathrm{C}}\}. \tag{6.157}$$

Finally, the space used for the analysis, $\mathcal{V}_h^e$, is obtained by enforcing the essential (Dirichlet) boundary conditions on $\mathcal{V}_h^{e,\mathrm{ag}}$:

$$\mathcal{V}_h^e = \{v_h \in \mathcal{V}_h^{e,\mathrm{ag}} : v_h = g_h^e \text{ on } \Gamma_D^e\}, \tag{6.158}$$

where g_h^e is the discrete representation of the boundary data.

The final global space used in the analysis of the coupled fluid-structure problem, $\mathcal{V}_h$, is obtained from the Cartesian product of the individual constrained spaces $\mathcal{V}_h^f$ and $\mathcal{V}_h^e$:

$$\mathcal{V}_h = \mathcal{V}_h^f \times \mathcal{V}_h^e. \tag{6.159}$$

6.5.4 Numerical integration

The computation of the system matrices requires the numerical integration of the weak form over each domain. Given the use of a non-conforming background mesh for the solid and a conforming mesh for the fluid, different strategies are employed for each.

The integrals for the solid domain $\Omega_e(t)$ are computed over the non-conforming background mesh $\mathcal{T}_h$. Since this mesh does not align with the physical boundary Γ, a specialized integration strategy is required. The type of integration adopted depends on the classification of each element $T \in \mathcal{T}_h$ with respect to the solid domain $\Omega_e(t)$. We distinguish between three cases:

- $T \cap \Omega_e = \emptyset$. These are inactive elements that lie entirely outside the solid domain and therefore have a zero integrand. Their contribution to the stiffness matrix is null, and they are ignored during assembly.

- $T \subset \Omega_e$. These are internal elements that lie entirely inside the solid domain, and they contain a smooth integrand. For these, a standard Gauss quadrature rule is employed, using a 2x2 point scheme for quadrilateral elements (2x2x2 for hexahedra).

- $T \cap \Gamma(t) \neq \emptyset$. These are cut elements that are intersected by the physical boundary $\Gamma(t)$. For these cells, the domain of integration is the complex, arbitrary shape formed by the intersection $T \cap \Omega_e(t)$. Therefore, the standard Gauss quadrature

rules cannot be applied directly to such a domain; otherwise, they would yield highly inaccurate results. To resolve this, a sub-tessellation technique is used where the solid domain, $T \cap \Omega_e(t)$, is decomposed into a set of simpler, non-overlapping sub-elements (e.g., triangles or tetrahedra) [Moës et al., 1999, Sanders et al., 2012]. Only at this point a standard Gauss rule is then applied to each sub-element, and the results are summed to compute the correct integral for the cut cell.

For the fluid domain $\Omega_f(t)$, which is discretized using a body-fitted mesh of isoparametric triangular (or tetrahedral) elements $\mathcal{T}_h^f$, the integration is straightforward. A standard Gauss quadrature rule is therefore employed directly for each element, ensuring an accurate and efficient computation.

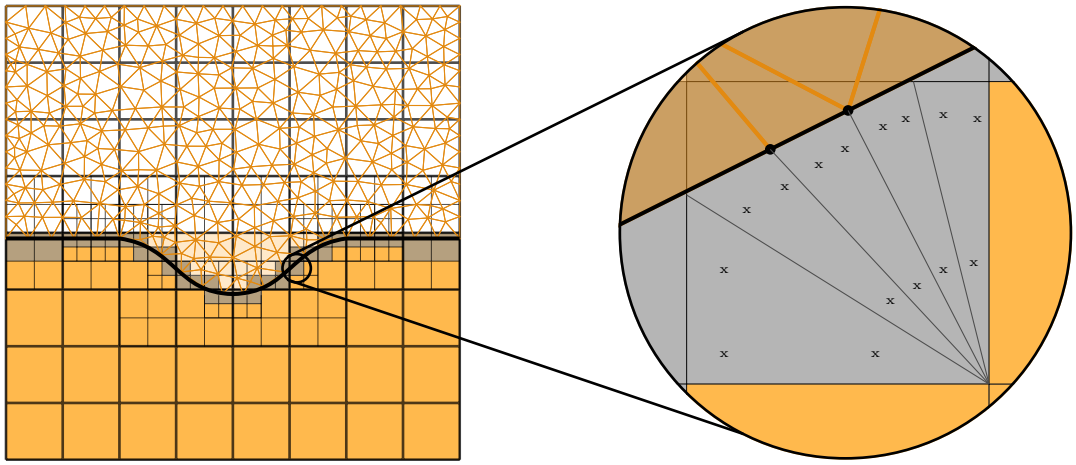

Figure 6.12: *Sub-tessellation of a Cut Element for Numerical Integration. In the left panel the overall computational domain is represented, while on the right is a zoomed-in view of a cut element sub-tessellated into integration triangles.*

6.5.5 Discretization of the governing equations

Having formally defined the time-discrete variational principle in Eq. (6.137) and constructed the stable, hybrid finite element space $\mathcal{V}_h$, the next step is to spatially discretize the minimization problem. This transforms the infinite-dimensional problem for the fields $\boldsymbol{\varphi}$ and $\boldsymbol{\psi}$ into a finite-dimensional system of nonlinear algebraic equations, which can then be solved numerically.

We begin by approximating the continuous fields with their discrete counterparts, which belong to the global coupled space $\mathcal{V}_h = \mathcal{V}_h^e \times \mathcal{V}_h^f$. To simplify the notation, we introduce a unified discrete field $\boldsymbol{\chi}_h$, such that:

$$\boldsymbol{\chi}_h(\mathbf{X}, t) = \begin{cases} \boldsymbol{\varphi}_h(\mathbf{X}, t) & \forall, \mathbf{X} \in \Omega_e^r(t) \\ \boldsymbol{\psi}_h(\mathbf{X}, t) & \forall, \mathbf{X} \in \Omega_f^r \end{cases} . \tag{6.160}$$

This discrete field is represented as a linear combination of global basis functions $N^a(\mathbf{X})$ and a set of time-dependent nodal degrees of freedom, $\boldsymbol{\chi}^a(t)$:

$$\boldsymbol{\chi}_h(\mathbf{X}, t) = \sum_a N^a(\mathbf{X}) \boldsymbol{\chi}^a(t). \tag{6.161}$$

Here, the shape functions N^a are constructed from the standard Lagrange polynomials, modified where necessary by the hanging node and aggregation constraints discussed in Sec. 6.5.3. The vectors $\boldsymbol{\chi}^a(t)$ contain the unknown nodal values of the field, which are the primary unknowns of our discrete problem.

It's important to point out that the entire formulation is developed from a Lagrangian point of view. This means that all kinematics are described with respect to an undeformed reference configuration. Direct consequence is that all spatial integrals defined over the time-dependent, deformed domains $(\Omega_e(t), \Omega_f(t))$ must be mapped to their corresponding reference domains $(\Omega_e^r(t), \Omega_f^r)$ for computation. The differential volume element in the deformed configuration, dV, is related to its material counterpart, dV_r, by the Jacobian J, which is the determinant of the deformation gradient $\mathbf{F}$:

$$dV = J\, dV_r \quad \text{where} \quad J = \det(\mathbf{F}) \quad \text{and} \quad \mathbf{F} = \frac{\partial \boldsymbol{\chi}}{\partial \mathbf{X}}. \tag{6.162}$$

Similarly, differential surface elements are related through Nanson's formula. This ensures all computations are performed on a fixed reference mesh.

Keeping in mind that the primary physical problem motivating this work is the study of a sessile biological tissue interacting with a substrate, and based on the experimental data found in literature, we assume that the body maintains an axisymmetric shape throughout its evolution. We therefore restrict our analysis to the axisymmetric case, using a cylindrical coordinate system (r, z, θ). The motion $\boldsymbol{\chi}$ occurs only in the r–z plane, and all field quantities are independent of the azimuthal coordinate θ. Consequently, the deformation gradient $\mathbf{F}$, which maps from the reference coordinates (R, Z, Θ) to the spatial coordinates (r, z, θ), takes the following matrix form in the cylindrical basis:

$$\mathbf{F} = \begin{bmatrix} \frac{\partial r}{\partial R} & \frac{\partial r}{\partial Z} & 0 \\ \frac{\partial z}{\partial R} & \frac{\partial z}{\partial Z} & 0 \\ 0 & 0 & \frac{r}{R} \end{bmatrix} = \begin{bmatrix} \tilde{\mathbf{F}} & \mathbf{0} \\ \mathbf{0}^T & \frac{r}{R} \end{bmatrix}. \tag{6.163}$$

Due to the fact that the metric in cylindrical coordinates is not Euclidean, we obtain the following expression for the jacobian and trace of $\mathbf{F}$

$$J = \frac{r}{R}\tilde{J}, \quad \mathrm{tr}\mathbf{F} = \frac{r}{R} + \mathrm{tr}\tilde{\mathbf{F}}. \tag{6.164}$$

All volume integrals are therefore performed over a 2D domain in the $R-Z$ plane, with the differential volume element given by $dV_r = 2\pi R\, dR\, dZ$. The detailed derivation of the residual and Jacobian components under these axisymmetric conditions is presented in Avenues for further research.

Discrete minimization problem and system of equations

For ease of representation, we here collect all nodal DOF vectors $\boldsymbol{\chi}^a(t)$ into a single global vector of unknowns, $\mathbf{d}(t) \in \mathbb{R}^m$, where m is the total number of degrees of freedom in the coupled system. The entire state of the discrete system at any time t is now uniquely described by this vector $\mathbf{d}$. Let us also denote with $\mathbf{d}^n$ the set of nodal DOFs at time t^n, thus $\mathbf{d}^n \equiv \mathbf{d}(t^n)$.

By substituting the finite element approximation $\boldsymbol{\chi}_h(\mathbf{X}, t)$ into the continuous functional $\mathcal{N}^n$ defined in Eq. (6.136), we transform it into its discrete counterpart, $\mathcal{N}_h^n$. This is now a scalar-valued function that depends only on the global vector of unknowns,

$\mathbf{d}^{n+1}$, at time t^{n+1} and is parameterized by the known solution from the previous step, $\mathbf{d}^n$. The Onsager's variational principle from Eq. (6.137) is thus transformed into a finite-dimensional, unconstrained minimization problem for the vector $\mathbf{d}^{n+1}$:

$$\mathbf{d}^{n+1} = \underset{\mathbf{d}\in\mathbb{R}^m}{\operatorname{argmin}}, \mathcal{N}_h^n \left[\mathbf{d}; \mathbf{d}^n\right]. \tag{6.165}$$

This minimization problem requires finding the stationary point of the functional $\mathcal{N}_h^n(\mathbf{d})$, which can be formally achieved by stating that the first variation of the functional must be zero for all admissible variations of the discrete field. Therefore, we can introduce an arbitrary variation of the discrete field, $\delta\boldsymbol{\chi}_h$, which plays the role of the test function in the standard Galerkin setting, and it must belong to the same discrete space $\mathcal{V}_h$. The stationarity condition is therefore:

$$\delta\mathcal{N}_h^n = 0 \quad \forall, \delta\boldsymbol{\chi}_h \in \mathcal{V}_h. \tag{6.166}$$

We can express the variation of the discrete functional, $\delta\mathcal{N}_h^n$, in terms of the gradient of the functional and the corresponding variation of the nodal DOFs, $\delta\mathbf{d}$, applying the chain rule as:

$$\delta\mathcal{N}_h^n = \frac{\partial\mathcal{N}_h^n}{\partial\mathbf{d}} \cdot \delta\mathbf{d} = \mathbf{R}(\mathbf{d}) \cdot \delta\mathbf{d}, \tag{6.167}$$

where $\mathbf{R}(\mathbf{d})$ is the usually called residual vector. Since the stationarity condition $\mathbf{R}(\mathbf{d}) \cdot \delta\mathbf{d} = 0$ must hold for any arbitrary variation $\delta\mathbf{d}$, it mathematically implies that the residual vector itself must be zero. This links the variational principle and the final algebraic system we need to solve:

$$\delta\mathcal{N}_h^n = 0 \quad \Longleftrightarrow \quad \mathbf{R}(\mathbf{d}) = \mathbf{0}. \tag{6.168}$$

Discrete residual and Jacobian

To implement the Newton-Raphson algorithm, we must derive the explicit algebraic expression for the residual vector $\mathbf{R}$ and for the Jacobian matrix $\mathbf{J}$. The global residual vector, $\mathbf{R}$, which we previously formally defined as the gradient of the discrete functional $\mathcal{N}_h^n$ with respect to the global vector of degrees of freedom, $\mathbf{d}$, practically is not computed directly. Instead, it is formed by assembling contributions calculated at the nodal level. We therefore derive the nodal residual vector, $\mathbf{R}^a$, for each node a, where its components are obtained by taking the partial derivative of the functional with respect to the nodal degrees of freedom $\boldsymbol{\chi}^a = [\chi_1^a, \chi_2^a, \dots]^T$. The i-th component of the residual at node a is:

$$R_i^a := \frac{\partial\mathcal{N}_h^n}{\partial\chi_i^a}. \tag{6.169}$$

Since the functional is a sum of elemental contributions ($\mathcal{N}_h^n = \sum_T (\mathcal{N}_h^n)_T$), the nodal residual is computed by summing the contributions from all elements T connected to node a. These nodal vectors $\mathbf{R}^a$ are then assembled into the global residual vector $\mathbf{R}$ according to the system's topology. Analogously, the global Jacobian matrix, $\mathbf{J}$, is formally defined as the Hessian of the discrete functional $\mathcal{N}_h^n$. the global Jacobian matrix $\mathbf{J}$ is the assembly of the elemental jacobian ,matrices, $\mathbf{J}_T$, for each element T in the computational domain. This elemental Jacobian matrix, $\mathbf{J}_T$, is a dense matrix that couples all degrees of freedom associated with T, and its components are given by

$$(J_T)_{im}^{ab} := \frac{\partial\left(\mathcal{N}_h^n\right)_T}{\partial\chi_m^b\partial\chi_i^a}, \tag{6.170}$$

where a and b are local node indices within element T These elemental Jacobian matrices are then assembled into the sparse global Jacobian $\mathbf{J}$ according to the system's topology.

The explicit derivation of the contribution of each term in the functional to the residual $\mathbf{R}$ and Jacobian $\mathbf{J}$ is, for the sake of clarity of the main text, presented in Avenues for further research. Here, the detailed derivations for the standard volume integral contributions are illustrated. The contributions from the surface integral terms, which are exceptionally complex to derive by hand, were implemented using the automatic differentiation capabilities of the high-performance parallel library for finite element Hiperlife [Santos Oliván et al., 2021]. This approach ensures an exact computation of the derivatives without the need for manual implementation of the complex underlying expressions.

Newton-Raphson method

The nonlinear system of algebraic equations, $\mathbf{R}(\mathbf{d}) = \mathbf{0}$, is solved using the iterative Newton-Raphson method (see, e.g., Belytschko et al. [2013]). The procedure generates a sequence of approximations $\mathbf{d}_k$ that iteratively converge to the solution $\mathbf{d}^{n+1}$. At each iteration k, the residual is linearized through a first-order Taylor expansion around the current guess $\mathbf{d}_k$. Subsequently, by setting the linearized residual to zero, we obtain a linear system for the unknown increment, $\Delta\mathbf{d}_k = \mathbf{d}_{k+1} - \mathbf{d}_k$:

$$\mathbf{J}(\mathbf{d}_k)\Delta\mathbf{d}_k = -\mathbf{R}(\mathbf{d}_k). \tag{6.171}$$

The Jacobian matrix, $\mathbf{J}(\mathbf{d}_k)$, is the Hessian of the functional $\mathcal{N}_h^n$, evaluated at the current iterate $\mathbf{d}_k$:

$$\mathbf{J}(\mathbf{d}_k) = \left.\frac{\partial \mathbf{R}}{\partial \mathbf{d}}\right|_{\mathbf{d}_k} = \left.\frac{\partial^2 \mathcal{N}_h^n}{\partial \mathbf{d}\,\partial \mathbf{d}}\right|_{\mathbf{d}_k}. \tag{6.172}$$

The standard algorithm for a single Newton-Raphson step is initialized by setting the iteration counter $k = 0$ and the initial guess $\mathbf{d}_0 = \mathbf{d}^n$. An iteration loop is then performed where, at each step k, the residual $\mathbf{R}(\mathbf{d}_k)$ and Jacobian $\mathbf{J}(\mathbf{d}_k)$ are assembled. The linear system $\mathbf{J}(\mathbf{d}_k)\Delta\mathbf{d}_k = -\mathbf{R}(\mathbf{d}_k)$ is solved for the increment $\Delta\mathbf{d}_k$, and the solution is updated via $\mathbf{d}_{k+1} = \mathbf{d}_k + \Delta\mathbf{d}_k$. This loop is therefore repeated until a convergence criterion is met. Upon convergence, the solution for the time step is set as $\mathbf{d}^{n+1} = \mathbf{d}_{k+1}$.

6.6 Numerical experiments

This section outlines a series of numerical experiments aimed at validating the theoretical and computational framework established in this thesis. The main objective is to demonstrate the model's accuracy, robustness, and predictive capabilities for handling complex fluid-structure interaction phenomena, specifically oriented for soft matter and biological systems.

The employed validation strategy is progressive. We begin with a standard benchmark problem of static wetting on a rigid substrate to validate the fundamental implementation of surface tension. We subsequently increase the complexity by simulating wetting on a soft, deformable substrate, a pivotal elastocapillary issue, allowing direct comparison with existing analytical theories and experimental data.

After validating the fundamental mechanics, we apply the model on a particular biological issue: the indentation of a human HCT-8 cell, comparing our findings with current experimental data. Ultimately, we leverage the validated model to conduct a novel parametric investigation, examining the interaction between cell surface tension and the mechanics of tissue invasion.

6.6.1 Static wetting on rigid substrates

The first validation case examines the static wetting of a liquid droplet on a rigid, non-deformable substrate. The objective is to verify that the model accurately reproduces the equilibrium contact angle predicted by the classical Young-Dupré equation.

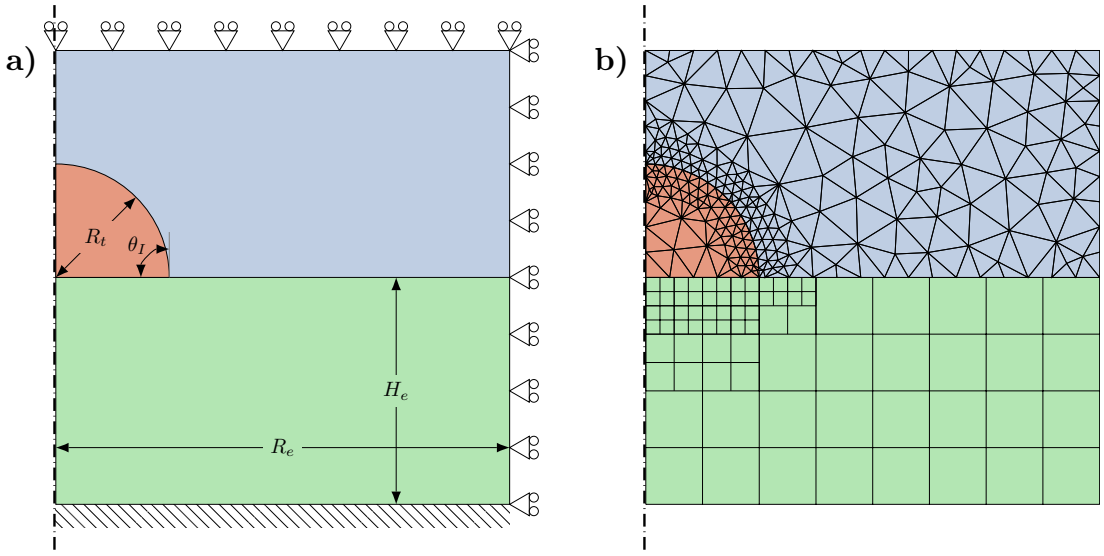

Figure 6.13: *a) Schematic of the axisymmetric problem geometry and boundary conditions. The key parameters, such as the hemispherical tissue radius R_t, initial contact angle θ_I, radius R_e and height H_e of the substrate, are shown. The bottom of the solid substrate is fixed, while roller constraints on the right and top boundaries are applied. b) Detail of the non-conforming mesh structure. The background (solid) mesh is refined under the droplet, and the body-fitted (fluid) mesh is refined at the fluid-fluid interface.*

The experiment is modeled in an axisymmetric configuration, as depicted in Figure 6.13a, where the key parameters and boundary conditions are detailed in the caption. Since both this and the subsequent validation on rigid and deformable substrates are not strictly biological, the active tissue will hereafter be referred to simply as the *liquid droplet*.

To simulate a non-deformable substrate, the solid is modeled as a hyperelastic material with a very large value of the Young's Modulus E, forcing the substrate to behave as a rigid body. By ensuring the elastocapillarity length $l = \gamma_{st}/E \to 0$, any potential deformation due to surface tension becomes negligible.

The system's physics are defined by the three interfacial tensions: tissue-external environment γ_{te}, solid-tissue γ_{st}, and solid-external environment γ_{se}. These tensions

define the theoretical equilibrium contact angle θ, through the Young-Dupré equation:

$$\cos(\theta) = \frac{\gamma_{se} - \gamma_{st}}{\gamma_{te}}. \tag{6.173}$$

The right-hand side, which we will vary in our tests, is the dimensionless solid surface ratio [Bico et al., 2018].

The simulations are initialized from a non-equilibrium hemispherical state with an initial contact angle $\theta_I = 90°$, and are run until the droplet settles into its final, static equilibrium configuration characterized by the equilibrium contact angle θ. A series of simulations were performed by varying the dimensionless solid surface ratio, $(\gamma_{se} - \gamma_{st})/\gamma_{te}$, over the full theoretical range from 1 (complete wetting, $\theta = 0°$) to -1 (complete non-wetting, $\theta = 180°$). The results are presented in Fig. 6.14. The plot compares the cosine of the equilibrium contact angle obtained from the FE simulation and the theoretical value obtained from the Eq. (6.173). The data points fall precisely on the line of corresponding to the Young-Dupré equation, demonstrating excellent quantitative agreement with the analytical solution. The figure also shows the final equilibrium shapes for four representative cases, which visually confirm the predicted contact angles.

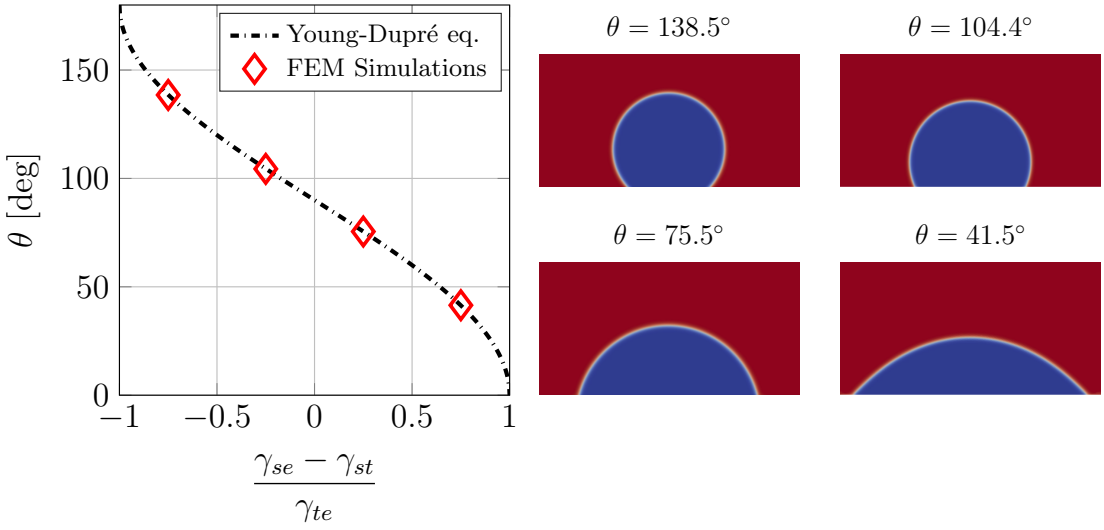

Figure 6.14: *The main plot compares the simulated equilibrium contact angle obtained through the FE simulations against the theoretical angle given by the Young-Duprè equation. The results of the simulations (red diamonds) show excellent agreement with the analytical solution (dash-dotted line). On the right, the final simulated equilibrium shapes are shown for four distinct cases, corresponding to the adimentional solid surface contrast of* $-0.75, -0.25, 0.25,$ *and* 0.75 *for which the corresponding equilibrium contact angle* θ *are reported above each shape.The solid substrate is omitted from these plots for clarity, as it remains undeformed in this rigid limit.*

This benchmark confirms the fundamental execution of the surface tension model and Nitsche's method for imposing contact conditions at the solid-fluid interface. The established accuracy within the rigid limit sets an essential benchmark for the subsequent, complex elastocapillary investigations.

6.6.2 Static wetting on soft substrates

After validating the model in the rigid limit, we now increase the complexity to a key elastocapillary problem: the static wetting of a liquid droplet on a soft, deformable substrate. The objective is to validate the fully coupled fluid-structure interaction framework and to test the model's ability to capture elastocapillary phenomena. In particular, we tested if the devised model can quantitatively reproduce the characteristic substrate deformation near the contact line, called the wetting ridge, comparing our results with the established analytical theory of Style and Dufresne [2012] and the experimental data of Style et al. [2013].

To perform a direct comparison with the literature, we simulate the specific systems studied by Style et al. [2013]: glycerol droplets of a range of sizes on a soft silicone gel substrate. The material and interfacial parameters used in the simulation are taken directly from the experimental paper and are summarized in Table 6.1. The viscosity of glycerol was adopted from literature data [Bueno et al., 2018]. The key parameter in this problem is the elastocapillary length, $l = \gamma_{st}/E \approx \gamma_{se}/E$, which was approximately 10 μm in the reference experiment. To resolve the dynamics of the partially wetting

Table 6.1: *Material and interfacial parameters for the static wetting on soft substrate, based on the glycerol/silicone gel system from Style et al. [2013]*

Binary fluid			**Solid**		**Interfaces**			
η_e	η_t	R_t	E	ν	γ_{st}	γ_{se}	γ_{te}	ϵ
Pas	Pas	μm	kPa		$\frac{\text{mN}}{\text{m}}$	$\frac{\text{mN}}{\text{m}}$	$\frac{\text{mN}}{\text{m}}$	μm
0.10	1.41	Variable	3	0.499	36.0	31.0	46.0	2.0

droplets, we adopt an adaptive time step that starts from $\Delta t = 3.5\mu$s and increases accordingly with the reaching of the steady state. The size of the initial time step was chosen accordingly with the mesh size. In fact, due to the non-conforming nature of the background mesh, the deformation of the interface must be smaller than the mesh size. The computational experiments are run from an initial non-equilibrium state until the system reaches a complete static equilibrium, with both the droplet shape and the substrate deformation no longer changing in time. The simulation successfully captures the hallmark of elastocapillarity with a correct evaluation of the sharp wetting ridge where the vertical component of the tissue-external environment (glycerol-air in the case of the replicated experiments) surface tension pulls the soft substrate upwards.

A quantitative comparison is presented in Figs. 6.15 and 6.16. The figure plots the deformed surface profiles for $H_e = 50\,\mu$m and $H_e = 20\,\mu$m thick substrates, respectively. Our numerical results (solid line) show excellent quantitative agreement in both the shape and magnitude of the deformation with the experimental data points from Style et al. [2013] and the analytical solution from Style and Dufresne [2012] (dashed line). The model correctly captures the physics of finite-size confinement. In fact, the ridge deformation for the thinner 20μm substrate (Fig. 6.16) is visibly suppressed (almost half) compared to the thicker 50μm case (Fig. 6.15), as also shown from the experimental data. The fact that our simulation precisely matches the analytical solution in both regimes further validates the model's robustness.

This successful validation confirms that the model's coupling between the phase-field fluid model for the binary fluid surface tension, the non-linear solid elasticity, and the

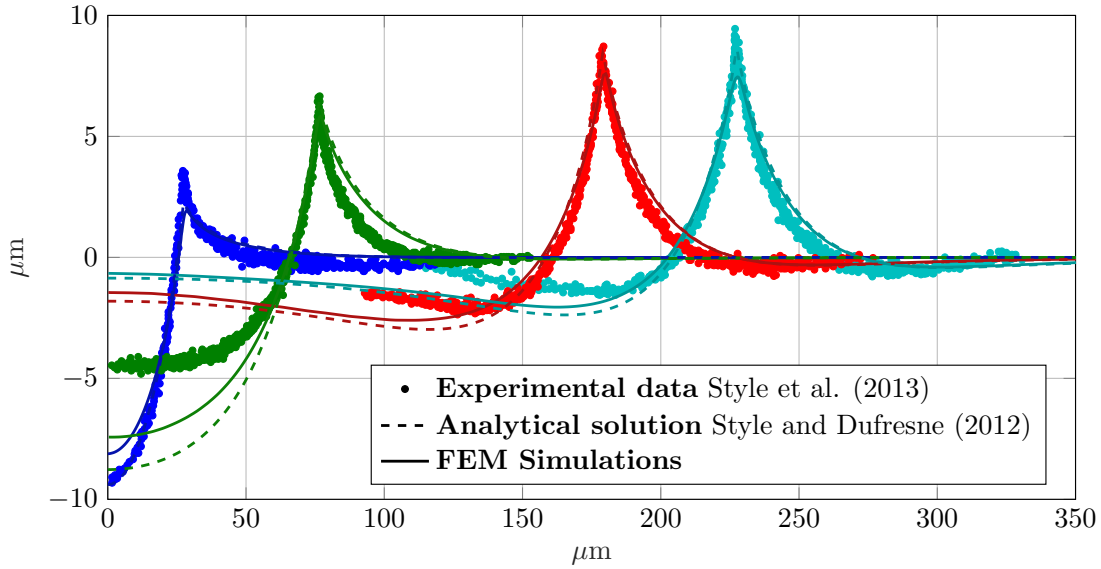

Figure 6.15: *Comparison between Simulations, experimental data, and analytical solutions. The figure shows the surface deformation profiles of a* 50 μm *thick silicone gel substrate beneath partially wetting droplets of glycerol with radii of* 26.8, 74.5, 176.7, *and* 225.5 μm.

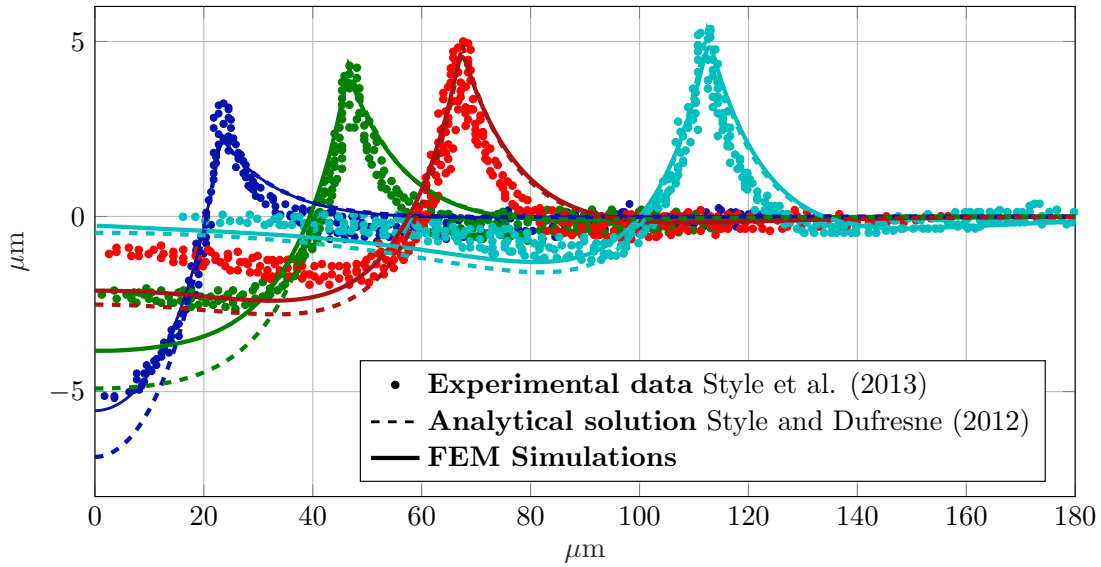

Figure 6.16: *Comparison between Simulations, experimental data, and analytical solutions. The figure shows the surface deformation profiles of a* 20 μm *thick silicone gel substrate beneath partially wetting droplets of glycerol with radii of* 23.5, 47.0, 65.8, *and* 112.8 μm.

contact line physics is correctly implemented. The model's ability to precisely replicate this canonical elastocapillary problem gives us confidence to apply it to more complex biological systems, such as the cell indentation problem in the following section.

6.6.3 Indentation of a human HCT-8 cell colony

To demonstrate the model's applicability to biological systems, we simulate the indentation of human colon carcinoma (HCT-8) cell colonies and compare the results with the experimental data from Shi et al. [2022]. In this experiment, colonies of HCT-8 are reported to indent a soft polyacrylamide (PAA) hydrogel in a colony-size-dependent manner. This indentation was shown to be not solely due to cell contractility. In fact, treating the colonies with a high concentration of blebbistatin, which inhibits the cell contractility, reduced the indentation but did not eliminate it. Moreover, their measurements showed that the elastocapillarity length of the colonies was of the same order of magnitude as the cell colony. Both these two pieces of evidence highlighted that the elastocapillarity effect is essential for the modeling of cell-ECM contacts.

Table 6.2: *Material and interfacial parameters adopted for the simulations of the indentation of human colon carcinoma (HCT-8) cell colonies*

Binary fluid			**Solid**		**Interfaces**			
η_e	η_t	R_t	E	ν	γ_{st}	γ_{se}	γ_{te}	ϵ
Pas	Pas	μm	kPa		$\frac{\text{mN}}{\text{m}}$	$\frac{\text{mN}}{\text{m}}$	$\frac{\text{mN}}{\text{m}}$	μm
0.10	1.41	Variable	Variable	0.499	5.0	4.0	3.8	2.0

To investigate if the model can reproduce the qualitative trends and magnitudes of indentation observed in biological experiments, we initially adopted the computational setup described in Fig. 6.13. We modeled the colony as a fluid and we adopted the parameters shown in Tab. 6.2. Where the surface tensions between the three interfaces and the Young modulus of the substrate were taken from Shi et al. [2022]. We note that the adopted viscosity parameter for the cell colony is the same as that of the glycerol droplet. Aware that the common viscosity for an organoid is of the order of 10^5 Pas, we are interested in the shape of the substrate after complete relaxation of the colony; for this reason, in order to reduce the computational cost, we adopted a smaller value corresponding to the glycerol viscosity.

To compare our simulation with the experimental data, according to the work of Shi et al. [2022], we define the dimple depth d as the indentation of the colony starting from the peak of the wetting ridge h^{peak} and the colony size as two times the contact radius a, as shown in Fig. 6.17.

In Fig. 6.18, we show the comparison of the experimental data for three different substrate stiffnesses with our FE simulations. The plot showing the colony dimple depth d as a function of the colony size points out a very good agreement between the experimental data and the FE simulation for the substrate stiffness of 2.6 and 0.5 KPa. Nevertheless, the FE simulation for the softer substrate highly underestimates the experimental data, showing a colony dimple 2-fold smaller. It is evident from the frames reported on the right side of Fig. 6.18, which correspond to the equilibrium shape of the colonies on the different substrates, that independently from the substrate stiffness, the final configuration always resembles a semisphere. Instead, as reported in Shi et al.

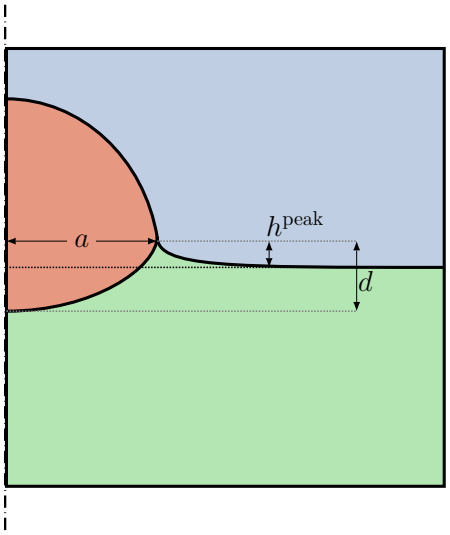

Figure 6.17: *Sketch of the deformed wetting ridge. The dimple depth d, peak height h^{peak}, and contact radius a are shown.*

[2022], the colonies on softer hydrogels tend to form spheroids, as is also evident from the colony dimple depth observed for the 0.2 KPa substrate, where the indentation is of the same order as the colony radius (which is half of the colony size). Lacking the data of the volume of the cell colonies, not measured in the reference literature, and in order to calibrate the model on this set of experiments, we changed the adopted computational setup for the simulation of the indentation of the softer substrate. In particular, for the cell colony, we adopted a semi-elliptic shape that lies on top of the incompressible soft polyacrylamide hydrogel, as shown in Fig. 6.19. The elliptic shape of the tissue is chosen in order to consider higher volumes for the organoid, keeping the initial wetting area and contact angle fixed.

Therefore, with this new setup, we calibrate our model on the softer substrate data. In particular, assuming a 2.5-fold larger volume compared to the semi-sphere (thus setting $R_t^{\max} = 2.5R_t^{\min}$), we obtained a good agreement with the experimental data, as shown by the black markers and line of Fig.6.20. The equilibrium shape of the colony-substrate systems is reported in the right part of the figure, which shows the vertical displacement of the substrate for all its different stiffnesses. It is evident that a stiffer substrate leads to a smaller dimple depth, which increases on a softer substrate, and it's worth noting that the equilibrium shape of the colony, corresponding to the E = 0.2KPa, compared to the one of Fig. 6.18 now bears a resemblance to a spheroid as reported in the literature. This comparison reveals that the model, with physically meaningful parameters, can reliably replicate the indentation behavior of HCT-8 cell colonies. The model accurately reflects the principal qualitative trend: a more rigid substrate leads to a reduced dimple depth. Although a straight quantitative prediction is unattainable without full knowledge of the experimental colony volumes, the good agreement obtained through reasonable assumptions validates the model's utility as an instrument for cell mechanobiology research.

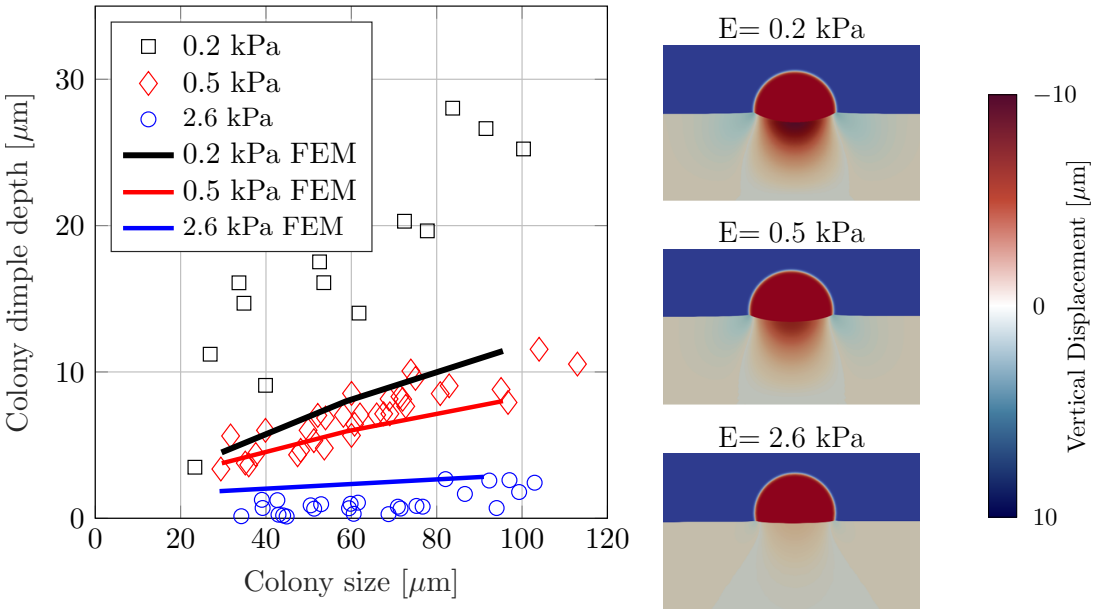

Figure 6.18: *Comparison plot between the experimental data of HCT-8 cell colony and the finite element simulation for three different substrate stiffnesses. On the right are reported the final frames of the indentation process corresponding to the different considered substrate stiffnesses. The colormap of the substrate represents its vertical displacement under the indentation of the semispherical colonies.*

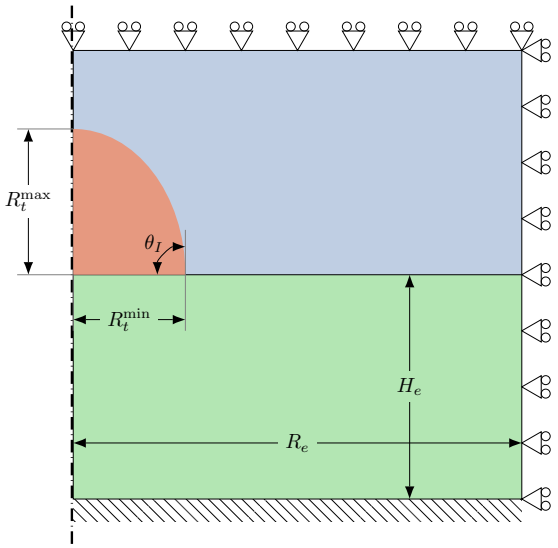

Figure 6.19: *Schematic of the adopted axisymmetric problem geometry and boundary conditions. The bottom of the solid substrate is fixed, while roller constraints on the right and top boundaries are applied. The key parameters, such as the major R_t^{max} and minor R_t^{min} axes of the ellipse, initial contact angle, radius R_e and height H_e of the substrate, are shown.*

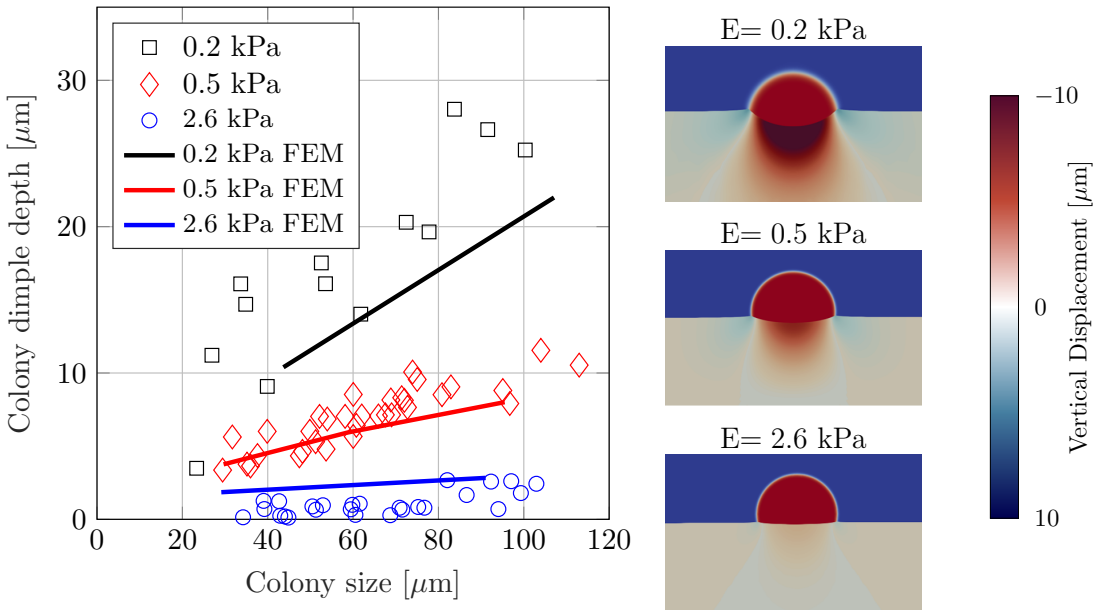

Figure 6.20: *Analogous comparison plot of the Fig. 6.18 but the initial shape of the colony for the softer substrate is assumed to have a 2.5-fold larger volume. On the right are reported the final frames of the indentation process corresponding to the different considered substrate stiffnesses. The colormap of the substrate represents its vertical displacement.*

6.6.4 Comprehensive analysis of the indentation

Before studying the invasion process, which is the object of the next section, we explore the interplay between substrate elasticity and surface tensions. The adopted computational setup is the same as the one described in Fig. 6.13 and the adopted model parameters are shown in Tab. 6.3. To comprehensively analyze the interplay between

Table 6.3: *Material and interfacial parameters adopted for the analysis of the indentation process*

Binary fluid				**Solid**				**Interfaces**			
η_e	η_t	R_t	f_d	E	ν	H_e	R_e	γ_{st}	γ_{se}	γ_{te}	ϵ
Pas	Pas	μm	kPa	kPa		μm	μm	$\frac{\text{mN}}{\text{m}}$	$\frac{\text{mN}}{\text{m}}$	$\frac{\text{mN}}{\text{m}}$	μm
0.10	1.41	45.0	0	Variable	0.499	350	450	45.0	Variable	45.0	2.0

Young's modulus and surface tensions, a parametric sweep is performed. The results are presented in Fig. 6.21 as a two-dimensional parameter space map. These plots show the final equilibrium indentation depth d and the peak height h^{peak} over a wide range of substrate Young's Moduli E, and dimensionless solid surface ratios $(\gamma_{se} - \gamma_{st})/\gamma_{te}$.

The results clearly quantify the competing nature of these two parameters. In particular, focusing on Fig. 6.21a, the effect of the substrate stiffness on the indentation depth d, can be seen. As expected, we observe a monotonically increasing indentation depth, which is large on soft substrates and inversely proportional to the substrate Young Modulus $d \propto 1/E$. On the other hand, looking at the influence of the solid

surface contrast ratio, a very small reduction of the indentation is observed in the wetting regime $\gamma_{se} > \gamma_{st}$. On the contrary, for negative contrast ratio, corresponding to the dewetting condition $\gamma_{se} < \gamma_{st}$, we observe a saturation effect. In this condition the indentation depth d becomes almost insensitive to the magnitude of the surface tension γ_{st}. Looking instead at Fig. 6.21b, the regime map for the peak height re-

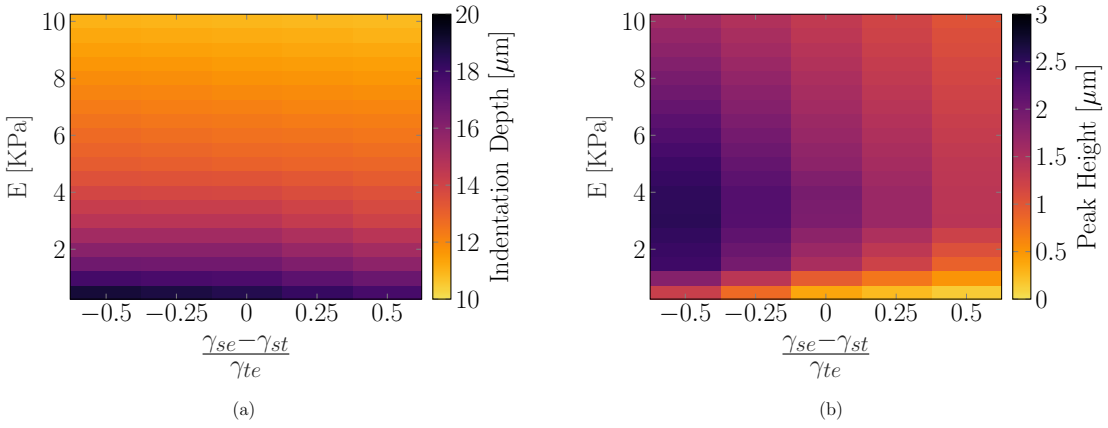

Figure 6.21: *a) Parameter space map of the equilibrium indentation depth d as a function of substrate stiffness E and the dimensionless solid surface ratio, $(\gamma_{se} - \gamma_{st})/\gamma_{te}$. The color bar indicates the magnitude of the indentation. b) Parameter space map of the peak height of the wetting ridge as a function of substrate stiffness E and the dimensionless solid surface ratio, $(\gamma_{se} - \gamma_{st})/\gamma_{te}$.*

veals a highly non-trivial and non-monotonic relationship with the substrate stiffness E. The peak height h^{peak} must be zero in both the liquid-like limit $E \to 0$, where a Neumann triangle governs the interface, and the rigid limit $E \to \infty$, where deformation is impossible. Consequently, a maximum peak height must exist at an intermediate, optimal stiffness. Our simulations capture this phenomenon. The results show that for the ultra-soft substrates, the peak height is proportional to the stiffness. This indicates our model is operating in the rising regime of this map. This finding is particularly significant, as the canonical elastocapillarity literature focuses almost exclusively on the well-established decaying regime for soft solids, where peak height is inversely proportional to stiffness, $h^{\text{peak}} \propto 1/E$. The ability of our model to robustly capture this full, non-monotonic behavior, spanning from the ultra-soft to the soft-solid regime, is a further powerful validation of its physical robustness and allows its application to a wide range of phenomena.

6.6.5 Competition between indentation and degradation

Finally, we leverage the validated model to compare the mechanics of simple indentation, described in the previous section, with active invasion, where the cell can degrade the surrounding elastic matrix, which leads to the tissue engulfment. To isolate the competition between mechanical indentation and degradation, a two-stage numerical experiment was performed with the parameters shown in Table 6.4. First, we set all interfacial tensions to be equal ($\gamma_{st} = \gamma_{se} = \gamma_{te} = 45.0$ mN/m) in order to isolate the mechanical indentation (driven by the tissue's Laplace pressure) from any wetting or dewetting effects. The simulation was run from the setup in Fig. 6.13 with the degra-

Table 6.4: *Material and interfacial parameters adopted for the analysis of the invasive process of an active tissue*

Binary fluid				Solid				Interfaces			
η_e	η_t	R_t	f_d	E	ν	H_e	R_e	γ_{st}	γ_{se}	γ_{te}	ϵ
Pas	Pas	μm	kPa	kPa		μm	μm	$\frac{\text{mN}}{\text{m}}$	$\frac{\text{mN}}{\text{m}}$	$\frac{\text{mN}}{\text{m}}$	μm
0.10	1.41	45.0	Variable	4.0	0.499	350	450	45.0	45.0	45.0	2.0

dation force set to zero, $f_d = 0$, until the purely mechanical equilibrium was reached. Second, after this initialization step, we activate the degradation process. Then at $t = 0$, we enabled the degradation force, $f_d \neq 0$, and the system was allowed to evolve, permitting us to observe the coupled invasion process. To reflect the fact that the dimple is now driven by two mechanisms, mechanical effects and active degradation, we refer to this process as engulfment.

The results for the $f_d = 0.5$ KPa case are reported in Figs. 6.22 and 6.23. Looking at Fig. 6.23, the initial state, corresponding to $t = 0$, shows the substrate in compression characterized by negative vertical displacements, jacobian $J < 1$ and a mean hydrostatic stress $\sigma_m < 0$. This is the result of the purely mechanical indentation, where the tissue's internal Laplace pressure pushes the elastic substrate down, and this force is balanced by the substrate's compressive elastic resistance. Once the degradation begins, for $t > 0$, the tissue engulfs the matrix. However, Fig. 6.22 clearly illustrates the decreasing spacing between the time curves, spaced 1 ms apart, suggesting that the rate of engulfment slows down over time. This central finding reveals the competitive nature of the engulfment process. While the engulfment is mechanically driven by the constant downward Laplace pressure, the degradation process itself acts as a mechano-sensitive thermodynamic process, modulated by the stress state. This reveals that the efficiency of this degradation is not constant, but it is coupled to the substrate's mechanical state, as it was already pointed out in Sec. 6.4.4 during the analysis of the generalized force balance conjugate to the d-velocity derived from the stationarity of the Nitsche-Lagrangian (Eq. (6.112)).

At $t = 0$, the compressive state of the substrate facilitates the degradation process, allowing for a high initial rate of the matrix removal. This degradation allows the constant Laplace pressure to push the tissue deeper into the substrate. As t increases, the tissue sinks further and starts to pull the underlying matrix, which turns to be in tension, with $J > 1$ and $\sigma_m > 0$, as clearly seen in the colormap of Fig. 6.23 for $t = 100$ ms. During this push-pull transition, the effect of the Laplace pressure turns out to be partially overpowered by the tensional restoring force from the surrounding elastic matrix. Nevertheless, its effect is still appreciable from the local compression near the contact line.

Therefore, this preliminary study reveals that the invasive process is a complex phenomenon. The increasing tensional field inhibits degradation, resulting in a gradual suppression of substrate removal as its advancement has to compete with an increasingly tense matrix. Consequently, throughout the invasion process, the system evolves from a simple pushing Laplace-dominated regime to a sophisticated push-pull state.

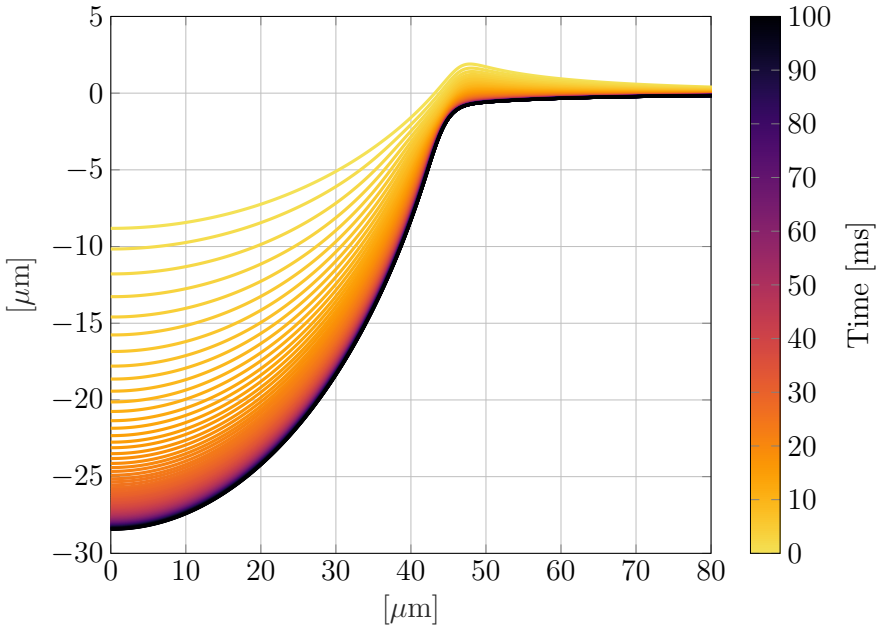

Figure 6.22: *Plot representing the tissue engulfment interface evolution over time for $f_d = 0.5$ kPa. The interface profiles are plotted at 1 ms intervals from $t = 0$ to $t = 100$ ms, where the color gradient indicates the time progression.*

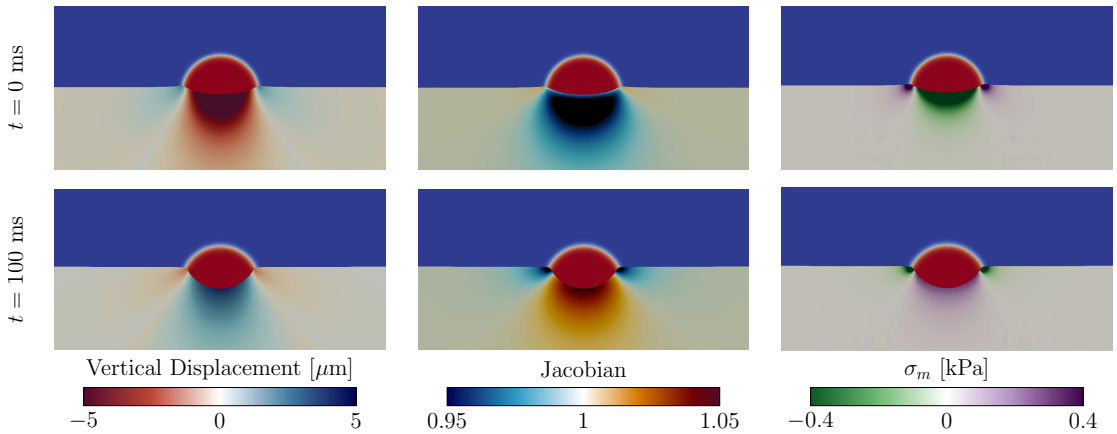

Figure 6.23: *System configuration at the onset of the degradation process for $t = 0$ ms and the configuration at $t = 100$ ms. The colormap of the substrate represents the vertical displacement of the substrate (left column), the jacobian J (central column) and the hydrostatic stress σ_m (right column).*

Effect of degradation force magnitude

To confirm and quantify this competition between substrate elasticity, capillarity force, and degradation, the simulation was repeated for degradation forces f_d ranging from 1 to 0.125 kPa. The results of the engulfment process are shown in Fig. 6.24. All the simulations exhibit a slowdown of the degradation process, but the rate and final depth of engulfment are, as expected, directly dependent on the magnitude of the degradation force f_d. The $f_d = 0.125$ kPa case (lowest force) achieves the shallowest engulfment before being inhibited by the tensional field, while the $f_d = 1.0$ kPa case is strong enough to push deeper before reaching its new equilibrium. This confirms that the tensional-inhibition feedback is a general feature of the system, acting as a regulator against the analyzed range of degradation force levels.

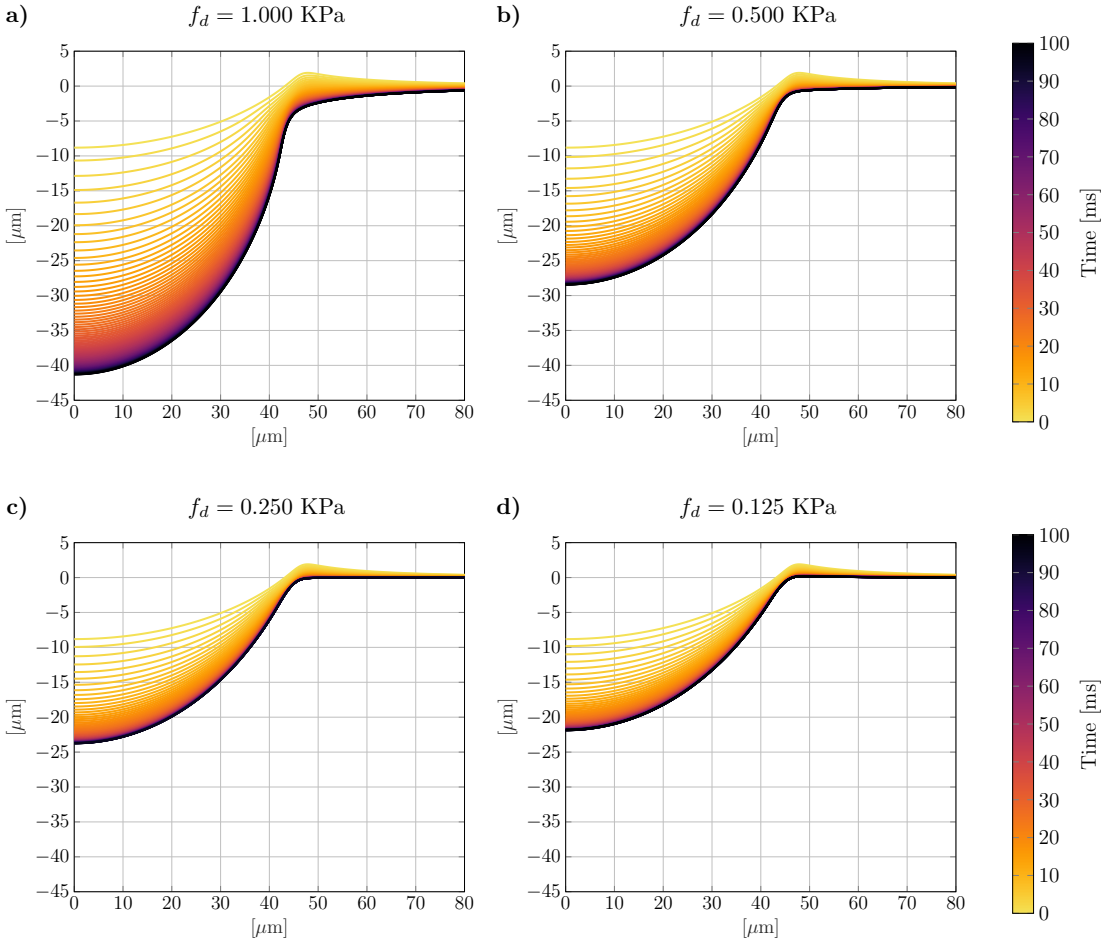

Figure 6.24: *Plot representing the tissue engulfment interface evolution over time for four different degradation forces. The interface profiles are plotted at* 1 *ms intervals from* $t = 0$ *to* $t = 100$ *ms, where the color gradient indicates the time progression.*

Residual substrate deformation: invasive signature

A final series of simulations was performed to isolate the permanent, irreversible changes of the substrate. Before and after the simulation performed with $f_d = 0.5$ kPa, thus for

the timeframe $t = 0$ and $t = 100$ ms, the active tissue was computationally removed from the domain, and the elastic substrate was allowed to relax to a new equilibrium. The results shown in Fig. 6.25 show that before invading the substrate, if we remove the tissue, the substrate naturally returns to its original flat state without residual stresses. This further corroborates the power of the developed model also for the relaxation

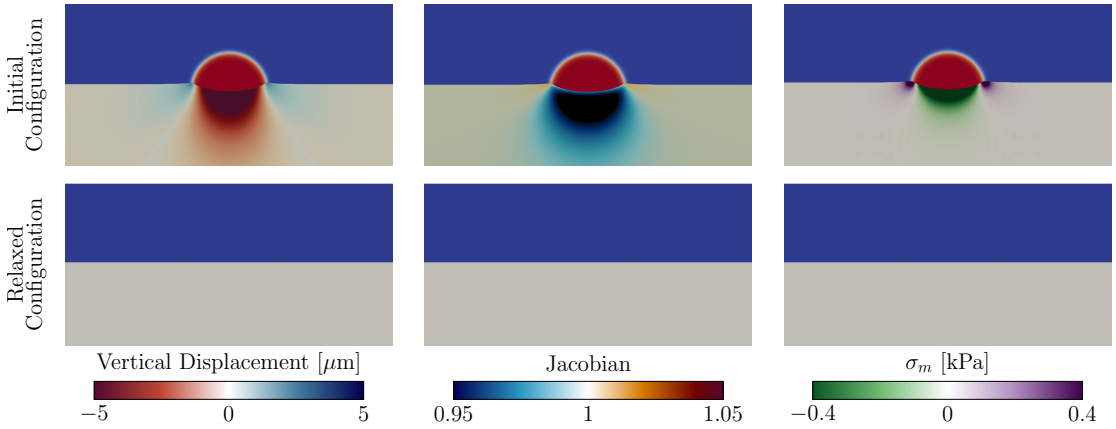

Figure 6.25: *Snapshot before computationally removing the tissue and after the complete relaxation phenomenon for an undegraded substrate. The colormap shows the vertical displacement (left column), the jacobian (central column), and the mean hydrostatic stress (right column).*

process and leads us to its application for the study of the invasion process.

Allowing the tissue to degrade the substrate following the same invasion process shown in Fig. 6.22, corresponding to $f_d = 0.5$ kPa, we remove the tissue once the new equilibrium is reached. The results are shown in Fig. 6.26. In this case, after the complete relaxation, the substrate does not return to its original flat state but shows a permanent dimple accompanied by the presence of residual stresses. This invasive signature is the sign that the material was irreversibly removed by the degradation process.

It is worth noting that the dimple depth decreases after the removal of the tissue while the tensional and compressional field increases. Indeed, by removing the tissue, we also remove the downward-pushing Laplace pressure (induced by the removed tissue-external environment surface tension γ_{te}). Consequently, the substrate recovers the deformation induced by it until it settles at its final equilibrium state. This final configuration is not stress-free because the substrate-external medium surface tension γ_{se}, which is still present, is competing against the substrate elastic restoring force that arose after the degradation of the substrate. Therefore, the computational removal of the tissue does not lead to complete relaxation but reveals the presence of an invasive signature into the substrate characterized by residual stresses.

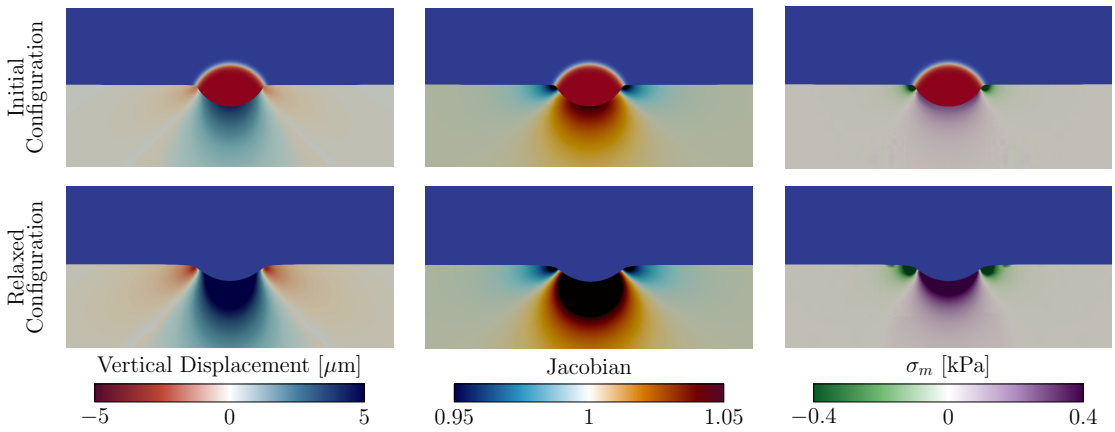

Figure 6.26: *Snapshot before computationally removing the tissue and after the complete relaxation phenomenon of the degraded substrate. The colormap shows the vertical displacement (left column), the jacobian (central column), and the mean hydrostatic stress (right column).*

6.7 Conclusion and future development

The findings of this thesis demonstrate that the simultaneous presence of active cell tractions, capillary forces, and substrate degradation can create complex, convoluted behaviors. The interaction between these mechanisms dramatically modifies the mechanical state of the ECM and the resulting stress distribution, which shapes tissue behavior, is shown to be highly dependent on which mechanism, purely mechanical indentation or active degradation, is dominant.

6.7.1 Key results

The model was progressively validated against a series of benchmarks, confirming its robustness as a predictive tool. In particular:

- It successfully reproduced the Young-Dupré law for static wetting on a rigid substrate.
- It accurately replicated the complex wetting ridge for droplets on a soft substrate, showing excellent quantitative agreement with the analytical theories of Style and Dufresne [2012] and the experimental data of Style et al. [2013].
- It was shown to plausibly reproduce the indentation of HCT-8 cell colonies observed by Shi et al. [2022], correctly capturing the qualitative trends.
- Crucially, the analysis of the parameter space revealed the model's ability to capture the full, non-monotonic physics of ridge formation, from the ultra-soft, liquid-like regime to the standard soft-solid regime, which is a powerful validation of its physical robustness.

A significant achievement of this work is the model's computational efficiency. While the underlying physics, combining a phase-field method with non-conforming agFEM, is complex, the resulting axisymmetric simulations are remarkably fast. The validation

of the Style et al. [2013] profile, for instance, was achieved in less than 24 hours on a standard workstation. This is a vast improvement over other published frameworks, such as the 3D model presented by Bueno et al. [2018] that can require over 47 hours on 128 cores for a similar problem. This efficiency is what makes the model a practical tool for the extensive parametric studies presented in this thesis.

Beyond validation, the application of the model to the active invasion process revealed a fundamental mechanosensing inhibition mechanism. The simulations demonstrated that the degradation rate is not constant but is regulated by the substrate's stress state, which turns out to be inhibited by tension. Indeed, as the tissue engulfs the substrate, it generates a tensional field that acts as a negative feedback, progressively suppressing the degradation rate, which leads the system from a Laplace-dominated pushing regime to a more complex push-pull equilibrium, where the constant capillary driving force is balanced by the growing elastic resistance of the tensed substrate. Finally, relaxation simulations revealed that this process leaves a permanent invasive signature in the substrate, a residual deformation field that persists even after the tissue is removed. This finding provides a physical basis for identifying past invasive events.

6.7.2 Perspectives

The validated framework presented here opens the door for a wide range of future investigations.

The present model is ready for further comprehensive parametric investigations. Regarding the elastocapillarity, a more detailed analysis can be performed to fully characterize the non-monotonic relationship between substrate stiffness and wetting ridge height and to systematically explore the influence of substrate thickness on the apparent contact angle. Regarding the invasive behavior of the cellular tissues, the study of the engulfment can be expanded to a full-scale parametric investigation into the roles of degradation force, substrate stiffness and thickness, surface energy, and tissue dimension. Furthermore, the key assumption about the degradation force f_d, here considered as a constant, can be dropped. A significant improvement would be to implement a mechano-sensitive constitutive law, where the degradation force is a function of the local mechanical stress or strain state. This would allow for the modeling of more realistic biological processes, such as regulated morphogenesis or deregulated, pathological invasion.

For what concerns, the computational framework, two major improvements are envisioned. The first one regards the parallelization. Indeed, the current implementation of the aggregation (agFEM) scheme is serial and its parallelization following the work of Badia et al. [2021], would further enhance its performance, enabling the rapid exploration of wider parameter spaces. The second one, instead, regards the formulation. After the parallelization of the model, a natural improvement is to make the formulation fully 3D. This further advancement would enable the study of complex, non-symmetric phenomena that intertwine the biology and the soft-matter field, e.g., the study of the durotaxis observed in the liquid droplets, or the crawling mechanisms of organoids, and the heterogeneous invasion patterns observed in cancerous tissues.

7

Conclusion and future directions

This thesis has addressed the complex, multi-scale nature of cell migration, a crucial process in biology occurring in both physiological and pathological conditions. The primary objective was to develop and apply a series of computational models designed to clarify the mechanical principles governing cell movement, progressing logically from the mechanics of an individual cell to the collective, invasive behavior of a tissue. To achieve this, a series of models with increasing complexity was formulated. This progression moved from discrete tensegrity systems to advanced continuum formulations and from modeling the cell's internal mechanisms to modeling its complex interaction with a dynamic, degrading substrate. The principal achievement and key findings of this investigation are outlined below.

7.1 Concluding remarks: Part I

Part I of this thesis work investigated the mechanochemical coupling between the cytoskeleton and the extracellular matrix through two complementary modeling approaches: a generalized nonlinear tensegrity model for analytical stability insights and a continuum finite element framework to validate elasto-damaging adhesive laws against experimental data.

The investigation proceeded in three stages:

- **The symmetric unit (Sec. 3.2).** We demonstrated that within a symmetric cytoskeletal unit, the competition between assembly and disassembly of the focal adhesion is a highly frustrated process regulated by the antagonistic interaction between actomyosin contraction and microtubule polymerization, further complicated by the potential instability of microtubules. A key finding is that while independently applied pre-stretches require high thresholds to induce the microtubule buckling, their simultaneous action destabilizes the system at remarkably lower levels ($\approx 1\%$). This implies the cell operates in a state of incipient instability, allowing for geometric reconfiguration at physiological strain levels. Furthermore, our model challenges the classical view that higher contractility necessarily leads to larger adhesions; instead, we show that microtubule-based antagonistic compressive load highly influences the adhesion plaque growth, a finding that is consistent with the hyper-contractility and focal adhesion enlargement observed in cells treated with microtubule-depolymerizing agents [Bershadsky et al., 1996, Rafiq et al., 2019]. Moreover, the adoption of a cubic growth law reveals that

the system is significantly more responsive to mechanical cues than linear models suggest. This non-linearity amplifies the impact of mechanical stress on protein flux, providing a theoretical justification for the rapid assembly/disassembly rates observed in vivo during migration, which standard linear diffusion models fail to capture.

- **The asymmetric cell (Sec. 3.3).** Recognizing that locomotion is inherently polarized, and following experimental evidence that the adhesive microenvironment governs the internal spatial organization of the cortex and organelles [Théry et al., 2006], we extended the framework to account for internal geometrical asymmetry via the rotational hinge position (η) and external asymmetry through substrate stiffness gradients. A key finding is that the system leverages these configuration changes to reach a stable adhesion state ($J = 0$). Furthermore, the model reveals that structural and environmental asymmetries fundamentally modulate adhesion kinetics:
  - Disassembly shielding. In highly asymmetric units, the disassembly flux is significantly weaker on steep stiffness gradients than on homogeneous substrates. This implies that the compressive-driven depolymerization [Hill and Kirschner, 1982] is dampened by the gradient.
  - Assembly attenuation. Conversely, while assembly rates typically intensify on homogeneous substrates (up to a saturation level k_{av}), this process is attenuated by internal structural asymmetry.

- **The adhesion integrity (Secs. 3.4 and 4.2).** By incorporating elasto-damaging cohesive laws, we investigated the material integrity of the cell-ECM linkage. We demonstrate that the reversal from positive to negative durotaxis is governed by the differential evolution of damage at the cell-substrate interface. The damage threshold Δ^0 can be interpreted as a phenomenological measure of adhesion robustness, capturing the effective ability of the molecular clutch to sustain force accumulation through integrinligand stability and force-dependent recruitment of reinforcing proteins such as talin and vinculin. Within this framework, negative durotaxis emerges as a mechanically consistent equilibrium state when the adhesion to the stiffer substrate is physically compromised. This suggests that the migration against the stiffness gradient may not always be an active preference but rather a passive consequence of an asymmetric adhesion failure. Moreover, the validation of the predictive ability of the model, checked against experimental data [Oakes et al., 2014], and the model outcomes, which concur with the existence of an optimal stiffness range where the cell exerts maximum traction [Chan and Odde, 2008, Elosegui-Artola et al., 2018, Isomursu et al., 2022, Sáez and Venturini, 2023], confirm that the phenomenological traction-separation laws provide a robust and efficient framework for modeling cell mechanics.

Tensegrity model limitations While the proposed tensegrity framework successfully captures the fundamental bifurcation instabilities and mechanosensing reversals observed in cells, it relies on necessary simplifications. First, the reduction of the cytoskeleton to a one-dimensional system ignores the complex spatial remodeling of the actin network and the lateral interaction between stress fibers. While this 1D approach

was instrumental in deriving closed-form analytical solutions for the stability thresholds, it cannot capture phenomena dependent on cell shape changes, such as spreading or polarization perpendicular to the migration axis. Second, the model treats the cytoskeletal components as homogenized continuum elements. This phenomenological approach averages out the discrete, stochastic nature of molecular events. Consequently, while the model predicts the macroscopic average behavior and thermodynamic equilibrium, it does not account for the noise-driven fluctuations that often characterize cell mechanics.

Despite these abstractions, the model's ability to reproduce complex behaviors suggests that these phenomena are driven by robust, low-dimensional mechanical principles rather than the fine details of molecular architecture.

7.2 Concluding remarks: Part II

Part II of the thesis scaled up to the tissue level to tackle the problem of collective invasion, particularly focusing on tissue engulfment. To overcome the 1D limitations of the tensegrity approach:

- We developed a theoretical and computational framework based on a Nitsche-Onsager variational formulation to consistently introduce the boundary conditions over the adopted non-conforming meshes and to include the thermodynamic forces driving the degradation process [Cicconofri et al., 2024]. This model captures the thermodynamics of an active fluid inclusion (the tissue) as it adheres to and dynamically degrades an elastic matrix. To resolve the complex fluid-structure interactions and the multi-phase flow problem inherent to tissue engulfment, we integrated the CutFEM approach (stabilized by agFEM to resolve fluid-structure interactions) with a phase-field method (to handle multi-phase fluid flow).

- We rigorously validated the numerical method against a series of canonical benchmarks. From the simple Young-Dupré law to the complex indentation profiles of glycerol droplets on a silicone gel and of the human colon carcinoma cell colonies on soft hydrogels, our model showed excellent agreement with the experimental data. It also demonstrated its possible applicability to the study of the multiphase flow interaction with ultra-soft substrates.

- Furthermore, with the study of the degradation processes, we revealed a competition between mechanical indentation and the degradation of the substrate. The degradation dynamics turned out to be nonconstant but regulated by the mechanical stress state of the substrate. In particular, the self-inhibition created by the engulfment process in response to the tensional field acts as a negative feedback that slows down the invasive process. Moreover, computationally removing the invasive tissue from the substrate reveals that the degradation process leaves a permanent signature and a residual stress state within the invaded matrix.

7.3 Avenues for further research

The frameworks developed in this thesis, while providing significant new insights, also lay a clear and ambitious foundation for future research.

Regarding the single-cell discrete models proposed in Part I, a strengthening of the biophysical consistency is required. Future research should focus on three main avenues:

1. **Bridging elasto-damaging laws and molecular kinetics**. While the damage parameters (Δ^0, Δ^u) effectively capture the macroscopic failure of adhesion, a quantitative link to molecular events is required. Extensive experimental data already exists regarding the force-dependent unfolding of mechanosensors like talin and the subsequent recruitment of vinculin [del Rio et al., 2009, Elosegui-Artola et al., 2016]. Specifically, the clutch model predicts that on stiff substrates, force builds up rapidly, triggering talin unfolding and reinforcement; however, if the force loading rate exceeds the bond lifetime, the adhesion fails [Elosegui-Artola et al., 2018]. Future work should focus on mapping the damage evolution laws proposed here to these specific kinetic rates, utilizing existing datasets to calibrate the model for different cell types.

2. **Hybrid tensegrity-clutch modeling**. A promising theoretical advancement involves replacing the passive springs at the system boundaries with active motor-clutch elements [Chan and Odde, 2008, Elosegui-Artola et al., 2018, Sáez and Venturini, 2023]. By integrating the clutch dynamics (stick-slip behavior) directly into the tensegrity nodes, the model could capture the stochastic nature of mechanosensing. This hybrid approach would link the global cytoskeletal rearrangement (tensegrity) with the local binding kinetics (clutch), offering a unified description of how cells sense stiffness gradients in real-time. Furthermore, this would allow the framework to move beyond quasi-static analysis to simulate dynamic cell motility, accounting for essential active processes such as retrograde flow, protrusion, and polarization [Betorz et al., 2023].

3. **Hierarchical three-dimensional architectures**. Finally, the simple two-element system could be expanded into three-dimensional, multi-strut hierarchical tensegrity structures [Ingber et al., 2014] or modeled via Hencky's chain elements. This would allow the model to capture more complex internal mechanics, such as the global rearrangement of the cytoskeleton in response to multi-axial loading and the interaction between distinct stress fibers.

For the future direction of the continuum invasion model of Part II, a much wider spectrum of possible developments is envisioned, ranging from fundamental constitutive refinements to clinical applications.

- **Dysregulated morphogenesis**. The current assumption of a constant baseline degradation force can be relaxed to develop constitutive relations that capture different biological realities. By making the degradation force dependent on specific biochemical cues or stress thresholds, the model could distinguish between regulated physiological morphogenesis and pathological invasion, effectively modeling cancer as dysregulated morphogenesis [Ewald et al., 2008].

- **Inverse analysis and clinical predictability**. The possibility to use the model for inverse problems and parameter inference opens a direct path toward clinical predictability. By combining the model with the experimental data, obtained from Particle Tracking Velocimetry (PTV) and Particle Image Velocimetry (PIV) of an invasive tissue or from the residual strain field measurement of the substrate, it

is possible to reverse-engineer the thermodynamic degradation force. This data-driven characterization would provide the quantitative, noninvasive measurements of this crucial parameter, which characterizes the tissue's specific invasive signature.

- **Digital twins and high-performance computing**. The final necessary computational step is the development of a fully parallelized [Badia et al., 2021], full-3D version of the model. The combination of this high-performance 3D framework with patient-specific parameters derived from the inverse method could lead to the ultimate goal of creating a patient-specific digital twin. Such a model would be a high-fidelity, predictive simulation environment capable of forecasting the invasive patterns of tissue invasion and, in the case of cancer progression, predicting its metastatic potential, thereby advancing clinical predictability.

Appendix A

The explicit derivation of the contribution of each term in the functional to the residual $\mathbf{R}$ and Jacobian $\mathbf{J}$ is here presented. We detailed the derivations for the volume integral contributions under the axisymmetric conditions.

Elastic Matrix Free Energy

We start from the contribution of the free energy, $\mathcal{F}_e$, to the nodal residual $\mathbf{R}^a$. This is given by the derivative of the strain energy density, W, integrated over the reference domain Ω_r^e The standard Neo-Hookean strain energy density function W is

$$W = \frac{\lambda}{2}\left(\ln\left(\widetilde{J}\frac{r}{R}\right)\right)^2 + \frac{\mu}{2}\left(\mathrm{tr}(\widetilde{\mathbf{C}}) + \left(\frac{r}{R}\right)^2 - 3\right) - \mu\ln\left(\widetilde{J}\frac{r}{R}\right), \tag{A.1}$$

Since W depends on both the 2D deformation gradient $\widetilde{\mathbf{F}}$ and explicitly on the radial coordinate r, the derivation of nodal residual is obtained by applying the chain rule:

$$(R_{\mathcal{F}_e})_i^a = \frac{1}{\Delta t}\frac{\partial \mathcal{F}_e}{\partial \chi_i^a} = \frac{1}{\Delta t}\int_{\Omega_r^e}\left(\frac{\partial W}{\partial \widetilde{F}_{kI}}\frac{\partial \widetilde{F}_{kI}}{\partial \chi_i^a} + \frac{\partial W}{\partial r}\frac{\partial r}{\partial \chi_i^a}\right) 2\pi R\, dR\, dZ \tag{A.2}$$

The first term in the integral involves the First Piola-Kirchhoff stress, $\widetilde{P}_{kI} = {}^{\partial W}/_{\partial \widetilde{F}_{kI}}$, and the derivative of the deformation gradient, ${}^{\partial \widetilde{F}_{kI}}/_{\partial \chi_i^a} = \delta_{ki}\partial_I N^a$.Substituting this gives the standard internal force vector:

$$\int_{\Omega_r^e} \widetilde{P}_{kI}\delta_{ki}\partial_I N^a\, 2\pi R\, dR\, dZ = \int_{\Omega_r^e} \widetilde{P}_{iI}\partial_I N^a\, 2\pi R\, dR\, dZ \tag{A.3}$$

For computational purposes, it is convenient to express this using the symmetric Second Piola-Kirchhoff stress, $\widetilde{\mathbf{S}}$, through the relation $\widetilde{\mathbf{P}} = \widetilde{\mathbf{S}}\widetilde{\mathbf{F}}^T$ (in index notation, $\widetilde{P}_{iI} = \widetilde{S}_{IR}\widetilde{F}_{iR}$). This yields the final form of the first term:

$$\int_{\Omega_r^e} \widetilde{S}_{IR}\widetilde{F}_{iR}\partial_I N^a\, 2\pi R\, dR\, dZ \tag{A.4}$$

The second term in Eq. (A.2) arises from the explicit dependence of W on the hoop stretch. Using $\partial r/\partial \chi_i^a = \delta_{i1} N^a$, this term becomes:

$$\int_{\Omega_r^e} \frac{\delta_{i1} N^a}{r} \left[\lambda \ln\left(\widetilde{J}\frac{r}{R}\right) + \mu \left(\frac{r}{R}\right)^2 - \mu \right] 2\pi R \, dR \, dZ \tag{A.5}$$

Combining these results gives the final expression for the residual contribution from the free energy.

$$\begin{aligned} (R_{\mathcal{F}_e})_i^a = & \frac{1}{\Delta t} \int_{\Omega_r^e} (\widetilde{S}_{IR} \, \widetilde{F}_{iR}) \, \partial_I N^a \, 2\pi R dR dZ \\ & + \frac{1}{\Delta t} \int_{\Omega_r^e} \frac{\delta_{i1} N^a}{r} \left[\lambda \ln\left(\widetilde{J}\frac{r}{R}\right) + \mu \left(\frac{r}{R}\right)^2 - \mu \right] 2\pi R dR dZ \end{aligned} \tag{A.6}$$

The contribution of the free energy to the Jacobian matrix, $\mathbf{J}_{\mathcal{F}_e}$, is obtained by differentiating the corresponding residual components with respect to the nodal DOFs. The block of the Jacobian coupling node a and node b is given by:

$$(J_{\mathcal{F}_e})_{im}^{ab} := \frac{\partial (R_{\mathcal{F}_e})_i^a}{\partial \chi_m^b} \tag{A.7}$$

Applying the derivative to the final expression for $(R_{\mathcal{F}_e})_i^a$ yields several terms. The derivative of the first integral (the internal force vector) results in two distinct parts. The first one is the material stiffness matrix arising from the differentiation of the stress tensor $\widetilde{\mathbf{S}}$ with respect to the Green-Lagrange strain $\widetilde{\mathbf{E}}$. This terms depends on the material's constitutive model and involves the fourth-order elasticity tensor $\mathbb{C} = \partial \widetilde{\mathbf{S}}/\partial \widetilde{\mathbf{E}}$

$$\int_{\Omega_r^e} \partial_I N^a \, \partial_{\chi_m^b} \tilde{S}_{IR} \, \tilde{F}_{iR} \, 2\pi R \, dR dZ = \int_{\Omega_r^e} \partial_I N^a \tilde{F}_{iR} \, \frac{\tilde{S}_{IR}}{\partial \widetilde{E}_{JL}} \frac{\partial \widetilde{E}_{JL}}{\partial \chi_m^b} \, 2\pi R \, dR dZ \tag{A.8}$$

recalling that $\widetilde{\mathbf{E}} = 1/2(\widetilde{\mathbf{F}}^T \widetilde{\mathbf{F}} - \mathbf{I})$ its derivation is:

$$\frac{\partial \widetilde{E}_{JL}}{\partial \chi_m^b} = \frac{1}{2} \left(\frac{\partial \widetilde{F}_{kJ}}{\partial \chi_m^b} \widetilde{F}_{kL} + \widetilde{F}_{kJ} \frac{\partial \widetilde{F}_{kL}}{\partial \chi_m^b} \right) \tag{A.9}$$

Using the relation $\partial \widetilde{F}_{kP}/\partial \chi_m^b = \delta_{km} \partial_P N^b$, this becomes:

$$\frac{\partial \widetilde{E}_{JL}}{\partial \chi_m^b} = \frac{1}{2} \left((\delta_{km} \partial_J N^b) \widetilde{F}_{kL} + \widetilde{F}_{kJ} (\delta_{km} \partial_L N^b) \right) = \frac{1}{2} \left(\partial_J N^b \widetilde{F}_{mL} + \widetilde{F}_{mJ} \partial_L N^b \right) \tag{A.10}$$

Inserting this expression in the previous expression for the material stiffness matrix and recalling the major symmetry of $\mathbb{C}$ (i.e., $\mathbb{C}_{IRJL} = \mathbb{C}_{JLIR}$), we can obtain that

$$\int_{\Omega_r^e} \partial_I N^a \tilde{F}_{iR} \, \frac{\widetilde{S}_{IR}}{\partial \widetilde{E}_{JL}} \frac{\partial \widetilde{E}_{JL}}{\partial \chi_m^b} \, 2\pi R \, dR dZ = \int_{\Omega_r^e} \partial_I N^a \tilde{F}_{iR} \, \mathbb{C}_{IRJL} \partial_J N^b \tilde{F}_{mL} \, 2\pi R \, dR dZ \tag{A.11}$$

The second term coming from the derivative of the internal force vector is the geometric stiffness matrix and it depends on the current stress state $\widetilde{\mathbf{S}}$ and accounts for the change in stiffness due to the deformed geometry. It is given by

$$\int_{\Omega_r^e} \partial_I N^a \, \tilde{S}_{IR} \partial_{\chi_m^b} \tilde{F}_{iR} \, 2\pi R \, dR dZ = \int_{\Omega_r^e} \partial_I N^a \, \tilde{S}_{IR} \delta_{im} \partial_R N^b \, 2\pi R \, dR dZ \tag{A.12}$$

Furthermore, differentiating the second integral of the residual (the term with explicit radial dependence) yields the additional terms

$$\begin{aligned}&\int_{\Omega_r^e} -\frac{\delta_{1i}N^a\,\delta_{1m}N^b}{r^2}\left[\lambda\ln\left(\tilde{J}\frac{r}{R}\right)+\mu\left(\frac{r}{R}\right)^2-\mu\right]2\pi R dR dZ\\&+\int_{\Omega_r^e}\frac{\delta_{1i}N^a}{r}\left[\lambda\frac{1}{\tilde{J}}\frac{R}{r}\left(\tilde{J}\tilde{F}^{-1}_{Im}\partial_I N^b\frac{r}{R}+\tilde{J}\frac{\delta_{1m}N^b}{R}\right)+2\mu\frac{r}{R}\frac{\delta_{1m}N^b}{R}\right]2\pi R dR dZ\end{aligned}\tag{A.13}$$

The complete expression for the Jacobian contribution from the free energy $\mathcal{F}_e$ is:

$$\begin{aligned}(J_{\mathcal{F}e})^{ab}_{im}=\frac{1}{\Delta t}\Bigg\{&\int_{\Omega_r^e}\partial_I N^a\tilde{F}_{iR}\,\mathbb{C}_{IRJL}\partial_J N^b\tilde{F}_{mL}\;2\pi R\,dR dZ\\&+\int_{\Omega_r^e}\partial_I N^a\,\tilde{S}_{IR}\delta_{im}\partial_R N^b\,2\pi R\,dR dZ\\&-\int_{\Omega_r^e}\frac{\delta_{1i}N^a\,\delta_{1m}N^b}{r^2}\left[\lambda\ln\left(\tilde{J}\frac{r}{R}\right)+\mu\left(\frac{r}{R}\right)^2-\mu\right]2\pi R dR dZ\\&+\int_{\Omega_r^e}\frac{\delta_{1i}N^a}{r}\left[\lambda\frac{1}{\tilde{J}}\frac{R}{r}\left(\tilde{J}\tilde{F}^{-1}_{Im}\partial_I N^b\frac{r}{R}+\tilde{J}\frac{\delta_{1m}N^b}{R}\right)+2\mu\frac{r}{R}\frac{\delta_{1m}N^b}{R}\right]2\pi R dR dZ\Bigg\}\end{aligned}\tag{A.14}$$

Phase Field Free Energy

We now analyze the contribution to the nodal residual $\mathbf{R}^a$ from the free energy of the phase field, $\mathcal{F}_\phi$. In the reference configuration and under the axisymmetric hypothesis, this functional takes the following form:

$$\mathcal{F}_\phi[\boldsymbol{\chi}]=\frac{3}{2\sqrt{2}}\int_{\Omega_f^r}\left(\frac{\sigma}{4\epsilon}(\phi_0^2-1)^2+\frac{\epsilon\sigma}{2}\left|\nabla\phi_0\widetilde{\mathbf{F}}^{-1}\right|^2\right)J\,2\pi R\,dR dZ\tag{A.15}$$

The contribution to the nodal residual is found by differentiating this functional with respect to the nodal DOFs,

$$(R_{\mathcal{F}_\phi})^a_i=\frac{1}{\Delta t}\frac{\partial\mathcal{F}_\phi}{\partial\chi^a_i}\tag{A.16}$$

The derivation requires making use of the key variational identity $\delta(\mathbf{F}^{-1})=-\mathbf{F}^{-1}(\delta\mathbf{F})\mathbf{F}^{-1}$ together with the product and the chain rules, which leads to

$$\begin{aligned}(R_{\mathcal{F}_\phi})^a_i=&\frac{3}{2\sqrt{2}}\frac{1}{\Delta t}\Bigg\{\int_{\Omega_f^r}-\epsilon\sigma\left(\partial_I\phi_0\widetilde{F}^{-1}_{Ij}\right)\left(\partial_K\phi_0\widetilde{F}^{-1}_{Ki}\partial_J N^a\widetilde{F}^{-1}_{Jj}\right)\tilde{J}\frac{r}{R}2\pi R\,dR dZ\\&+\int_{\Omega_f^r}\left(\frac{\sigma}{4\epsilon}(\phi_0^2-1)^2+\frac{\epsilon\sigma}{2}(\partial_I\phi_0\widetilde{F}^{-1}_{Ij})^2\right)\left(\partial_K N^a\widetilde{F}^{-1}_{Ki}+\frac{\delta_{i1}N^a}{r}\right)\tilde{J}\frac{r}{R}2\pi R\,dR dZ\Bigg\}\end{aligned}\tag{A.17}$$

The contribution of the free energy of the phase field to the Jacobian matrix, $\mathbf{J}_{\mathcal{F}_\phi}$, is obtained by differentiating the corresponding residual components with respect to the nodal DOFs. The block of the Jacobian coupling node a and node b is given by:

$$(J_{\mathcal{F}_\phi})^{ab}_{im}:=\frac{\partial(R_{\mathcal{F}_\phi})^a_i}{\partial\chi^b_m}\tag{A.18}$$

Applying the derivative to the final expression for $(R_{\mathcal{F}_\phi})_i^a$ we obtain

$$
\begin{aligned}
(J_{\mathcal{F}_\phi})_{im}^{ab} = \frac{3}{2\sqrt{2}\Delta t}\Bigg\{ & \int_{\Omega_0} \epsilon\sigma \left(\partial_I\phi_0(\tilde{F}^{-1}_{Im}\partial_L N^b \tilde{F}^{-1}_{Lj})\right)\left(\partial_K\phi_0(\tilde{F}^{-1}_{Ki}\partial_J N^a \tilde{F}^{-1}_{Jj})\right)\tilde{J}\frac{r}{R}2\pi RdRdZ \\
& + \int_{\Omega_0} \epsilon\sigma \left(\partial_I\phi_0\tilde{F}^{-1}_{Ij}\right)\left(\partial_K\phi_0\left(\tilde{F}^{-1}_{Km}\partial_L N^b \tilde{F}^{-1}_{Li}\right)\partial_J N^a \tilde{F}^{-1}_{Jj}\right)\tilde{J}\frac{r}{R}2\pi RdRdZ \\
& + \int_{\Omega_0} \epsilon\sigma \left(\partial_I\phi_0\tilde{F}^{-1}_{Ij}\right)\left(\partial_K\phi_0\tilde{F}^{-1}_{Ki}\partial_J N^a(\tilde{F}^{-1}_{Jm}\partial_L N^b \tilde{F}^{-1}_{Lj})\right)\tilde{J}\frac{r}{R}2\pi RdRdZ \\
& - \int_{\Omega_0} \epsilon\sigma \left(\partial_I\phi_0\tilde{F}^{-1}_{Ij}\right)\left(\partial_K\phi_0(\tilde{F}^{-1}_{Ki}\partial_J N^a \tilde{F}^{-1}_{Jj})\right)\frac{r}{R}(\tilde{J}\tilde{F}^{-1}_{Lm}\partial_L N^b)2\pi RdRdZ \\
& - \int_{\Omega_0} \epsilon\sigma \left(\partial_I\phi_0\tilde{F}^{-1}_{Ij}\right)\left(\partial_K\phi_0\tilde{F}^{-1}_{Ki}\partial_J N^a \tilde{F}^{-1}_{Jj}\right)\tilde{J}\frac{\delta_{1m}N^b}{R}2\pi RdRdZ \\
& - \int_{\Omega_0} \epsilon\sigma \left(\partial_I\phi_0\tilde{F}^{-1}_{Ij}\right)\left(\partial_K\phi_0\tilde{F}^{-1}_{Km}\partial_L N^b \tilde{F}^{-1}_{Lj}\right) \\
& \qquad \left(\partial_L N^a \tilde{F}^{-1}_{Li} + \frac{\delta_{1i}N^a}{r}\right)\tilde{J}\frac{r}{R}2\pi RdRdZ \\
& + \int_{\Omega_0} \left(\frac{\sigma}{4\epsilon}(\phi_0^2-1)^2 + \frac{\epsilon\sigma}{2}\left(\partial_I\phi_0\tilde{F}^{-1}_{Ij}\right)^2\right) \\
& \qquad \left(\tilde{J}\tilde{F}^{-1}_{Lm}\partial_L N^b\right)\partial_K N^a \tilde{F}^{-1}_{Ki}\frac{r}{R}2\pi RdRdZ \\
& - \int_{\Omega_0} \left(\frac{\sigma}{4\epsilon}(\phi_0^2-1)^2 + \frac{\epsilon\sigma}{2}\left(\partial_I\phi_0\tilde{F}^{-1}_{Ij}\right)^2\right) \\
& \qquad \tilde{J}\left(\partial_K N^a \tilde{F}^{-1}_{Km}\partial_L N^b \tilde{F}^{-1}_{Li}\right)\frac{r}{R}2\pi RdRdZ \\
& + \int_{\Omega_0} \left(\frac{\sigma}{4\epsilon}(\phi_0^2-1)^2 + \frac{\epsilon\sigma}{2}\left(\partial_I\phi_0\tilde{F}^{-1}_{Ij}\right)^2\right)\tilde{J}\partial_K N^a \tilde{F}^{-1}_{Ki}\frac{\delta_{1m}N^b}{R}2\pi RdRdZ \\
& + \int_{\Omega_0} \left(\frac{\sigma}{4\epsilon}(\phi_0^2-1)^2 + \frac{\epsilon\sigma}{2}\left(\partial_I\phi_0\tilde{F}^{-1}_{Ij}\right)^2\right)\left(\tilde{J}\tilde{F}^{-1}_{Lm}\partial_L N^b\right)\frac{\delta_{1i}N^a}{R}2\pi RdRdZ\Bigg\}
\end{aligned}
\tag{A.19}
$$

where we used the fact that $\partial\widetilde{J}/\partial\widetilde{\mathbf{F}} = J\widetilde{\mathbf{F}}^{-T}$

Fluids Dissipation Potential

The contribution to the nodal residual $\mathbf{R}^a$ from the fluids dissipation potential, $\mathcal{D}_f$, expressed in the reference configuration and under the axisymmetric hypothesis, is

$$
\mathcal{D}_f[\boldsymbol{\chi}] = \frac{\mu(\phi_0)}{4}\int_{\Omega_f^r}\left[\left|\dot{\widetilde{F}}\widetilde{F}^{-1} + \left(\dot{\widetilde{F}}\widetilde{F}^{-1}\right)^T\right|^2 + 4\left(\frac{\dot{r}}{r}\right)^2\right]\tilde{J}\frac{r}{R}2\pi\, dR\, dZ \tag{A.20}
$$

Differentiating this functional with respect to the nodal DOFs, we can find the contributions to the nodal residual as

$$
(R_{\mathcal{D}_f})_i^a = \frac{\partial\mathcal{D}_f}{\partial\chi_i^a}. \tag{A.21}
$$

Differently from the free energy terms, here the time discretization directly affects the terms inside the integrals. Adopting a backwards Euler time integration scheme for the time derivatives, we have that

$$
\dot{\widetilde{F}} = \frac{\widetilde{F}^{n+1} - \widetilde{F}^n}{\Delta t}, \qquad \dot{r} = \frac{r^{n+1} - r^n}{\Delta t}
$$

Hereafter, the apex n and $n+1$ correspond to the previous and current time steps, respectively. Therefore the nodal contributions $(R_{\mathcal{D}_f})_i^a$ are

$$(R_{\mathcal{D}_f})_i^a = \frac{\mu(\phi_0)}{(\Delta t)^2}\int_{\Omega_f^r}\left[\left((\widetilde{F}_{iK}^{n+1}-\widetilde{F}_{iK}^{n})\widetilde{F}_{Kj}^{n^{-1}}+(\widetilde{F}_{jK}^{n+1}-\widetilde{F}_{jK}^{n})\widetilde{F}_{Ki}^{n^{-1}}\right)\left(\partial_L N^a \widetilde{F}_{Lj}^{n^{-1}}\right)\right.$$
$$\left.+\,2\left(\frac{r^{n+1}-r^n}{r^n}\right)\frac{\delta_{i1}N^a}{r^n}\right]\widetilde{J}^n\frac{r^n}{R}2\pi R dR dZ \tag{A.22}$$

The contribution of the dissipation potential of the fluids to the jacobian matrix, $\mathbf{J}_{\mathcal{D}_f}$, is obtained by differentiating the residual $(R_{\mathcal{D}_f})_i^a$ with respect to the nodal DOFs. Thus, its contribution to the jacobian matrix is

$$(J_{\mathcal{D}_f})_{im}^{ab} := \frac{\partial (R_{\mathcal{D}_f})_i^a}{\partial \chi_m^b}, \tag{A.23}$$

from which we obtain

$$(J_{\mathcal{D}_f})_{im}^{ab} = \frac{\mu(\phi_0)}{(\Delta t)^2}\int_{\Omega_f^r}\left[\left(\partial_K N^b \delta_{im}\widetilde{F}_{Kj}^{n^{-1}}+\partial_K N^b\delta_{jm}\widetilde{F}_{Ki}^{n^{-1}}\right)\left(\partial_L N^a\widetilde{F}_{Lj}^{n^{-1}}\right)\right.$$
$$\left.+\,2\frac{\delta_{1m}N^b}{r^n}\frac{\delta_{i1}N^a}{r^n}\right]\widetilde{J}^n\frac{r^n}{R}2\pi R dR dZ \tag{A.24}$$

Incompressibility Fluids Constraint

The contribution to the nodal residual $\mathbf{R}^a$ due to the incompressibility constraints, $\mathcal{C}_\lambda$, which expressed in the reference configuration and under the axisymmetric hypothesis, corresponds to the term

$$\mathcal{C}_\lambda[\boldsymbol{\chi}] = \frac{\lambda(\phi_0)}{2}\int_{\Omega_f^r}\left(\mathrm{tr}\left(\dot{\widetilde{\mathbf{F}}}\widetilde{\mathbf{F}}^{-1}\right)+\frac{\dot{r}}{r}\right)^2\widetilde{J}\frac{r}{R}2\pi R\,dR\,dZ. \tag{A.25}$$

Differentiating this functional with respect to the nodal DOFs, we obtain its contribution to the nodal residual

$$(R_{\mathcal{C}_\lambda})_i^a = \frac{\partial \mathcal{C}_\lambda}{\partial \chi_i^a} = \frac{\lambda(\phi_0)}{(\Delta t)^2}\int_{\Omega_f^r}\left(\widetilde{F}_{iK}^{n+1}-\widetilde{F}_{iK}^{n})\widetilde{F}_{Ki}^{n^{-1}}+\frac{r^{n+1}-r^n}{r^n}\right)$$
$$\left(\partial_L N^a\widetilde{F}_{Li}^{n^{-1}}+\frac{\delta_{1i}N^a}{r^n}\right)\widetilde{J}^n\frac{r^n}{R}2\pi R dR dZ. \tag{A.26}$$

The contribution of the fluid incompressibility constraint to the jacobian matrix, $\mathbf{J}_{\mathcal{C}_\lambda}$, is obtained by differentiating the residual $(R_{\mathcal{C}_\lambda})_i^a$ with respect to the nodal DOFs. Thus, its contribution to the jacobian matrix is

$$(J_{\mathcal{C}_\lambda})_{im}^{ab} := \frac{\partial (R_{\mathcal{C}_\lambda})_i^a}{\partial \chi_m^b}. \tag{A.27}$$

Applying the derivative to $(R_{\mathcal{C}_\lambda})_i^a$ we obtain

$$(J_{\mathcal{C}_\lambda})_{im}^{ab} = \frac{\lambda(\phi_0)}{(\Delta t)^2}\int_{\Omega_f^r}\left(\partial_K N^b\widetilde{F}_{Km}^{n^{-1}}+\frac{\delta_{1m}N^b}{r^n}\right)\left(\partial_L N^a\widetilde{F}_{Li}^{n^{-1}}+\frac{\delta_{i1}N^a}{r^n}\right)\widetilde{J}^n\frac{r^n}{R}2\pi R dR dZ \tag{A.28}$$

Bibliography

M. Abercrombie, J. E.M. Heaysman, and S. M. Pegrum. The locomotion of fibroblasts in culture i. movements of the leading edge. *Experimental Cell Research*, 59(3):393–398, 1970. ISSN 0014-4827. doi: https://doi.org/10.1016/0014-4827(70)90646-4.

R. Abeyaratne and J.K. Knowles. *Evolution of Phase Transitions: A Continuum Theory*. Cambridge University Press, 2006. ISBN 9780511547133. doi: https://doi.org/10.1017/CBO9780511547133.

J. Ackermann and M. Ben Amar. Onsagers variational principle in proliferating biological tissues, in the presence of activity and anisotropy. *The European Physical Journal Plus*, 138(12):1103, 2023. doi: 10.1140/epjp/s13360-023-04669-9.

F. Alam, S. Kumar, and K.M. Varadarajan. Quantification of adhesion force of bacteria on the surface of biomaterials: Techniques and assays. *ACS Biomaterials Science & Engineering*, 5(5):2093–2110, 2019. doi: 10.1021/acsbiomaterials.9b00213.

Ricard Alert and Xavier Trepat. Physical models of collective cell migration. *Annual Review of Condensed Matter Physics*, 11:77–101, 2020. ISSN 1947-5462. doi: 10.1146/annurev-conmatphys-031218-013516.

D. J. Andrew and A. J. Ewald. Morphogenesis of epithelial tubes: Insights into tube formation, elongation, and elaboration. *Developmental Biology*, 341(1):34–55, 2010. ISSN 0012-1606. doi: https://doi.org/10.1016/j.ydbio.2009.09.024.

M. Arroyo and A. DeSimone. Relaxation dynamics of fluid membranes. *Phys. Rev. E*, 79:031915, 2009. doi: 10.1103/PhysRevE.79.031915.

M. Arroyo, N. Walani, A. Torres-Sánchez, and D. Kaurin. *Onsager's Variational Principle in Soft Matter: Introduction and Application to the Dynamics of Adsorption of Proteins onto Fluid Membranes*, pages 287–332. Springer International Publishing, 2018. ISBN 978-3-319-56348-0. doi: 10.1007/978-3-319-56348-0.

G. A. Ateshian. On the theory of reactive mixtures for modeling biological growth. *Biomechanics and Modeling in Mechanobiology*, 6(6):423–445, 2007. ISSN 1617-7940. doi: 10.1007/s10237-006-0070-x.

S. Badia, A. F. Martin, and F. Verdugo. Mixed aggregated finite element methods for the unfitted discretization of the stokes problem. *SIAM Journal on Scientific Computing*, 40(6):B1541–B1576, 2018a. doi: 10.1137/18M1185624.

S. Badia, F. Verdugo, and A. F. Martín. The aggregated unfitted finite element method for elliptic problems. *Computer Methods in Applied Mechanics and Engineering*, 336: 533–553, 2018b. ISSN 0045-7825. doi: https://doi.org/10.1016/j.cma.2018.03.022.

S. Badia, A. F. Martín, E. Neiva, and F. Verdugo. A generic finite element framework on parallel tree-based adaptive meshes. *SIAM Journal on Scientific Computing*, 42 (6):C436–C468, 2020. doi: 10.1137/20M1328786.

S. Badia, A. F. Martín, E. Neiva, and F. Verdugo. The aggregated unfitted finite element method on parallel tree-based adaptive meshes. *SIAM Journal on Scientific Computing*, 43(3):C203C234, 2021. doi: 10.1137/20m1344512.

N. Q. Balaban, U. S. Schwarz, D. Riveline, P. Goichberg, G. Tzur, I. Sabanay, D. Mahalu, S. Safran, A. Bershadsky, L. Addadi, and B. Geiger. Force and focal adhesion assembly: a close relationship studied using elastic micropatterned substrates. *Nature Cell Biology*, 3(5):466–472, 2001. doi: 10.1038/35074532.

S. Banerjee and M.C. Marchetti. Contractile stresses in cohesive cell layers on finite-thickness substrates. *Physics Review Letters*, 109:108101, 2012. doi: https://doi.org/10.1103/PhysRevLett.109.108101.

Benjamin L. Bangasser, Ghaidan A. Shamsan, Clarence E. Chan, Kwaku N. Opoku, Erkan Tüzel, Benjamin W. Schlichtmann, Jesse A. Kasim, Benjamin J. Fuller, Brannon R. McCullough, Steven S. Rosenfeld, and David J. Odde. Shifting the optimal stiffness for cell migration. *Nature Communications*, 8:15313, 2017. ISSN 2041-1723. doi: 10.1038/ncomms15313.

Y. D. Bansod, T. Matsumoto, K. Nagayama, and J. Bursa. A finite element bendotensegrity model of eukaryotic cell. *Journal of Biomechanical Engineering*, 140(10), 2018. doi: 10.1115/1.4040246.

S. Barrasa-Ramos, C. A. Dessalles, M. Hautefeuille, and A. I. Barakat. Mechanical regulation of the early stages of angiogenesis. *Journal of The Royal Society Interface*, 19(197):20220360, 2022. doi: 10.1098/rsif.2022.0360.

A.E.M. Beedle and P. Roca-Cusachs. In search of a softer environment. *Nature Materials*, 21:995–996, 2022. doi: https://doi.org/10.1038/s41563-022-01345-8.

G.I. Bell. Models for the specific adhesion of cells to cells. *Science*, 200(4342):618–627, 1978. doi: 10.1126/science.347575.

T. Belytschko, W. K. Liu, B. Moran, and K. Elkhodary. *Nonlinear Finite Elements for Continua and Structures*. John Wiley & Sons, Hoboken, NJ, 2 edition, 2013. ISBN 9781118632703.

M. Bennett, M. Cantini, J. Reboud, J. M. Cooper, P. Roca-Cusachs, and M. Salmeron-Sanchez. Molecular clutch drives cell response to surface viscosity. *Proceedings of the National Academy of Sciences of the United States of America*, 115(6):1192–1197, 2018. doi: 10.1073/pnas.1710653115.

E. Benvenuti. Damage integration in the strain space. *International Journal of Solids and Structures*, 41:3167–3191, 2004. doi: https://doi.org/10.1016/j.ijsolstr.2004.01.024.

E. Benvenuti and G.A. Reho. An elastic-damaging cohesive law for cellsubstrate adhesion with positive and negative durotaxis. *Journal of the Mechanics and Physics of Solids*, 185:105569, 2024. doi: https://doi.org/10.1016/j.jmps.2024.105569.

E. Benvenuti, G.A. Reho, S. Palumbo, and M. Fraldi. Pre-strains and buckling in mechanosensitivity of contractile cells and focal adhesions: A tensegrity model. *Journal of the Mechanical Behavior of Biomedical Materials*, 135:105413, 2022. doi: 10.1016/j.jmbbm.2022.105413.

E. Benvenuti, G.A. Reho, S. Palumbo, and M. Fraldi. Mechanics of tensegrity cell units incorporating asymmetry and insights into mollitaxis. *Journal of the Royal Society Interface*, 20:20230082, 2023. doi: https://doi.org/10.1098/rsif.2023.0082.

A. Bershadsky, A. Chausovsky, E. Becker, A. Lyubimova, and B. Geiger. Involvement of microtubules in the control of adhesion-dependent signal transduction. *Current Biology*, 6(10):1279–1289, 1996. doi: 10.1016/S0960-9822(02)70714-8.

J. Betorz, G. R. Bokil, S. M. Deshpande, S. Kulkarni, D. R. Araya, C. Venturini, and P. Sáez. A computational model for early cell spreading, migration, and competing taxis. *Journal of the Mechanics and Physics of Solids*, 179:105390, 2023. ISSN 0022-5096. doi: 10.1016/j.jmps.2023.105390.

A. D. Bicek, E. Tüzel, A. Demtchouk, M. Uppalapati, W. O. Hancock, D. M. Kroll, and D. J. Odde. Anterograde microtubule transport drives microtubule bending in llc-pk1 epithelial cells. *Molecular Biology of the Cell*, 20(12):2943–2953, 2009. doi: 10.1091/mbc.E08-09-0909.

J. Bico, E. Reyssat, and B. Roman. Elastocapillarity: When surface tension deforms elastic solids. *Annual Review of Fluid Mechanics*, 50:629–659, 2018. doi: https://doi.org/10.1146/annurev-fluid-122316-050130.

B. P. Bouchet, A. Akhmanova, and A. Ewald. Microtubules in 3D cell motility. *Journal of Cell Science*, 130(1):39–50, 2017. ISSN 0021-9533. doi: 10.1242/jcs.189431.

C. P. Brangwynne, F. C. MacKintosh, S. Kumar, N. A. Geisse, J. Talbot, L. Mahadevan, K. K. Parker, D. E. Ingber, and D. A. Weitz. Microtubules can bear enhanced compressive loads in living cells because of lateral reinforcement. *Journal of Cell Biology*, 173(5):733–741, 2006. doi: https://doi.org/10.1083/jcb.200601060.

J. Bueno, H. Casquero, Y. Bazilevs, and H. Gómez. Three-dimensional dynamic simulation of elastocapillarity. *Meccanica*, 53(6):1221–1237, 2018. doi: 10.1007/s11012-017-0667-4.

E. Burman, S. Claus, P. Hansbo, M. G. Larson, and A. Massing. Cutfem: Discretizing geometry and partial differential equations. *International Journal for Numerical Methods in Engineering*, 104(7):472–501, 2015. doi: https://doi.org/10.1002/nme.4823.

N. Caille, T. Olivier, T. Yanik, and J.J. Meister. Contribution of the nucleus to the mechanical properties of endothelial cells. *Journal of Biomechanics*, 35(2):177–187, 2002. doi: https://doi.org/10.1016/S0021-9290(01)00201-9.

C. R. Calladine. Buckminster fuller's tensegrity structures and clerk maxwell's rules for the construction of stiff frames. *International Journal of Solids and Structures*, 14(2): 161–172, 1978. ISSN 0020-7683. doi: https://doi.org/10.1016/0020-7683(78)90052-5.

X. Cao, Y. Lin, T.P. Driscoll, J. Franco-Barraza, E. Cukierman, R.L. Mauck, and V.B. Shenoy. A chemomechanical model of matrix and nuclear rigidity regulation of focal adhesion size. *Biophysical Journal*, 109(9):1807–1817, 2015. doi: https://doi.org/10.1016/j.bpj.2015.08.048.

E. A. Cavalcanti-Adam, A. Micoulet, J. Blümmel, J. Auernheimer, H. Kessler, and J. P. Spatz. Lateral spacing of integrin ligands influences cell spreading and focal adhesion assembly. *European Journal of Cell Biology*, 85(3):219–224, 2006. doi: https://doi.org/10.1016/j.ejcb.2005.09.011.

C.E. Chan and D.J. Odde. Traction dynamics of filopodia on compliant substrates. *Science*, 322(5908):1687–1691, 2008. doi: DOI:10.1126/science.1163595.

R. Changede and M. Sheetz. Integrin and cadherin clusters: A robust way to organize adhesions for cell mechanics. *BioEssays*, 39(1):1–12, 2017. doi: 10.1002/bies.201600123.

K. J. Cheung, Z. Gabrielson, E.and Werb, and A. J. Ewald. Collective invasion in breast cancer requires a conserved basal epithelial program. *Cell*, 155(7):1639–1651, 2013. doi: https://doi.org/10.1016/j.cell.2013.11.029.

C. K. Choi, M. Vicente-Manzanares, J. Zareno, L. A. Whitmore, A. Mogilner, and A. R. Horwitz. Actin and α-actinin orchestrate the assembly and maturation of nascent adhesions in a myosin ii motor-independent manner. *Nature Cell Biology*, 10 (9):1039–1050, 2008. ISSN 1476-4679. doi: 10.1038/ncb1763.

G. Cicconofri, P. Blanco, G. Vilanova, Sáez P., and Arroyo M. Active interfacial degradation/deposition of an elastic matrix by a fluid inclusion: Theory and pattern formation. *Journal of the Mechanics and Physics of Solids*, 191:105773, 2024. ISSN 0022-5096. doi: https://doi.org/10.1016/j.jmps.2024.105773.

M.F. Coughlin and D. Stamenović. A tensegrity structure with buckling compression elements: Application to cell mechanics. *Journal of Applied Mechanics*, 64(3):480–486, 1997. doi: 10.1115/1.2788918.

E. Cukierman, R. Pankov, and K.M. Yamada. Cell interactions with three-dimensional matrices. *Current Opinion in Cell Biology*, 14(5):633 640, 2002. doi: 10.1016/s0955-0674(02)00364-2.

M. Cóndor and J.M. García-Aznar. A phenomenological cohesive model for the macroscopic simulation of cellmatrix adhesions. *Biomechanics and Modeling in Mechanobiology*, 16:12071224, 2017. doi: 10.1007/s10237-017-0883-9.

P. de Gennes, F. Brochard-Wyart, and D. Quéré. *Capillarity and Wetting Phenomena: Drops, Bubbles, Pearls, Waves*. Springer New York, 2004. ISBN 978-0-387-21656-0. doi: 10.1007/978-0-387-21656-0.

C. De Pascalis and S. Etienne-Manneville. Single and collective cell migration: the mechanics of adhesions. *Molecular Biology of the Cell*, 28(14):1833–1846, 2017. doi: 10.1091/mbc.E17-03-0134.

S. Deguchi, O. Toshiro, and S. Masaaki. Tensile properties of single stress fibers isolated from cultured vascular smooth muscle cells. *Journal of Biomechanics*, 39(14): 2603–2610, 2006. doi: 10.1016/j.jbiomech.2005.08.026.

A. del Rio, R. Perez-Jimenez, R. Liu, P. Roca-Cusachs, J. M. Fernandez, and M. P. Sheetz. Stretching single talin rod molecules activates vinculin binding. *Science*, 323 (5914):638–641, 2009. doi: 10.1126/science.1162912.

V.S. Deshpande, R.M. McMeeking, and A.G. Evans. A bio-chemo-mechanical model for cell contractility. *Proceedings of the National Academy of Sciences*, 103(38): 14015–14020, 2006. doi: 10.1073/pnas.0605837103.

V.S. Deshpande, M. Mrksich, R.M. McMeeking, and A.G. Evans. A bio-mechanical model for coupling cell contractility with focal adhesion formation. *Journal of the Mechanics and Physics of Solids*, 56(4):1484–1510, 2008. doi: https://doi.org/10.1016/j.jmps.2007.08.006.

M. Doi. Onsagers variational principle in soft matter. *Journal of Physics: Condensed Matter*, 23(28):284118, 2011. doi: 10.1088/0953-8984/23/28/284118.

M. Doi. Onsager principle as a tool for approximation. *Chinese Physics B*, 24(2):020505, 2015. doi: 10.1088/1674-1056/24/2/020505.

S. Douezan, K. Guevorkian, R. Naouar, Dufour S., D. Cuvelier, and F. Brochard-Wyart. Spreading dynamics and wetting transition of cellular aggregates. *Proceedings of the National Academy of Sciences*, 108(18):7315–7320, 2011. doi: 10.1073/pnas.1018057108.

Q. Du, C. Liu, and X. Wang. A phase field approach in the numerical study of the elastic bending energy for vesicle membranes. *Journal of Computational Physics*, 198 (2):450–468, 2004. ISSN 0021-9991. doi: https://doi.org/10.1016/j.jcp.2004.01.029.

X. Du, G. Zhao, W. Wang, and H. Fang. Nitsches method for non-conforming multipatch coupling in hyperelastic isogeometric analysis. *Comput. Mech.*, 65(3):687710, 2020. doi: 10.1007/s00466-019-01789-x.

C. Duprat and H. Stone. *FluidStructure Interactions in Low-Reynolds-Number Flows*. The Royal Society of Chemistry, 2015. ISBN 978-1-84973-813-2. doi: 10.1039/9781782628491.

A. Dupré. *Théorie Mécanique de la Chaleur*. Gauthier-Villars, Paris, 1869.

L. Dvir, R. Nissim, M. B. Alvarez-Elizondo, and D. Weihs. Quantitative measures to reveal coordinated cytoskeleton-nucleus reorganization during in vitro invasion of cancer cells. *New Journal of Physics*, 17(4):043010, 2015. doi: 10.1088/1367-2630/17/4/043010.

D.G.B. Edelen. A nonlinear onsager theory of irreversibility. *International Journal of Engineering Science*, 10(6):481–490, 1972. ISSN 0020-7225. doi: https://doi.org/10.1016/0020-7225(72)90091-2.

M. Egeblad, M. G. Rasch, and V. M. Weaver. Dynamic interplay between the collagen scaffold and tumor evolution. *Current Opinion in Cell Biology*, 22(5):697–706, 2010. ISSN 0955-0674. doi: https://doi.org/10.1016/j.ceb.2010.08.015.

A. Elosegui-Artola, R. Oria, Y. Chen, A. Kosmalska, C. Perez-Gonzalez, N. Castro, C. Zhu, X. Trepat, and P. Roca-Cusachs. Mechanical regulation of a molecular clutch defines force transmission and transduction in response to matrix rigidity. *Nature Cell Biology*, 18(5):540–548, 2016. ISSN 1476-4679. doi: 10.1038/ncb3336.

A. Elosegui-Artola, X. Trepat, and P. Roca-Cusachs. Control of mechanotransduction by molecular clutch dynamics. *Trends in Cell Biology*, 28(5):356–367, 2018. ISSN 0962-8924. doi: https://doi.org/10.1016/j.tcb.2018.01.008.

A. Erlich, J. Étienne, J. Fouchard, and T. Wyatt. How dynamic prestress governs the shape of living systems, from the subcellular to tissue scale. *Interface Focus*, 12(6): 20220038, 2022. doi: https://doi.org/10.1098/rsfs.2022.0038.

E.A. Evans. Detailed mechanics of membrane-membrane adhesion and separation. i. continuum of molecular cross-bridges. *Journal of Biophysical Society*, 48:175–183, 1985a. doi: 10.1016/S0006-3495(85)83770-X.

E.A. Evans. Detailed mechanics of membrane-membrane adhesion and separation. ii. discrete kinetically trapped molecular cross-bridges. *Journal of Biophysical Society*, 48:185–192, 1985b. doi: https://doi.org/10.1016/S0006-3495(85)83771-1.

A. J. Ewald, A. Brenot, M. Duong, B. S. Chan, and Werb Z. Collective epithelial migration and cell rearrangements drive mammary branching morphogenesis. *Developmental Cell*, 14(4):570–581, 2008. doi: https://doi.org/10.1016/j.devcel.2008.03.003.

Robert Finn. *Equilibrium Capillary Surfaces*, volume 284 of *Grundlehren der mathematischen Wissenschaften*. Springer-Verlag, New York, 1986. ISBN 978-0-387-96174-8.

T. E. Fisher, A.F. Oberhauser, M. Carrion-Vazquez, P.E. Marszalek, and J.M. Fernandez. The study of protein mechanics with the atomic force microscope. *Trends in Biochemical Sciences*, 24(10):379–384, 1999. doi: 10.1016/s0968-0004(99)01453-x.

J. S. Fitzgerald, T. G. Poehlmann, E. Schleussner, and U. R. Markert. Trophoblast invasion: the role of intracellular cytokine signalling via signal transducer and activator of transcription 3 (stat3). *Human Reproduction Update*, 14(4):335–344, 2008. doi: 10.1093/humupd/dmn010.

D. A. Fletcher and R. D. Mullins. Cell mechanics and the cytoskeleton. *Nature*, 463 (7280):485–492, 2010. doi: 10.1038/nature08908.

R. A. Foty, C. M. Pfleger, G. Forgacs, and M.S. Steinberg. Surface tensions of embryonic tissues predict their mutual envelopment behavior. *Development*, 122(5):1611–1620, 1996. ISSN 0950-1991. doi: 10.1242/dev.122.5.1611.

M. Fraldi, S. Palumbo, A.R. Carotenuto, A. Cutolo, L. Deseri, and L. Pugno. Buckling soft tensegrities: Fickle elasticity and configurational switching in living cells. *Journal of the Mechanics and Physics of Solids*, 124:299–324, 2019. doi: Bucklingsofttensegrities:Fickleelasticityandconfigurationalswitchinginlivingcells.

C.M. Franz and D.J. Müller. Analyzing focal adhesion structure by atomic force microscopy. *Journal of Cell Science*, 118(22):5315–5323, 2005. doi: 10.1242/jcs.02653.

P. Friedl. Prespecification and plasticity: shifting mechanisms of cell migration. *Current Opinion in Cell Biology*, 16(1):14–23, 2004. ISSN 0955-0674. doi: https://doi.org/10.1016/j.ceb.2003.11.001.

P. Friedl and S. Alexander. Cancer invasion and the microenvironment: Plasticity and reciprocity. *Cell*, 147(5):992–1009, 2011. doi: https://doi.org/10.1016/j.cell.2011.11.016.

P. Friedl and D. Gilmour. Collective cell migration in morphogenesis, regeneration and cancer. *Nature Reviews Molecular Cell Biology*, 10(7):445–457, 2009. doi: 10.1038/nrm2720.

P. Friedl and K. Wolf. Plasticity of cell migration: a multiscale tuning model. *Journal of Cell Biology*, 188(1):11–19, 2009. doi: 10.1083/jcb.200909003.

H. Gao, J. Qian, and B. Chen. Probing mechanical principles of focal contacts in cell-matrix adhesion with a coupled stochastic-elastic modelling framework. *Journal of the Royal Society Interface*, 8(62):1217–1232, 2011. doi: 10.1098/rsif.2011.0157.

M. L. Gardel, B. Sabass, L. Ji, G. Danuser, U. S. Schwarz, and C. M. Waterman. Traction stress in focal adhesions correlates biphasically with actin retrograde flow speed. *Journal of Cell Biology*, 183(6):999–1005, 12 2008. ISSN 0021-9525. doi: 10.1083/jcb.200810060.

K. Garikipati. The kinematics of biological growth. *Applied Mechanics Reviews*, 62(3):030801, 2009. doi: 10.1115/1.3090829.

M. Geers. *Experimental analysis and computational modelling of damage and fracture*. PhD thesis, TU Delft, 1997.

B. Geiger and A. Bershadsky. Assembly and mechanosensory function of focal contacts. *Current opinion in cell biology*, 13(5):584–592, 2001. doi: 10.1016/s0955-0674(00)00255-6.

B. Geiger and A. Bershadsky. Exploring the neighborhood: Adhesion-coupled cell mechanosensors. *Cell*, 110(2):139–142, 2002. ISSN 0092-8674. doi: https://doi.org/10.1016/S0092-8674(02)00831-0.

B. Geiger, J. P. Spatz, and A. D. Bershadsky. Environmental sensing through focal adhesions. *Nature Reviews Molecular Cell Biology*, 10(1):21–33, 2009. ISSN 1471-0080. doi: 10.1038/nrm2593.

E. Gentleman, A.N. Lay, D. A. Dickerson, E. A. Nauman, G. A. Livesay, and K. C. Dee. Mechanical characterization of collagen fibers and scaffolds for tissue engineering. *Biomaterials*, 24(21):3805–3813, 2003. doi: https://doi.org/10.1016/S0142-9612(03)00206-0.

F. Gittes, B. Mickey, J. Nettleton, and J. Howard. Flexural rigidity of microtubules and actin filaments measured from thermal fluctuations in shape. *Journal of Cell Biology*, 120(4):923–934, 1993. doi: 10.1083/jcb.120.4.923.

Bo Gong, Xi Wei, Jin Qian, and Yuan Lin. Modeling and simulations of the dynamic behaviors of actin-based cytoskeletal networks. *ACS Biomaterials Science & Engineering*, 5(8):3720–3734, 2019. doi: 10.1021/acsbiomaterials.8b01228.

N.B. Gudimchuk, E.V. Ulyanov, E. OToole, C.L. Page, D.S. Vinogradov, G. Morgan, G. Li, J.K. Moore, E. Szczesna, A. Roll-Mecak, F.I. Ataullakhanov, and J. Richard McIntosh. Mechanisms of microtubule dynamics and force generation examined with computational modeling and electron cryotomography. *Nature Communications*, 11:3765, 2020. doi: 10.1038/s41467-020-17553-2.

M.E. Gurtin. *Configurational Forces as Basic Concepts of Continuum Physics*. Springer New York, NY, 1999. ISBN 978-0-387-98667-8. doi: https://doi.org/10.1007/b97847.

A. Hall. The cytoskeleton and cancer. *Cancer and Metastasis Reviews*, 28(1):5–14, 2009. doi: 10.1007/s10555-008-9166-3.

P. Hansbo. Nitsche's method for interface problems in computational mechanics. *GAMM-Mitteilungen*, 28(2):183–206, 2005. doi: https://doi.org/10.1002/gamm.201490018.

J. Happel and H. Brenner. *Low Reynolds Number Hydrodynamics: With Special Applications to Particulate Media*. Prentice-Hall, Englewood Cliffs, NJ, 1965.

S. He, Y. Su, Y. Su, Ji B., and H. Gao. Some basic questions on mechanosensing in cellsubstrate interaction. *Journal of the Mechanics and Physics of Solids*, 70:116–135, 2014. doi: https://doi.org/10.1016/j.jmps.2014.05.016.

S.R. Heidemann and R.E. Buxbaum. Mechanical tension as a regulator of axonal development. *Neurotoxicology*, 15(1):95107, 1994.

H. Herrmann, H. Bär, L. Kreplak, S. V. Strelkov, and U. Aebi. Intermediate filaments: from cell architecture to nanomechanics. *Nature Reviews Molecular Cell Biology*, 8 (7):562–573, 2007. doi: 10.1038/nrm2197.

C. Hidalgo-Carcedo, S. Hooper, S.I. Chaudhry, P. Williamson, K. Harrington, B. Leitinger, and E. Sahai. Collective cell migration requires suppression of actomyosin at cellcell contacts mediated by ddr1 and the cell polarity regulators par3 and par6. *Nature Cell Biology*, 13(1):49–59, 2011. doi: 10.1038/ncb2133.

Y. Hideki, W. Jeffrey, and C. John. Cell migration in tumors. *Current Opinion in Cell Biology*, 17(5):559–564, 2005. doi: https://doi.org/10.1016/j.ceb.2005.08.002.

T.L. Hill. Microfilament or microtubule assembly or disassembly against a force. *Proceedings of the National Academy of Sciences*, 78(9):5613–5617, 1981. doi: 10.1073/pnas.78.9.5613.

T.L. Hill and M.W. Kirschner. Bioenergetics and kinetics of microtubule and actin filament assembly-disassembly. *International Review of Cytology*, 78:1–125, 1982. doi: https://doi.org/10.1016/S0074-7696(08)60105-9.

M. Hoffmann and U.S. Schwarz. A kinetic model for RNA-interference of focal adhesions. *BMC Systems Biology*, 7(2):1–18, 2013. doi: https://doi.org/10.1186/1752-0509-7-2.

G.A. Holzapfel. *Nonlinear solid mechanics: a continuum approach for engineering*. John Wiley and Sons, 2000.

R. Horwitz and D. Webb. Cell migration. *Current Biology*, 13(19):R756–R759, 2003. doi: 10.1016/j.cub.2003.09.014.

D. E. Ingber. Cellular tensegrity: defining new rules of biological design that govern the cytoskeleton. *Journal of Cell Science*, 104(3):613–627, 1993. doi: 10.1242/jcs.104.3.613.

D. E. Ingber. Tensegrity: the architectural basis of cellular mechanotransduction. *Annual Review of Physiology*, 59:575–599, 1997. doi: 10.1146/annurev.physiol.59.1.575.

D. E. Ingber, N. Wang, and D. Stamenovi. Tensegrity, cellular biophysics, and the mechanics of living systems. *Reports on Progress in Physics*, 77(4):046603, 2014. doi: 10.1088/0034-4885/77/4/046603.

B. C. Isenberg, P. A. DiMilla, M. Walker, S. Kim, and J. Y. Wong. Vascular smooth muscle cell durotaxis depends on substrate stiffness gradient strength. *Biophysical Journal*, 97(5):1313–1322, 2009. ISSN 0006-3495. doi: https://doi.org/10.1016/j.bpj.2009.06.021.

A. Isomursu, KY. Park, J. Hou, and et al. Directed cell migration towards softer environments. *Nature Materials*, 21:1081–1090, 2022. doi: https://doi.org/10.1038/s41563-022-01294-2.

D.G. Jay. The clutch hypothesis revisited: Ascribing the roles of actin-associated proteins in filopodial protrusion in the nerve growth cone. *Journal of Neurobiology*, 44(2):114–125, 2000. doi: https://doi.org/10.1002/1097-4695(200008)44:2<114::AID-NEU3>3.0.CO;2-8.

P. Kanchanawong, G. Shtengel, A. M. Pasapera, E. B. Ramko, M. W. Davidson, H. F. Hess, and C. M. Waterman. Nanoscale architecture of integrin-based cell adhesions. *Nature*, 468(7323):580–584, 2010. ISSN 1476-4687. doi: 10.1038/nature09621.

J. Z. Kechagia, J. Ivaska, and P. Roca-Cusachs. Integrins as biomechanical sensors of the microenvironment. *Nature Reviews Molecular Cell Biology*, 20(8):457–473, 2019. ISSN 1471-0080. doi: 10.1038/s41580-019-0134-2.

D-H. Kim and D. Wirtz. Focal adhesion size uniquely predicts cell migration. *The FASEB Journal*, 27(4):1351–1361, 2013. doi: 10.1096/fj.12-220160.

R. Kolasangiani, T. C. Bidone, and M. A. Schwartz. Integrin conformational dynamics and mechanotransduction. *Cells*, 11(22), 2022. ISSN 2073-4409. doi: 10.3390/cells11223584.

F. Kong, A. J. Garcia, A. P. Mould, M. J. Humphries, and C. Zhu. Demonstration of catch bonds between an integrin and its ligand. *Journal of Cell Biology*, 185(7):1275–1284, 2009. doi: 10.1083/jcb.200810002.

D. E. Koser, A. J. Thompson, S. K. Foster, A. Dwivedy, E. K. Pillai, G. K. Sheridan, H. Svoboda, M. Viana, L. da F. Costa, J. Guck, C. E. Holt, and K. Franze. Mechanosensing is critical for axon growth in the developing brain. *Nature Neuroscience*, 19(12):1592–1598, 2016. ISSN 1546-1726. doi: 10.1038/nn.4394.

R. Kristal-Muscal, L. Dvir, and D. Weihs. Metastatic cancer cells tenaciously indent impenetrable, soft substrates. *New Journal of Physics*, 15(3):035022, 2013. doi: 10.1088/1367-2630/15/3/035022.

K. Kruse, J. F. Joanny, F. Jülicher, J. Prost, and K. Sekimoto. Generic theory of active polar gels: a paradigm for cytoskeletal dynamics. *European Physical Journal E: Soft Matter*, 16(1):5–16, 2005. doi: 10.1140/epje/e2005-00002-5.

M. Kurachi, M. Hoshi, and H. Tashiro. Buckling of a single microtubule by optical trapping forces: direct measurement of microtubule rigidity. *Cell Motil Cytoskeleton*, 30(3):221–8, 1995. doi: 10.1002/cm.970300306.

L. Lamalice, F. Le Boeuf, and Huot J. Endothelial cell migration during angiogenesis. *Circulation Research*, 100(6):782–794, 2007. doi: 10.1161/01.RES.0000259593.07661.1e.

T. Lämmermann and M. Sixt. Mechanical modes of 'amoeboid' cell migration. *Current Opinion in Cell Biology*, 21(5):636–644, 2009. doi: 10.1016/j.ceb.2009.05.003.

D. A. Lauffenburger and A. F. Horwitz. Cell migration: A physically integrated molecular process. *Cell*, 84(3):359–369, 1996. doi: 10.1016/s0092-8674(00)81280-5.

C.-T. Lee and E. M. Terentjev. Microtubule buckling in an elastic matrix with quenched disorder. *The Journal of Chemical Physics*, 149(14):145101, 2018. ISSN 0021-9606. doi: 10.1063/1.5049538.

A. Lew, J. E Marsden, M. Ortiz, and M. West. Variational time integrators. *International Journal for Numerical Methods in Engineering*, 60(1):153–212, 2004. doi: https://doi.org/10.1002/nme.958.

Z. Li, H. Lee, and C. Zhu. Molecular mechanisms of mechanotransduction in integrin-mediated cell-matrix adhesion. *Experimental Cell Research*, 349(1):85–94, 2016. ISSN 0014-4827. doi: https://doi.org/10.1016/j.yexcr.2016.10.001.

C.H. Lin, E.M. Espreafico, M.S. Mooseker, and P Forscher. Myosin drives retrograde f-actin flow in neuronal growth cones. *Neuron*, 16(4):769–782, 1996. ISSN 0896-6273. doi: https://doi.org/10.1016/S0896-6273(00)80097-5.

P. Liu, Y.W. Zhang, Q.H. Cheng, and C. Lu. Simulations of the spreading of a vesicle on a substrate surface mediated by receptor-ligand binding. *Journal of the Mechanics and Physics of Solids*, 55(6):1166–1181, 2007. doi: https://doi.org/10.1016/j.jmps.2006.12.001.

C.M. Lo, H.B. Wang, M. Dembo, and Y.L. Wang. Cell movement is guided by the rigidity of the substrate. *Biophysical Journal*, 79:144–152, 2000. doi: https://doi.org/10.1016/S0006-3495(00)76279-5.

M. C. Marchetti, J. F. Joanny, S. Ramaswamy, T. B. Liverpool, J. Prost, M. Rao, and R. A. Simha. Hydrodynamics of soft active matter. *Reviews of Modern Physics*, 85 (3):1143–1189, 2013. doi: 10.1103/RevModPhys.85.1143.

A.B. Mathur, W.M. Reichert, and G.A. Truskey. Flow and high affinity binding affect the elastic modulus of the nucleus, cell body and the stress fibers of endothelial cells. *Annals of Biomedical Engineering*, 35:1120–1130, 2007. doi: 10.1007/s10439-007-9288-8.

J. G. McGarry and P. J. Prendergast. A three-dimensional finite element model of an adherent eukaryotic cell. *European Cells & Materials*, 7:27–33, 2004. URL `https://api.semanticscholar.org/CorpusID:16497496`.

A. Mielke, D. R. M. Renger, and M. A. Peletier. A generalization of onsagers reciprocity relations to gradient flows with nonlinear mobility. *Journal of Non-Equilibrium Thermodynamics*, 41(2):141149, 2016. doi: 10.1515/jnet-2015-0073.

W. Mirza, A. Torres-Sánchez, G. Vilanova, and M. Arroyo. Variational formulation of active nematic fluids: theory and simulation. *New Journal of Physics*, 27(4):043025, 2025. doi: 10.1088/1367-2630/adcd93.

T. Mitchison and M. Kirschner. Dynamic instability of microtubule growth. *Nature*, 312(5991):237–242, 1984. doi: 10.1038/312237a0.

T. Mitchison and M. Kirschner. Cytoskeletal dynamics and nerve growth. *Neuron*, 1(9): 761–772, 1988. ISSN 0896-6273. doi: https://doi.org/10.1016/0896-6273(88)90124-9.

N. Moës, J. Dolbow, and T. Belytschko. A finite element method for crack growth without remeshing. *International Journal for Numerical Methods in Engineering*, 46(1): 131–150, 1999. doi: https://doi.org/10.1002/(SICI)1097-0207(19990910)46:1<131::AID-NME726>3.0.CO;2-J.

A. Mogilner and G. Oster. Cell motility driven by actin polymerization. *Biophysical Journal*, 71(6):3030–3045, 1996. doi: 10.1016/S0006-3495(96)79496-1.

R. Motro. *Tensegrity: Structural Systems for the Future*. Elsevier Science, 2003. ISBN 9781903996379. URL `https://books.google.it/books?id=6aWtlMqwdnsC`.

M. Murrell, P. Oakes, M. Lenz, and M.L. Gardel. Forcing cells into shape: the mechanics of actomyosin contractility. *Nature Reviews Molecular Cell Biology*, 16:486–498, 2015. doi: https://doi.org/10.1038/nrm4012.

M.P. Murrell and M.L. Gardel. F-actin buckling coordinates contractility and severing in a biomimetic actomyosin cortex. *Proceedings of the National Academy of Sciences*, 109(51):20820–20825, 2012. doi: https://doi.org/10.1073/pnas.1214753109.

F. Neumann. *Vorlesungen über die Theorie der Capillarität*. B.G. Teubner, Leipzig, Ger., 1894.

T. Nguyen and Y. Gu. Investigation of cell-substrate adhesion properties of living chondrocyte by measuring adhesive shear force and detachment using afm and inverse fea. *Scientific Reports*, 6:38059, 2016. doi: https://doi.org/10.1038/srep38059.

A. Nicolas, Geiger B., and S.A. Safran. Cell mechanosensitivity controls the anisotropy of focal adhesions. *Proceedings of the National Academy of Sciences*, 101(34):12520 12525, 2004. doi: https://doi.org/10.1073/pnas.0403539101.

Johannes C. C. Nitsche. Über ein variationsprinzip zur lösung von dirichlet-problemen bei verwendung von teilräumen, die keinen randbedingungen unterworfen sind. *Abhandlungen aus dem Mathematischen Seminar der Universität Hamburg*, 36:9–15, 1971. URL `https://api.semanticscholar.org/CorpusID:122609590`.

Patrick W. Oakes, Shiladitya Banerjee, M. Cristina Marchetti, and Margaret L. Gardel. Geometry regulates traction stresses in adherent cells. *Biophysical Journal*, 107(4): 825–833, 2014. doi: 10.1016/j.bpj.2014.06.045.

R.W. Ogden. *Nonlinear Elasticity with Application to Material Modelling.* Series: AMAS Lecture Notes, 6. Polish Academy of Sciences: Warsaw, Poland, 2003.

L. Onsager. Reciprocal relations in irreversible processes. i. *Physical Review*, 37:405–426, 1931. doi: 10.1103/PhysRev.37.405.

M. Ortiz and A. Pandolfi. Finite-deformation irreversible cohesive elements for three-dimensional crack-propagation analysis. *International Journal for Numerical Methods in Engineering*, 44(9):1267–1282, 1999. doi: https://doi.org/10.1002/(SICI)1097-0207(19990330)44:9<1267::AID-NME486>3.0.CO;2-7.

M. Ortiz and E.A. Repetto. Nonconvex energy minimization and dislocation structures in ductile single crystals. *Journal of the Mechanics and Physics of Solids*, 47(2): 397–462, 1999. doi: https://doi.org/10.1016/S0022-5096(97)00096-3.

A. Palamidessi, C. Malinverno, E. Frittoli, S. Corallino, E. Barbieri, S. Sigismund, G. V. Beznoussenko, E. Martini, M. Garre, I. Ferrara, C. Tripodo, F. Ascione, E. A. Cavalcanti-Adam, Q. Li, P. P. Di Fiore, D. Parazzoli, F. Giavazzi, R. Cerbino, and G. Scita. Unjamming overcomes kinetic and proliferation arrest in terminally differentiated cells and promotes collective motility of carcinoma. *Nature Materials*, 18 (11):1252–1263, 2019. ISSN 1476-4660. doi: 10.1038/s41563-019-0425-1.

E. K. Paluch and E. Raz. The role and regulation of blebs in cell migration. *Current Opinion in Cell Biology*, 25(5):582–590, 2013. doi: 10.1016/j.ceb.2013.05.005.

S. Palumbo, A.R. Carotenuto, A. Cutolo, L. Deseri, and M. Fraldi. Nonlinear elasticity and buckling in the simplest soft-strut tensegrity paradigm. *International Journal of Non-Linear Mechanics*, 106:80–88, 2018. doi: https://doi.org/10.1016/j.ijnonlinmec.2018.08.011.

S. Palumbo, E. Benvenuti, and M. Fraldi. Actomyosin contractility and buckling of microtubules in nucleation, growth and disassembling of focal adhesions. *Biomechanics and Modeling in Mechanobiology*, 21:1187–1200, 2022. doi: 10.1007/s10237-022-01584-3.

F. Pampaloni, G. Lattanzi, A. Jonáš, T. Surrey, E. Frey, and E. L. Florin. Thermal fluctuations of grafted microtubules provide evidence of a length-dependent persistence length. *Proceedings of the National Academy of Sciences of the United States of America*, 103(27):10248–10253, 2006. doi: 10.1073/pnas.0603931103.

J. T. Parsons. Focal adhesion kinase: the first ten years. *Journal of Cell Science*, 116 (8):1409–1416, 2003. doi: 10.1242/jcs.00373.

P. Paul, R.and Heil, J.P. Spatz, and U. S. Schwarz. Propagation of mechanical stress through the actin cytoskeleton toward focal adhesions: Model and experiment. *Biophysical Journal*, 94(4):1470–1482, 2008. doi: 10.1529/biophysj.107.108688.

C. Peco, A. Rosolen, and M. Arroyo. An adaptive meshfree method for phase-field models of biomembranes. part ii: A lagrangian approach for membranes in viscous fluids. *Journal of Computational Physics*, 249:320–336, 2013. doi: https://doi.org/10.1016/j.jcp.2013.04.038.

R. Peerlings, R. Borst, W. Brekelmans, and J. Vree. Gradient enhanced damage for quasi-brittle material. *International Journal for Numerical Methods in Engineering*, 39:3391–3403, 1996. doi: https://doi.org/10.1002/(SICI)1097-0207(19961015)39:19<3391::AID-NME7>3.0.CO;2-D.

S. Peihong, T. Ye, Y. Chaofei, M. Xiaoli, W. Xue, P. Jiawei, and Q. Airong. Mesenchymal stem cell migration during bone formation and bone diseases therapy. *International Journal of Molecular Sciences*, 19(8), 2018. doi: 10.3390/ijms19082343.

Mark A. Peletier. Variational modelling: Energies, gradient flows, and large deviations, 2014.

S. Pellegrin and H. Mellor. Actin stress fibres. *Journal of Cell Science*, 120(20): 3491–3499, 2007. doi: 10.1242/jcs.018473.

C. Pérez-González, R. Alert, C. Blanch-Mercader, M. Gómez-González, T. Kolodziej, E. Bazellieres, J. Casademunt, and X. Trepat. Active wetting of epithelial tissues. *Nature Physics*, 15(1):79–88, 2019. doi: https://doi.org/10.1038/s41567-018-0279-5.

Charles S. Peskin. The immersed boundary method. *Acta Numerica*, 11:479517, 2002. doi: 10.1017/S0962492902000077.

S. V. Plotnikov, A. M. Pasapera, B. Sabass, and C. M. Waterman. Force fluctuations within focal adhesions mediate ecm-rigidity sensing to guide directed cell migration. *Cell*, 151(7):1513–1527, 2012. doi: 10.1016/j.cell.2012.11.034.

T. D. Pollard, L. Blanchoin, and R. D. Mullins. Molecular mechanisms controlling actin filament dynamics in nonmuscle cells. *Annual Review of Biophysics*, 29(Volume 29, 2000):545–576, 2000. ISSN 1936-1238. doi: https://doi.org/10.1146/annurev.biophys.29.1.545.

M. Prager-Khoutorsky, A. Lichtenstein, R. Krishnan, K. Rajendran, A. Mayo, Z. Kam, B. Geiger, and A.D. Bershadsky. Fibroblast polarization is a matrix-rigidity-dependent process controlled by focal adhesion mechanosensing. *Nature cell biology*, 13(12):1457–65, 2011. doi: https://doi.org/10.1038/ncb2370.

I. Prigogine. *Introduction to Thermodynamics of Irreversible Processes*. John Wiley & Sons, 1967.

A. J. Putnam, K. Schultz, and D. J. Mooney. Control of microtubule assembly by extracellular matrix and externally applied strain. *American Journal of Physiology-Cell Physiology*, 280(3):C556–C564, 2001. doi: 10.1152/ajpcell.2001.280.3.C556.

T. Qian, X.-P. Wang, and P. Sheng. A variational approach to moving contact line hydrodynamics. *Journal of Fluid Mechanics*, 564:333360, 2006. doi: 10.1017/S0022112006001935.

N. B. M. Rafiq, Y. Nishimura, S. V. Plotnikov, V. Thiagarajan, Z. Zhang, S. Shi, M. Natarajan, V. Viasnoff, P. Kanchanawong, G. E. Jones, and A. D. Bershadsky. A mechano-signalling network linking microtubules, myosin iia filaments and integrin-based adhesions. *Nature Materials*, 18(6):638–649, 2019. doi: 10.1038/s41563-019-0371-y.

M. Rahimi and M. Arroyo. Shape dynamics, lipid hydrodynamics, and the complex viscoelasticity of bilayer membranes. *Phys. Rev. E*, 86:011932, 2012. doi: 10.1103/PhysRevE.86.011932.

M.K. Rausch and E. Kuhl. On the effect of prestrain and residual stress in thin biological membranes. *Journal of the Mechanics and Physics of Solids*, 61(9):1955–1969, 2013. doi: https://doi.org/10.1016/j.jmps.2013.04.005.

T. Razafiarison, C.N. Holenstein, T. Stauber, M. Jovic, E. Vertudes, M. Loparic, M. Kawecki, L. Bernard, U. Silvan, and J.G. Snedeker. Biomaterial surface energy-driven ligand assembly strongly regulates stem cell mechanosensitivity and fate on very soft substrates. *Proceedings of the National Academy of Sciences*, 115(18):4631–4636, 2018. doi: 10.1073/pnas.1704543115.

P. Recho, T. Putelat, and L. Truskinovsky. Contraction-driven cell motility. *Physical Review Letters*, 111:108102, 2013. doi: https://doi.org/10.1103/PhysRevLett.111.108102.

A.J. Ridley, M.A. Schwartz, K. Burridge, R.A. Firtel, M.H. Ginsberg, G. Borisy, J.T. Parsons, and A.R. Horwitz. Cell migration: Integrating signals from front to back. *Science*, 302(5651):1704–1709, 2003. doi: 10.1126/science.1092053.

D. Riveline, E. Zamir, N. Q. Balaban, U. S. Schwarz, T. Ishizaki, S. Narumiya, Z. Kam, B. Geiger, and A. D. Bershadsky. Focal contacts as mechanosensors: Externally applied local mechanical force induces growth of focal contacts by an mdia1-dependent and rock-independent mechanism. *Journal of Cell Biology*, 153(6):1175–1186, 06 2001. ISSN 0021-9525. doi: 10.1083/jcb.153.6.1175.

P. Robison, M. A. Caporizzo, H. Ahmadzadeh, A. I. Bogush, C. Y. Chen, K. B. Margulies, V. B. Shenoy, and B. L. Prosser. Detyrosinated microtubules buckle and bear load in contracting cardiomyocytes. *Science*, 352(6284):aaf0659, 2016. doi: 10.1126/science.aaf0659.

E. K. Rodriguez, A. Hoger, and A. D. McCulloch. Stress-dependent finite growth in soft elastic tissues. *Journal of Biomechanics*, 27(4):455–467, 1994. doi: 10.1016/0021-9290(94)90021-3.

W. Ronan, V. S. Deshpande, R. M. McMeeking, and J. P. McGarry. Cellular contractility and substrate elasticity: a numerical investigation of the actin cytoskeleton and cell adhesion. *Biomechanics and Modeling in Mechanobiology*, 13(2):417–435, 2014. doi: 10.1007/s10237-013-0506-z.

B. Rubinstein, M. F. Fournier, K. Jacobson, A. B. Verkhovsky, and A. Mogilner. Actin-myosin viscoelastic flow in the keratocyte lamellipod. *Biophysical Journal*, 97(7): 1853–1863, 2009. doi: 10.1016/j.bpj.2009.07.020.

P.L. Ryan, R.A. Foty, J. Kohn, and M.S. Steinberg. Tissue spreading on implantable substrates is a competitive outcome of cellcell vs. cellsubstratum adhesivity. *Proceedings of the National Academy of Sciences*, 98(8):4323–4327, 2001. doi: 10.1073/pnas.071615398.

P. Saez, P. U. Shirke, J. R. Seth, J. Alegre-Cebollada, and A. Majumder. Competing elastic and viscous gradients determine directional cell migration. *Mathematical Biosciences*, 380:109362, 2025. doi: 10.1016/j.mbs.2024.109362.

J. D. Sanders, T. A. Laursen, and M. A. Puso. A nitsche embedded mesh method. *Comput. Mech.*, 49(2):243257, 2012. doi: 10.1007/s00466-011-0641-2.

D. Santos Oliván, A. Torres Sánchez, G. Vilanova Caicoya, M. R. Bayat, J. Font i Reverter, W. A. Mirza, and M. Arroyo Balaguer. hiperlife: High performance parallel library for finite elements, 2021.

E. Scarpa and R. Mayor. Collective cell migration in development. *Journal of Cell Biology*, 212(2):143–155, 2016. ISSN 0021-9525. doi: 10.1083/jcb.201508047.

S. M. Schoenwaelder and K. Burridge. Bidirectional signaling between the cytoskeleton and integrins. *Current Opinion in Cell Biology*, 11(2):274–286, 1999. ISSN 0955-0674. doi: https://doi.org/10.1016/S0955-0674(99)80037-4.

M Serpelloni, M. Arricca, C. Bonanno, and A. Salvadori. Modeling cells spreading, motility, and receptors dynamics: a general framework. *Acta Mechanica Sinica*, 37: 1013–1030, 2021. doi: https://doi.org/10.1007/s10409-021-01088-w.

A. Shellard and R. Mayor. Durotaxis: The hard path from in vitro to in vivo. *Developmental Cell*, 56(2):227–239, 2021. doi: 10.1016/j.devcel.2020.11.019.

T. Shemesh, B. Geiger, A. D. Bershadsky, and M. M. Kozlov. Focal adhesions as mechanosensors: A physical mechanism. *Proceedings of the National Academy of Sciences*, 102(35):12383–12388, 2005. doi: https://doi.org/10.1073/pnas.0500254102.

Z. Shen, H. Ye, X. Yi, and Y. Li. Membrane wrapping efficiency of elastic nanoparticles during endocytosis: Size and shape matter. *ACS Nano*, 13(1):215–228, 2019. doi: 10.1021/acsnano.8b05340.

V. B. Shenoy, H. Wang, and X. Wang. A chemo-mechanical free-energy-based approach to model durotaxis and extracellular stiffness-dependent contraction and polarization of cells. *Interface Focus*, 6(1):20150067, 2016. doi: 10.1098/rsfs.2015.0067.

X. Shi, Z. Liu, L. Feng, T. Zhao, C.-Y. Hui, and S. Zhang. Elastocapillarity at cell-matrix contacts. *Physical Review X*, 12:021053, 2022. doi: 10.1103/PhysRevX.12.021053.

R. Shuttleworth. The surface tension of solids. *Proceedings of the Physical Society. Section A*, 63(5):444, 1950. doi: 10.1088/0370-1298/63/5/302.

J.C. Simo and R.L. Taylor. Quasi-incompressible finite elasticity in principal stretches. continuum basis and numerical algorithms. *Computer Methods in Applied Mechanics and Engineering*, 85(3):273–310, 1991. doi: https://doi.org/10.1016/0045-7825(91)90100-K.

M. C. Skelton, R. E.and Oliveira. *Tensegrity Systems*. Springer New York, NY, 1 edition, 2009. ISBN 978-0-387-74242-7. doi: https://doi.org/10.1007/978-0-387-74242-7.

M. Soheilypour, M. Peyro, S.J. Peter, and M.R.K. Mofrad. Buckling behavior of individual and bundled microtubules. *Biophysical Journal*, 108(7):1718–1726, 2015. doi: 10.1016/j.bpj.2015.01.030.

D. Stamenović and D.E. Ingber. Models of cytoskeletal mechanics of adherent cells. *Biomechanics and Modeling in Mechanobiology*, 1:95–108, 2002. doi: 10.1007/s10237-002-0009-9.

D. Stamenović and D.E. Ingber. Tensegrity-guided self assembly: from molecules to living cells. *Soft Matter*, 5(6):1137–1145, 2009. doi: 10.1039/b806442c.

E. Staun-Ram and E. Shalev. Human trophoblast function during the implantation process. *Reproductive Biology and Endocrinology*, 3(1):56, 2005. doi: 10.1186/1477-7827-3-56.

R. W. Style and E. R. Dufresne. Static wetting on deformable substrates, from liquids to soft solids. *Soft Matter*, 8:7177–7184, 2012. doi: 10.1039/C2SM25540E.

R. W. Style, R. Boltyanskiy, Y. Che, J. S. Wettlaufer, L. A. Wilen, and E. R. Dufresne. Universal deformation of soft substrates near a contact line and the direct measurement of solid surface stresses. *Phys. Rev. Lett.*, 110:066103, 2013. doi: 10.1103/PhysRevLett.110.066103.

R. W. Style, A. Jagota, C.-Y. Hui, and E. R. Dufresne. Elastocapillarity: Surface tension and the mechanics of soft solids. *Annual Review of Condensed Matter Physics*, 8:99–118, 2017. doi: https://doi.org/10.1146/annurev-conmatphys-031016-025326.

S.-Y. Sun, L.-Y. Zhang, X. Chen, and X.-Q. Feng. Biochemomechanical tensegrity model of cytoskeletons. *Journal of the Mechanics and Physics of Solids*, 175:105288, 2023. ISSN 0022-5096. doi: 10.1016/j.jmps.2023.105288.

Y. Sun, Z. Liu, and L. Wang. A tensegrity-based mechanochemical model for capturing cell oscillation and reorientation. *Journal of Applied Physics*, 136(7):074701, 2024. doi: 10.1063/5.0210831.

R. Sunyer and X. Trepat. Durotaxis. *Current Biology*, 30(9):R383–R387, 2020. ISSN 0960-9822. doi: 10.1016/j.cub.2020.03.051.

P. Sáez and C. Venturini. Positive, negative and controlled durotaxis. *Soft Matter*, 19:2993–3001, 2023. doi: 10.1039/D2SM01326F.

D. T. Tambe, C. Corey Hardin, T. E. Angelini, K. Rajendran, C.Y. Park, X. Serra-Picamal, E. H. Zhou, M. H. Zaman, J. P. Butler, D. A. Weitz, J. J. Fredberg, and X. Trepat. Collective cell guidance by cooperative intercellular forces. *Nature Materials*, 10(6):469–475, 2011. doi: 10.1038/nmat3025.

E. Tanaka and M.W. Kirschner. The role of microtubules in growth cone turning at substrate boundaries. *Journal of Cell Biology*, 128(1):127–137, 1995. doi: 10.1083/jcb.128.1.127.

M. Théry, V. Racine, M. Piel, A. Pépin, A. Dimitrov, Y. Chen, J.-B. Sibarita, and M. Bornens. Anisotropy of cell adhesive microenvironment governs cell internal organization and orientation of polarity. *Proceedings of the National Academy of Sciences*, 103(52):19771–19776, 2006. doi: 10.1073/pnas.0609267103.

C. Venturini and P. Sáez. A multi-scale clutch model for adhesion complex mechanics. *PLOS Computational Biology*, 19(7):1–26, 2023. doi: 10.1371/journal.pcbi.1011250.

F. Verdugo, A. F. Martín, and S. Badia. Distributed-memory parallelization of the aggregated unfitted finite element method. *Computer Methods in Applied Mechanics and Engineering*, 357:112583, 2019. ISSN 0045-7825. doi: https://doi.org/10.1016/j.cma.2019.112583.

C. Villeneuve, A. Hashmi, I. Ylivinkka, E. Lawson-Keister, Y. A. Miroshnikova, C. Pérez-González, S.-M. Myllymäki, F. Bertillot, B. Yadav, T. Zhang, D. Matic Vignjevic, M. L. Mikkola, M. L. Manning, and S. A. Wickström. Mechanical forces across compartments coordinate cell shape and fate transitions to generate tissue architecture. *Nature Cell Biology*, 26(2):207–218, 2024. doi: https://doi.org/10.1038/s41556-023-01332-4.

N. Wang, K. Naruse, D. Stamenović, J. J. Fredberg, S. M. Mijailovich, I. M. Tolić-Nørrelykke, R. Polte, T.and Mannix, and D. E. Ingber. Mechanical behavior in living cells consistent with the tensegrity model. *Proceedings of the National Academy of Sciences*, 98(14):7765–7770, 2001. doi: https://doi.org/10.1073/pnas.141199598.

X. Wang. *Phase field models and simulations of vesicle bio-membranes*. The Pennsylvania State University, 2005.

Y. Wang, C. Liu, P. Liu, and B. Eisenberg. Field theory of reaction-diffusion: Law of mass action with an energetic variational approach. *Physical Review E*, 102(6), 2020. ISSN 2470-0053. doi: 10.1103/physreve.102.062147.

D. J. Webb, J. T. Parsons, and A. F. Horwitz. Adhesion assembly, disassembly and turnover in migrating cells – over and over and over again. *Nature Cell Biology*, 4(4):E97–E100, 2002. doi: 10.1038/ncb0402-e97.

M. D. Welch and R. D. Mullins. Cellular control of actin nucleation. *Annual Review of Cell and Developmental Biology*, 18(Volume 18, 2002):247–288, 2002. ISSN 1530-8995. doi: https://doi.org/10.1146/annurev.cellbio.18.040202.112133.

K. Wolf, I. Mazo, H. Leung, K. Engelke, U. H. von Andrian, E. I. Deryugina, A. Y. Strongin, E.-B. Broöcker, and P. Friedl. Compensation mechanism in tumor cell migration : mesenchymalamoeboid transition after blocking of pericellular proteolysis. *Journal of Cell Biology*, 160(2):267–277, 2003. doi: 10.1083/jcb.200209006.

X. Xu and T. Qian. Hydrodynamic boundary conditions derived from onsager's variational principle. *Procedia IUTAM*, 20:144–151, 2017. ISSN 2210-9838. doi: https://doi.org/10.1016/j.piutam.2017.03.020.

X. Xu, Y. Wang, and Y. Luo. Numerical modeling of force-stiffness response of cross-linked actin networks using tensegrity systems. *Mathematical Problems in Engineering*, 2015(1):182918, 2015. doi: 10.1155/2015/182918.

Z. Xu, F. Xu, and B. Cheng. The motor-clutch model in mechanobiology and mechanomedicine. *Mechanobiology in Medicine*, 2(3):100067, 2024. ISSN 2949-9070. doi: 10.1016/j.mbm.2024.100067.

K. M. Yamada and B. Geiger. Molecular interactions in cell adhesion complexes. *Current Opinion in Cell Biology*, 9(1):76–85, 1997. ISSN 0955-0674. doi: https://doi.org/10.1016/S0955-0674(97)80155-X.

K. M. Yamada and M. Sixt. Mechanisms of 3d cell migration. *Nature Reviews Molecular Cell Biologyl*, 20:738–752, 2019. doi: https://doi.org/10.1038/s41580-019-0172-9.

W. Yang, M. Luo, Y. Gao, X. Feng, and J. Chen. Mechanosensing model of fibroblast cells adhered on a substrate with varying stiffness and thickness. *Journal of the Mechanics and Physics of Solids*, 171:105137, 2023. doi: https://doi.org/10.1016/j.jmps.2022.105137.

M. Yao, B. T. Goult, H. Chen, P. Cong, M. P. Sheetz, and J. Yan. Mechanical activation of vinculin binding to talin locks talin in an unfolded conformation. *Scientific Reports*, 4(1):4610, 2014. ISSN 2045-2322. doi: 10.1038/srep04610.

X. Yi and H. Gao. Kinetics of receptor-mediated endocytosis of elastic nanoparticles. *Nanoscale*, 122, 2016. doi: 10.1039/C6NR07179A.

T. Young. An essay on the cohesion of fluids. *Philosophical Transactions of the Royal Society of London*, 95:65–87, 1805. doi: https://doi.org/10.1098/rstl.1805.0005.

L. Zhang, A. Gerstenberger, X. Wang, and W. Kam Liu. Immersed finite element method. *Computer Methods in Applied Mechanics and Engineering*, 193(21):2051–2067, 2004. ISSN 0045-7825. doi: https://doi.org/10.1016/j.cma.2003.12.044. Flow Simulation and Modeling.

S. Zhang, H. Gao, and G. Bao. Physical principles of nanoparticle cellular endocytosis. *ACS Nano*, 9(9):8655–8671, 2015. doi: 10.1021/acsnano.5b03184.

Scientific Production

International Journals Publications

1. Benvenuti E. and Reho G.A., An elastic-damaging cohesive law for cell-substrate adhesion with positive and negative durotaxis. *Journal of the Mechanics and Physics of Solids*, 185:105569,2024.
doi: https://doi.org/10.1016/j.jmps.2024.105569

2. Benvenuti E., Reho G.A., Palumbo S. and Fraldi M., Mechanics of tensegrity cell units incorporating asymmetry and insights into mollitaxis, *Journal of the Royal Society Interface*, 20:20230082, 2023.
doi: https://doi.org/10.1098/rsif.2023.0082

3. Benvenuti E., Reho G.A., Palumbo S. and Fraldi M., Pre-strains and buckling in mechanosensitivity of contractile cells and focal adhesions: A tensegrity device, *Journal of the Mechanical Behavior of Biomedical Materials*, 135:105413, 2022.
doi: https://doi.org/10.1016/j.jmbbm.2022.105413

Conferences/Workshops with Peer Review

1. Reho G.A. and Benvenuti E., Modelling the mechanobiology of cell-substrate adhesion through elastic-damaging cohesive laws. *Proceedings of the XXVI Congresso AIMETA 2024*, In Press.

Manuscripts in Preparation

1. Reho G.A., Blanco P. and Arroyo M. "A Hybrid Fitted-CutFEM Framework for Elastocapillary Problems in Mechanobiology." (Working Title). Expected submission: 2026.

2. Reho G.A., Blanco P. and Arroyo M. "The Mechanics of Collective Invasion: Competition Between Elastocapillary Indentation and Active Degradation." (Working Title). Expected submission: 2026.

Abstract in Conferences

1. Reho G.A., Blanco D.P. and Arroyo B.M., Invasive Behaviour of an Active Biological Tissue Into an Elastic Matrix: Competition Between Degradation and Indentation. Abstract Submitted to Young Investigators Conference, Pescara, Italy, September 17-19 2025.

2. Reho G.A., Blanco D.P. and Arroyo B.M., Competition between degradation and indentation in the invasive behaviour of an active biological tissue. Abstract Submitted to the 1st HICOMP Conference, Rhodes, Greece, June 19-21 2025.

3. Reho G.A. and Benvenuti E., Modelling the mechanobiology of cell-substrate adhesion through elastic-damaging cohesive laws. Abstract Submitted to XXVI Conference AIMETA, Napoli, Italy, September 2-6, 2024.

4. Reho G.A. and Benvenuti E., Elastic-damaging cohesive law for cell-substrate adhesion: positive and negative durotaxis. Abstract Submitted to GIMC SIMAI Young 2024, Napoli, Italy, July 10-12 2024.

5. Benvenuti E., Reho G.A., Palumbo S. and Fraldi M., Durotaxis of tensegrity cell units incorporating asymmetry. Abstract Submitted to the Convegno GIMC GMA GBMA, Reggio Calabria, Italy, July 12-14 2023. ISBN 978-88-99352-95-0.

6. Benvenuti E., Reho G.A., Palumbo S. and Fraldi M., A tensegrity contractile device for pre-strained cells linked to focal adhesions Abstract Submitted to XXV Convegno AIMETA, Palermo, Italy, September 4-8, 2022.

Poster

1. Reho G.A. and Benvenuti E. Elasto fracturing adhesion and durotaxis of cell ECM systems. Colloquium 638 Cellular Mechanobiology and Morphogenesis, Sirmione, Italy, August 21-24, 2023.